The Dissertation Committee for Vasileios Samaras Certifies that this is the approved version of the following dissertation:

Computation of Vehicular-Induced Vibrations and Long-Term Instrumentation Reliability for Structural Health Monitoring of Highway Bridges

Committee:

Todd A. Helwig, Supervisor

Sharon L. Wood, Supervisor

Karl H. Frank

Michael D. Engelhardt

Richard H. Crawford

Computation of Vehicular-Induced Vibrations and Long-Term Instrumentation Reliability for Structural Health Monitoring of Highway Bridges

by

Vasileios Samaras, D.C.E.; M.S.E.

Dissertation

Presented to the Faculty of the Graduate School of

The University of Texas at Austin

in Partial Fulfillment

of the Requirements

for the Degree of

Doctor of Philosophy

The University of Texas at Austin

August 2013

Dedication

To my sister who inspired me to follow my dreams

and

To my parents for their enduring encouragement and support

Acknowledgements

I would like to express my deep appreciation to the National Institute of Standards and Technology for sponsoring this project. I am grateful to have had the unique chance to be part of this research program. Over the last few years, I gained a lot of experience by visiting, instrumenting, testing, and analyzing highway bridges.

I would like to express my gratitude to my supervising professors Dr. Helwig and Dr. Wood. Dr Helwig is a great mentor to me. His personal interest in my progress within and beyond this research project encouraged me to progress as an engineer. Dr. Wood's guidance and sincere advice were very important for my research. I also want to thank my Doctoral Committee, Dr. Frank, Dr. Engelhardt, and Dr. Crawford for their valuable comments and suggestions.

I am very thankful and fortunate to have Jeremiah Fasl, and Matt Reichenbach as research partners. Their personality and willingness to work hard made every field trip very enjoyable and successful. The scene of Jeremiah driving the lab truck to the site while the radio plays the famous Bobby Bones show, and Matt taking a power nap on the back seat, will be unforgettable. I would like to acknowledge the rest of the research project team, including Dr. Dean Niekirk, Dr. Kristin Wood, Dr. Praveen Pasupathy, Rich Lindenberg, David Potter, Ali AbuYousef, Jason Weaver, Eric Dierks, Travis McEvoy, Krystian Zimowski, Sumedh Inamdar, Ye Chen.

The staff of Ferguson Engineering Laboratory, Barbara Howard, Jessica Hanten, Michelle Damvar, Anise Langley, Andrew Valentine, Eric Schell, Mike Wason, Blake Stasney, and Dennis Fillip, deserve my thanks for their continual support.

Finally, several great friends from UT should be acknowledged because they contributed both academically and socially to my pleasant Austin experience. Andres Stambuk for the Saturday bike rides around Austin, Arcan Bundur for the unlimited MSc adventures, Perla and Lalo for exposing me to the Mexican traditions, Hrag Hayrabedian for showing me the “positive” side of life, Chungwook and Jisun Kim for the delicious Korean food, In addition, Taner Sensoy and Enes Hosgor for improving my chakal aspect, Christian Vazquez for the salsa dancing advices, Jose and Ailenne Gallardo for the great smile and food gatherings, Jaime Barredo for the soccer games and the amazing roadtrip. Finally, I want to express my gratitude to Kostas Belivanis, George Zalachoris, Michalis Hadjioannou, George Moutsanidis, and Stergios Koutrouvelis for reminding me the Greek way of living.

Computation of Vehicular-Induced Vibrations and Long-Term Instrumentation Reliability for Structural Health Monitoring of Highway Bridges

Vasileios Samaras, PhD

The University of Texas at Austin, 2013

Supervisors: Todd A. Helwig, and Sharon L. Wood

Real-time monitoring of fracture critical steel bridges can potentially enhance inspection practices by tracking the behavior of the bridge. Significant advances have occurred in recent years on the development of robust hardware for field monitoring applications. These systems can monitor, process, and store data from a variety of sensors (e.g. strain gages, crack propagation gages etc.) to track the behavior of the bridge. The research outlined in this dissertation is part of a large study focused on the development of a wireless system for use in long-term monitoring of bridges. The wireless monitoring system had a target maintenance-free life of ten years, and independent from the power grid. Thus, the feasibility to harvest energy for the monitoring system is an important step in the development of the system. In addition, the reliability of the sensors in the bridge is very important upon the success of the system.

The focus of this dissertation is on two primary aspects of the wireless monitoring system. First, the feasibility to harvest energy from vehicular-induced vibrations is evaluated through analytical models of highway bridges under truck loads. Acceleration results from simple line-element models and detailed finite element models of five steel bridges in Texas and Oregon are compared with actual field data from the same bridges.

Second, the dissertation also highlights studies on the identification of strain gages and installation procedures that result in long lives. In addition, the effect of temperature fluctuations and other environmental factors on the sensor drift and noise is also considered. In long-term monitoring applications, slight sensor drift and noise can build up over time to produce misleading results.

This dissertation presents the results of transient dynamic analyses of bridges under moving truck loading and laboratory tests on gage durability that were conducted as part of a research project sponsored by the National Institute of Standards and Technology (NIST).

Table of Contents

List of Tables

List of Figures

CHAPTER 1

Introduction and Research Motivation

1.1. INTRODUCTION

A series of major expansions began taking place on the interstate highway system in the United States (US) at the end of 1950s (Weingroff, 1996). The dependence of the public on the transportation network for commuting, traveling, and transportation of goods and services has progressively increased since these expansions and the highway system has become a critical element of the country's infrastructure. Highway bridges serve as a vital component of the US transportation system because they provide passage over obstacles such as rivers and other geological features, or other roadways. Therefore, maintaining and keeping the bridges functional is one of the primary roles for the state departments of transportation (DOTs) and bridge owners. Two of the primary responsibilities of bridge owners are safety of the traveling public as well as minimizing the economic costs associated with traffic disruptions due to maintenance issues associated with deterioration in the bridge infrastructure. According to Kowalik (2009), a typical cost for a single inspection of a bridge is approximately $22,000. The cost per bridge may not seem high, but if it is taken into account that more than 300,000 bridges must be inspected every year, then the total inspection cost increases dramatically. This inspection cost only includes the cost of man power, travel time, and other equipment associated with the inspection. Gaining access to the structural components of the bridge often requires special equipment as shown in Figure 1-1. Another costly aspect of routine inspections is traffic control to protect the maintenance crews conducting the inspections as well as the traveling public. The approximate cost of traffic control is $2,500 per inspection (Kowalik, 2009). In some cases, the inspection may require multiple traffic

control set ups. Finally, the road user cost (RUC) is a substantial economic consequence of bridge inspection. According to NCHRP (1972) and NJDOT (2001) the RUC per hour for a passenger car and a semi-truck is approximately $19 and $52 respectively. These average values change as a function of the length of the work zone, the length of the detour, and a number of other factors. For example, the cost to displaced sum cost to motorists who depended on I-35W Bridge in Minneapolis was estimated to be approximately $400,000 per day (Olson, 2008).

Figure 1-1: Current inspection practices for fracture critical bridges

1.2. RESEARCH MOTIVATION

1.2.1. Current inspection practices – Aging infrastructure

The National Bridge Inspection Program was initiated in 1967, after the collapse of the Silver Bridge in Point Pleasant, WV and included major changes to the inspection and maintenance procedures for bridges. Subsequent failures of the tension elements of other bridges raised concerns and led to the establishment of additional new provisions. These new provisions required the increase of the material toughness and fabrication standards for critical members. Moreover, they required more stringent inspections

during construction as well as hands-on inspection during the service life of such bridges. In 1970, the American Association of State Highway and Transportation Officials (AASHTO) for the first time used the term 'fracture critical bridge' to describe a bridge which is likely to collapse if a tension component fractures (AASHTO, 2012).

As of 2009 (LePatner, 2012), there are approximately 18,000 fracture critical bridges across the US that require a detailed inspection at least once every two years regardless of their age or condition. The objectives of the inspection are to identify and track fatigue cracks in the tension elements and to evaluate the remaining life of those fracture critical components of a bridge. The inspections are important for the structural integrity of the bridge, yet are labor intensive and extremely expensive for the owners and the public.

Moreover, as bridges approach the end of their design service life, the risks of deterioration are expected to be higher. As of 2012, there are 605,086 bridges across the United States (FHWA, 2012) owned by State or local agencies. This number does not include bridges that are locally owned. A substantial number of these bridges have exceeded 50 years of service life as shown in Figure 1-2. In addition, FHWA (2012) reported that 67,526 bridges (i.e. 11.2% of total bridges population) and 76,363 bridges (12.6% of total bridges) were respectively classified as structurally deficient and functionally obsolete. Structurally deficient and functionally obsolete are two definitions used in the current bridge rating system. The first definition is used to describe bridges that require significant maintenance, rehabilitation or replacement, and the second definition is employed to show that the design of a bridge is not suitable for its current use (e.g. inability to handle current traffic volume, speed, size, or weight). Consequently, 23.8% of the bridges across US require immediate attention or repair to ensure public safety. Since it is not economically feasible to replace all the older bridges, new

approaches to maximize the safety and service life of each bridge must be developed. This suggests a need for effective and reliable structural health monitoring systems to identify problems at early stages and prevent possible failures by prioritizing the rehabilitation/replacement of bridges.

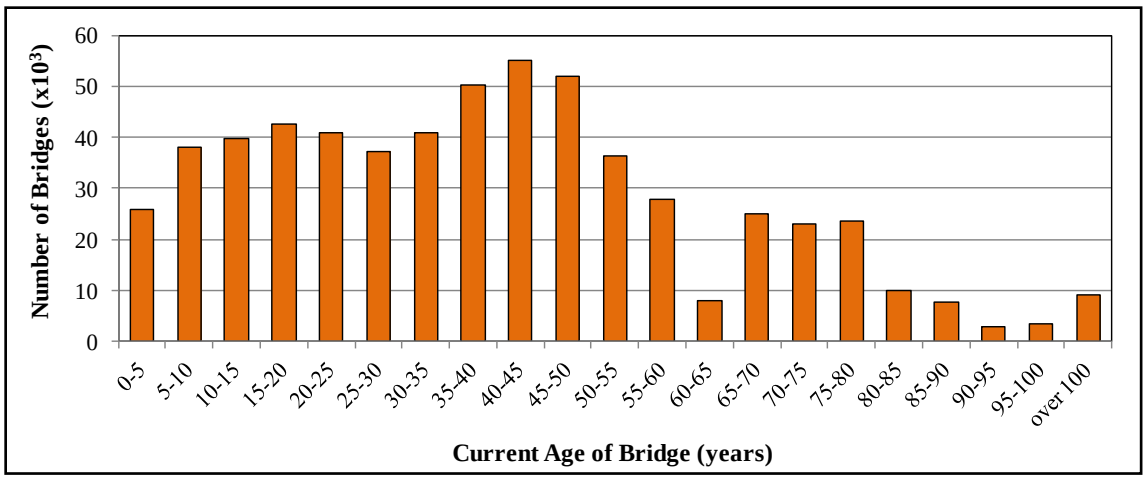

Figure 1-2: Age distribution of bridges across USA (National Bridge Inventory, 2012)

The scope of this research project is to develop a monitoring system that compliments the current inspection practices. Based on the current inspection practices, the accumulated damage is only evaluated at discrete points in time. The lack of continuous monitoring could lead to a loss of important information on damage that occurs between inspections. Additionally, the existing provisions for inspection intervals are independent of the age or fatigue performance of the bridge. Thus, utilizing a monitoring system to obtain information of the bridge condition can help bridge owners to use their resources more efficiently. Finally, the rating system established by the National Bridge Inspection (NBI) Program to evaluate the condition of bridges has a high degree of variability. This is due to the fact that the condition rating is assigned by the inspectors based on their engineering judgment and experience. Even if inspectors have

extensive training and references to guide them how they can correctly rate bridges, there is a high possibility of inconsistency between assessments (e.g. bridge defects may be overlooked) due to human error (Al-Wazeer et al., 2008). Hence, the NBI rating system can potentially result to erroneous bridge assessment.

1.2.2. Advances in wireless monitoring

Wired monitoring systems have been utilized in the past to detect structural damage to bridges. In wired systems, each sensor is directly connected (or hard wired) to the data acquisition system. However, in larger structures such as bridges, the cost of installing and maintaining the large amount of required wiring in these systems is very high and can exceed the cost of the other components of the monitoring system. An alternative method to monitor structures is through a wireless monitoring system. Since the late 1990's, significant advances have occurred in wireless monitoring systems. The most significant advances are:

- The radio transmission technology has been improved allowing the wireless monitoring systems to transmit a signal over a longer distance.
- The memory capacity of wireless node has increased permitting data processing at local level.
- The power consumption of monitoring system components (e.g. gateway, wireless nodes) decreased resulting to a more economical system because the span between battery replacements has been extended.

These advances lowered the cost of monitoring applications and improved the installation efficiency compared to hard wired systems. The instrumentation can be installed without the necessity of distributing wiring throughout the bridge. Even though it is required to periodically replace the batteries of wireless nodes, the cost of battery is less than the cost

of replacing or maintaining the cables of a wired system. In addition, the likelihood of confusion and trouble shooting in sensor locations is greatly reduced since wiring errors are virtually eliminated. Thus, the cost associated with instrumentation has the potential to be minimized due to reductions in the costs of wiring and installation times. Though,

1.2.3. Development of a wireless structural health monitoring system

This dissertation presents results from a research study focused on the development of a reliable, economical, low-power wireless system for long-term monitoring of bridges. More specifically, the two main objectives of this project were to develop a monitoring system with at least a 10-year maintenance-free life and independent from the power grid. These two important conditions have the potential to keep the system efficient and economical. For example, in the case of a remote bridge it would not be economical to require the dispatch of a crew for frequent maintenance issues. In addition, many of remote sites may not have direct access to the power grid. As depicted in Figure 1-3, the resulting wireless monitoring system includes the following five components:

a) Remote access
b) Gateway/controller
c) Router node
d) End nodes
e) Sensors

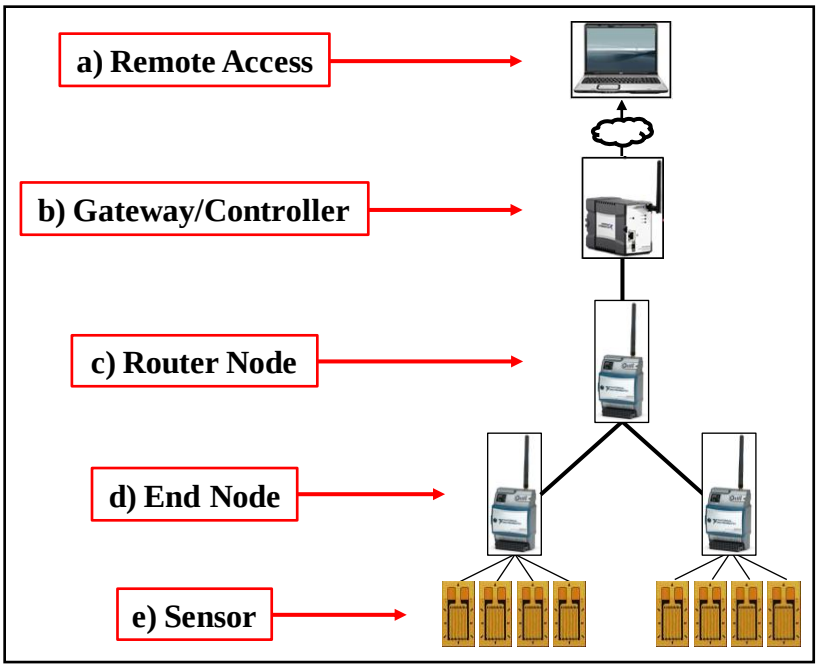

Figure 1-3: Schematic of the wireless monitoring system components

The sensors are installed at the critical locations of the bridge. In many situations the target data of interest will include changes in strain that can be measured with strain gages, or crack growth that can be monitored using crack propagation gages. The nodes and routers used in this investigation are Wireless Sensor Network (WSN) nodes developed by National Instruments (NI) (Figure 1-4). For the purposes of this research project, two different types of WSN nodes were used. One was the programmable strain node (NI WSN-3214) and the other the programmable thermocouple node (NI WSN-3212) (National Instruments, 2012). The WSN nodes can be configured either as end nodes or router nodes. The end nodes transmit data to nearby router nodes or gateway(s) whereas the router nodes receive data from nearby nodes and pass them on to the gateway(s), creating an efficient and reliable network mesh. Both node configurations

can collect raw data from sensors, subsequently process them, and then transmit them along the length of the bridge.

Figure 1-4: NI WSN node

1.3. PROJECT OVERVIEW

In order to develop a wireless monitoring system that can monitor fracture-critical bridges, the National Institute of Standards and Technology (NIST) funded in a research project beginning in February 2009 that is entitled "Development of Rapid, Reliable and Economic Methods for Inspection and Monitoring of Highway Bridges". The research project is a joint venture between the Civil, Architectural, and Environmental Engineering, Mechanical, and Electrical Engineering Departments of the University of Texas (UT) at Austin, National Instruments (NI), and Wiss, Janney, Elstner Associates (WJE). The main objective of this research project is to develop a structural health monitoring system and necessary algorithms to monitor and evaluate the performance of fracture-critical bridges and in some cases to estimate the remaining life. The developed system compliments and improves the inspection practices, allowing bridge owners to more efficiently utilize their resources while improving the safety of the civil infrastructure system. Although this research project focused on fracture-critical bridges, the monitoring system, damage detection algorithms, and knowledge can also be applied to a variety of other types of structural systems.

1.4. DISSERTATION OBJECTIVES

The direct cost associated with instrumenting a bridge with sensors and deploying a wireless structural health monitoring system can be relatively high. However, there are significant benefits gained from obtaining data in real time between visual inspections. The monitoring data, after being analyzed by an engineer, can provide significant information that helps the engineer to make crucial decisions to prevent structural failures and to minimize danger to the traveling public. However, for economy, the developed wireless system should be reliable and require low power, thereby requiring the following requirements. First, the life-cycle costs must be minimized by minimizing the maintenance costs. A ten-year service life was one of the requirements set for the developed system at the beginning of the research study. Second, to minimize operational costs, it is required for the system to be low power and independent of the power grid. In order to achieve this goal, researchers within the UT Mechanical Engineering Department was tasked with researching potential methods to harvest energy (e.g. solar, wind, vibration, etc) to sufficiently power the system for ten years. Last, the sensors and hardware of the monitoring system must provide reliable data and have sufficient durability to withstand the environmental effects of the bridge site.

1.4.1. Energy harvesting methods

As mentioned before, requiring access to the power grid to power the wireless sensor network system needs is not practical for many of the components in the infrastructure system. Many bridges in remote locations do not have access to the power grid. The researchers have been studying three different energy sources for harvesting:

a) Solar energy
b) Wind energy
c) Energy due to vehicular induced vibrations

Each of these energy types has different features as well as advantages and disadvantages. Multiple sources were investigated since the presence of the individual sources is highly variable depending on the location of the instrumentation on the structure as well as the location of structure itself. For example, although a large solar panel can power the entire wireless system, running cables from the solar panel to each node and gateway would defeat the purpose of developing a wireless system. In addition, depending on the geographical location of the bridge, the solar exposure during certain months is greatly diminished and may limit the practical aspects of solar energy harvesting. The next section provides information regarding the power requirements of each component of the developed wireless system and the suggested energy source.

1.4.2. Power requirements of structural health monitoring system

The hardware components of the structural health monitoring (SHM) system were developed by National Instruments (NI). The main devices are the gateway, the modem, and the nodes. Based on specification tests, it was found that the modem and gateway together require approximately 12-15 W of operational power. The other primary components of the system are the programmable WSN strain node (NI WSN-3214) and the programmable thermocouple node (NI WSN-3212). The power consumption of these elements depends highly on the way they are configured to operate. UT researchers investigated the power requirements of the WSN nodes and found the required power for various activities. Weaver et al. (2010) and Dierks (2011) computed the functional requirements and found that the average power of a WSN node configured as a router node (i.e. the radio is always on) is 207mW, whereas the average power for the node to acquires one sample per day and goes into deep sleep mode for the rest of the time is only 9 μW, which is different by more than a factor of 20000. However, because the deep

sleep mode is not yet fully developed, the average power consumption of a WSN node configured as an end node is approximately 0.5 mW, which is still different by a factor of over 400.

1.4.3. Feasibility of energy harvesting

Due to the high power requirements of the gateway and modem, the employed energy harvester should offer high power densities. Among the three alternative energy solutions, only the solar panels can provide adequate energy to power the gateway and modem. Solar panels have been widely used for harvesting power from the environment and the technology has been well-studied. Inamdar (2012) considered the requirements for the modem and gateway of the developed system and determined the following system requirements: a 120W Polycrystalline Photovoltaic (PV) panel, a 120 A-hr Lithium Iron Phosphate (LiFePO4) battery bank, an optimal solar tilt angle 15 degrees higher than the location latitude and 0 degrees solar azimuth angle (i.e. south), and an maximum power point tracking (MPPT) controller. Energy from wind and vehicular-induced vibrations do not generally offer power densities near this level, and therefore these sources can only be utilized to power the WSN nodes.

Wind energy may be produced due to either ambient or vehicular-induced wind. Initial field test data showed that the ambient wind is the dominant source to harvest in bridges. One of the project requirements for energy harvesting was the minimization of cable distance between harvester and monitoring system components (e.g. WSN node). Thus, in a typical bridge instrumentation the wind harvester should be mounted on a bridge component (e.g. cross frame, stiffener) near the WSN node location. Another requirement for wind energy harvesting was the position of the wind harvester. In most situations the wind harvester blades cannot extend below the bottom flange of the girder

due to clearance issues from truck traffic below the bridge. McEvoy (2011) found that the power generated by a wind harvester is highly dependent on the depth of the bridge girder. Thus, installing the wind harvester at these locations decreases its efficiency due to shielding effects. However, Zimowski (2012) found that an 18-in. radius horizontal axis wind turbine (HAWT) is the most efficient turbine type to harvest wind energy. Harvesting wind energy with this HAWT type for one hour at an average wind speed of 8 mph and storing it to a battery is adequate to power a WSN node that is configured as a router node.

The other method to power the WSN nodes is to harvest energy from vehicular-induced vibrations. As mentioned above, both vibration and wind energy do not generally provide the high power densities associated with solar energy. Based on Roundy et al. (2003), the average energy produced by a solar panel is approximately 60 times higher than the energy harvested by vehicular-induced vibrations. However, one of the major advantages of a vibration harvester is the relatively small size that makes it possible to be placed close to the WSN node, minimizing the amount of cable needed to deploy the system. On the contrary, the main disadvantage of utilizing a vibration energy harvester on a bridge environment is the variability of dynamic response as a function of the location on the bridge, and the time of the day (i.e. higher traffic volume during morning than night). Some locations on the bridge do not vibrate with sufficient amplitude for the energy harvester to produce adequate energy to power the WSN node.

One of the main objectives of this dissertation is to dynamically analyze bridges under moving truck loads, to characterize the dynamic response of different bridge types and compute the feasibility to power the WSN node utilizing a vibration harvester. The feasibility results are achieved by comparing the computed vibration energy with the power requirements of the WSN node as outlined previously. The best method to

characterize the dynamic response of a specific structural system is to obtain detailed results through field instrumentation. However, although field instrumentation may provide the most accurate results, obtaining the necessary data requires substantial effort and time. A more practical approach is to develop guidelines so that an engineer can obtain an estimate of the dynamic behavior through an analysis of the idealized structural system. Although detailed structural models can be developed for the structural system, for practicality, the necessary model should be as simple as possible. If the analytical models are adequate to compute the vibrational characteristics at different locations in the structure, then engineers can predict the feasibility to power a WSN node through vibration energy and potentially save a significant amount of time. Otherwise, a more detailed field instrumentation using accelerometer is needed to determine the dynamic characteristics of bridge components.

For this dissertation, a set of guidelines is developed to compute the dynamic response of bridge components by comparing the results including both simple and detailed analytical models. Field data were recorded through four in-service instrumentations of bridges around Texas and Oregon. The bridges were instrumented with accelerometers to capture the vehicular-induced vibrations and monitor the dynamic characteristics of different bridge components. These field data provide important information in the calibration of the analytical models presented in this dissertation.

1.4.4. Instrumentation methods

As previously mentioned, a significant portion of the highway bridges in the US has exceeded or is near to the end of their design life. Thus, more attention should be given when inspecting these aging bridges. Currently, the federal requirements for periodic bridge inspections have three major limitations. First, there is no distinction

among bridges for the rate of damage or the accumulated damage of the bridge. Second, the fixed inspection intervals cannot capture accumulated damage between intervals and escalating damage may be missed leading to severe structural issues and danger to the traveling public. Third, there is no distinction on the inspection intervals for the age of the bridge. An effective approach to mitigating problems associated with these limitations is to utilize recent technological developments in real-time monitoring. Using this technology, the inspection practices can be enhanced, thereby improving the public safety by reducing the risk of severe structural issues.

There are different ways to monitor structures to assess the damage accumulation and the risk of failure. In the past, researchers and bridge owners have used accelerometers, strain gages, acoustic sensors, and video cameras to detect structural damage. These sensors have different features and as well as varying installation and power requirements. The envisioned monitoring system is desired to be low power, free of the power grid, and to possess a minimum ten-year maintenance-free life. Thus, utilizing sensors such as accelerometers, which require more power to operate, defeats the purpose of a low power system. Several low-power sensors were reviewed at the beginning of this research project. Among all the sensors that were considered, it was concluded that bondable foil gages, sealed weldable/bondable gages (Figure 1-5), and crack propagation gages (Figure 1-6) can potentially satisfy the requirements of the envisioned system.

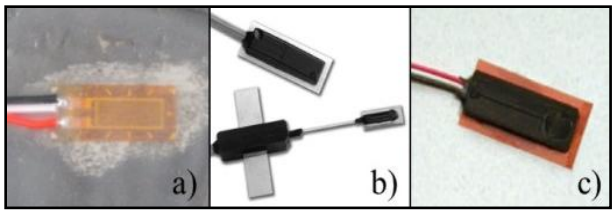

Figure 1-5: Types of strain gages, a) bondable foil gage, b) sealed weldable gage with or without amplification, c) sealed bondable gage.

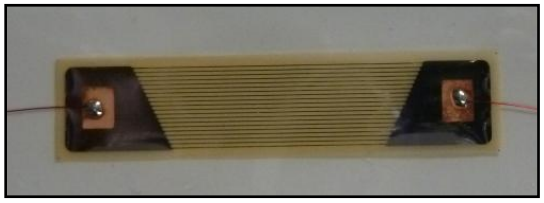

Figure 1-6: Crack propagation gage

1.4.5. Long-term reliability of strain gages of sensors.

The success of a monitoring system is dependent on the reliability of the measured data. The use of measured data can provide the owner with information on how to prioritize bridge inspections or even rehabilitations based upon performance and traffic demand. For the system to be successful and free of maintenance for ten years, the gages must also operate properly for the same life span. The gage can remain functional, if it is properly protected against environmental contaminants, such as moisture, with protective coatings that can be applied on top of the gage. In order to investigate the durability and the performance of different protective coating types and gages, a series of tests were developed as part of this research project. Additionally, during these tests the effect of temperature fluctuations, loading conditions, and gage location on the gage performance was examined.

1.5. ORGANIZATION OF THE DISSERTATION

There are two main goals in this dissertation. The first goal is the development of bridge modeling guidelines for obtaining the dynamic characteristics of the bridge locations where the energy harvester will be installed, and to estimate the vehicular-induced energy. The second goal is to evaluate the performance and durability of several sensors that can potentially be used to instrument bridges, and determine the advantages and disadvantages of each type of sensor.

The dissertation is divided into seven chapters. Following this introductory chapter, background information of vehicular-induced energy harvesting, dynamic analysis of bridges under moving loads, instrumentation of structures, types of sensors and protective coatings is provided in Chapter 2. Moreover, an extensive description of previous work conducted on vibration energy harvesting characterization, bridge modeling (e.g. simple line element vs. detailed finite element model), and sensor durability is presented.

The four bridges from that states of Texas and Oregon that were instrumented during this research project to obtain acceleration histories are discussed in Chapter 3. The scope of the field instrumentations was first to determine the dynamic response of typical bridges, and second to compare the field data with the analytical results and calibrate the analytical models. Typical acceleration history data of each bridge are provided.

A summary of the methods to analyze bridges in order to estimate the vibration power potential is provided in Chapter 4. A description of the two main modeling methods (a simple line element model vs. a detailed model) as well as the comparison of the two methods is given in this chapter. Finally, the dynamic analyses results and the comparison with the field data are presented.

The sensor types that can be used in a bridge long-term monitoring are introduced and discussed in Chapter 5. The chapter also includes a detailed description of the durability tests that were carried out on each sensor. The results of the durability tests are then presented in Chapter 6. Methods to eliminate thermally-induced strain are also discussed in Chapter 6. Finally, in Chapter 7, conclusions from this research are presented along with recommendations for future work.

CHAPTER 2

Background and Literature Review

2.1. INTRODUCTION

The research documented in this dissertation is part of a larger study at the University of Texas at Austin focused on the development of a structural health monitoring (SHM) system to enhance bridge safety and inspection practices. Part of the research program was to investigate the feasibility to power sensor nodes through vibrational energy harvesting, as well as to examine the durability and the reliability of several sensors. A detailed discussion of these two topics is presented in this dissertation. Background information and a review of literature from previous research conducted on bridge vibrational analyses, vibration energy harvesting, as well as durability and reliability of sensors is provided in this chapter so that the reader can better understand the scope of the dissertation.

2.2. VEHICULAR-INDUCED VIBRATION HARVESTING METHODS

There has been a significant amount of work focused towards the harvesting of energy from mechanical vibrations. Many companies have developed vibration energy harvesters for motor-type applications where high-frequency and high-amplitude steady-state vibrations occur. Based on the literature review, it was found that current trends tend to optimize existing technology rather than exploring other features of the vibration energy harvesting. However, in the recent years more researchers have examined energy harvesting from transient vibrations (e.g. vehicular-induced bridge vibrations). Harvesting energy from transient vibrations can be relatively challenging due to the fluctuation of vibrations. Roundy et al. (2003) investigated the feasibility to power wireless sensor nodes from low amplitude transient vibrations. He examined two

different types of harvesters, piezoelectric and capacitive converters. He concluded that the piezoelectric converters are more efficient than the capacitive converters because the output energy per unit volume is greater, and it is more possible to integrate capacitive converters into microsystems. Thus, the engineer should take into consideration the advantages and disadvantages of each mechanical energy conversion type before developing a vibration energy harvester. In general there are four major types of energy conversion, namely electrostatic or capacitive, magnetostrictive, piezoelectric, and electromagnetic or inductive.

Electrostatic/capacitive conversion is the process of harvesting energy based on the change in capacitance of vibration-dependent varactors. Varactor is a semiconductor device, also known as tuning diode, designed to be used as a voltage controlled capacitor. The capacitance variation is caused by a change in charge or voltage due to the relative motion of the harvester components. In other words, the components of the varactor separate due to the bridge vibrations and the mechanical energy is converted into electrical energy. Typically, capacitive mechanical energy conversion produces smaller power densities compared to the other types.

Magnetostrictive conversion uses the magnetostrictive property of ferromagnetic materials. The magnetostriction causes the ferromagnetic material to change its geometry during the process of magnetization and as a result power is produced. Yet, this type of mechanical energy conversion is very difficult to incorporate into a vibration energy harvester because the harvester size should be very large to produce adequate energy. The size limitation is the main reason why this technology is not used as widely as the other types.

Piezoelectric energy is produced by converting mechanical strain into electric current or voltage. Most piezoelectric harvesters are cantilever beams embedded with

piezoelectric material at the areas of high strain (Weaver et al., 2010). For optimum energy conversion, the natural frequency of the cantilever should match the dominant frequency of the source location (i.e. bridge). That can be achieved by changing the length and mass of the cantilever beam. Lastly, the majority of the piezoelectric harvesters are able to produce power on the order of milliwatts.

The last type of mechanical energy conversion is the electromagnetic conversion. This type utilizes Faraday's Law of Induction to produce energy through the movement of a magnet relative to a coil. This relative motion between the magnet and the coil provides a rate of change of flux, which results in voltage at the ends of the coil. This technology is widely used in daily life (e.g. shake flashlight). Moreover, Dierks (2011) concluded that the best option to harvest energy from low-frequency and low-amplitude vibrations is to utilize inductive-based harvesters.

Researchers in the Department of Mechanical Engineering (ME) of UT Austin (Dierks, 2011) developed an inductive-based vibration energy harvester. In order to optimize the design of the energy harvester, the research team first investigated transient vibrations of typical highway bridges to understand the source of energy, and second, examined parameters of the harvester that affect its efficiency (e.g. effect of shaft bearing on frictional losses). More details of the UT harvester are provided in the following section.

2.3. THE UT AUSTIN VIBRATION ENERGY HARVESTER

As mentioned above, researchers in the Mechanical Engineering (ME) Department of UT Austin developed a vibration energy harvester (Figure 2-1) as part of this research project. Based on previous research on bridge vibration and initial field instrumentation of bridges, it was concluded that vehicular-induced accelerations are low

amplitude and low frequency vibrations. Hence, the ME research team decided to develop an energy harvester based on the electromagnetic inductive principles and optimized its performance at low frequencies.

Figure 2-1: UT Austin vibration energy harvester (Dierks, 2011)

2.3.1 Specifications of the UT Austin vibration energy harvester

Figure 2-1 shows a prototype of the UT Austin vibration energy harvester that consists of a cylindrical housing. The housing is approximately 12-in tall and with a 3-in diameter and has two adjustable fixtures for mounting the harvester on a bridge element. The cylindrical housing contains a spring, a shaft, series of magnets and iron rotors, and coils. Figure 2-2 illustrates a schematic of the UT energy harvester. The bridge vibrates due to the vehicular-induced motions inducing the magnet to move relative to the coil inside the housing. The magnet motion changes the magnetic environment of the coil and as a result voltage is induced in the coil. The main function of the spring is to introduce damping into the system. The damping mainly depends on the specified spring stiffness. Given that the vehicular-induced vibrations of the bridge are sporadic, the researchers in the ME Department integrate a lithium-ion battery into the system to utilize its energy to

power the WSN nodes during low-traffic times. The total weight of the vibration energy harvester is between 10 and 15 lb.

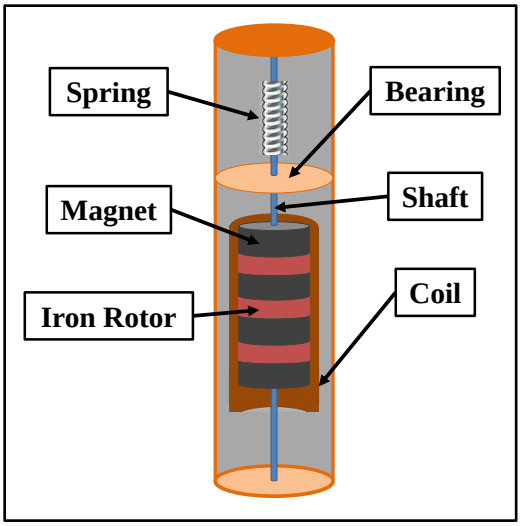

Figure 2-2: Schematic of the UT Austin vibration energy harvester (Dierks, 2011)

To optimize the design of the vibration energy harvester, two main pieces of information are needed, the amplitude of accelerations and the dominant frequencies of vibrations. Field instrumentation of bridges provided acceleration data that were used to determine the amplitude of transient vibrations. In addition, Reichenbach (2012) performed spectral analyses on the recorded acceleration data to determine the dominant frequencies of the bridge vibrations. Consequently, the harvester should be tuned to a dominant frequency in order to produce the maximum possible energy. The developed harvester is a single degree-of-freedom system (i.e. vertical motion) and thus it has a single fundamental frequency. Equation 2-1 relates the fundamental frequency (f_h) of the single degree-of-freedom system with the spring stiffness (k_s) and mass (m).

$$f_h = \frac{1}{2\pi}\sqrt{\frac{k_s}{m}} \qquad \text{Equation 2-1}$$

Knowing the spring stiffness and the moving mass, the fundamental frequency of the harvester can be calculated based on Equation 2-1. The dominant frequency of the harvester can be adjusted to be close to the dominant frequency of the bridge location that the harvester will be mounted by either changing the spring stiffness or the moving mass. The latter is not practical due to the tight fitting of the magnet and iron rotor array into the coil. Dierks (2011) decided that it is more conventional to adjust the spring stiffness. He fabricated the harvester such that the spring stiffness can be externally adjusted by twisting the end cap.

The harvester response depends primarily on the spring stiffness, the mass of magnets and iron rotors, and the damping. The damping has two components contributing to the total damping, the mechanical and the electrical damping. The mechanical damping is associated with the frictional losses occurring during the vertical motion of the shaft. The frictional losses impact the efficiency of the harvester and thus they have to be minimized. The electrical damping is the ratio of the output impedance to the source impedance and it directly influences the power output of the harvester. The power generated also depends on the moving mass. Thus, within this dissertation the actual mass of the energy harvester is not considered in any analysis and all calculations are based on a unit mass (power density). Dierks (2011) conducted parametric studies to determine the damping parameters as well as the moving mass. Through laboratory tests, he found that the mechanical and electrical damping coefficients of the UT harvester are 4.4 % and 5.46 % respectively, which yield a total damping of 9.86 %. He selected the mass to be 1.454 kg (3.206 lb) due to the size constraints of the housing. Therefore, it can

be easily concluded that the moving mass and the damping coefficients cannot be easily modified after the fabrication of the harvester.

2.4. PREVIOUS RESEARCH ON VEHICULAR-INDUCED BRIDGE VIBRATION ANALYSIS

The previous research completed on bridge vibration analyses and vehicular-induced vibration energy harvester design investigated these two problems independently of each other. One of the main goals of this research program was to unite these two well-investigated areas of expertise. Work done by Reichenbach (2012) significantly contributed to the combination of these two areas and drew conclusions to help engineers in the future to optimize the design of vibration energy harvesters. Part of his work was to evaluate the efficiency of the vibration energy harvester, which was developed by the researchers in the Mechanical Engineering Department of UT Austin, while focusing on the vibrational characteristics of several bridges. He used acceleration histories obtained from field instrumentations to compute the output energy of the vibration harvester, and the potential to power the sensor nodes with vibrational energy harvesting. While field instrumentation is the most accurate method to obtain information of the dynamic characteristics of a given location on a bridge, such an approach is an expensive and time consuming procedure to be performed on every single bridge that needs to be monitored. Moreover, Mazurek et al. (1990) concluded that the dynamic characteristics of a bridge are a function of truck traffic patterns, and temperature. Thus, field instrumentation should be performed over a significant period of time and during different seasons of the year to better capture the fluctuations in the dynamic characteristics of a bridge.

One of the main goals of this dissertation is to developed guidelines on how to analyze bridges to estimate vehicular-induced vibrations. Although a significant amount of energy can be harvested from vehicular-induced vibrations, the behavior is not a trivial

problem because bridges typically vibrate at a non-periodic, low frequency, and low amplitude trend. Thus, accurately computing the acceleration histories of certain locations on a bridge can be vital to the optimization of vibration harvesters. Moreover, Patten et al. (1996) concluded that the vehicle suspension is very important when a dynamic analysis is performed to calculate the vehicle-induced vibrations on a bridge. In the past, many researchers studied the dynamic characteristics of bridges. In most cases, the studies focused on the global natural frequencies of bridges, rather than obtaining the vehicular-induced vibrations of specific locations or components of a bridge. The literature review reveal two major trends to model a bridge superstructure when considering dynamic behavior. The first trend tends to idealize the bridge as a simple beam, whereas the other utilizes shell elements to develop a more detailed model.

Memory, et al. (1995) concluded that modeling a bridge with a single beam provides accurate results of the natural frequency of vibration for straight, non-skewed bridges and for some continuous superstructures. However, he found that bridges with different geometry require a more detailed model to obtain the natural frequencies and this is due to the fact that the single beam is incapable to capture the transverse or torsional mode(s) of vibration in a bridge.

It is very important to accurately estimate the material properties of the bridge under investigation. Wills (1977) analyzed nine simply supported, straight, non-skewed bridges, and he found differences of 7.8-18.3% between the observed and calculated frequencies. He concluded that the modulus of elasticity of concrete highly influenced the calculated results. After adjusting the concrete modulus of elasticity to better fit the actual concrete properties of the bridge, the difference between the observed and calculated frequencies reduced to approximately 5%.

Billing (1979) suggested that for straight, non-skewed bridges of approximately uniform mass and stiffness, the single beam idealization underestimates the fundamental frequencies by approximately 5% compared to field results. Given that the vibration harvester has a wide frequency band of operation, this error is insignificant. Moreover, Billing found that when significantly skewed or curved continuous bridges are modeled with a single beam analogy, the errors range from 10% to 25%. This observation suggests that detailed modeling may be required for many curved or skewed continuous bridges.

Another method to model bridges is stick models. Stick models combine the advantages and features of a single beam idealization and detailed finite element models. A typical stick model consists of line-elements in the longitudinal direction simulating the girders of the bridge and an array of stiff weightless line-elements in the transverse direction to better model the translational and torsional connectivity of the girders. Stick models have been widely used in dynamic analyses of bridges for two primary reasons. First, it is a reliable method to obtain approximate results, and second it is an easy and quick modeling method compared to the difficult or time-consuming methods required to construct detailed models. In the past, stick models have been utilized by several researchers to model regular bridges. However, the application of such models to skewed highway bridges continues to present challenges. Meng (2002) found that the single beam model used to represent the bridge section is incapable of capturing certain vibrational modes to accurately calculate the dynamic response of the bridge. He also proposed a refined stick model to dynamically analyze skewed bridges, and he validated the proposed stick model by comparing results obtained from the proposed stick model with results from detailed finite element models. Finally, he proved that the proposed stick model provides better results than the conventional single-beam model in estimating the natural vibration frequencies and in predicting the predominant vibration modes of the

bridge. Thus, this research further exploited the features of stick models in predicting the vehicular-induced vibration of certain bridge locations or components.

It should be noted that accurately computing the transient vibrations as well as optimizing the design of the energy harvester is equally important. Part of the research outlined in this dissertation contributed to the advancement of the methods to compute vehicular-induced vibrations. It is important to determine the feasibility to harvest energy from transient vibrations before deploying this technology to structures. Thus, it is critical to define the factors that affect the bridge vibrations (e.g. type of truck loads, boundary conditions etc), and which analytical method provides the most accurately results.

2.5. ANALYTICAL METHODS TO COMPUTE VEHICULAR-INDUCED VIBRATIONS ON BRIDGES

Highway bridges are subjected to time-dependent loads when traversed by moving vehicles. These time-dependent loads excite the bridge and the bridge vibrations depend on many parameters of both the bridge and the moving trucks. As mentioned above, the two main pieces of information needed to design a vibration energy harvester are the amplitude of accelerations and the dominant frequencies of vibration. Transient response analyses of moving truck loads must be performed to obtain the acceleration time history and verify the feasibility to harvest energy from vehicular-induced vibrations. Knowing the acceleration time history, spectral analyses can be implemented to attain the dominant frequencies of the computed acceleration time history to calibrate the harvester. These two pieces of information were extracted from field data and used in the design of the UT Austin vibration energy harvester, which was described previously.

Transient dynamic analysis, also called time-history analysis, is the most common method to determine the dynamic response of a structure (e.g. bridge) subjected to time dependent loads from a moving truck. The applied forces are known for each time step.

The transient response analysis can be performed with two different numerical methods: 1) the direct integration transient dynamic analysis and 2) the modal transient dynamic analysis. The two methods are described in greater detail in the next two sections.

2.5.1. Direct transient dynamic analysis

The direct method utilizes direct numerical integration to solve the coupled equations of motion. The fundamental dynamic equation of motion in matrix form is given in Equation 2-2:

$$[\boldsymbol{M}]\{\ddot{\boldsymbol{u}}(\boldsymbol{t})\} + [\boldsymbol{C}]\{\dot{\boldsymbol{u}}(\boldsymbol{t})\} + [\boldsymbol{K}]\{\boldsymbol{u}(\boldsymbol{t})\} = \{\boldsymbol{F}(\boldsymbol{t})\} \qquad \text{Equation 2-2}$$

where, $[M]$ is the mass matrix, $[C]$ is the damping matrix, and $[K]$ is the stiffness matrix. $\{\ddot{u}(t)\}$, $\{\dot{u}(t)\}$, $\{u(t)\}$, and $\{F(t)\}$ are the respective nodal acceleration, nodal velocity, nodal displacement, and nodal force vectors with respect to time.

At each time step, the fundamental equation of motion is solved as a set of coupled equations that take into account inertia forces $[M]\{\ddot{u}(t)\}$ and damping forces $[C]\{\dot{u}(t)\}$. Newmark-Beta direct integration method can be utilized to solve these equations at each time step. All the analyses in this dissertation were performed with SAP2000 v14.1.0 and ANSYS 11.0. In ANSYS 11.0, a transient dynamic analysis can be performed using the full solution method, reduced solution method, and modal superposition method. The first two methods utilize the Newmark-Beta direct time integration method to solve the equation of motion, whereas the last method, which is described in the next section, uses the structure's natural frequencies and mode shapes to compute the dynamic response. SAP2000 v14.1.0 lets the user decide whether a Newmark-Beta direct time integration or modal method should be performed.

2.5.2. Modal transient dynamic analysis

The modal method is an alternative way to perform a transient dynamic analysis of a structure subjected to time-dependant loads. This approach utilizes certain mode shapes of the structure, which are chosen by the user, to reduce the size of the equations of motion and to approximately calculate the transient response of the structure. It is important to note that the modal transient analysis is an approximate numerical solution and its accuracy depends on how many mode shapes are included in the analysis. Yet this method is more computational efficient than the direct integration method, which is an accurate numerical solution.

The modal method employs the mode shapes to transform the problem from behavior of nodes to behavior of modes. This can be achieved by transforming the physical coordinates $\{u\}$ in the equation of motion to modal coordinates $\{\xi\}$. Then, the set of equations of motion are solved to obtain the modal displacements. The modal displacements are used at every step to calculate the total physical displacements. Based on the physical displacements, the element stresses are computed.

2.6. COMPUTER MODELING OF BRIDGES

In order to study the effect of moving vehicles on structural vibrations, bridges must be analyzed utilizing the finite element method. The finite element method is a numerical procedure that can be applied to obtain solutions to variety of problems in engineering, including but not limited to static, transient, linear, or nonlinear problems. Currently there are several commercially available software programs capable of analyzing structures with the finite element method. Two widely used finite element (FE) programs are ANSYS (2012), and SAP2000 from CSI (2011). ANSYS is a general purpose FE program; whereas SAP2000 is a design software package that utilizes the FE method to analyze structures. Both programs can perform 3-D analyses to calculate the

static or dynamic behavior of structures. Moreover, these programs have capabilities to model complex structural problems. SAP 2000 also contains a bridge module, which is an interface that assists engineers to increase the efficiency of the modeling and analyzing bridges.

2.6.1. Methods for modeling bridges

During this research project, two different methods to model bridges are used. The first method utilizes shell elements, beam elements, truss elements, and springs to develop a detailed three-dimensional finite element model of the bridge and its supports (Figure 2-3). The shell elements were used to model the steel girders (e.g. top and bottom flanges, web) and the concrete bridge deck. Beam elements are employed along the length of the bridge to model the cross frames and other secondary components of the bridge. Truss elements are used to represent the top lateral bracing system commonly used in box girders, or cross frames between girders. Lastly, the spring elements are placed at the locations of the abutments and piers to simulate the boundary conditions of the bridge.

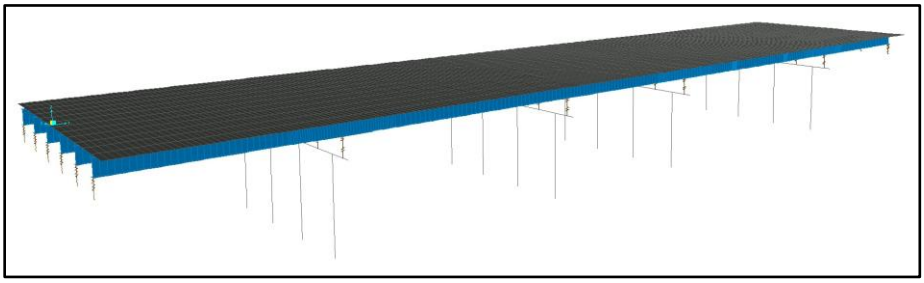

Figure 2-3: A detailed three-dimensional finite element model of a bridge

The second method to dynamically analyze bridges for moving truck loads consists of a three-dimensional grillage model that utilizes line elements (i.e. beam elements) and spring elements (Figure 2-4). This method simplifies the structure and

significantly reduces the computational time. However, in order to simplify the modeling of the bridge many assumptions are made. Each line element along the length of the bridge represents the steel girder and the concrete deck portion. In addition, the line elements transverse to the longitudinal girder line elements represent two of the bridge components. The two components are, first the concrete deck portion between the girders and second the cross frames or floor beams connecting two adjacent girders. More details on the models are provided in Chapter 4.

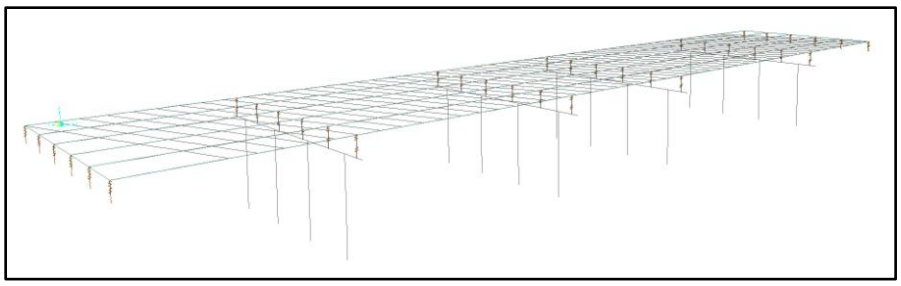

Figure 2-4: A simplified three-dimensional bridge model with line elements

2.6.2. Types of finite elements

The two modeling methods described above utilize four types of finite elements:

- Shell element
- Beam element
- Truss element
- Spring element

A typical shell element is depicted in Figure 2-5 and is used in all the transient analyses described in this dissertation. The element is suitable for simulating thin to moderately-thick plate-type structural components. It is a 4-node element with six degrees of freedom at each node (i.e. three translations in the x, y, and z directions, and three rotations about the x, y, and z-axes). The shell elements that were utilized in the

analysis are suitable for linear, large rotation, and/or large strain nonlinear applications. The shell thickness can be varied to account for changes in the bridge geometry. This element can be meshed into layers for modeling laminated composite shells. However, the computational accuracy in composite shell modeling is governed by the first-order shear deformation theory, which is widely referred to as Mindlin-Reissner shell theory.

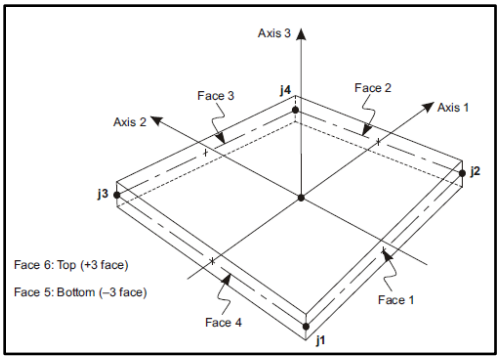

Figure 2-5: Typical shell element (CSI, 2011)

A beam element as depicted in Figure 2-6 was utilized in all the analyses. The beam element that was used has tension, compression, torsion, and bending capabilities, and is suitable for modeling slender to moderately thick beam structural components. In addition, this beam element is based on Timoshenko beam theory, and thus shear-deformation effects were considered. The element is a linear, two-node element with six degrees of freedom at each node (i.e. translations in the x, y, and z directions and rotations about the x, y, and z axes). Moreover, this beam element also offers the option to account for unrestrained warping and restrained warping in the cross-section. Stress stiffness terms and large deflection capabilities are included in the element features. The stress stiffening features allow the element to be utilized for solving flexural, lateral, and torsional stability problems. Finally, a cross-section assigned to this element type can be developed by a built-up section accounting for complex cross-section geometries.

The truss element as depicted in Figure 2-7 is a three-dimensional uniaxial element with three degrees of freedom at each node (i.e. translations in the x, y, and z directions), without any bending capabilities. Plasticity, stress stiffening, and large deflection features can be included.

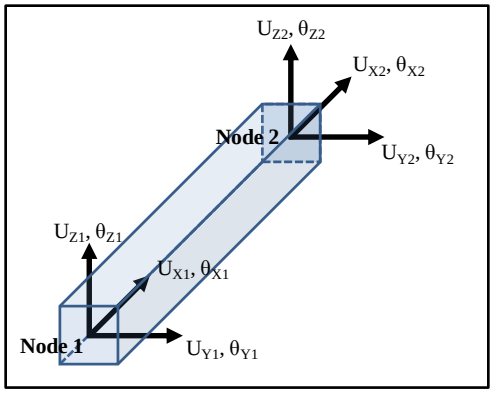

Figure 2-6: Typical beam element

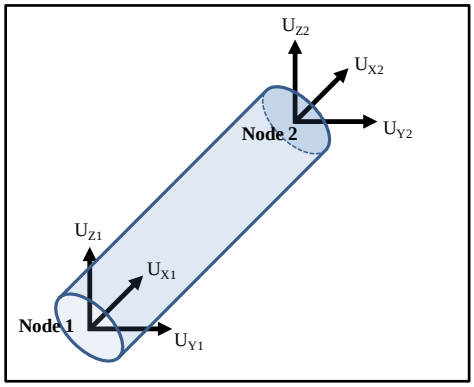

Figure 2-7: Typical truss element

The last element used in the transient analyses to simulate boundary conditions is a spring element. In general, springs are capable of storing mechanical energy and returning to its original shape after the removal of the applied force. The spring that was used is an elastic element that generates forces based on linear displacements and

rotations. SAP2000 v14.1.0 provides the capability to define three-dimensional spring elements with linear and rotational stiffness.

2.7. INSTRUMENTATION METHODS OF STRUCTURES FOR HEALTH MONITORING

The primary concerns of fracture critical systems are the possibility of structural collapse without warning. The increased demand on maintenance and inspection in the infrastructure has placed owners in difficult times with respect to care of the bridge inventory. At a period of time with tight budgets, the required costly visual inspections cannot guarantee that failures would not occur between inspection visits. Therefore, structural health monitoring offers improved capabilities for improving inspection practices and public safety of bridge systems.

The behavior of bridges can vary over time and as a result both long-term and short term monitoring periods should be considered when evaluating the performance of a bridge. When monitoring a bridge to examine the performance and better understand the behavior of the bridge, sensors must be carefully installed at critical locations of the bridge where damage is expected to occur. Recent advancements in the instrumentation technology can assist the engineer to gain a good understanding of the typical trends in traffic trends and distributions as well as evaluating the bridge response. With built-in algorithms combined with improvements in the monitoring and network instrumentation, real-time monitoring can be used to provide significant information to the bridge owners. The information may consist of a summary of the structural behavior of isolated points on the structure which can be recorded and processed and then sent to the bridge owner at a predetermined time interval. Alternatively, the owner may be interested in damage escalation and the monitoring system can provide alerts to the owner of potential problems based upon sensor feedback. The owner can then use the feedback to distribute

maintenance crews to investigate potential problems before the damage escalates to critical stages. The monitoring system may also be used at intermittent periods throughout the life of the bridge to provide an indication of changes in the bridge behavior due to aging or deterioration as well as changes in traffic loading patterns.

2.8. TYPES OF SENSORS

There are several commercially available types of sensors to instrument and monitor bridges. Engineers typically monitor bridges to obtain a variety of different data sets including distributions or accumulation of strain/stress, deflections, temperature readings, as well as a variety of other desired measurements. The sensors that are capable of recording some of these measurable quantities are discussed in more detail below. The sensors that were studied in this investigation are designed for long-term outdoor use.

2.8.1. Bondable foil strain gage

Foil strain gages are one of the most common sensors that are used for structural monitoring. A typical gage as shown in Figure 2-8 is bonded to the surface of the base material at the location of interest to obtain a measure of the strain change at that location. The gage consists of a resister with a backing material that is glued to the surface with a quick-setting adhesive. The adhesive is designed so that the gage experiences the same strain change as the base material. The change in strain may be caused by the application of external forces or environmental effects such as changes in the ambient or local temperature of the structure. Strain is a measurable quantity that indicates the deformation of a body, and it is defined as the ratio of the body length change to the original length. For linear-elastic materials, the strain (ε) at a specific location can be easily converted to stress (σ) by applying Hooke's law ($\sigma = E \cdot \varepsilon$, where E is the modulus of elasticity of the base material).

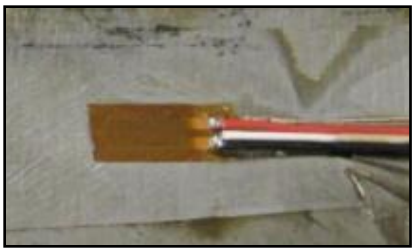

Figure 2-8: Bondable foil gage

As shown in Figure 2-9, the strain gage is a thin metallic foil grid that is mounted on an insulating flexible backing material to support the metallic foil pattern. The metallic foil patterns are made of certain alloys and the thermal output characteristics of these alloys are capable of minimizing the thermally-induced strain error over a range of temperatures (50 °F - 100 °F). The gages are typically encapsulated for enhanced durability. The active grid is the main part of the strain gage. The wire of the gage grid is responsible for the resistance change measured across the solder tabs. The end loops at the top and bottom of the grid are generally insensitive to strain due to their low resistance and the relatively large area compared to active grid. Most foil gages have four alignment marks at the mid-length of each side of the gage. The alignment marks assist the engineer to accurately place and orient the gage at the desirable location.

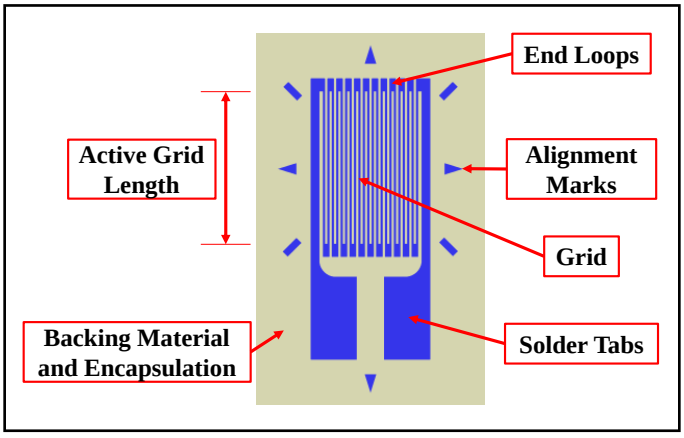

Figure 2-9: Typical components of strain gage

The technology of the strain gage is based on the fundamentals of solid mechanics and electricity. The sensor is rigidly bonded to the specimen surface and the gage grid deforms accordingly as the structural component elongates or contracts due to changes in the state of stress. Changes in the state of strain result a change in the resistance of the gage. A measure of the strain change in the gage can be found by converting the measured change in the electrical signal based on the electrical resistance change to a mechanical strain change. The gage resistance changes depending on the deformation that the structural components experiences. The strain component parallel to the gage grid can be measured by recording the fluctuation of voltage across the Wheatstone bridge that is occurring due to the change of electrical resistance of the wire in the active grid.

Finally, it is important to note that the gage size plays a very significant role on the quality and resolution of the measurement. The voltage measured across the Wheatstone bridge depends on the average change of resistance across the active grid length. For a case in which the strain change over the gage length is constant, the recorded strain will be relatively accurate. For a case in which there is significant strain gradient over the length of the gage, the active grid length should be minimized to improve the precision of the results.

2.8.2. Weldable strain gage

A typical weldable strain gage is shown in Figure 2-10. This gage is designed for long-term outdoors applications, and utilizes similar technology as outlined for the foil strain gage. The weldable gage consists of a precision foil strain gage (as described in the previous section) that is bonded to a thin metal backing shim and fully-encapsulated with molded waterproofing material to prevent moisture and humidity from damaging the

sensor. The metal backing shim is attached to the structural components through spot welding.

Figure 2-10: Weldable strain gage

2.8.3. Bondable shield strain gage

A variation of the weldable strain gage is the bondable shield strain gage which is fabricated exactly the same way as the weldable strain gage that was described in the previous section. The major difference compared to the weldable strain gage is the bonding technique. This type of gage utilizes a special two-part adhesive – fast curing medium viscosity cyanoacrylate adhesive and cyanoacrylate activator (i.e. amine) – to rigidly bond to the specimen surface, in contrast to the spot welding technique of the weldable gages. Figure 2-11 illustrates two different types of backing materials. The bondable shield strain gage typically employs a stainless steel shim and a polyimide shim as the backing material.

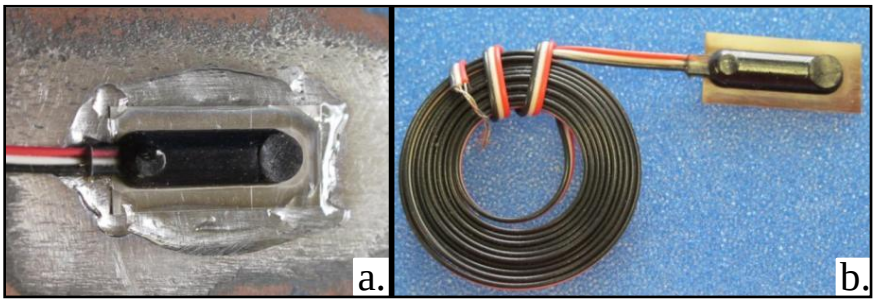

Figure 2-11: Bondable shield strain gage with: a) stainless steel shim, b) polyimide shim

2.8.4. Crack propagation gage

A crack propagation (CP) gage is a type of sensor used to monitor the rate of crack growth. The gage consists of an array of resistor strands connected in parallel as shown in Figure 2-12. The gage is encapsulated into a glass-fiber-reinforced epoxy matrix backing material with a nominal gage thickness of approximately 0.0017 in. (0.043 mm). The CP gage is bonded to the surface of the structural component and the gage edge with the shortest strand is placed next to the crack tip. The strands are equally spaced over the width of the gage. The crack propagates and successively breaks the individual strands of the gage. Each time a strand breaks, the total resistance of the gage increases because the circuit has a smaller area (less strands). By recording the step wise increase of resistance (Figure 2-13), the crack growth can be determined based on how many strands were broken. Figure 2-13 illustrates a typical CP gage output diagram and the successive stepped increase of resistance. The step height increases with the number of fractured strands because each strand that fractures is longer than the previous one. Thus, the total resistance, which depends on area and length of wires, increases.

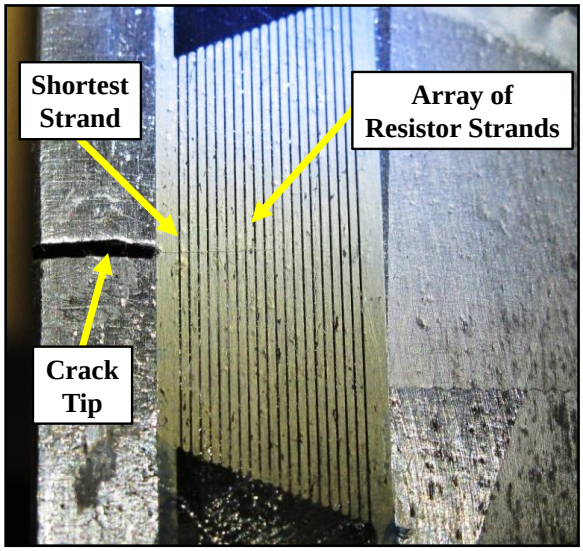

Figure 2-12: Crack propagation gage

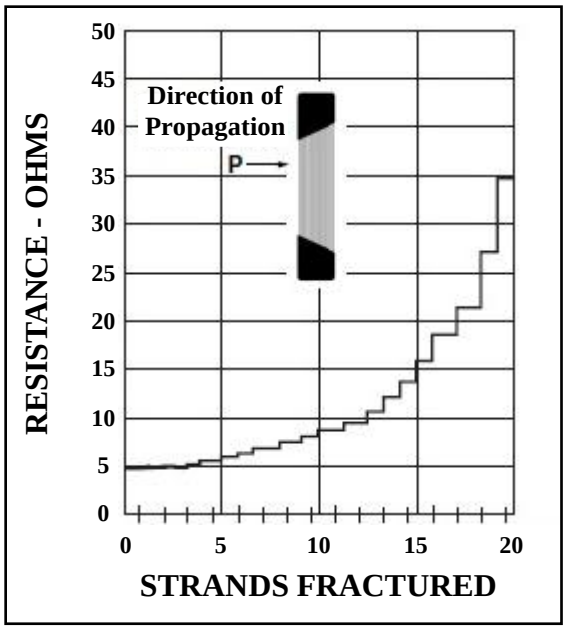

Figure 2-13: Typical crack propagation gage output diagram (Vishay, 2012)

2.8.5. Vibrating wire strain gage

A typical vibrating wire (VW) strain gage is shown in Figure 2-14. This type of sensor has been used in long-term engineering applications, when protection from harsh environment is important. Although there has not been conclusive evidence that the gage stability is better than foil strain gages, VW gages have also been used in long-term applications where the perceived stability of the gage readings is better than for bondable gage systems. The reason the gage is perceived to have better long-term stability is that the sensor technology is based off of mechanical principles. The sensor employs the principle of vibrating wire, where a tensioned wire vibrates at a specific frequency based on the strain of the wire. Figure 2-15 presents the main components of the VW strain gage. The vibrating wire is enclosed into a protective tube. The gage shown in Figure 2-15 is for application on the surface of the member, such as a steel beam, in which case the gage is supported on two mounting blocks. The mounting blocks can be either bonded

to the surface of the structural component with epoxy or spot welded to the metal surface. For concrete applications, a similar gage is available in which the ends of the gage are flared and the gage is cast directly into the concrete. For surface mounted or concrete applications, the support blocks or flared ends serve as the anchor points of the gage that define the gage length over which length the strain change is defined. In the middle of the protective tube, a coil and thermistor housing is plucked. The housing consists of a thermistor to monitor the temperature, and an electromagnet (pluck and read coil) to measure the wire frequency of vibration. The output signal is an AC voltage signal whose frequency is proportional to the measured strain. The vibrating wire strain gage is excluded from the durability tests, described in Chapter 5 due to their inability to record strain data at a high rate.

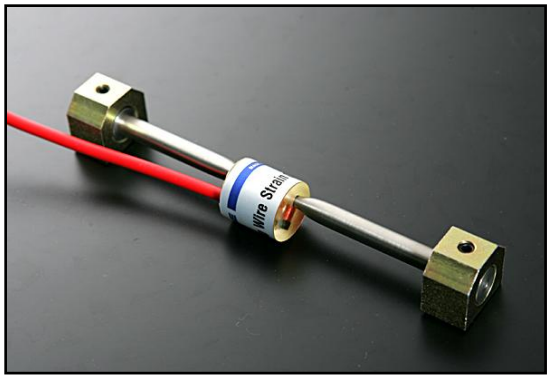

Figure 2-14: Vibrating wire strain gage (Geokon Inc., 2012)

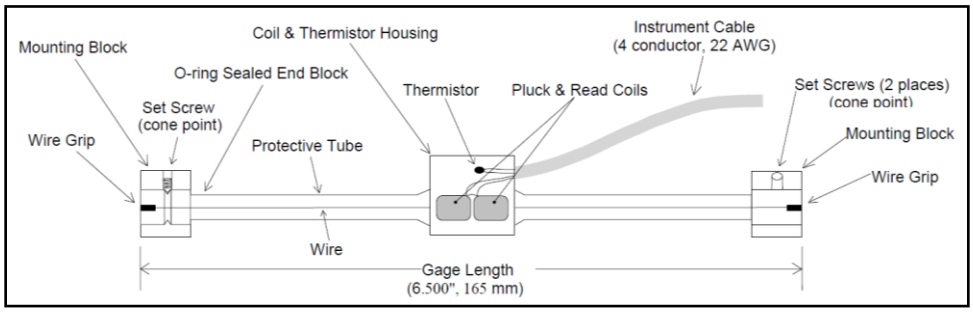

Figure 2-15: Components of vibrating wire strain gage (Geokon Inc., 2009)

2.8.6. Accelerometers

Accelerometers (Figure 2-16) are high precision sensors that are used to record the vibration history at a particular location in the structure. These sensors can be manufactured as single-axis, or triple-axis accelerometers to measure vibrations in different directions based on the application. Typically, the sensors can capture acceleration ranges of ±2g, ±4g, or ±10g. However, as the acceleration range increases, the sensitivity and the resolution of the output signal generally decreases.

Figure 2-16: Typical one axis accelerometer (Crossbow Technology, 2012)

2.8.7. Thermocouple

A thermocouple is a sensor utilized to measure temperature. A typical thermocouple sensor as shown in Figure 2-17 consists of two wires joined together at the end of the cable tip. As the thermocouple tip is exposed to a change in temperature, a voltage is produced between the joined wires. The voltage is produced due to a reaction between the two different wire materials, since each of the two wires is manufactured from different alloys. Depending on the properties of the thermal couple wires, the voltage change can be correlated with the change in temperature.

Table 2-1 summarizes a number of different types of thermocouples and the respective alloy combinations. Each type is used to measure different temperature ranges or characteristics, and can be employed in different environments. The most common types of thermocouples are E, J, K, N, and T. For applications in which large temperature

ranges are expected, the engineer should use the B, C, R, and S types of thermocouples. The recorded temperature range does not solely depend on the type, but is also limited by the diameter of the thermocouple wire. Thus, the temperature range decreases with a decrease in the diameter of the wires.

The final feature of the thermocouple is the tip style of the joined wires. Depending on the engineering application, the engineer should decide the type of thermocouple tip style to use. Generally, there are three different methods to connect the two wires at the tip of the thermocouple, namely grounded, ungrounded, and exposed. The thermocouple tips of the grounded style are directly mounted to the inside of a probe wall, whereas in the ungrounded style the tips are not physically connected to the probe. The probe wall provides a protection against environmental contaminants such as corrosion or excessive humidity. Thus, these two tip styles are generally used for long-term applications in harsh environments. On the other hand, thermocouples with the exposed tip style provide the best response time compared to the other two types; however the exposed tip style should only be used in dry, non-corrosive environments.

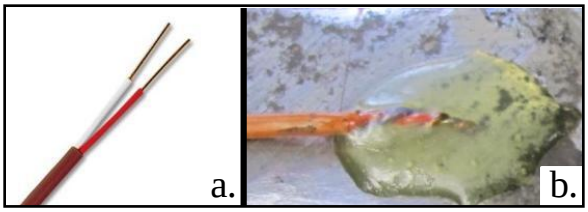

Figure 2-17: Thermocouple wire duplex insulated

Table 2-1: Types of thermocouples

Type	Alloy Combination
B	Platinum (30%) - Rhodium
C	Tungsten - Rhenium
E	Chromel - Constantan
J	Iron - Constantan
K	Chromel - Alumel
N	Nicrosil - Nisil
R	Platinum (13%) - Rhodium
S	Platinum (10%) - Rhodium
T	Copper - Constantan

2.9. SENSOR INSTALLATION TECHNIQUES

The instrumentation of structures can be a challenging endeavor. Bridge sites can be particularly challenging since instrumentation conditions do not provide a clean controlled environment such as often found in a laboratory. As a result, the instrumentation personnel should have significant installation experience to improve the likelihood for successful monitoring behavior. In many situations sensor failures occur due to defective installation practice. Thus, considerable care and caution should be given to the installation procedure. The three main parts of the installation procedure are surface preparation, sensor bonding, and sensor protection. This installation procedure only applies to strain gages and crack propagation (CP) gages. Vibrating wire stain gages, accelerometers, and thermocouples are manufactured with a basic environmental protection and can often be readily attached structural component with either conventional epoxy or mechanical fasteners. The next three sections of this chapter provide more information of the installation procedure for strain gages and CP gages.

2.9.1. Surface preparation

The first step of the installation procedure is to prepare the member surface around the location that the sensor will be installed. The surface must be free of dirt, rust, paint, grease, and other defects that can jeopardize the successful sensor installation. First, the surrounding surface should be ground with a sanding disc to remove any coating (e.g. paint, rust, galvanizing coatings etc.), and to develop a smooth surface appropriate for bonding. Once the surface is cleaned, the installation personnel should mark the desired location with alignment marks. As noted earlier, the purpose of the alignment marks is to properly position and orient the gage. After marking the gage layout lines, the surface should be thoroughly degreased with an appropriate solvent to remove any residue and contaminants that can affect the bonding performance.

The surface preparation, which is described in this section, is required for all the types of strain gage and CP gage. The surface preparation for weldable strain gages is less critical than the rest of the bondable gages due to the different bonding technique. All the different types of sensor bonding are described in the next section.

2.9.2. Types of sensor bonding

Proper sensor bonding is one of the factors to ensure a successful instrumentation. Imperfect gage installation can result in inaccurate or unstable gage measurements. A rigid and durable bond between the sensor and the structural member surface is essential to obtain reliable data from the sensor.

Typically, a bondable strain gage (e.g. foil or shield strain gage) is installed by utilizing a heavy duty adhesive. The adhesive rigidly bonds the gage to the structural component, allowing the gage grid to experience the same deformation as the surface of the instrumented member. Vishay Micro-Measurements has published guidelines on how to select the adhesive depending on the instrumentation type and the expected

environmental contaminants (Vishay, 2010). For typical civil instrumentations, general-purpose cyanoacrylate bonding agents is recommended. However, for superior and durable bonding performance two-part (i.e. epoxy resin and diethylaminopropylamine compound) heavy duty epoxy should be used. These types of adhesive create a tough, rigid, high strength bond that is resistant to moisture and most common solvents. The normal operating temperature range of these adhesives is -25° to +150°F (-32° to +65°C).

In the case of crack propagation gages, a solvent-thinned adhesive should be utilized to attach the CP gage to the structural member. The CP gage manufacturer recommends using adhesive with high temperature curing. However, conventional adhesives, as the ones utilized for bondable gages, have been employed to successfully install CP gages during this research project.

As previously described, weldable gages are attached to the surface of the monitored member through spot welding. Spot welding is a very convenient bonding technique for structural instrumentations in weather conditions that curing of adhesives is difficult or requires special treatment. Spot welding can be achieved by using a portable spot welder. The spot welder is capacitive discharge equipment with a welding probe and a ground wire. For proper welding, the output power of spot welder should be set according to the thickness of the metal shim of the weldable gage. However, weld energy of 30-40 joules is sufficient to properly weld most weldable gages. Apart for the suitable weld energy, the spot welder user should apply a force of 3-6 pounds on the welding probe while the spot weld is produced. Based on manufacture specifications, each spot weld must be 40 to 60 mils in diameter. Weldable gages should be installed with two lines of welds. Both lines of welds should be parallel to each other and 1/32 in. apart. Some bridge owners may be resistant to allow weldable gages due to fatigue concerns associated with welding on bridges; however the spot welds are extremely small and will

generally have an insignificant impact on the fatigue performance of the structural member.

2.9.3. Types of sensor protective coatings

Most sensors are vulnerable to environmental contaminants (e.g. humidity, moisture, etc.) and thus the instrumentation has to be protected against these effects as soon after installation as possible. Several products are commercially available to protect sensors and manufacturers recommend different combinations of these products as protection schemes. The protection schemes are layers of coatings and depending on the material, the user can achieve different levels of protection. Although the discussion in this section applies to protection of the adhesive, many of the materials below also provide some level of mechanical protection for the gages as well.

The most widely used protective materials are:

- Solvent-thinned (MEK) nitrile rubber is used as a primer on vinyl-insulated wire to improve the bonding with other protection coatings.
- Solvent-thinned acrylic, which is applied in thin coats to prevent solvent entrapment and to insulate lead wires from moisture.
- Microcrystalline wax provides an intermediate moisture barrier due to its very low water-vapor transmission rate.
- A one-part solvent free RTV silicone is utilized as exterior protective coating against moisture and other contaminant.
- Polysulfide liquid polymer compound is applied as exterior coating to protect sensors installed in harsh environments. The coating also serves as a moisture barrier for long-term instrumentations.
- Butyl rubber sealant is used as a vapor protection.

- Aluminum Foil Tape is used as a moisture barrier.
- Contact cement paint, is used as a sealant on top of the aluminum tape to increase the moisture protection.
- Zinc based spray paint without MEK, is a protective coating applied on metallic parts of weldable gages to prevent corrosion.

A durable instrumentation for long-term applications can be achieved if one of the following environmental protection schemes is utilized. Apart from protecting the general area around the sensor against environmental contaminants, the instrumentation personnel should paint any solder or open air connections with a solvent-thinned acrylic and seal the wire splices with heat shrinkable tubing to insulate the wires and keep them from having resistance to ground.

2.9.3.1. Protection scheme 1 – Long-term applications

Exceptional long-term gage protection for typical bridge instrumentations can be achieved by utilizing a protection coating combination, which is summarized in Figure 2-18. The first step, after properly installing the gage and cleaning the surrounding installation area with a degreasing solvent, is to paint the lead wires with a primer and allow to air dry. The primer enhances the bondability of the wires with the next protective layers. Next, all the open air connections and the metal shim of sealed gages should be painted with a solvent-thinned acrylic to insulate them from moisture. Only in the case of foil bondable gages and solder connections, Teflon tape should be added on top to prevent other waterproofing materials from bonding to the gage.

The following step is to use a butyl rubber patch to seal the gage. In the case that the installation occurs when ambient temperature is below 40 °F (5 °C), it is recommended to warm the surface of the specimen with a heat gun; however care should

be taken with the level of heat in proximity to the gage so as to avoid damage to the sensor. Furthermore, to improve the bondability of the rubber sealant, it is recommended to keep the release paper and heat the sealant with a heat gun at a temperature of 300-400 °F. To increase the moisture protection, the rubber patch should be at least 1/2 in. past the three open sides of the gage and 1-1/4 in. beyond the gage side on which the lead wires are connected. Once everything is dry, the release paper can be removed and the entire area can be cover with aluminum tape at least 1 in. larger than the area covered by the rubber patch. The next step is to paint over the tape and cover the edges and laps with contact cement to seal any imperfection or defect.

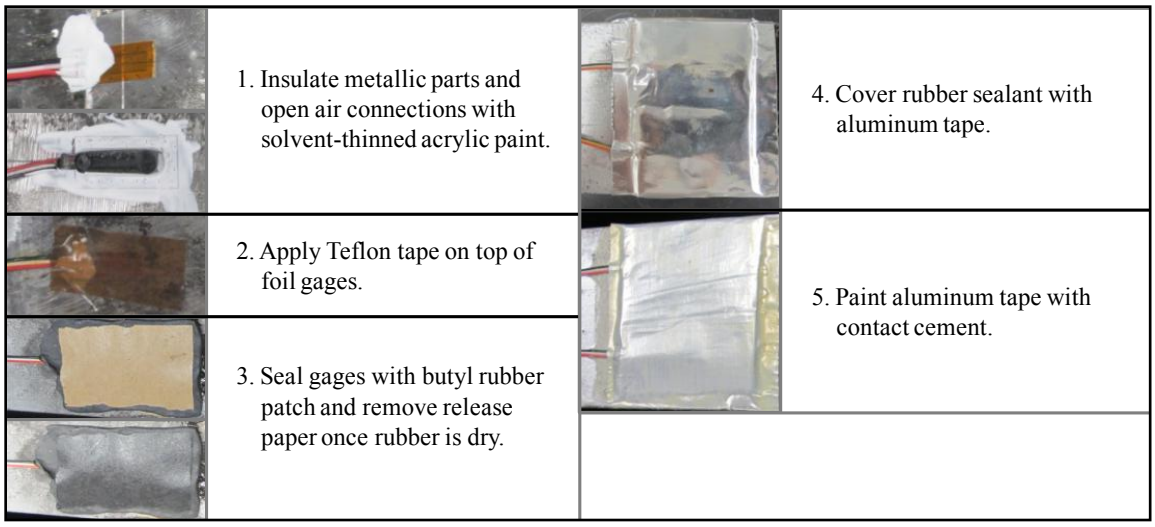

Figure 2-18: Steps of protection scheme 1

2.9.3.2. Protection scheme 2 – Long-term applications

An additional protection method suitable for long-term bridge instrumentations is described in this section. The main steps of Protection scheme 2 are abridged in Figure 2-19. Some of the steps are similar to the Protection scheme 1. For instance, the installation area around the sensor should be cleaned with proper solvent. Moreover, the

lead wires of the gage should be painted with a primer to increase the bondability of the wires with the other protective coatings. The last common step with the previous protection method is the insulation of the open air connections and the metal shim of sealed gages with solvent-thinned acrylic.

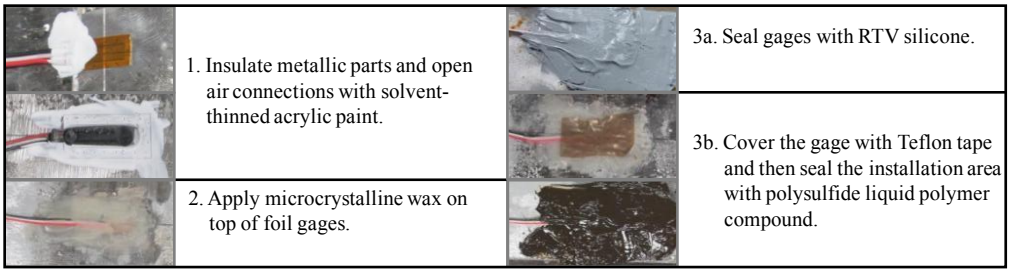

Figure 2-19: Steps of protection scheme 2

The following step is to sufficiently cover the gage area with a layer of microcrystalline wax. Microcrystalline wax provides a barrier against humidity but due to its limited ability to provide mechanical protection to the gage, it is usually used as an intermediate protective coating. On top of the wax, a layer of RTV silicone is applied to increase the protection against environmental and mechanical effects. The thickness of the silicone layer should be based on engineering judgment; however, the thicker the coating is, the more resistant to moisture the silicone coating becomes. RTV silicone is recommended when installation environmental conditions are not extreme. An alternative coating for more enhanced and durable performance is the polysulfide liquid polymer compound. A layer of polysulfide liquid polymer compound should be added instead of RTV silicone to protect the gage from moisture. If polysulfide liquid polymer compound is used instead of RTV silicone, then a piece of Teflon tape should be first added above the gage to sufficiently cover the gage area and the wire connections. The curing time of this specialty polymer compound highly depends on the ambient temperature. In case the

instrumentation takes place during a cold day, then hot vacuum bonders, which are available in different sizes and shapes, should be utilized to warm up the installation area to decrease the curing time.

2.9.3.3. Protection scheme 3 – Short-term applications using sealed strain gages

For short-term instrumentations, the gages can be protected with different protection schemes that may be a more economical solution and easier to apply. In this Protection scheme 3, as before, the lead wires should be painted with a primer, and the open air connections and stainless steel shim should be cover with a solvent-thinned acrylic. A butyl rubber patch is then used as the main gage sealant. As previously mentioned, if low temperatures exist during the instrumentation procedure, then the specimen should be heated. In addition, the rubber sealant should be warmed up with a heat gun at a temperature of 300-400 °F. To achieve maximum moisture protection, the rubber sealant should be large enough to sufficiently protect the gage and its wire connection. Once the rubber patch is dry, then the protection scheme is complete.

2.9.3.4. Protection scheme 4 – Short-term applications using sealed strain gages

As previously mentioned, the sealed strain gages are encapsulated into a molded water-proofing material to protect the conventional foil strain gage against environmental effects. Thus, for short-term applications it is recommended to only protect the stainless steel shim and the gage bonding. The weldable and bondable gages that utilize a stainless steel shim to be attached to the specimen should be sprayed with zinc-rich paint to prevent corrosion on the stainless steel shim. It should be noted that according to manufacturing specifications, the zinc-rich paint should not contain Methyl Ethyl Ketone (MEK).

2.10. LITERATURE REVIEW ON DURABILITY AND RELIABILITY OF SENSORS

In long-term field instrumentation of structures, the effects of temperature variation, moisture, and other environmental variables on both the instrumentation and the structure must be quantified. One of the major goals of this study outlined in this dissertation was to assess the durability of sensors used on bridges as well as assessing the performance of the sensors as a function of temperature changes that occur on the bridge. The importance of factors that may affect the durability of the gages are relatively obvious since any degradation in the bond of the sensor to the structure will have detrimental effects on the accuracy and reliability of the data. The impact and importance of temperature effects on the gage readings may not be obvious to individuals inexperienced in bridge environments. Bridges are subjected to substantial changes in the ambient temperature of the bridge setting as well as thermal gradients that arise due to uneven heating from solar exposure. Local and global temperature fluctuations on the structure can be very large. Although many of the gages that are used may be compensated for temperature, the suitability and accuracy of the temperature compensation as well as additional corrections that can be applied to gage reading are not clear. The rate of heating or cooling on the structure can be relatively high and the impact of the rate of temperature change on the measured sensor readings may require further study.

Thus as part of this research project, durability and reliability tests were developed. Prior to designing the durability and reliability tests of sensors, an extensive literature review was performed. While extensive research has been performed to understand thermal effects on sensors in transient environments [Adams (1983), Blosser et al. (1988), Wilson (1970)], limited information was found available in the literature about thermally-induced strain errors produced in bridge environments, as well as general

recommendations to correct these strain errors. Finally, some research has been completed to investigate the reasons of sensor failure in long-term instrumentations.

Recently, Vishay Micro-Measurements Group, Inc. (2012) published Technical Note TN-504-1, which discusses the effects of temperature fluctuations on strain gage thermal output and gage factor. This technical note provides important information through equations and graphs on how to correct the thermal output from strain readings.

Gomes et al. (2003) analyzed the thermal effects on two different types of weldable strain gages over a temperature range from 68 to 932 °F (20 - 500 °C). He found that the thermal output was efficiently compensated when a quarter-bridge configuration was utilized instead of a half-bridge configuration, which provided thermal output of larger relative error. He also concluded that the thermal output for the quarter-bridge configuration could be minimized when appropriate corrections were made based on experimental data and material properties information provided by the manufacturer.

Laman et al. (2006) studied the temperature effects on vibrating wire strain gages for long-term structural monitoring on highway bridges. He concluded that in free-ended and fully fixed members, temperature-induced strains in vibrating wire gages can be excluded from the total strain through a simple calculation. However, for any other case, temperature-induced strain can only be determined through experiments.

Ellis et al. (2009) investigated the failure modes of foil strain gages. He found that the main effect of a strain gage undergoing debonding at one of its ends is the loss in signal amplitude. His experiments also showed that two factors can distort the output signal. The first factor is the debonding of the strain gage central region and the other is the deterioration of the strain gage lead termination. Thus, he concluded that it may be difficult to distinguish the reason of a distorted output signal.

Richards (1996) introduced a new correction procedure for strain gage measurements acquired in transient temperature environments, and he compared his proposed correction technique with the conventional correction method. He also concluded that temperature gradients may be insignificant in slowly varying temperature environments and thus their effect on strain gage measurement accuracy may be negligible. However, it is uncertain at which thermal rates and conditions this assumption is not valid.

Vishay Micro-Measurements Group, Inc. (2007) investigated the fatigue characteristics of strain gages and summarized the results in Technical Note 508-1. Based on their test results, the fatigue life of typical foil gage is approximately 10^6 cycles at a strain range of ±1500 με, which corresponds to a stress range of ± 44 ksi. This magnitude of stress range is not typically observed on structures due to cyclic loading. Thus, it can be concluded that fatigue does not impact the performance of strain gages, which are utilized to instrument structures. However, if fatigue of foil strain gages becomes a concern, then installation recommendations to maximize the fatigue life of strain gages are provided in the same technical note.

The previous research found in the literature along with the research project objectives served as a basis on the development of the durability and reliability testing program. A detailed discussion of the testing program and test results are provided in Chapter 5 and 6 respectively.

CHAPTER 3

Instrumentation of Bridges

3.1. INTRODUCTION

During this research project several bridges in two states (Texas and Oregon) were instrumented with accelerometers, strain gages, and crack propagation (CP) gages to monitor their behavior under moving loads and to evaluate their fatigue performance. The data obtained from the accelerometers were utilized to validate the dynamic analysis results produced by the computer models that are presented in Chapter 4. On the other hand, the strain and CP gage data were employed to evaluate the performance of these sensors in a real life scenario. More details of the sensor data are given in Chapter 6.

In all the instrumented bridges, the main load-carrying components are fabricated from steel. Table 3-1 tabularizes the structural system of the instrumented bridges. Some of the bridges that were instrumented were categorized as fracture critical, which indicates that the systems are potentially susceptible to collapse with the loss of a primary structural member due to a lack of redundancy. Thus, in non-redundant steel bridges fracture propagation due to fatigue becomes a major concern.

Table 3-1: Structural system of the instrumented bridges

	Bridge Structural System
Bridge A	Riveted twin plate girder
Bridge B	Twin trapezoidal steel box girder
Bridge C	Six rolled steel girders
Bridge E	Steel through truss
*Bridge D was not part of the investigation presented in this dissertation. The bridge IDs were retained same as in Fasl (2013) for consistency.	

Four of the six instrumented steel bridges were analyzed under moving truck loads to determine their behavior and dynamic response. Two of the analyzed bridges are I-girder bridges, of which one is consider fracture critical. The third bridge is a twin trapezoidal box girder bridge. According to AASHTO (2012), this type of bridge is also classified as fracture critical. The last bridge is a simply supported truss bridge. The decision to analyze only these four bridges was made based on the availability of bridge drawings and the desire of examining different types of bridges that represent the majority of US highway bridges. A detailed description of the analyzed bridge geometries and the instrumentation plans is given in this chapter. Finally, the computational results were compared with the field data to verify the accuracy level of the predicted response that can be achieved by finite element programs. These results are presented in Chapter 4.

3.2. BRIDGE A

Bridge A (Figure 3-1) is located in Texas on an interstate highway. Based on data from a weigh-in-motion station south of the bridge, the annual daily truck traffic (ADTT) was 4,000 in 2005. Thus, in addition to the obvious importance due to public safety, the structural integrity of Bridge A is also important for the US economy.

Figure 3-1: Overall view of Bridge A

Bridge A was designed in 1935-36 and constructed in 1937. The bridge consists of eleven spans in total. The four 50-ft northern and the four 48-ft southern approach spans are simply supported. Although from a distance the three middle spans appear to be continuous girders, the middle span contains a drop in segment with hinges at both ends, thereby creating a statically determinate system. These three middle spans are supported by plate girders. The northern and southern approach spans consist of an eight plate girder system. Due to the redundancy of the structural system, the approach spans are not considered fracture-critical and thus they are excluded from this investigation. The investigation is only focused on the three middle spans of Bridge A, which are classified as fracture-critical.

For approximately the first 40 years of its service, the bridge carried total two lanes of traffic, one in each direction (i.e. northbound and southbound). In 1974, the bridge was widened to accommodate more traffic and changed to only carry the northbound direction of the highway. The traffic lane widths increased from 12 ft. to 14 ft. The widening of the concrete deck was achieved by adding cantilever brackets to the outside of each of the existing girders as shown in Figure 3-2. Moreover, as part of the widening project, a separate bridge, which consists of three I-girders, was constructed on the eastern side of the original three middle spans to carry an additional lane for on-ramp and exit traffic. The separate multi-girder bridge system is isolated from the original bridge through a longitudinal gap, which can be seen from under the bridge looking up in Figure 3-3, and thus the existence of the new bridge portion does not affect the behavior of the original three-span bridge. Since the three-girder addition is considered redundant and it does not influence the behavior of the fracture-critical bridge, it is not part of the instrumentation plan and it is not described within this dissertation.

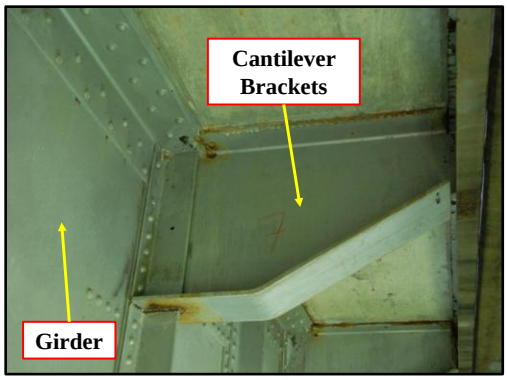

Figure 3-2: Cantilever brackets

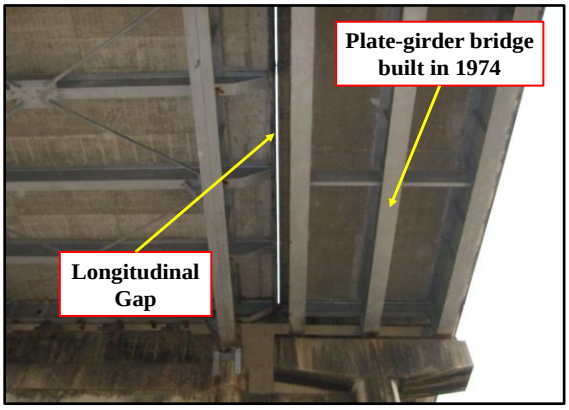

Figure 3-3: Longitudinal gap and I-girder bridge built during 1974 widening project

3.2.1. Geometry of Bridge A

As mentioned above, only the three middle spans of the original Bridge A are of interest in this investigation. Therefore, only this portion of the bridge was modeled and analyzed. Henceforth, the three middle spans of the original bridge are referred as Bridge A.

Figure 3-4 demonstrates the elevation view and the main geometric characteristics of Bridge A. The overall length of the bridge is 272 ft, consisting of two identical end spans at the north and south end of the bridge and a center span. The respective lengths of the two end spans and the center span are 73.5 ft. and 125 ft. The center span is

composed of two 30.58-ft overhang sections and a suspended span that has a length of 63.83 ft. The suspended span is supported by the overhang sections through hangers as shown in Figure 3-5. To accommodate the pin connections at the ends of the suspended span, a transverse deck discontinuity was constructed at that location (Figure 3-5).

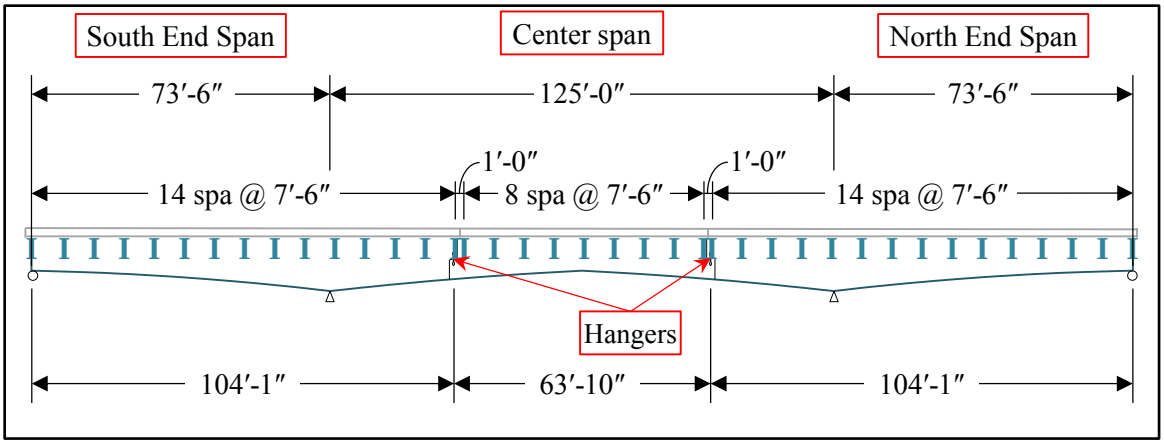

Figure 3-4: Elevation view of Bridge A

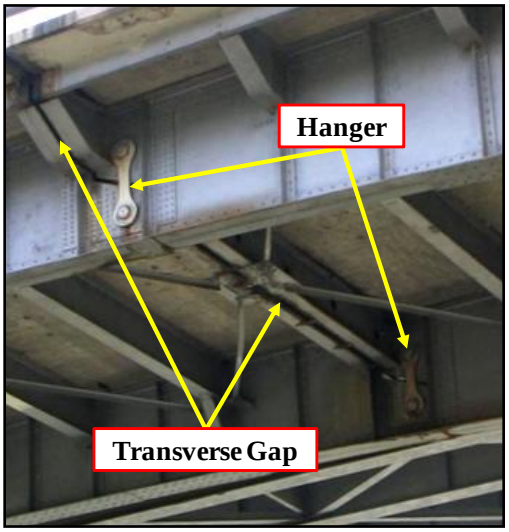

Figure 3-5: Suspended span details

The two longitudinal girders consist of built-up plate girders. The plate girders were fabricated by riveting double angles on the top and bottom of the steel web plate.

The double angles serve as flanges. In addition, angles are riveted vertically on the web every 45 in. to act as stiffeners. The twin girders are haunched and their depth variation is shown in Figure 3-6. The haunched girder profile is symmetric about the midspan of the suspended section. The girders are 5.54 ft. deep at the end supports, and it gradually increases to 8 ft. over the interior supports. For the middle span, the girder depth decreases past the interior piers to reach a depth of 5 ft. at the midspan of the suspended section.

The girder sections around the negative moment region (i.e. interior supports) and the midspan of the drop-in section are reinforced with cover plates to increase the moment capacity. Figure 3-6 demonstrates the locations of the cover plates and their lengths. The cover plates are 18 in. wide and are riveted to the double angles. Over the interior supports, the girder sections are reinforced with three layers of cover plates, which are riveted to the top and bottom double angles of the longitudinal girders. Each layer has different lengths varying from 17.25 ft. to 52.25 ft. (Figure 3-6). Due to the different cover plate lengths, the flange thickness around the interior supports varies from ¾ in. (no cover plate) to 2-¼ in. (three layers of cover plates). On the contrary, only two layers of cover plates were utilized to reinforce the top and bottom flanges at the midspan of the suspended section. In this case the flange thickness varies from ½ in. (no cover plate) to 2⅓ in. (two layers of cover plates).

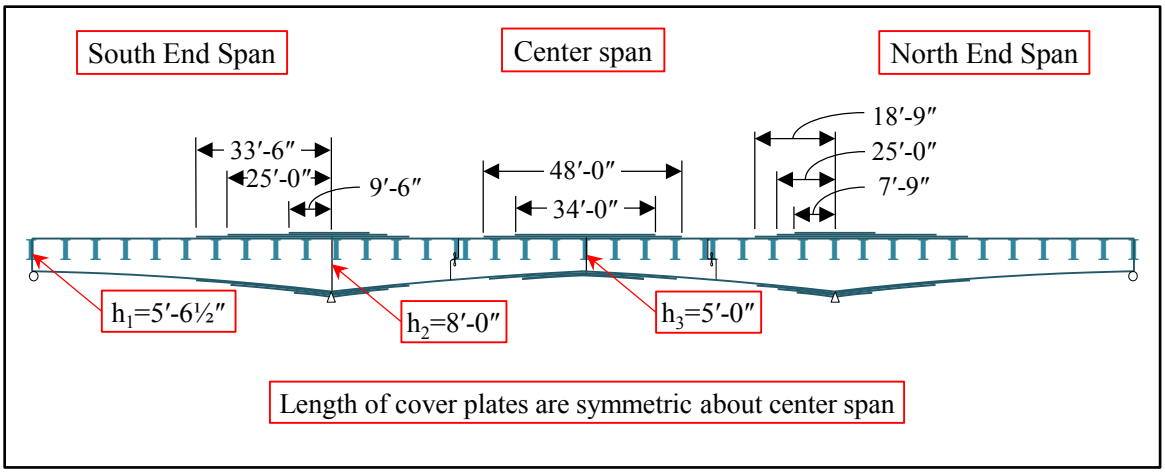

Figure 3-6: Girder height variation and locations of the cover plates

Figure 3-7 shows a typical cross section of Bridge A after the widening project that took place in 1974. The typical cross section does not include the additional three I-girder bridge, which in reality is next to the east girder. The distance between the two longitudinal girders is 23 ft., and the overall width of the concrete deck increased to 33.125 ft. The main reason of the widening project was to increase the number and width of lanes on the bridge. Thus, the lane width increased from 12 ft to 14 ft. In order to support the wider concrete deck, cantilever brackets were welded to the longitudinal girders. A special detail of the cantilever brackets is the shear stud at the tip of the cantilever (Figure 3-8). Although bridge was designed with the deck non-composite with the girders, shear studs were installed every 30 in. as a single line along the length of the channel shape section that connects the cantilever bracket tips.

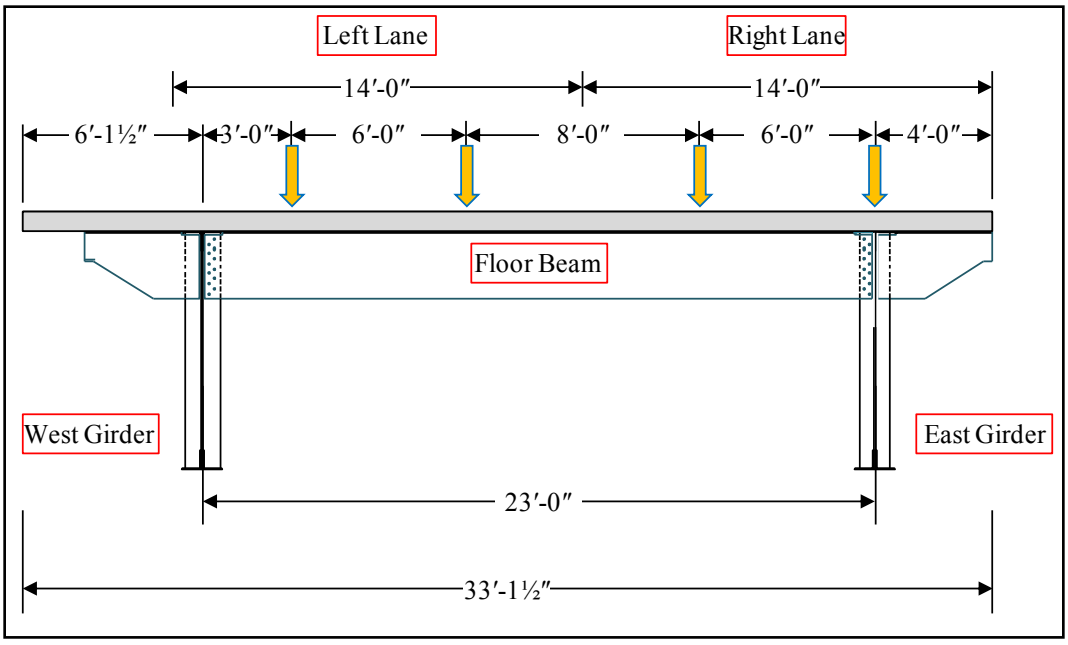

Figure 3-7: Typical cross section of Bridge A

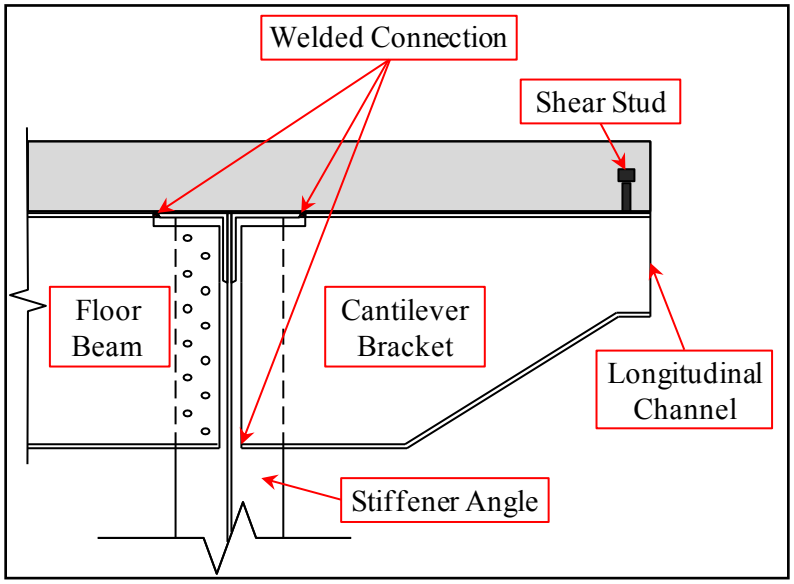

Figure 3-8: Typical cantilever bracket detailed connection

To stabilize the longitudinal girders during construction and in-service, a series of floor beams (39 floor beams) were provided to transversely connect the two longitudinal

girders. The floor beams of Bridge A are 2.25 ft. deep (W27x91 sections) and are spaced 7.5 ft. on center. Apart for the floor beams, an X-shaped top lateral bracing system was added to improve the lateral stiffness of the twin girder bridge. The top lateral system consisted of 3 in. by 3 in. by 5/16 in. angles bolted to gusset plates. Due to the diagonals slenderness, the top lateral bracing is a tension-only system (Figure 3-9). An overall plan view of the bridge, including the top lateral system, is shown in Figure 3-10. Note that the floor beams have been numbered. These numbers are used throughout this dissertation to describe instrumentation locations.

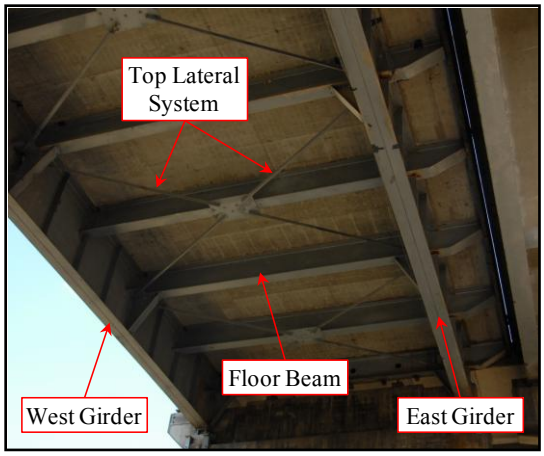

Figure 3-9: Top lateral system of Bridge A

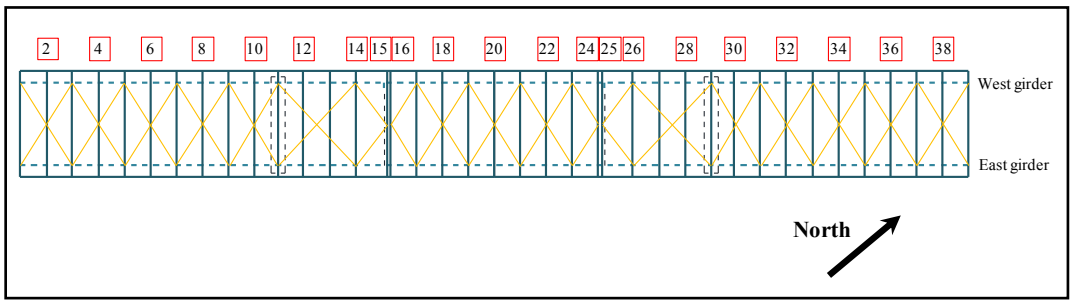

Figure 3-10: Floor beam numbering and plan view of the top lateral system

3.2.2. Instrumentation plan of Bridge A

Bridge A was the most extensively instrumented bridge among all the bridges, which were investigated during this research project, because it was approaching the end of its service life. Therefore, beginning in October of 2010 several strain gages, crack propagation (CP) gages, and accelerometers were installed on various locations of the bridge to better assess the response from truck traffic on the bridge.

The strain gages were mainly used to monitor the induced stress ranges at various bridge locations. The strain histories for the bridge were recorded using the rainflow-counting algorithm to provide data to estimate the remaining fatigue life of the structure. More details regarding the processing of data with rainflow-counting algorithm are given in Fasl (2013).

Moreover, a number of cracks and been identified through the routine fracture-critical inspections on the bridge. A number of the cracks had documented growth that had been logged in the inspection reports. All of the cracks initiated at the intersection of the top flanges of the floor beam and the longitudinal girder (Figure 3-11). Initially, it was decided to monitor the crack growth of two cracks near floor beams 34 and 38 (Figure 3-12). At Bridge A, the crack propagation gage was employed to monitor active cracks. The overall length and width of this gage are 2 in. and 0.5 in. respectively. However, the active grid area of the gage consists of 20 strands over a width of 0.4 in. As a crack propagates, it causes the strands to consecutively break and as a result the gage resistance increases. The crack growth can be determined by measuring the resistance and calculating how many strands have been broken. Typically, the crack propagation (CP) gage is bonded next to the tip of a known crack (Figure 3-13) using a general-purpose cyanoacrylate bonding agent. To protect the bonding surface against environmental effects, two layers of environmental coatings were applied. A layer of

crystalline wax and then a layer of RTV silicone were applied on top of the gage. The contribution of the CP gages to the structural monitoring of Bridge A was significant because they provided a direct indication of the fast growth of cracks on the bridge. More details of crack propagation data are given in Chapter 6.

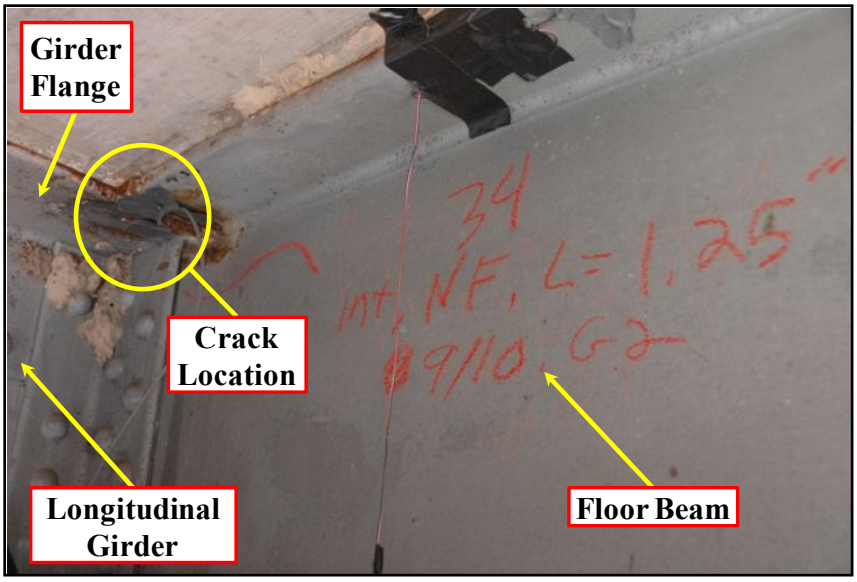

Figure 3-11: Crack location

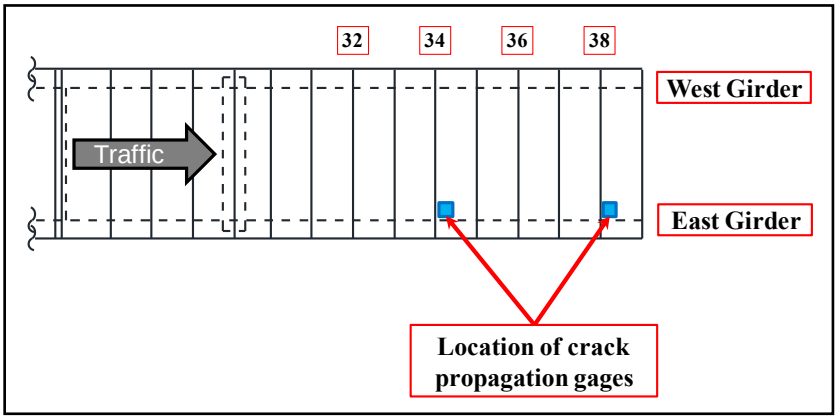

Figure 3-12: Locations of crack propagation gages at Bridge A

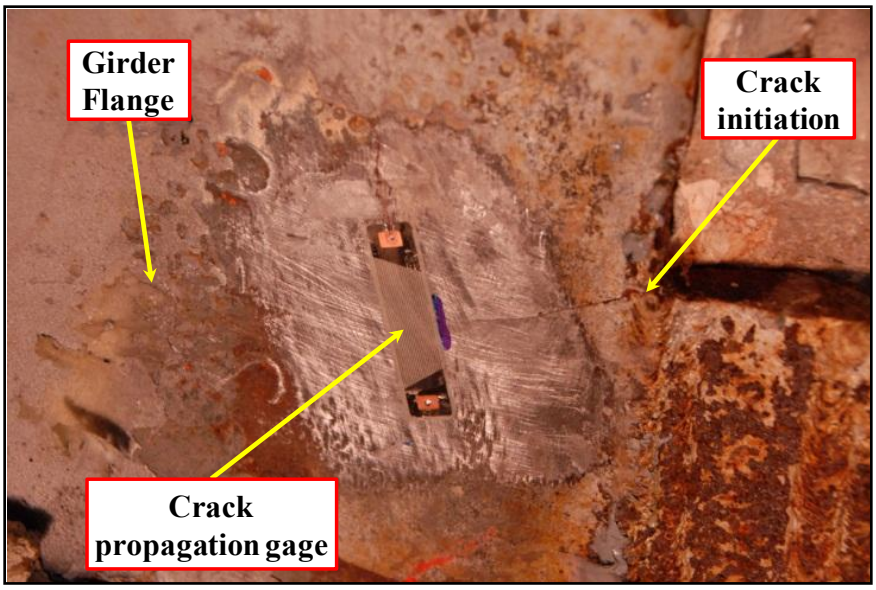

Figure 3-13: Installed crack propagation gage

The last type of sensor used to instrument Bridge A was the accelerometer. Accelerometers were utilized to quantify the characteristics of the bridge vibrations (i.e. amplitude and frequency) along its length and width. To achieve a detailed profile of the vibration characteristics, a dense array of accelerometers needs to be deployed throughout the bridge. During this research project six, ±2g accelerometers were used to measure the dynamic response of the bridge under moving loads. To increase the density of the array of readings required the frequent repositioning of the accelerometers.

The accelerometers were placed at 28 different locations along the length of the bridge, and at each location, vibrations were continuously recorded for at least one week. Due to boom-lift height restrictions, only the north end span and overhang section were instrumented with accelerometers. Figure 3-14 illustrates the exact location the accelerometer readings were obtained.

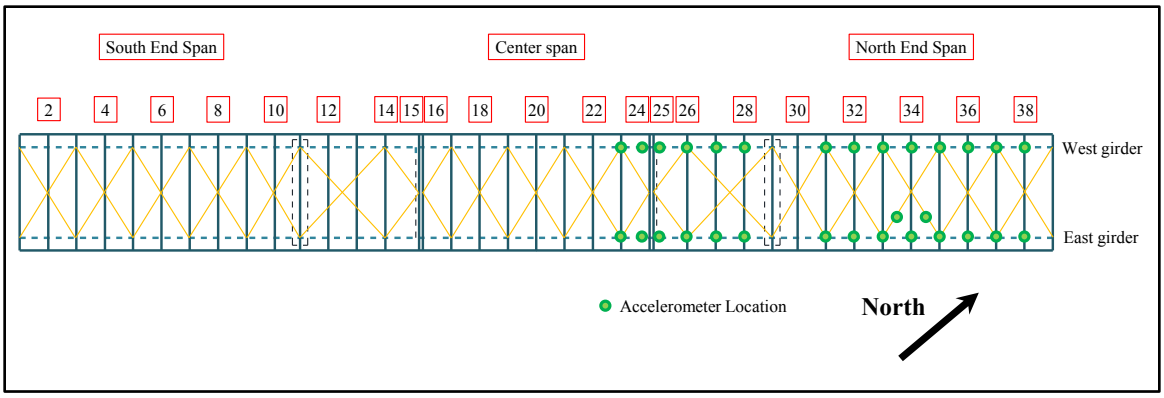

Figure 3-14: Locations of the accelerometers at Bridge A

Typically, the accelerometers were clamped on the bottom flange of the longitudinal girder (Figure 3-15a) at a location where the floor beam framed into the girder. However, in one case the accelerometer was clamped to the midspan of a lateral brace (Figure 3-15b) to examine the dynamic response of the brace for two different scenarios. In the first scenario, the accelerometer was mounted directly to the brace. In the second, a 13-lb weight was added below the accelerometer to replicate the weight of an energy harvester. The weight of the lateral brace was comparable to the weight of the energy harvester. The added weight was included to investigate the impact that the mass of the harvester on the natural frequencies and dampening effects on the braces dynamic response.

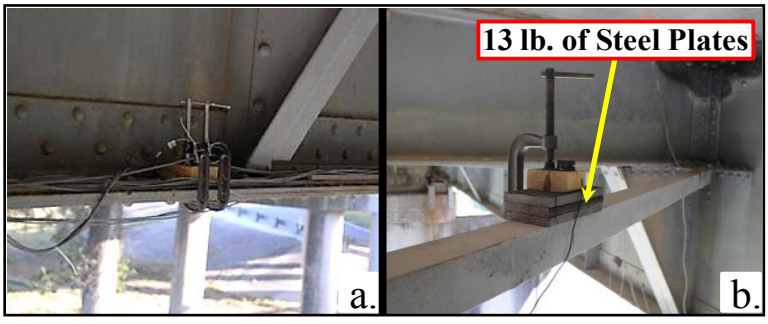

Figure 3-15: Accelerometer at: a) the bottom flange of the longitudinal girder, and b) midspan of a lateral brace

3.2.3. Field instrumentation results of Bridge A

As mentioned above, Bridge A was instrumented with strain gages, crack propagation gages, and accelerometers. These instruments were useful to assess the performance of the bridge. In this section, only the results of the accelerometers are discussed. The results from the two crack propagation gages are presented in more detail in Chapter 6.

Between October 2010 and December 2011, acceleration data from 28 locations were collected for a total of 55 days. As part of the monitoring of Bridge A, a controlled load test was performed. For this load test, a TxDOT inspection truck (Aspen Aerials UB-60 snooper truck) drove over the bridge with no other traffic present. The truck passed the bridge in various lane positions and at speeds of 10 mph, 30, 45 and 63 mph. The total weight of the inspection truck was approximately 65 kips and the axle spacing and weights were measured prior to the test. Figure 3-16 illustrates the truck used in this load test. The objective of this investigation was to determine the characteristics of the vehicle-induced bridge vibrations, and consequently to optimize the design of the vibration energy harvester. For the purpose of this dissertation, only acceleration data from important locations are presented. Strain data from these tests were also recorded and are presented in Fasl (2013).

The acceleration amplitudes measured in Bridge A were considerably higher than those measured at the other bridges. This observation can be explained by the inherent flexibility of the discontinuous flanges as well as the deterioration of the bridge due to the age. Figure 3-17 demonstrates the acceleration histories recorded during the tests at the midspan location (i.e. floor beam 35). The first subfigure of Figure 3-17 shows a typical sample of acceleration signal recorded during rush hour, and the second subfigure is the acceleration output captured during the controlled load test. The results from the random

sample compare reasonably well with the load test data. However, significant differences exist at some locations due to the different vehicle mass that is present on top of the bridge. The mass of traffic crossing the bridge can affect its dynamic response. Thus, the random sample has higher amplitude and more noise (i.e. small vehicles) than the load test, whereas the TxDOT truck was the only vehicle on top of the bridge.

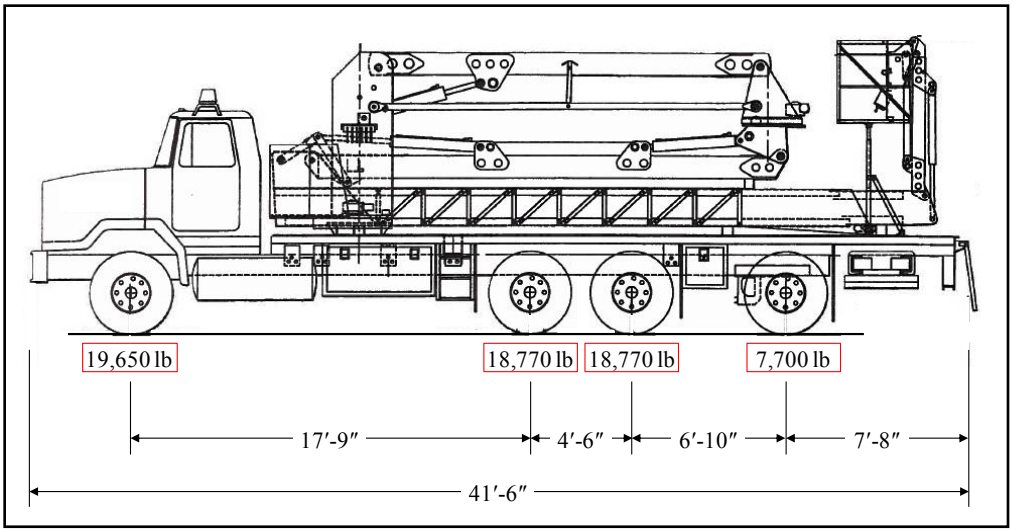

Figure 3-16: Truck used in the controlled load test (Aspen Aerials)

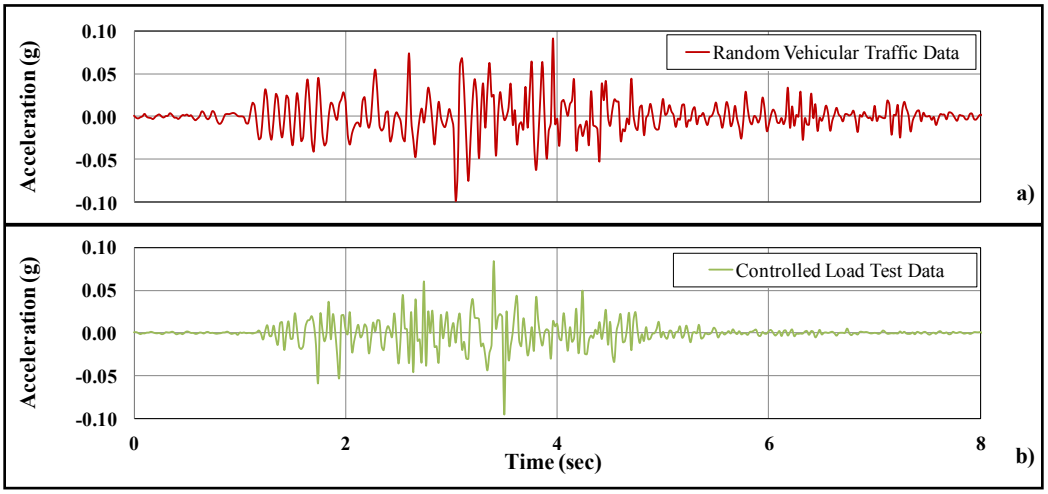

Figure 3-17: Acceleration histories of Bridge A from a) random vehicular traffic data, and b) controlled load test

As previously mentioned, two lateral braces on Bridge A were instrumented with accelerometers to examine the dynamic response of this bridge component with and without the mass of the harvester. Previously, it was hypothesized that the mass of the harvester was negligible compared with the mass of the girder. This assumption was valid for the girder locations, but it was not accurate for a slender brace. Figure 3-18 shows the resulting acceleration histories from braces with and without additional mass. It can be observed that by adding the harvester weight the dynamic response of the brace changes significantly. The acceleration amplitude changes from ± 0.35g for the case without mass to ± 0.15g for the case with the additional mass. Lastly, the additional harvester mass affects the frequency content of brace vibrations. More conclusions are drawn from the response spectra of the vibration histories that are presented in Chapter 4.

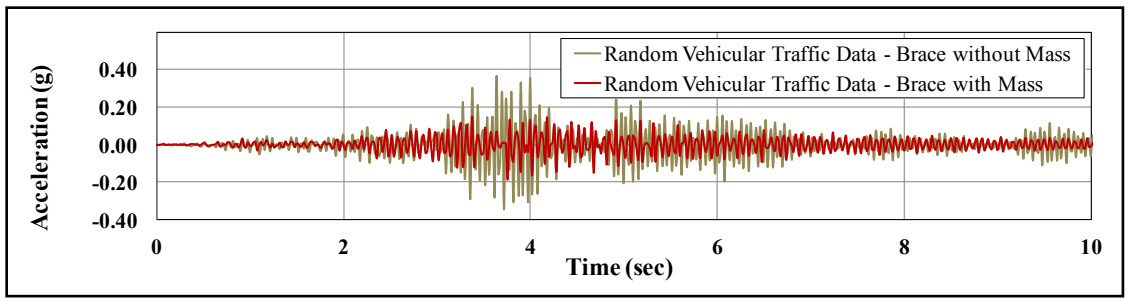

Figure 3-18: Acceleration histories of Bridge A braces with and without mass

3.3. BRIDGE B

Bridge B is also located in Texas and is shown in Figure 3-19. The bridge consisted of a single-lane direct connector (i.e. ramp structure) between two highways with an intersection angle of approximately 90 degrees. This bridge was constructed in 2002 as a four span continuous twin trapezoidal box-girder bridge. Since this type of bridge has two girders, AASHTO (2012) classifies the two tension flanges over the positive moment region as fracture-critical members.

Figure 3-19: Overall view of Bridge B

3.3.1. Geometry of Bridge B

Bridge B has four continuous spans with an overall length of 880 ft. Figure 3-20 demonstrates the plan view of Bridge B. The two end spans (i.e. Span 1 and Span 4) have a length of 210 ft. whereas the two middle spans (i.e. Span 2 and Span 3) are 230 ft. long. The plan view in Figure 3-20 shows that the bridge is straight for the first span and for 116 ft. of the second span. The remaining portion of the second span and the rest of the bridge have a horizontal radius of curvature at the mid-width of the concrete deck of 458 ft and an angle change of approximately 90°. Bridge B is supported by an elastomeric bearing under each girder, except for the steel straddle cap at the middle support, where the girder is supported by a steel pin connection located on top of the steel box straddle cap.

Within each box girder, chevron type cross frames and a top flange lateral bracing system are provided. The purpose of the top lateral truss is to provide stability during construction. In addition to the internal cross frames, a ¾-in. thick steel plate diaphragm is welded to the box girder at each interior support to prevent distortion of the section. Each diaphragm features two 1¼ in. by 12 in. stiffeners, and an access port, which is 2 ft. 8 in. tall and 1 ft. 4 in. wide, to allow the inspectors access along the entire length of the girder.

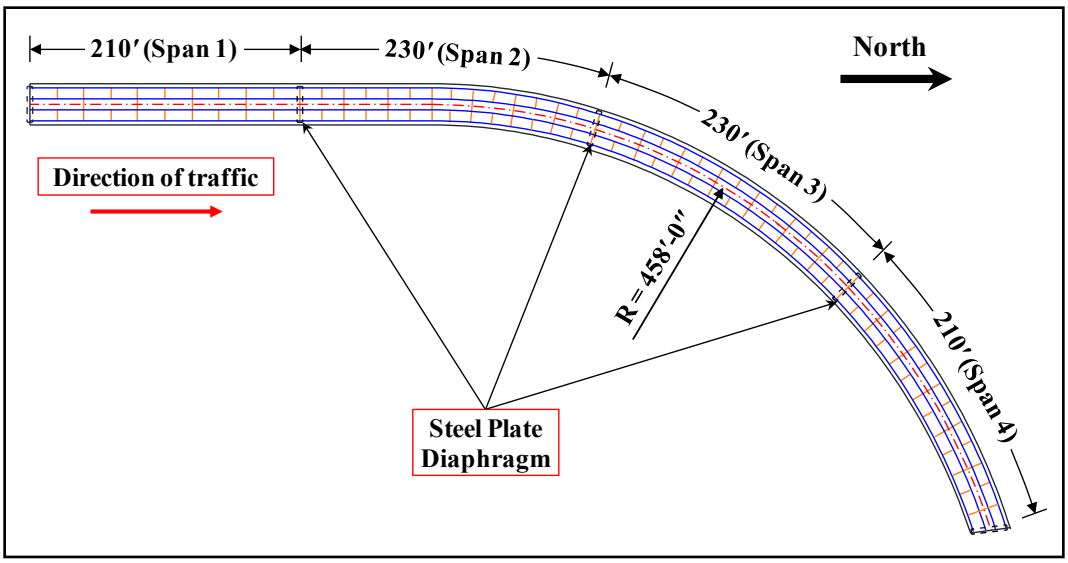

Figure 3-20: Plan view of Bridge B

Figure 3-21 demonstrates a typical cross section of Bridge B. The overall width of the concrete deck is 30 ft. The exit ramp features a 14-ft. traffic lane and two shoulders of 6 ft. and 8 ft. respectively on each side of the bridge (6 ft. shoulder on the outside of the curve). The surface of the concrete deck and the box sections have a cross slope of 2.5% (Span 1), and 6% (Span 2-4) with the direction of slope indicated in Figure 3-21. This inclination is mandatory to provide drivers with a safer turn radius. The concrete deck is

rigidly connected to the steel section through shear studs that are welded on the top flange of the box-girders

The twin trapezoidal box girders are spaced 15.67 ft. center-to-center, and they are 6.5 ft. deep. The bottom flange of the girders is 59 in. wide, and its thickness varies along the length of the bridge from ¾ in. to 2¼ in. All the top flanges are 24 in. wide except for a region above the third intermediate support, where the width of the top flanges is 28 in. Their thickness varies from 1 in. to 2¾ in.

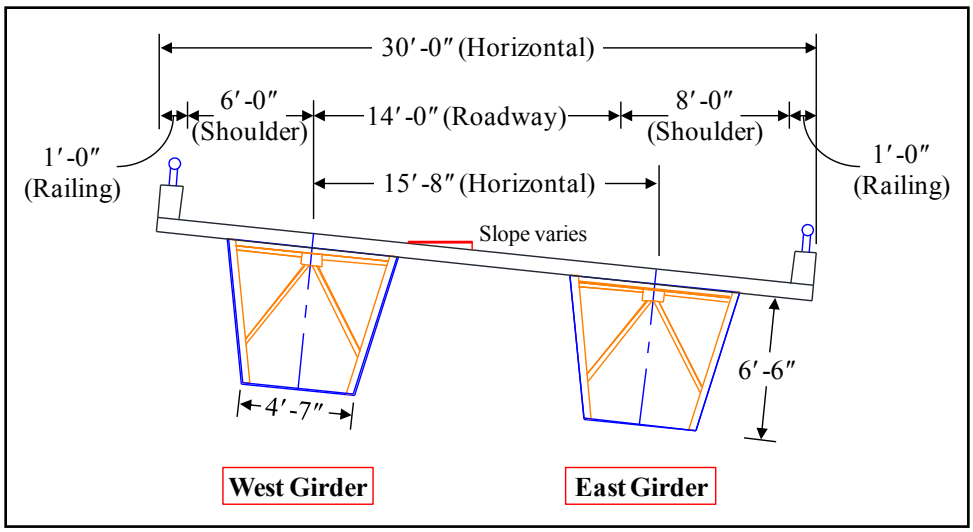

Figure 3-21: Typical cross section of Bridge B

3.3.2. Instrumentation plan of Bridge B

Bridge B was mainly instrumented with accelerometers at ten different locations along the length of the bridge. The same type of accelerometer as used on Bridge A was utilized to capture the vibration characteristics of Bridge B. Accelerometers could be installed at any longitudinal location of the bridge because the interior of the box girders was accessible through the entire length. In contrast to Bridge A, the accelerometers at Bridge B were mounted to wood blocks that were glued to the mid-width of the girder

bottom flange with epoxy (Figure 3-22). Figure 3-23 shows the accelerometer location on a typical cross section of Bridge B.

Due to the symmetry of the bridge and the limited instrumentation, it was decided to monitor only the two southern spans (i.e. Span 1 and 2) of the east box girder. Five accelerometers were installed at each span, two of them approximately 20 ft. from the supports and the other three at the quarter, half, and three-quarter locations of each span. Figure 3-24 shows the exact locations of the accelerometers along the length of Bridge B.

Figure 3-22: Typical accelerometer installation at Bridge B

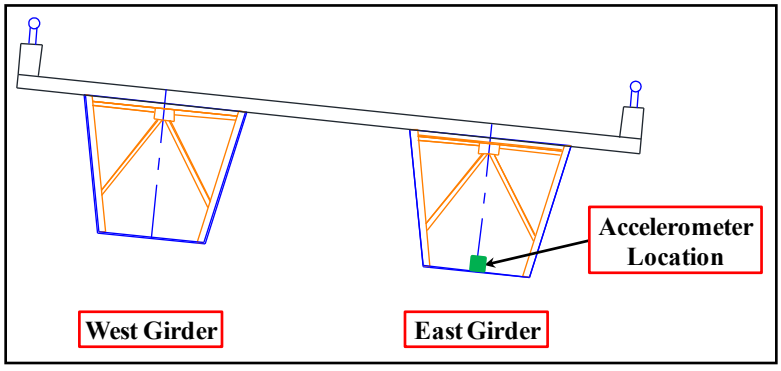

Figure 3-23: Location of the accelerometer at the cross section of Bridge B

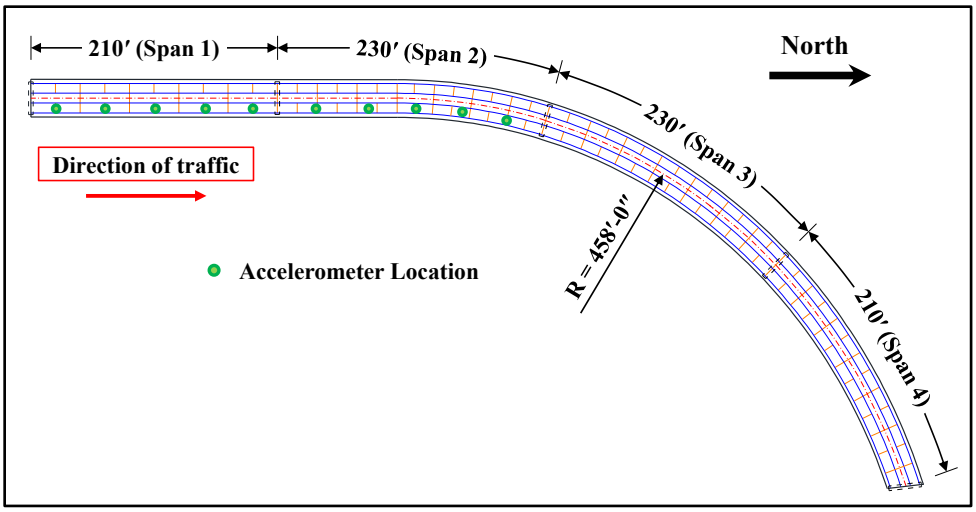

Figure 3-24: Locations of the accelerometers along the length of Bridge B

3.3.3. Field instrumentation results of Bridge B

Acceleration data at ten different locations of the Bridge B east box girder were collected during July 2009. It was observed that vehicles tend to reduce speed when approaching the connector bridge. In addition, the truck traffic volume is significantly less than at Bridge A. Due to the limited number of large vehicles crossing Bridge B as well as geometrical differences between the two bridges, the recorded vibrational amplitudes were not as high as at Bridge A. Figure 3-25 illustrates a typical acceleration signal from the middle of Span 2. The maximum acceleration amplitude is ± 0.05g, which is almost 50% less than the maximum amplitude observed at Bridge A.

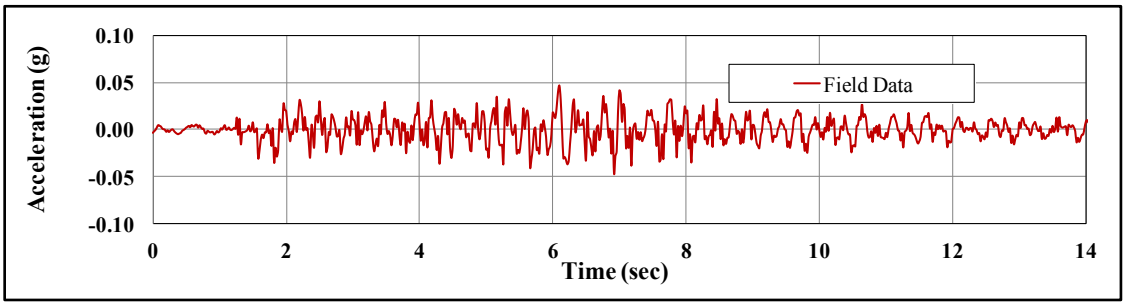

Figure 3-25: Acceleration history from the mid-length of the second span of Bridge B

3.4. BRIDGE C

Bridge C (Figure 3-26) is located in central Texas and consists of a system with six built-up I-girders across the width of the bridge. Bridge C is not considered fracture-critical due to the inherent redundancy. Even though this research project focuses on fracture-critical bridges, it was decided to instrument this bridge to obtain significant information to assess the feasibility of vibration energy harvesting at many different types of steel bridges in the U.S.

Figure 3-26: Overall view of Bridge C

Bridge C was constructed in 1959, and it has three traffic lanes with traffic running west to east (left to right in Figure 3-26). The right lane of the bridge serves as the feeder lane for an exit ramp that exists just past the end of the bridge. Based on observations during the field instrumentation, the daily truck traffic at this bridge is considerably less than the traffic of Bridge A. Consequently, lower truck volume coupled with the relatively short spans of the bridge lead to amplitudes of truck-induced vibration that were significantly less that bridge A. More details of the vibration results are presented in a subsequent section.

3.4.1. Geometry of Bridge C

Bridge C is a non-composite five-span continuous bridge with an overall length of 210 ft. (Figure 3-27). The two end spans (Span 1 and 5) and the middle span (Span 3) are

35 ft. long. Span 2 and Span 4 are 47.5 ft. and 57.5 ft. long respectively. The total width of the concrete deck is 49.5 ft. The six longitudinal girders are spaced 8.33 ft. on center. For stability, cross frames were provided with a spacing of 16.25 ft. The supports of Bridge C are skewed (20°-40′) due to the geometry of the interchange.

A typical cross section of Bridge C is presented in Figure 3-28. The concrete deck is supported by six identical I-girders (W27X102). The I-girders are reinforced with ½ in. thick cover plates on the top and bottom flange at the negative moment regions above the interior supports and at the midspan of the longest span (i.e. Span 4).

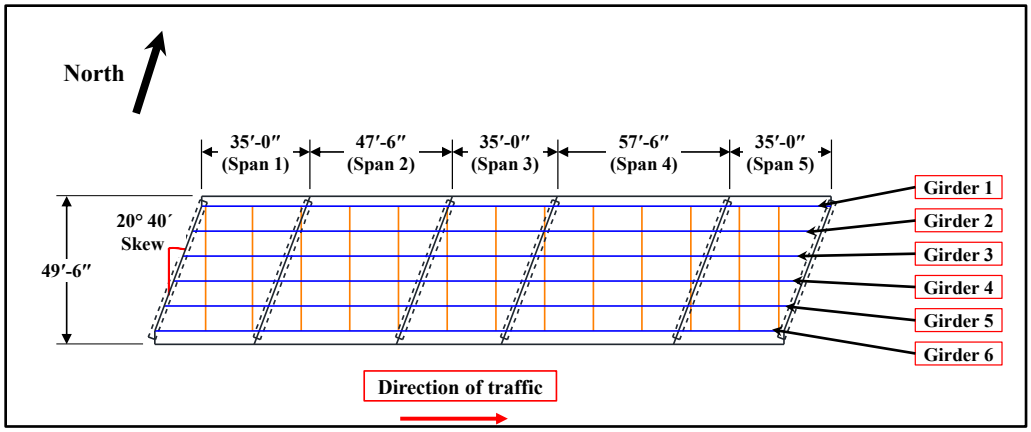

Figure 3-27: Plan view of Bridge C

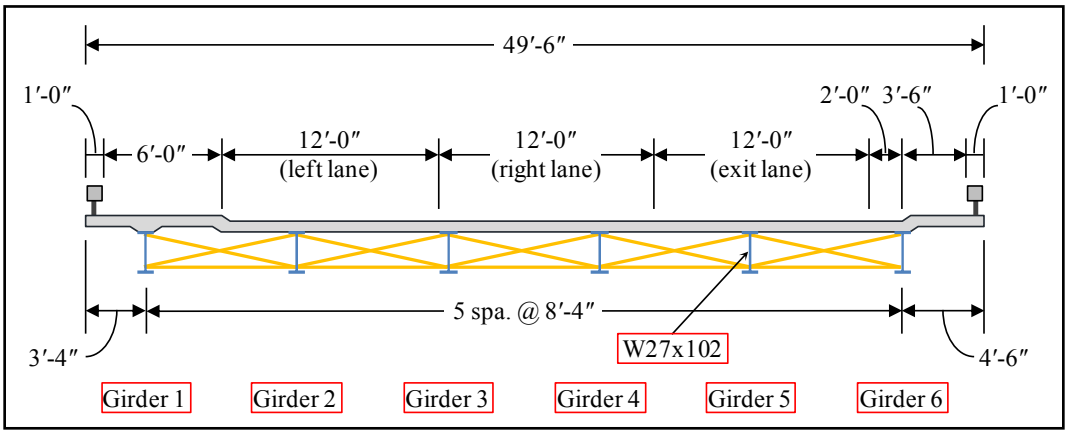

Figure 3-28: Typical cross section of Bridge C

3.4.2. Instrumentation plan of Bridge C

The instrumentation on this bridge was somewhat limited for two reasons. First, this type of bridge is not fracture critical and second the major objective of this investigation was to quantify the temperature effects and the acceleration amplitudes. Since traffic passes underneath the two longest spans, the instrumentation was limited only to the middle span (Span 3). Figure 3-29 demonstrates the two locations of the accelerometers. One accelerometer was mounted on the bottom flange at midspan of Girder 3, and the other accelerometer was positioned third interior support of Girder 3.

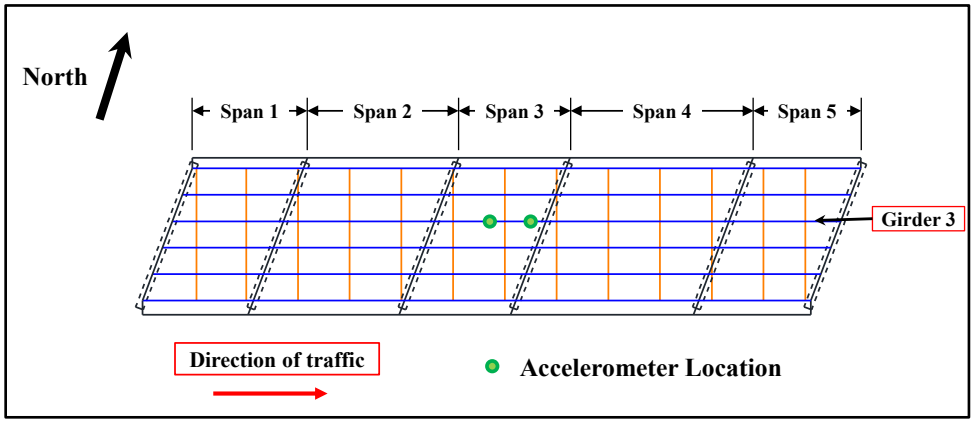

Figure 3-29: Plan view with the accelerometer locations at Bridge C

3.4.3. Field instrumentation results of Bridge C

The acceleration monitoring in this bridge was completed in March 2010. Acceleration data were acquired for nine days from the two locations shown in Figure 3-29. A sample of acceleration history is presented in Figure 3-30. The data were obtained from the midspan of Girder 3. The maximum vibration amplitude was approximately ± 0.02g, which is significantly less than the previous two bridges – ± 0.10g (Bridge A) and ± 0.05g (Bridge B). The small amplitude is attributed to the short span length and to the type of bridge (i.e. multi-girder bridge). This is also the reason

why the duration for which the accelerometer is excited is less than at the previous bridge. At Bridge C, the accelerometer was typically excited for approximately 2 sec, whereas at Bridge A and Bridge B the accelerometers were excited for 4 sec and 10 sec, respectively.

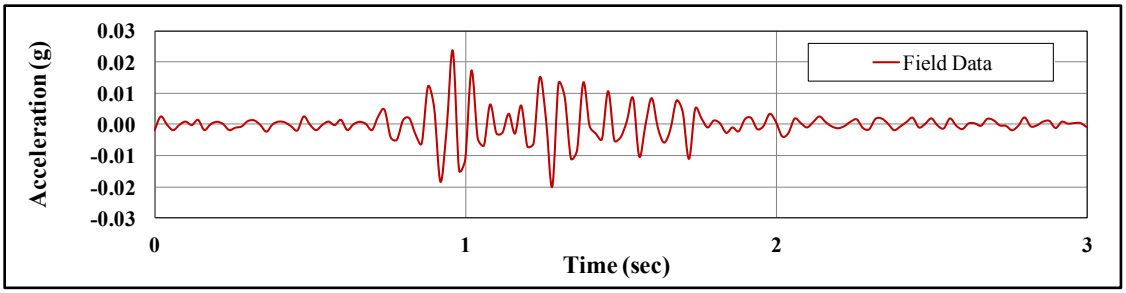

Figure 3-30: Acceleration history from the Girder 3 midspan of Bridge C

3.5. BRIDGE D

Bridge D was described in Fasl (2013) and was not instrumented with accelerometers nor was it dynamically analyzed with the finite element programs. Therefore, Bridge D is not discussed further in this dissertation. The main reason for listing the bridge in this dissertation was for consistency in the bridge identification between Fasl (2013).

3.6. BRIDGE E

Bridge E (Figure 3-31) is located in Oregon and provides highway access across a river. It is a twin multiple-span steel through truss bridge. The original bridge was built nearly 100 years ago and served two-way traffic until 1958 when a second, identical multi-span truss bridge was built adjacent to the original bridge. Since then, each truss bridge only carries single directional traffic (i.e. northbound or southbound). Moreover, each of the twin truss bridges carries three traffic lanes. The fifth span from the north of Bridge E is a vertical-lift span for river navigational clearance.

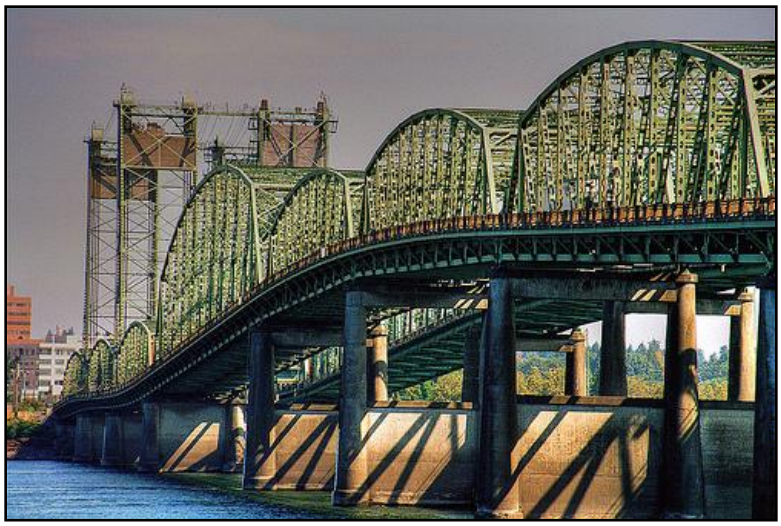

Figure 3-31: Overall view of Bridge E

3.6.1. Geometry of Bridge E

Bridge E has fourteen, simply-supported spans ranging from 256.67 ft. to 278.75ft., with a total bridge length of 3531 ft. Ten of the fourteen spans are over water and their access is therefore limited. However, the other four spans are above ground and their instrumentation is easier. Most of the trusses have approximately the same geometry. The fourteenth span of the original bridge was monitored and analyzed as part of this dissertation. The height of the truss is 44.5 ft. and the center-to-center distance between the two adjacent trusses is 45.5 ft.

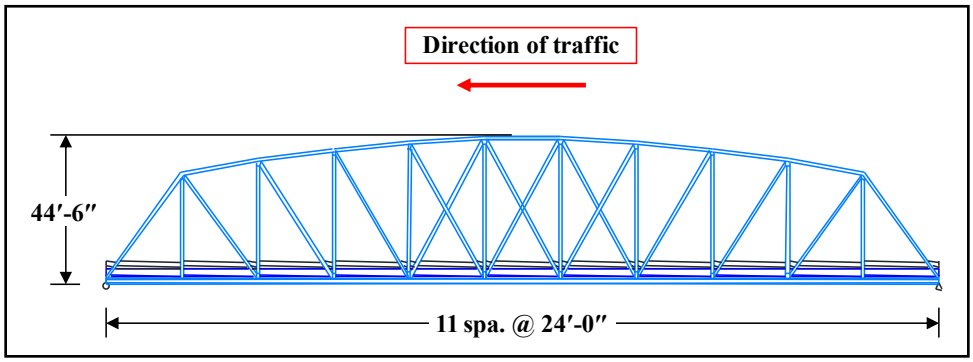

Figure 3-32: Typical elevation view of Bridge E

Figure 3-33 illustrates the different components of the floor system. The floor system is the main support of the concrete deck. The concrete deck rested on six longitudinal stringers that frame into a deep girder. The deep girder consists of a plate girder system in the case of the original truss bridge and of a built-up truss in the new truss bridge. The two typical cross sections of the deck structure are shown in Figure 3-34 and Figure 3-35.

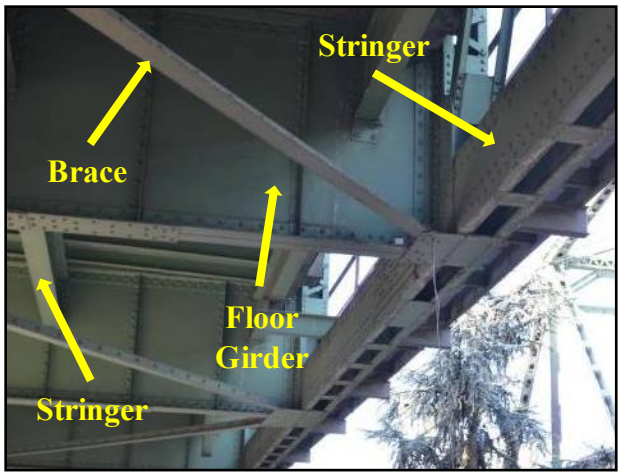

Figure 3-33: Floor system of Bridge E

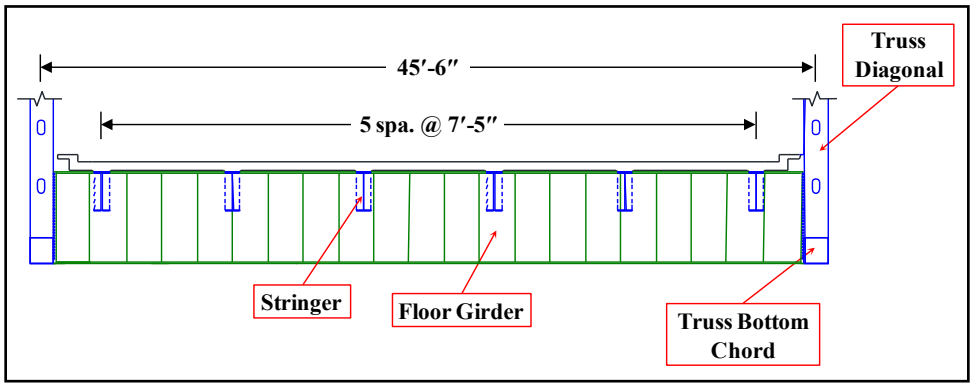

Figure 3-34: Typical deck cross section of the original truss bridge built in 1917

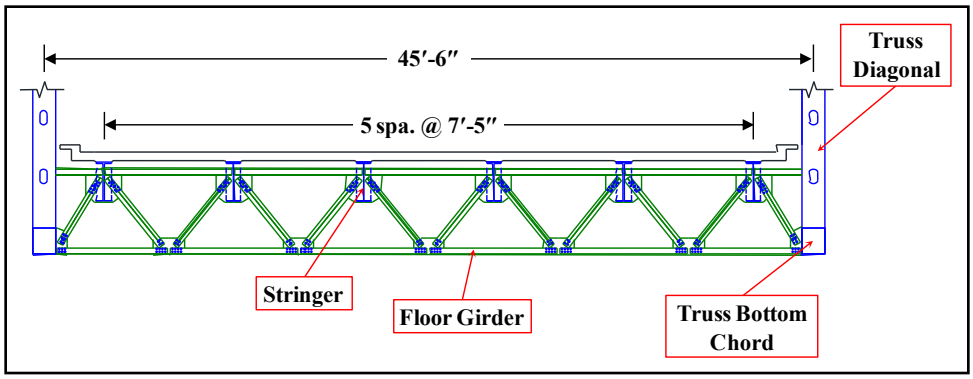

Figure 3-35: Typical deck cross section of the new truss bridge built in 1958

A typical elevation view of the fourteenth span of Bridge E is shown in Figure 3-32. The bottom chords of the truss are braced against lateral movement with approximately 26-ft long WT 4x12 braces. Figure 3-36 illustrates a plan view of Span 14 showing the floor system, lateral braces, and stringers.

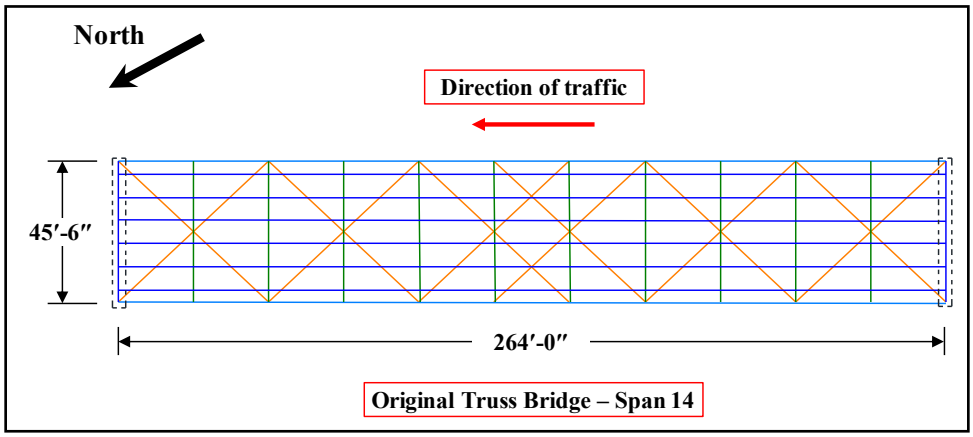

Figure 3-36: Plan view of Span 14

3.6.2. Instrumentation plan of Bridge E

The instrumentation of Bridge E was limited to the Span 14 of each truss bridge due to the ease of access from the ground. Span 14 was instrumented with three accelerometers. Figure 3-37 demonstrates the locations of the three accelerometers. Two

of the sensors were mounted to the connection plate at the intersection of the floor girder and bottom chord (Figure 3-38). The first sensor was placed near the northwestern support and the second at the midspan of the truss bridge. The third sensor was clamped at the midpoint of a long, slender brace (Figure 3-39). The new truss bridge was later instrumented in a similar fashion. All the locations were instrumented and data were collected for three hours. A detailed summary of the instrumentation results is provided in the next section.

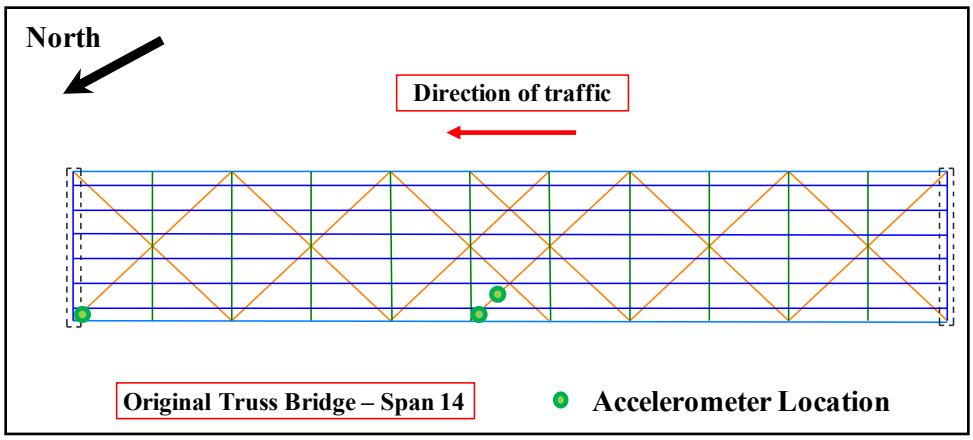

Figure 3-37: Accelerometer locations at Span 14 of Bridge E

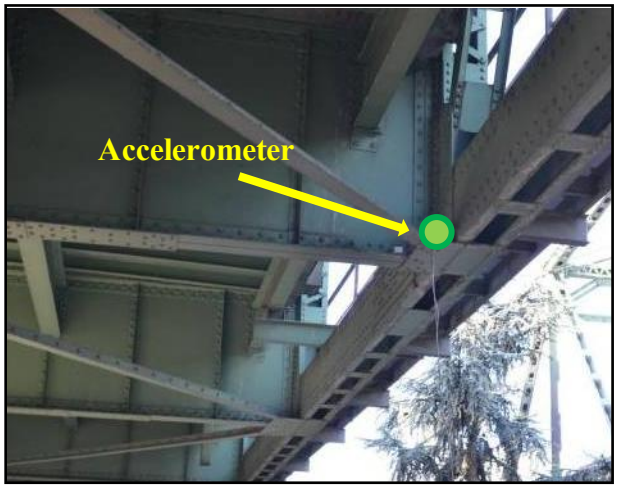

Figure 3-38: Typical accelerometer installation on a floor girder of Bridge E

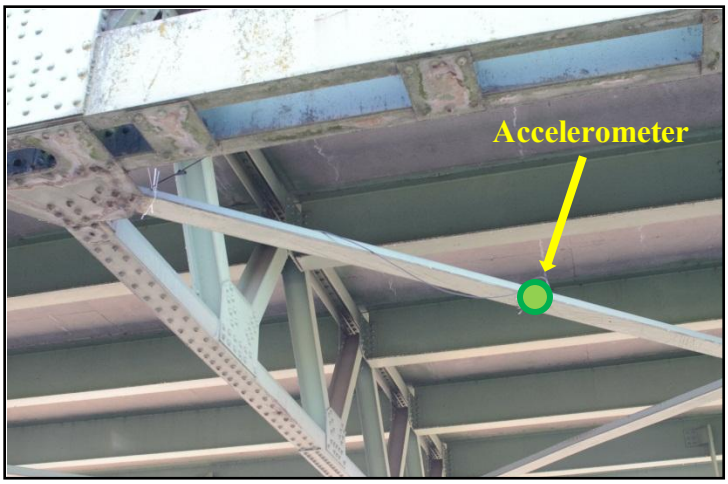

Figure 3-39: Accelerometer placed to the midpoint of the bottom chord of Bridge E

3.6.3. Field instrumentation results of Bridge E

The instrumentation of Bridge E was completed in August 2011. A team of Wiss, Janney, Elstner Associates accessed the bridge and placed accelerometers near the support, midspan, and mid-length of a brace Figure 3-37. Due to high traffic volume and limited recorded data (about three hours), a clear vibration event was not recorded. Figure 3-40 illustrates a typical vibrational signal recorded from the midspan of Bridge E. For this random sample the maximum acceleration amplitude is approximately ± 0.04g, which is similar to the dynamic response of Bridge B.

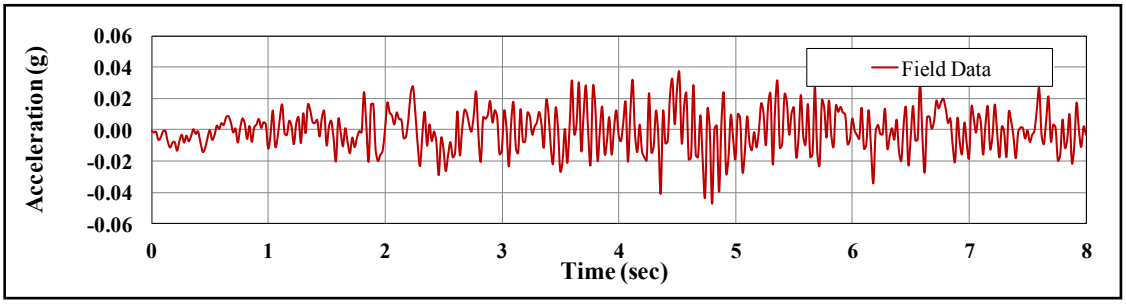

Figure 3-40: Acceleration history from the midspan of Bridge E

3.7. CHAPTER SUMMARY

A summary of the instrumentation of the bridges during this research project is provided in this chapter. One of the main goals of the monitoring was to obtain important information and determine the vehicular-induced dynamic behavior of typical US highway bridges. All the necessary instrumentation information was presented in this chapter. The basic geometric properties and the instrumentation plan of each bridge were previously described. This information is necessary for the reader to fully understand all the work conducted during this project, as well as understanding the results and comparisons of field data analysis and computational analysis that are outlined in Chapter 4.

CHAPTER 4

Analyses of Bridges

4.1. INTRODUCTION

There are a number of limit states that need to be evaluated in the design of highway bridges. The design loads that must be considered include a combination of dead and live loads. While the dead loads are relatively predictable, there is a great deal of variability in the actual magnitudes and locations for the live loads on bridge systems. From a design and behavior perspective, the primary vehicles of interest in bridges generally consist of multi-axle trucks. The design truck that is part of the AASHTO HL-93 design load (i.e. HL-93 live load is a combination of a design truck or design tandem, and a design lane load) consists of three axles. The weight on the front axle of the design load is 8 kips, whereas each of the middle and rear axles carry 32 kips. In addition, the spacing between the front and middle axle is 14 ft (constant). On the other hand, the spacing of the two 32-kip axles varies between 14 ft and 30 ft depending on which spacing produces the most extreme force effects. Although statistically the truck provides a good representation of the critical truck that can be used to determine factored design forces, the actual vehicles that utilize the bridge have a wide spectrum of loads as well as the number and spacing of the axles. The wide spectrum of vehicles, variations in speed, as well as other geometrical intricacies of the bridge has a dramatic effect on the dynamic response of a specific bridge, which is critical to understand the potential for energy harvesting from dynamic vibrations from the bridge.

As mentioned in previous chapters, the design and optimization of a vibration energy harvester requires two pieces of information, namely the acceleration amplitude and the dominant frequencies of vibration. The most accurate method of obtaining the

amplitude and frequency of vibration for a specific bridge is by instrumenting the structural components at the desired locations. While this approach provides the most representative information, field monitoring is costly and time consuming and may not be practical in many situations. Thus, models of the instrumented bridges were developed to determine if vehicular-induced acceleration histories can be reliably predicted from analytical methods. The type of computational analysis that needs to be performed to obtain the acceleration time history is a transient response analysis. Once the acceleration time history induced by the moving truck loads is computed, a spectral analysis must be implemented to obtain the dominant frequencies to calibrate the vibration harvester and maximize the amount of energy harvested from the bridge.

A transient dynamic analysis is required to examine the effect of moving truck loads on bridge vibrations. This type of analysis can be carried out by computer programs utilizing the finite element analytical (FEA) method. Although 3D FEA models can be created of the bridge system, such a model is time consuming to develop and is often not practical. Therefore investigating the performance of simplified modeling techniques is highly desirable. There are several commercially available software programs capable of performing these analyses. ANSYS (2012), and SAP2000 from CSI (2011) were primarily employed to develop the respective 3D and grillage models of the bridges under investigation and compute their dynamic response. A summary of guidelines for modeling and dynamically analyzing bridges is outlined in this chapter. Finally, the calculated acceleration histories were compared with the acceleration histories that were previously recorded in field tests to determine how well computer models predict the behavior of a given bridge. The comparison of the results is presented in this chapter.

4.2. METHODS TO MODEL BRIDGES

During this research project, two different methods to model bridges were employed. The first method is to create a 3D finite element model of the bridge, and the second method focuses on simplified models utilizing line elements to develop a grillage model of the bridge. More information of the two methods is provided in the next two sections.

4.2.1. 3D finite element model

3D models of steel bridge systems typically utilize shell elements, beam elements, truss elements, and springs to closely simulate the bridge under examination. Although solid elements can be used to model the bridge, such a model will usually possess far too many degrees of freedom and as a result these elements are rarely used in models of the complete structure. In most applications, the bridge girders (i.e. top and bottom flanges, web) and the concrete deck are modeled with shell elements. Cross frames and other secondary elements along the length of the bridge are usually simulated with either beam or truss elements. Truss elements are often employed to model the top lateral bracing system of box girders, or other compression or tension struts used for bracing on the bridge. Although idealized support conditions such as pins or rollers are sometimes used in bridge modeling, springs can also be used to consider flexibility in the supporting elements. Considering support flexibility can be extremely important in a dynamic analysis since the boundary conditions can potentially influence the dynamic response of the bridge. Hence, boundary conditions must be accurately simulated to represent as close as possible the actual bridge support properties. In all the analyses performed during this research program, it was assumed that the substructure (foundation) elements such as the abutments, piers, and pier caps were rigid with springs used to model the flexibilities in the bearings. In other modeling situations, if fixed

foundation conditions do not capture the real foundation characteristics, then the engineer needs to modify them accordingly to better model the actual conditions.

Comparisons of field data and analytical results on this study showed that the number of springs per support generally has a minor influence on the vibrational results. The number of the springs (i.e. three springs vs. one spring per support) mostly affected the local stress induced at the bottom flange of the girder.

The above mentioned modeling decisions were employed to develop 3D models of the bridges from the field studies that were discussed in Chapter 3 (i.e. Bridge A, B, C, and E) and compute the vibration time histories induced by moving trucks. The next step was to perform a response spectrum analysis on the acceleration histories and transform the data into a response spectrum, from which the dominant frequencies and their respect average power could be determined. Later in this chapter, the extracted acceleration histories are compared with the field data obtained from the instrumented bridges. Table 4-1 provides a brief overview of the general characteristics of the instrumented bridges.

Table 4-1: Structural characteristics of the instrumented bridges

	Bridge Structural System	**# of Spans**
Bridge A	Riveted twin plate girder	3
Bridge B	Twin trapezoidal box girder	4
Bridge C	Six rolled I-girders	5
Bridge E	Steel through truss	1

The first bridge to be modeled with the 3D method was Bridge A. Due to the inherent complexity of the structural system; Bridge A was initially modeled using ANSYS (Figure 4-1). Before performing the dynamic analyses, the model was validated with the recorded data from a controlled live-load test that was performed in the field.

The goal of the test was to obtain strain and acceleration data induced by a known truck traveling at specified speeds. The solid line in Figure 4-2 illustrates the response from a strain gage during the controlled load test (10 mph) that was installed at the top flange of west girder at floor beam 34. The corresponding results from the ANSYS computer analysis are shown in the dashed line. The next step was to perform a transient dynamic analysis and determine the dynamic response. Bridge A was analyzed for the moving truck with axle load shown previous in Figure 3-16 at speeds used in the load tests of 10 mph and 63 mph.

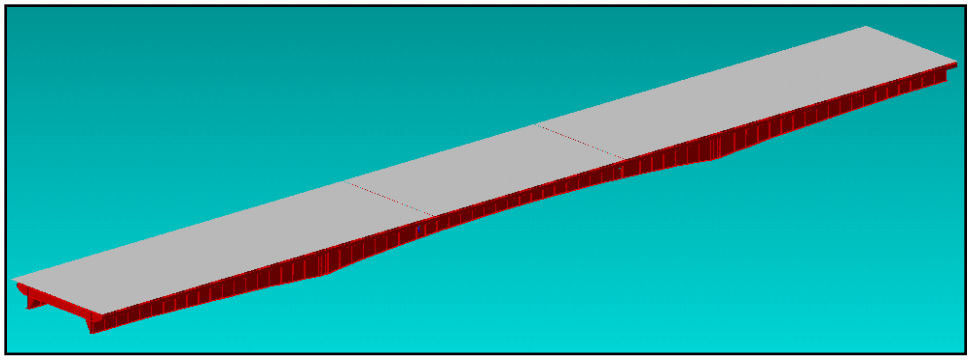

Figure 4-1: 3D model of Bridge A produced in ANSYS 11.0

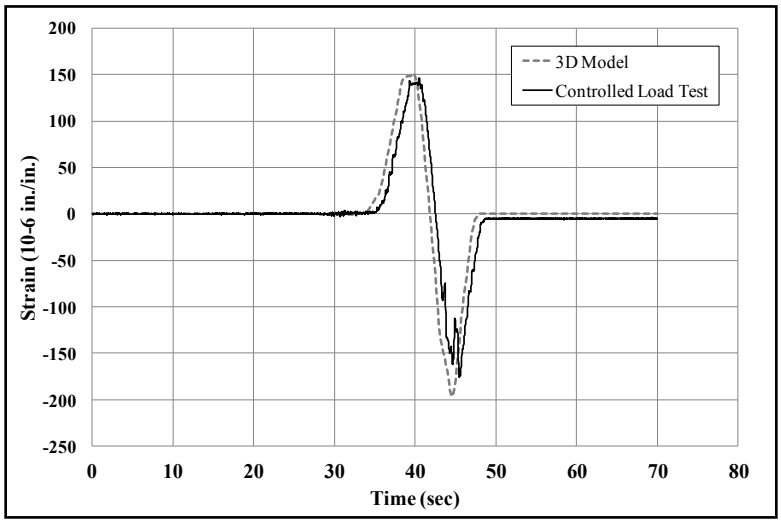

Figure 4-2: Comparison of measured and calculated data for Bridge A

For the purposes of comparison, 3D models were created in both SAP2000 and ANSYS. Figure 4-3 shows the 3D SAP2000 model that was created for Bridge A. The dynamic results from the two computer programs were relatively close and therefore it was decided to use SAP2000 to create 3D models of the rest of the bridges from the field studies in SAP2000. The SAP2000 program is a relatively common program used by bridge engineers, and with a bridge module that simplifies the development of the bridge geometry. Following the same methodology as in Bridge A, the models of Bridge B, Bridge C, and Bridge E were developed. Figure 4-4, Figure 4-5, and Figure 4-6 illustrate the 3D models of the bridges under investigation. Shell elements were employed to model the main structural components (i.e. steel girders and concrete deck) of Bridge A, Bridge B, and Bridge C. In the case of Bridge E, the truss components and floor beams were modeled with 3D beam elements, and the concrete deck was simulated with shell elements.

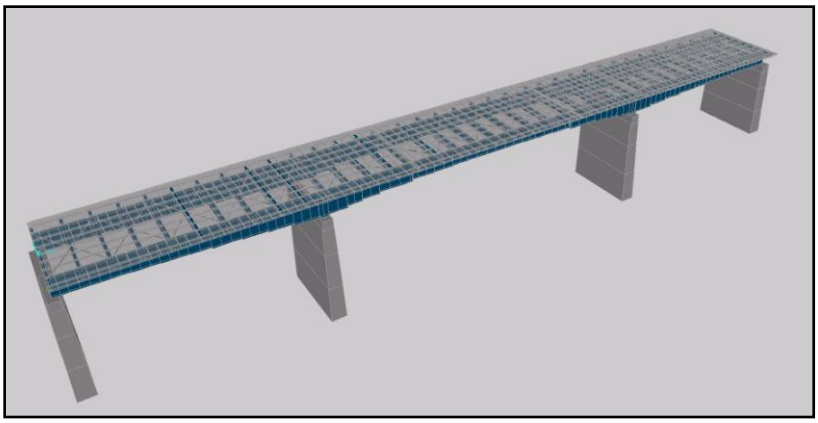

Figure 4-3: 3D model of Bridge A in SAP 2000

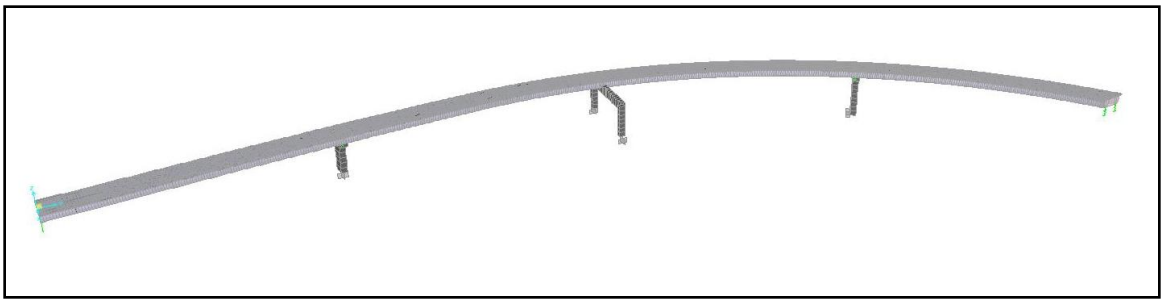

Figure 4-4: 3D model of Bridge B in SAP 2000

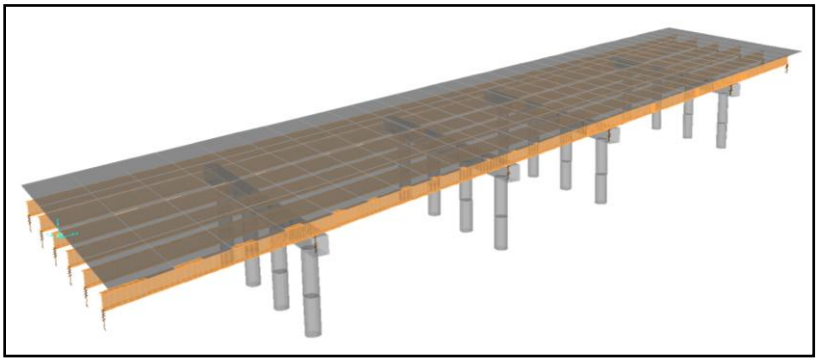

Figure 4-5: 3D model of Bridge C in SAP 2000

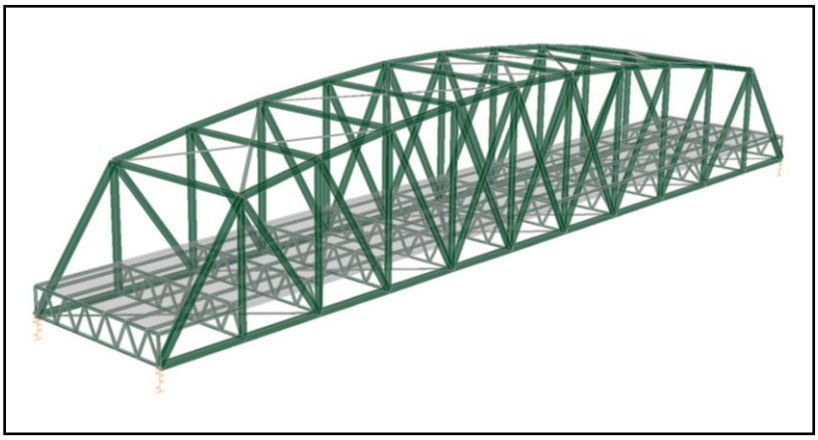

Figure 4-6: 3D model of Bridge E in SAP 2000

4.2.2. Grillage line element model

Bridges are complicated systems and to simplify the analysis engineers typically reduce the systems down into more manageable components. Components of a bridge

may consist of elements such as the longitudinal girders, floor beams, cross frames, concrete deck, bent caps, and columns. For example, a bridge girder can be modeled in several ways ranging from a single line-element beam model (i.e. simplest method) to a 3D model of the girder using shell elements (most sophisticated method used in this study). Among all these methods, the 3D shell element model provides the most accurate rendering of the structure since the cross sectional flexibility can be fully captured. Yet, this method requires considerable amount of time to develop the bridge model, and the 3D model is computationally more costly than a line element model. Thus, guidelines were developed that can be followed when utilizing line elements for modeling the primary structural components of a bridge.

The simplest method of analyzing a bridge is through a line-girder analysis that represents the overall behavior of the bridge by considering a single girder. While considering the impact of dead load on such a model is relatively straight forward, the impact of live loads with a line girder analysis are generally more complex. The AASHTO specification includes girder live load distribution factors that can be used to extrapolate the behavior of the overall bridge. In such an analysis, the loading on the line girder typically consists of the dead and live loads associated with a lane of traffic. The behavior of the overall system is then usually extrapolated using live load girder distribution factors. In some analysis cases, modeling straight, non-skewed bridges with a single line girder analysis can produce reasonable estimates of the bridge behavior. However, a line girder analysis is not generally an appropriate method to dynamically analyze bridges for moving truck loads. There are a number of different mode shapes of interest for the bridge including longitudinal, transverse, or torsional modes. In many cases, combination modes may dominate the behavior of the bridge (ie. combinations of longitudinal, transverse and torsional modes). Moving vehicles may excite one or more of

these modes. The longitudinal flexural mode, which is the most common mode to be excited, can typically be captured using a line girder model. However, the line girder analysis model cannot capture the other types of modes (i.e. transverse, torsional, etc.).

Previous studies on grillage models, which utilize line elements (i.e. beam elements), were considered in this study to investigate methods to accurately capture the bridge modes of vibration. Grillage models represent the individual girders using line elements, which greatly simplifies the structure and reduces the computational time for the analysis. However, a grillage model requires a number of assumptions about the interaction between the girders, bracing, and supports. Figure 4-7 illustrates the plan view of a typical grillage model. The bridge girders and the tributary portion of the concrete deck between the girders are represented by a series of line elements. The number of the longitudinal line elements that were used to represent the girders are located at the transverse location that coincides with the web of the girders. The mass of each longitudinal line element is determined in such way so that the total mass of the grillage model and its distribution along the length of the bridge is the same as in the actual bridge. According to AASHTO, bridges are designed as fully composite or non-composite. Thus, in many cases, the moment of inertia that is assigned to each line element considers the full composite action between the steel girders and the concrete bridge deck. A non-composite bridge would consider only the stiffness of the steel girder alone. Although the AASHTO specifications do not recognize partially composite systems, there are cases where an accidental partial composite action exists in the structure (e.g. Bridge A, and Bridge C), due to specific details (e.g. cover plates) that may be present in the structure. An example of such a case would be Bridge A that was modified by the bridge owner during this study with the addition of cover plates that were incorporated on the girder to floor beam locations. The interaction between the concrete

deck and the ends of the steel plates were found to engage some composite action between the deck and girders (Fasl, 2013). For this application, partial composite action was assumed due to model dynamic performance of the rehabilitated bridge. In general, it is very difficult to estimate the contribution of the steel plate on partially composite action and substantial engineering judgment needs to be employed. Equation C-I3-4 of the AISC Commentary Chapter I (2011) can be a good starting point to compute the effective moment of inertia of non-composite bridges where accidental partial composite action exists. Equation 4-1 represents the Equation C-I3-4. Finally, non-prismatic girders can be modeled by discretizing the girders into a number of line elements with the appropriate structural properties at the element location as the actual structure. The number of elements required to accurately model non-prismatic beams is dependent on the geometry of the system. In the study presented in this dissertation, an element length of approximately 10 ft. was found to provide a reasonable approximation of the dynamic response of the bridge.

$$I_{eff} = I_s + \sqrt{\left(\sum Q_n / C_f\right)} \cdot (I_{tr} - I_s) \qquad \textbf{Equation 4-1}$$

where:

I_{eff} : effective moment of inertia of a partially composite beam.

I_s : moment of inertia of the steel section.

ΣQ_n : strength of shear connectors between the point of maximum positive moment and the point of zero to either side (kips).

C_f : compression force in the concrete slab for fully composite beam; smaller of $A_s \cdot F_y$ and $0.85 \cdot f'_c \cdot A_c$

I_{tr} : moment of inertia of the fully composite uncracked transformed section.

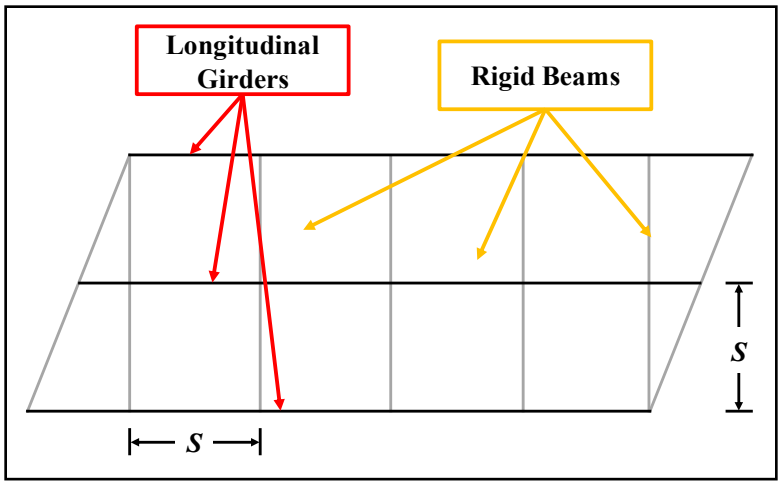

Figure 4-7: Typical plan view of line element grillage model

A major assumption that is necessary in the grillage model is estimating the transverse stiffness of the bridge that considers the effect of cross frames or diaphragms as well as the impact of the concrete bridge deck related to girder connectivity. As mentioned below, the impact of cross frames and diaphragms can be specifically modeled through beam elements; however capturing the impact of the girder connectivity through the concrete deck is a more complex problem with a grillage model. In many situations (Meng et al., 2002, and Fathali et al., 2012), the transverse connectivity may be modeled by assuming adjacent girders are connected by rigid beams. Although the rigid beams provide the transverse connectivity, the beams are typically assumed to be massless so as not to impact the dynamic bridge response (the mass of the deck is often included in the mass of the girder line elements). As shown in Figure 4-7, the rigid beams are spaced at a distance *S*, where *S* is the distance between the two adjacent girders. Meng et al. (2002) propose the distance of two rigid beams to be between ⅔ *S* and *S*. Furthermore, the rigid beams are framed perpendicular to the longitudinal line elements (i.e. bridge girders) to ensure that no axial force is induced to the girders. A rigid beam is also added at each

support location to sufficiently simulate the boundary conditions. The rigid beams constrain the longitudinal girders to vibrate in-phase in the deck in-plane direction, and both in-phase and out-of-phase in the deck out-of-plane direction. Therefore, this modeling method can capture the transverse and torsional vibration modes. Finally, additional line elements are utilized to model the bent caps, the columns, and other structural components of the bridge such as cross frames. When cross frames are converted to line elements an equivalent stiffness for the cross frames needs to be computed for each line element.

This method was followed to develop the grillage models of the bridges under investigation. Figure 4-8 to Figure 4-11 illustrate the line element grillage models of Bridge A, Bridge B, Bridge C, and Bridge E, respectively. One of the challenging aspects of the grillage model is the application of the truck loads. In the case of the 3D model, the truck loads are directly applied on the bridge deck, which is modeled with shell elements, and the finite element program is able to compute how the load spreads away from the point loads simulating truck tires. This method cannot be used in the grillage models because the concrete deck is incorporated in the structural properties of the longitudinal line elements. In twin girder bridges, the lateral distribution the truck loads is a trivial process and can be computed with the lever rule. However, the distribution of the truck loads to multiple girders is a complex problem.

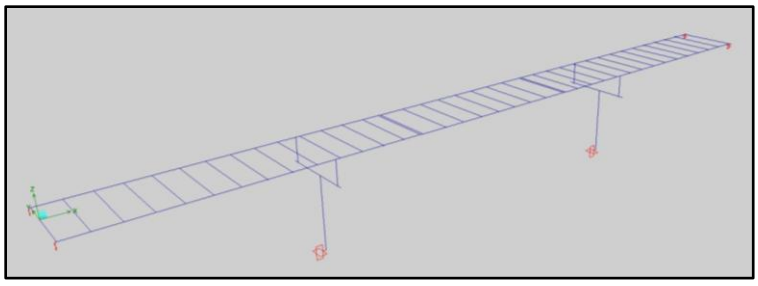

Figure 4-8: Grillage model of Bridge A

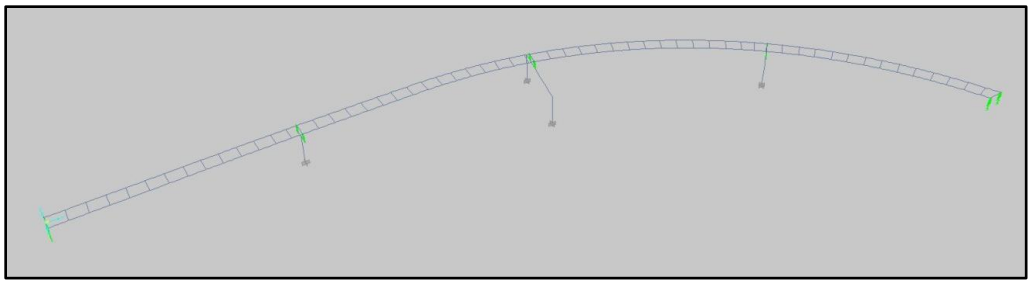

Figure 4-9: Grillage model of Bridge B

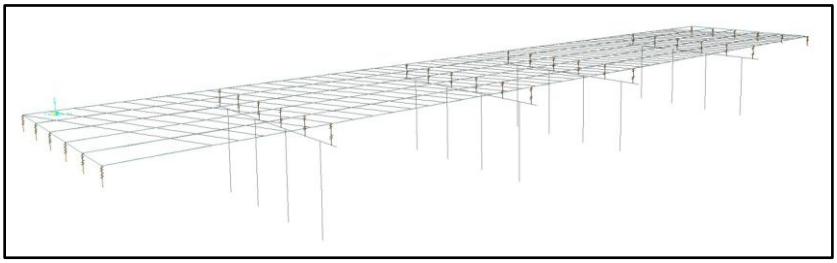

Figure 4-10: Grillage model of Bridge C

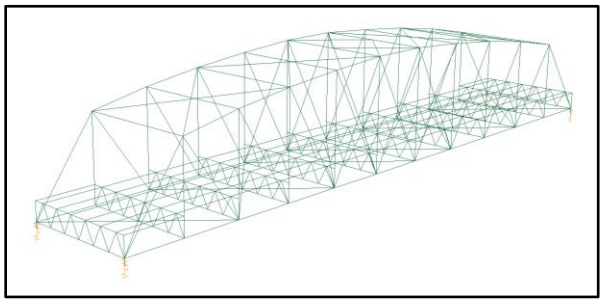

Figure 4-11: Grillage model of Bridge E

The distribution of the loads to each of the bridge components requires that equilibrium and the compatibility are maintained. AASHTO specifications contain approximate methods to calculate the live load distribution factors, but these methods are only intended for the design of the bridge components. These distribution factors are the result of a statistical analysis that was used to estimate the critical load effect on interior and exterior girders. The AASHTO distribution factors cannot be utilized to compute how a truck load, placed at a certain location, is distributed among multiple girders.

Therefore, the engineer is required to determine the load distribution among the structural components with other analytical procedures. The analytical model should be based on modeling assumptions that are concurrent with equilibrium and compatibility of the structure. Most analytical models assume that the structural material has a linear behavior, and the load is distributed to each girder proportionally to the displacement. Thus, girders close to the load location carry more load than those further away.

In the research documented in this dissertation, different methods to calculate the load distribution factors were considered. First, the load distribution was examined with the 3D model of Bridge C. Figure 4-12 show the girder layout of Bridge C, which consists of six girders. As the truck load was repositioned along one traffic lane (e.g. left lane), the reactions at the supports of each girder were recorded for each analysis step because the percentage of the truck load distributed to each girder varied due to the bridge geometry and boundary conditions. Once the moving load analysis was completed, the output data were analyzed to compute the average, minimum, and maximum distribution percentages of the truck load to each girder. The average value was computed to be utilized as a mean to compare the data between the different load distribution methods. In an ideal case that the minimum and maximum values coincide, then the distribution of truck load does not change as the truck is moving along the length of the bridge on a given lane. This scenario can occur when the supports are not skewed (e.g. Bridge A). Table 4-2 summarizes the results of this analysis. The results in the Table are used below to evaluate the accuracy of predictions from simplified models.

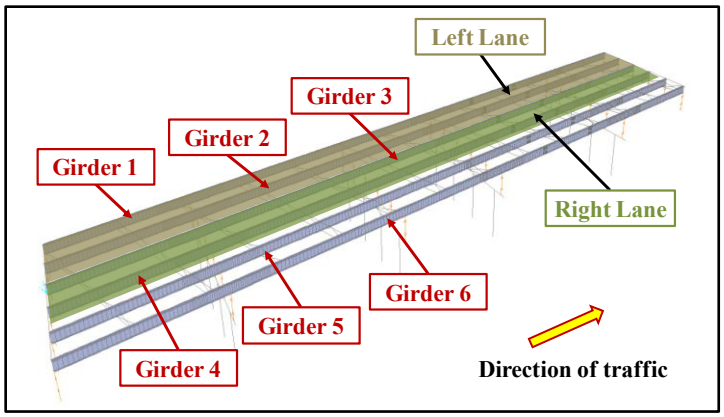

Figure 4-12: Girder layout of Bridge C

Table 4-2: SAP2000 results of 3D model for truck traveling in the left lane

	Girder 1	Girder 2	Girder 3	Girder 4	Girder 5	Girder 6
Average % of Total Truck Load	16.0%	53.9%	29.4%	2.1%	-0.3%	-1.1%
Min % of Total Truck Load	12.4%	47.5%	23.7%	-0.8%	-1.1%	-1.7%
Max % of Total Truck Load	20.6%	60.9%	32.5%	5.2%	0.4%	-0.4%

Another approximate numerical model to obtain a solution to the non-trivial problem of load distribution is commonly referred to as the lever rule. Figure 4-13 illustrates the calculation of the girder reactions when the truck load is placed in the left lane. To calculate the reaction at Girder 1, a hinge is placed over Girder 2 creating a statically determinate system that can be solved from equilibrium. For the reaction at Girder 2, a hinge is placed over Girder 3. Knowing the reaction from Girder1 from the first step, a summation of moments is taken about the hinge over Girder 3. Following this procedure, the reaction of Girder 3 can be computed if a hinge is placed over Girder 4. Table 4-3 summarizes the results from the lever rule calculation. The lever rule method predicts a load percentage for Girder 1 that is 50% lower than the average truck load percentage obtained from the 3D model summarized in Table 4-1. However, the results of the lever rule method for Girder 2 to Girder 6 have reasonable agreement with the

results of the 3D model. Based upon the comparisons made in this study, the lever rule provides a conservative and promising method to easily and quickly obtain reasonable results of the truck load distribution.

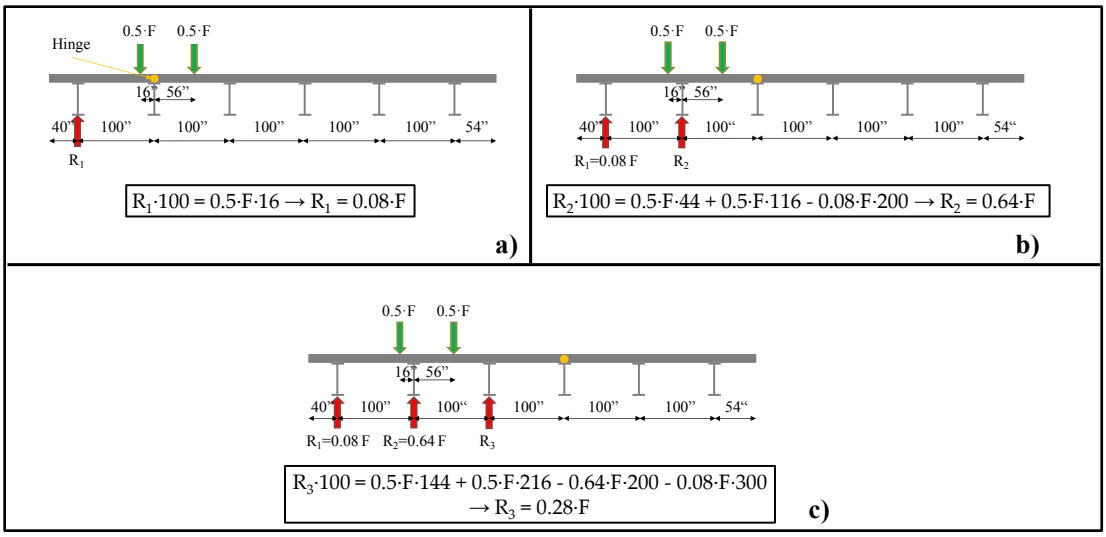

Figure 4-13: Lever rule calculation of the Bridge C reactions on Girder 1 (a), Girder 2 (b), and Girder 3 (c)

Table 4-3: Lever rule hand calculation results for truck on left lane

	Girder 1	Girder 2	Girder 3	Girder 4	Girder 5	Girder 6
% of Total Truck Load	8%	64%	28%	0%	0%	0%

The last proposed method to determine the truck load distribution factors is a method that was developed during this research project. This method utilizes massless line elements to simulate 12-in. widths of the concrete deck, which were positioned over the bridge girders as depicted in Figure 4-14. The number of line elements is defined by the number of truck axles, as these line elements are used as "deck joist" to transfer the applied truck point loads to the girders. The distance between each "deck joist" is defined by the axle spacing of the truck (Figure 4-14). The entire group of the loaded "deck joists" is positioned above the bridge girders and manually moved along the length of the

bridge. Each time that the "deck joist" system is moved, a static analysis is performed to obtain the summation of reactions of each girder. Table 4-4 summarizes the results of the proposed method. The results for all 6 girders are within a few percent of the 3D model results in Table 4-1. However, the proposed method is a tedious procedure since the "deck joists" must be manually moved before every static analysis to simulate the moving truck load. Finally, it is extremely important for the engineer to understand the limitations of the numerical models presented in this sections and potential inaccuracies that may result.

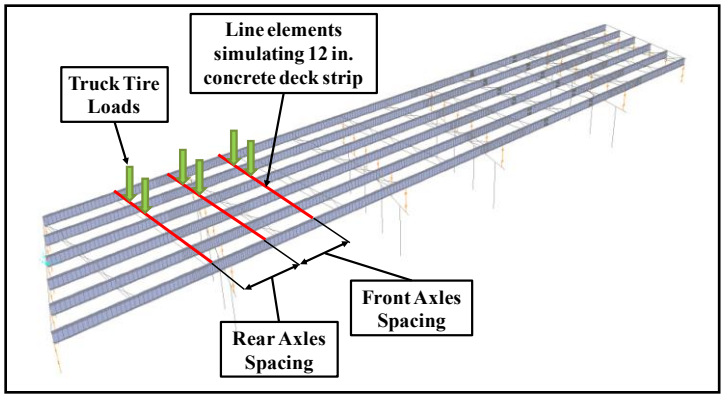

Figure 4-14: Proposed simple line element analysis to determine the truck load distribution factors

Table 4-4: Proposed simple line element analysis results for truck on left lane

	Girder 1	Girder 2	Girder 3	Girder 4	Girder 5	Girder 6
Average % of Total Truck Load	16.7%	48.3%	29.4%	6.9%	0.8%	-2.2%
Min % of Total Truck Load	11.9%	39.2%	26.1%	2.3%	0.0%	-3.1%
Max % of Total Truck Load	22.0%	57.4%	36.1%	11.2%	1.4%	-0.9%

4.3. ANALYSIS GUIDELINES

The magnitude and frequency of vehicular-induced acceleration history vary at each location along a bridge. Thus, considering the effectiveness of a vibration energy

harvester requires the determination of the dynamic response of the bridge. Once the vibrational behavior of the bridge location where the energy harvester would be placed has been evaluated, the engineer can determine if adequate energy would be produced to power the monitoring equipment. The vibration behavior can be estimated through a dynamic analysis. The next sections summarize the analysis guidelines along with results from a dynamic analysis performed during this research project.

4.3.1. Type of analysis

A transient dynamic analysis was performed in this investigation to obtain all the acceleration histories out of each bridge. Two methods that can be used to carry out the transient dynamic analyses are the modal transient dynamic analysis, and the direct integration transient dynamic analysis. The modal transient dynamic analysis method can be used to perform transient dynamic analyses of a structure subjected to time-dependent loads. This method utilizes certain mode shapes of the structure, which are chosen by the user, to approximately calculate the transient response of the structure. However this method was not selected in this study because its accuracy depends on the number mode shapes included in the analysis, and the bridge models size was adequately small to analyze them with a direct integration method. Instead, the Newmark-Beta direct time integration was selected as the time history method. This method utilizes direct numerical integration to solve the coupled equations of motion.

A modal analysis was only used to calculate the natural frequencies of the structure, which were later used to specify the proportional damping coefficients. Apart from determining the damping of the bridge, this analysis type was not a preferred numerical method for the objectives of this project. This type of analysis only calculates the dominant frequencies of vibration of the global structure, but it cannot compute

acceleration amplitudes induced by moving trucks. Both of these pieces of information are need to optimize the design of the vibration energy harvester. Moreover, the frequency content and vibration amplitudes vary along the width and length of the bridge. Even though the dominant frequencies of a structure remain constant within a given span, the acceleration amplitude in each mode varies along the length of the span. In other words, the output power of a harvester is different at each location of the span and the peaks of the power occur for different frequencies. This concept is based on basic vibration theory, which is depicted in Figure 4-15.

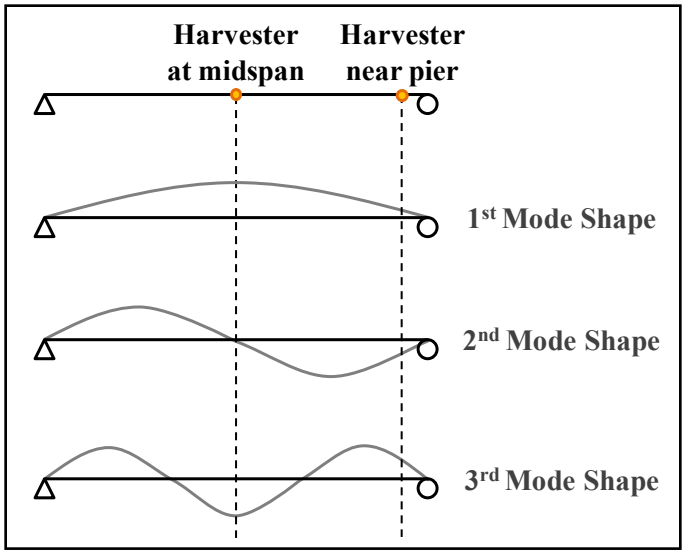

Figure 4-15: Modes of vibration of a simply-supported beam

The first and second mode shapes of a simply-supported beam typically consist of a half-sine and full sine curve, respectively. The third mode is one and a half times the full sine curve. If the energy harvester is installed at the midspan, then it is exposed to a vibration history dominated by the frequencies of the first and third mode. The second mode shape will not contribute since the midspan point does not translate in this mode shape. On the contrary, if the harvester is placed near a support, then all three modes

contribute to the acceleration signal and thus all three of the first natural frequencies exist in that signal. A final conclusion is that the acceleration amplitudes, and consequently the output power, are more likely higher close to midspan compared to the support regions. This is due to the fact that the displacements at midspan are the greatest.

4.3.2. Proportional damping

Damping exists in most structures. Typically, the amount of damping ranges from 5% to 15% in the majority of structures. For most transient dynamic analyses, variations of damping between 5% and 15% do not significantly affect the structural response. However, damping can greatly influence the structural behavior if the response is close to the resonant frequency. Thus, the engineer should define the damping based on natural frequencies. There are several methods to incorporate damping in finite element programs. The most widely used method is the mass and stiffness proportional damping which is commonly referred to as Rayleigh damping.

In this method, the damping matrix is considered to be proportional to the mass and stiffness matrices. The relationship of damping, mass, and stiffness is given in Equation 4-2.

$$C = \alpha \cdot M + \beta \cdot K$$ **Equation 4-2**

where:

C : damping matrix.

α : mass proportional damping coefficient.

M : mass matrix.

β : stiffness proportional damping coefficient.

K : stiffness matrix.

The values of α and β can be calculated from Equation 4-3and Equation 4-4.

$$\xi_1 = \frac{\alpha}{4 \cdot \pi \cdot f_1} + \beta \cdot \pi \cdot f_1 \qquad \textbf{Equation 4-3}$$

$$\xi_2 = \frac{\alpha}{4 \cdot \pi \cdot f_2} + \beta \cdot \pi \cdot f_2 \qquad \textbf{Equation 4-4}$$

where:

ξ_i : damping ratios of interest.

α : mass proportional damping coefficient.

β : stiffness proportional damping coefficient.

f_I : natural frequency.

The mass proportional damping coefficient (α) is inversely proportional to the frequency, which means that the lower frequencies are damped out more than higher frequencies. On the other hand, stiffness proportional damping coefficient (β) is directly proportional to frequency and thus higher frequencies are damped more. This concept is represented in Figure 4-16. To determine the proportional coefficients, the engineer should choose two damping ratios that are particular to the natural frequencies of two modes of interest. However, if the two damping ratios are set to be equal (i.e. $\xi = \xi_1 = \xi_2$) for both frequencies of interest, then the computation of the proportional damping coefficient is simplified, and stiffness and mass coefficients are equal to $\beta = \frac{2 \cdot \xi}{f_1 + f_2}$ and $\alpha = f_1 \cdot f_2 \cdot \beta$, respectively.

SAP2000 allows the user to either specify the proportional coefficients α and β directly, or these coefficients are automatically calculated based on the user input of a damping ratio (ξ) at two different frequencies (f_i), or at two different periods (T_i). For all the dynamic analyses a damping ratio of 10% was assumed. Before each transient dynamic analysis, a modal analysis was performed and the lowest and highest natural

frequencies of the flexural modes were recorded for the first 20 modes. Based on these two frequencies and for 10% damping the proportional coefficients were computed.

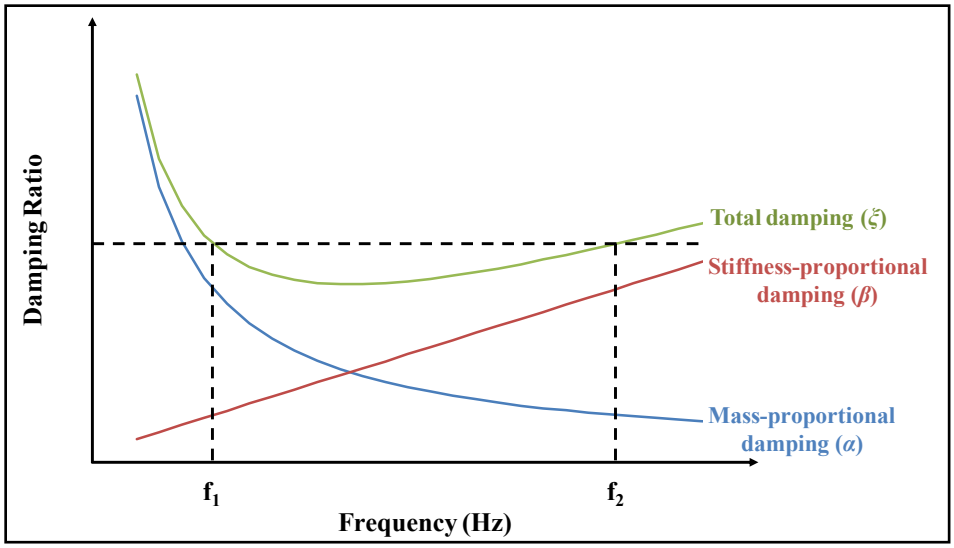

Figure 4-16: Mass and stiffness proportional damping

4.4. RESULTS OF THE TRANSIENT DYNAMIC ANALYSES

A transient dynamic analysis was carried out on all of the bridges discussed in Chapter 3. The analytical results were validated with the field results, and the comparison results showed the possibility to predict the vehicular-induced vibration energy harvester output power. Knowing the vibration response of each bridge, the engineer can quantify the feasibility of energy harvesting as a potential way to power the health monitoring system.

4.4.1. Dynamic response of Bridge A (Riveted twin plate girder)

The measured vibrations of Bridge A contained more energy relative to the other analyzed bridges. Figure 4-17 provides a comparison of the East girder midspan (i.e. floor beam 35) acceleration histories for Bridge A induced from i) random vehicular traffic, ii) the controlled load test, and iii) the grillage model analysis. The test truck at

the controlled load test was moving at 63 mph along the right lane of Bridge A, which almost coincides with the East girder. The grillage analysis was carried out utilizing the test truck (Figure 3-16) as moving load with the same loading conditions as in controlled load test (i.e. traveling at 63 mph on the right lane). All of the acceleration amplitude ranges are relatively close to each other; however there are significant differences between the characteristics of the computer analysis and the measurements from using the random vehicular traffic data, which is expected due to the likely differences in the vehicle masses on the bridge. Better correlation was achieved between the controlled load test response and the SAP 2000 computer analyses of grillage model because the test truck was the only vehicle passing Bridge A and the dynamic analysis was performed knowing the geometry, weight, and speed of truck.

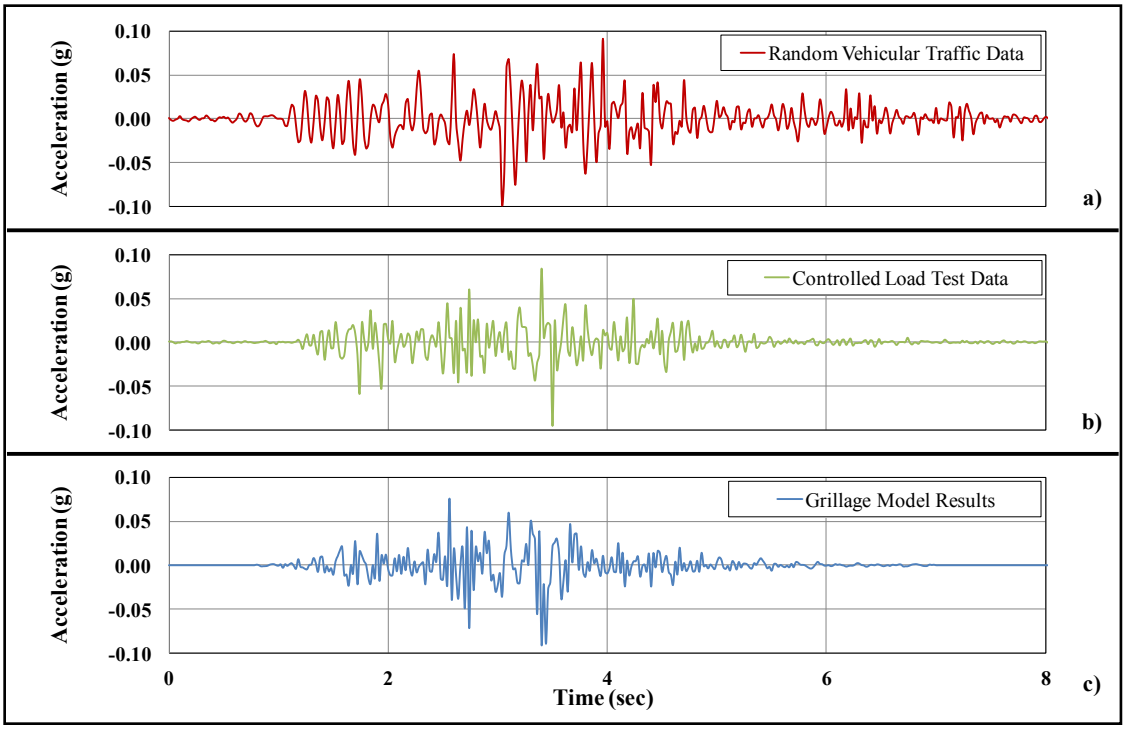

Figure 4-17: Comparison of Bridge A acceleration histories from a) random vehicular traffic data, b) controlled load test data, and c) grillage model analysis

The next step was to compute the average power response spectra of the previous acceleration histories. Reichenbach (2012) provides a comprehensive description on the development of the power response spectrum of a vibration signal. Figure 4-18 shows the average power response spectra of the three cases from Figure 4-17. The power spectrum of the random vehicular traffic data shows a wide band of frequencies between 2 Hz and14 Hz, and a maximum power of 350 μW (assuming the harvester has a 1-kg moving mass). The wide bandwidth of the random vehicular traffic data spectrum from the case with the controlled load test data transforms to a spectrum with two distinct frequencies of narrow bandwidth. The dominant modal frequency shifts from 9.5 Hz (random vehicular traffic data) to 2.5 Hz and 8 Hz for the controlled load test spectrum. The peak spectral power is increased to 350 μW at 2.5 Hz and reduced to 250 μW at 8 Hz. The results from the field instrumentation (i.e. random vehicular traffic and controlled load test data) have varying levels of agreement with the computer analysis results. The computer analysis indicates that the performance of the harvester would be best if tuned to 2.5 Hz. or 9 Hz. The results of the controlled load test also support the peak in average power at 2.5 Hz, but differ in pointing to a significant peak at the 9Hz. level. The results from the random vehicular traffic data, on the other hand, have relatively poor agreement with the computer analysis at 2.5 Hz., but have better agreement with the prediction for a peak in the power generation at approximately 9 Hz. Based on the analysis results, it is more favorable to tune the harvester at 9 Hz. since there is a better correlation with the results from both field data sources (i.e. random vehicular traffic and controlled load test data).

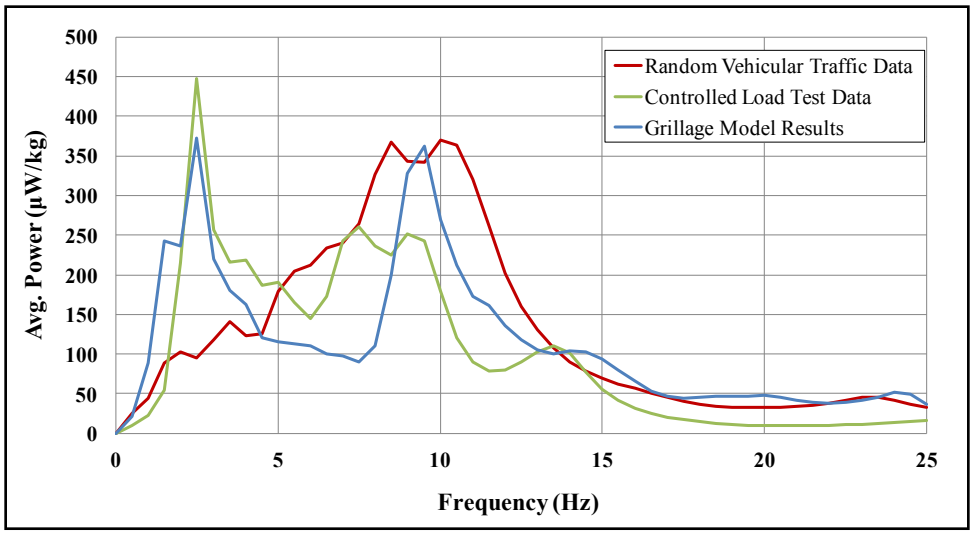

Figure 4-18: Response spectra of Bridge A from random vehicular traffic data, the controlled load test, and grillage model analysis

Regarding the response of the braces, the data showed that the additional mass significantly changes the response of the brace. Figure 4-19 demonstrates the comparison of the acceleration histories from random vehicular traffic field data and analytical results. The analytical results are closer to the field acceleration data of the brace with the mass. This is due to the fact that a concentrated mass in the midpoint of the instrumented brace (Figure 3-14) was included in the bridge model. The acceleration amplitude (± 0.20g) of the finite element model is slightly higher than the one of the random field data with the mass (± 0.15g). Finally, the brace acceleration output of the random field data and analysis do not have similar characteristics because the actual brace has a different damping ratio than the one used in the analysis (10%).

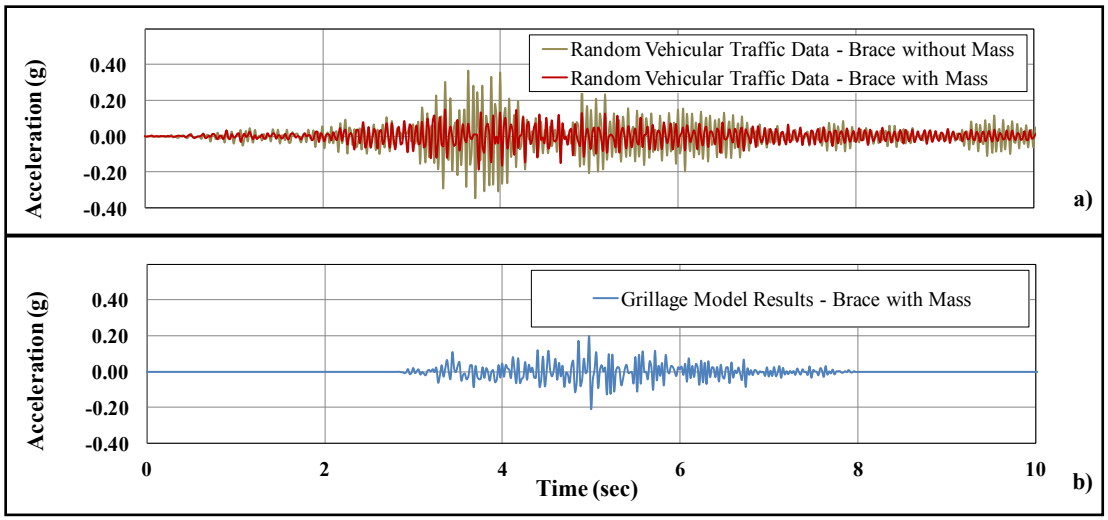

Figure 4-19: Comparison of Bridge A braces acceleration histories from a) random vehicular traffic data with and without mass, and b) grillage model analysis

Since the brace vibration is affected by the harvester mass, the power production of the system is also affected. Therefore, the power spectra of the braces were computed with and without the additional mass to compare the difference in behavior. Figure 4-20 illustrates the effect of the harvester mass on the dynamic response of the brace. More specifically, the dominant modal frequency shifts from 23.5 Hz (no mass) to 17 Hz (with mass). The peak spectral power is reduced by a factor of four when the mass is added. Therefore, in cases where the harvester is likely to be mounted on relatively slender structural members, the engineer should consider the harvester mass so that the computed power is not significantly overestimated.

As mentioned above, a concentrated mass was included in the analysis of the brace. Even with this detail incorporated in the grillage model the calculated performance of a harvester is 39.4% less than the calculated harvester performance from the random vehicular traffic data (Figure 4-21). From the figure, it can be seen that the dominant frequencies of both cases falls at 17 Hz. Therefore, the match in the dominant frequency

indicates that in the case that was considered in the comparison, the dynamic analysis can provide an accurate prediction the tuning frequency.

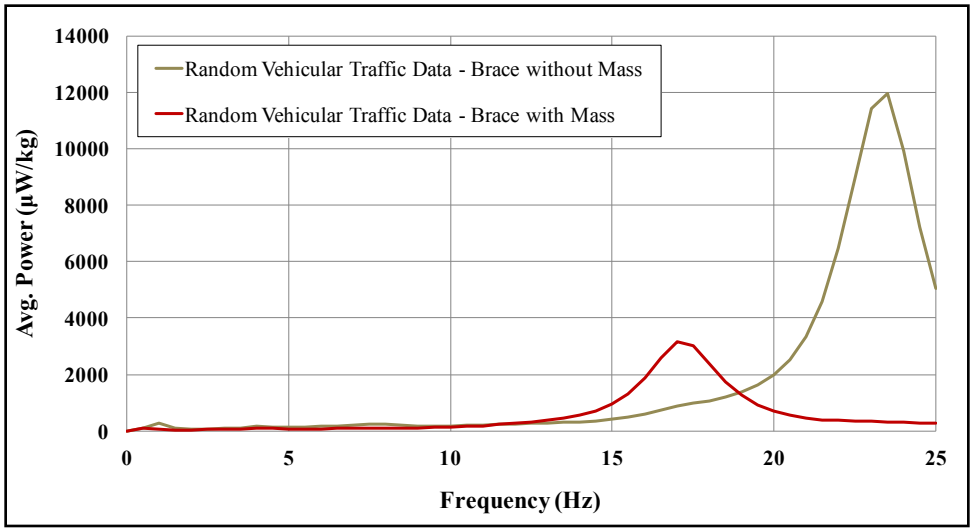

Figure 4-20: Response spectra of Bridge A braces with and without mass

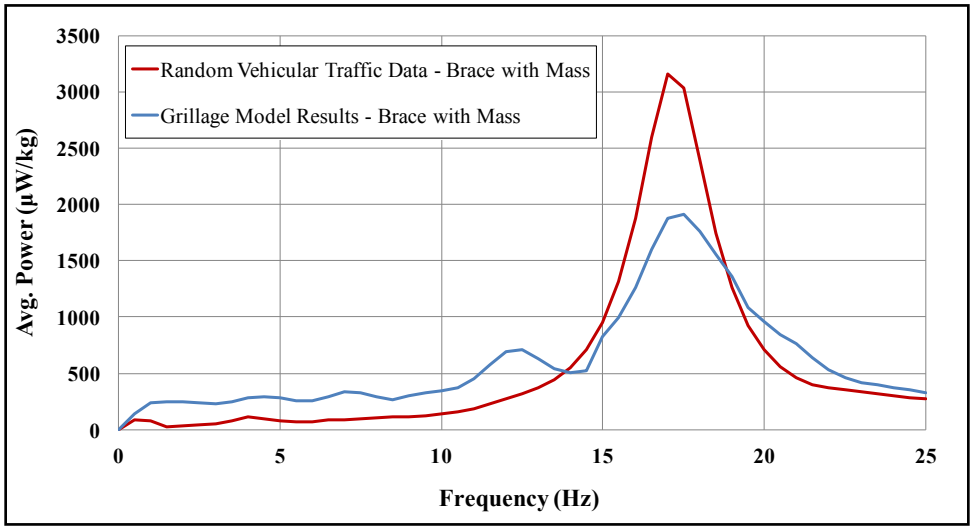

Figure 4-21: Response spectra of Bridge A braces with mass from random vehicular traffic data, and grillage model analysis

4.4.2. Dynamic response of Bridge B (Twin trapezoidal box girder)

The lower truck traffic volume that utilized Bridge B compared to Bridge A seemed to have a measurable influence on the results. The maximum permitted speed at Bridge B is almost half the maximum permitted speed at Bridge A, and hence, the acceleration amplitude is lower. The structural system in the two bridges are significantly different (trapezoidal box girder versus riveted I-girder), and the pattern of moving trucks was generally more predictable than in Bridge B compared to Bridge A (i.e. one vs. two lanes, respectively). For this reason, the analytical results are similar to the field results (Figure 4-22). The data shown in this graph were recorded at the middle of Span 2. Finally, it can be noted that the frequency content of the two signals is slightly off.

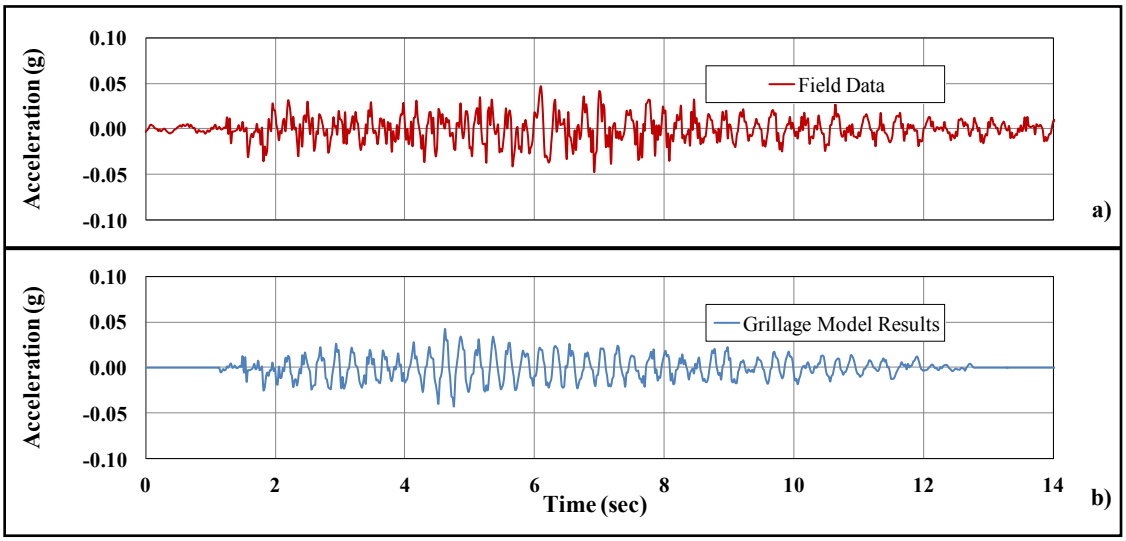

Figure 4-22: Comparison of Bridge B acceleration histories from a) random field data, and b) grillage model analysis

To achieve a better comparison of the frequency content and the output power, response spectra of the two signals were computed. Figure 4-23 illustrates the results of the spectral analysis. The two dominant frequencies of the field data shift from 2.0 Hz and 5.5 Hz compared to 1.2 Hz and 4.5 Hz for the response spectrum computed based on

analytical results. The peak spectral power is almost the same for both data sets are approximately 5 Hz. However, the peak average power based on the field data is 28% higher than the one calculated from the computer analysis data. A final remark is that bridge with the longer spans (e.g. Bridge B) had lower peak frequencies compared to bridge with the shorter spans (e.g. Bridge A).

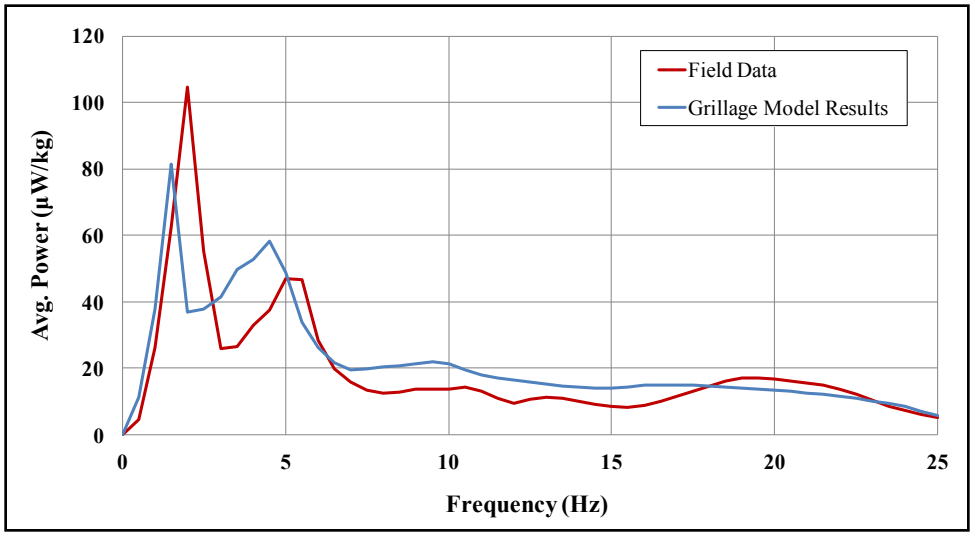

Figure 4-23: Response spectra of Bridge B from random field data, and grillage model analysis

4.4.3. Dynamic response of Bridge C (Six rolled I-girders)

During the transient dynamic analyses of Bridge C, a three-axle truck was modeled crossing the bridge at 55 mph. Truck-induced acceleration histories were then extracted and compared with the measured data. Figure 4-24 shows a graph of the acceleration results captured from Girder 3 at the mid-length of Span 3. The computed dynamic data were obtained from: a) a 3D finite element model, b) a grillage model where the truck load was distributed among the girder based on the lever rule, and c) a grillage model where the proposed method outlined in section 4.2.2 was utilized to assign the portion of truck load on each girder. The results from the computer analyses and the

field data match relatively well with respect to the amplitude of the accelerations. The transient analysis computed accelerations ranged from -0.02 g to +0.025 g, which is almost equal with the acceleration range recorded during the field tests.

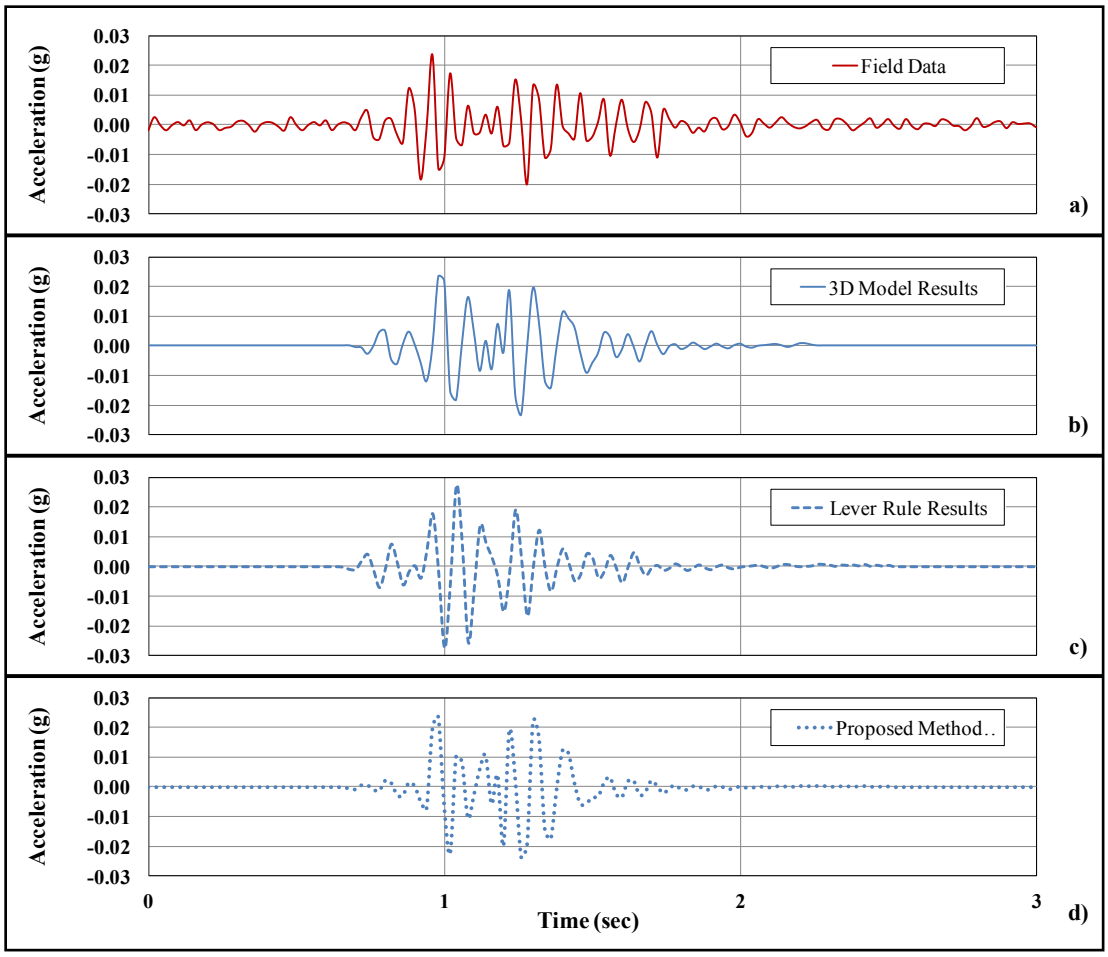

Figure 4-24: Comparison of Bridge C acceleration histories from a) random field data, b) 3D model, c) grillage model loaded based on lever rule, and c) grillage model loaded with proposed method

The power spectra of the vibration signals are presented in Figure 4-25. In all cases, the dominant modal frequencies are almost the same and vary only 0.5 Hz. This is due to the fact that Bridge C has a relatively simple structural system that can be easily

and accurately modeled with either of the two methods. Moreover, it can be noted that Bridge C has short spans so the higher frequencies tend to dominate the power spectra, but the excitation amplitudes are relatively small. In contrast, the longer spans of Bridge A and Bridge B lead to lower dominant frequencies.

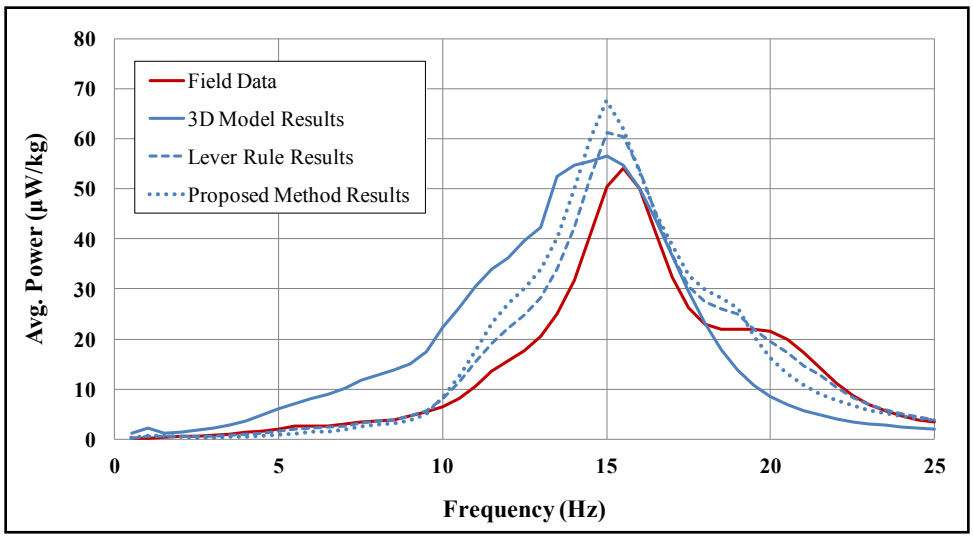

Figure 4-25: Response spectra of Bridge B from random field data, 3D FE model, grillage model loaded based on lever rule, and grillage model loaded with proposed method

4.4.4. Dynamic response of Bridge E (Steel through truss)

Due to the limited recorded vibrational data of Bridge E, there was no possibility to capture and examine a single track event. As shown in Figure 4-26a, the acceleration signal at midspan is exhibited a significant amount of noisy. Moreover, the amplitude of the field acceleration ranges from -0.04g to +0.04g. The calculated amplitude (Figure 4-26b) varies from -0.04g to +0.03g. Finally, it is difficult to compare the frequency content of the two signals, but it seems that they are slightly different.

Figure 4-27 demonstrates the power spectra of Bridge E for computed and recorded data. Although the girders of Bridge E did not provided a higher power

compared to Bridge A, the girders did exhibit a higher power compared to Bridge B and Bridge C. Moreover, the power spectra of the computed accelerations match closely with the field data until 8 Hz. After this frequency, the two trends start to divert. At 18 Hz, the peak spectral power is almost 250 μW and 50 μW for the field data and the computed data, respectively.

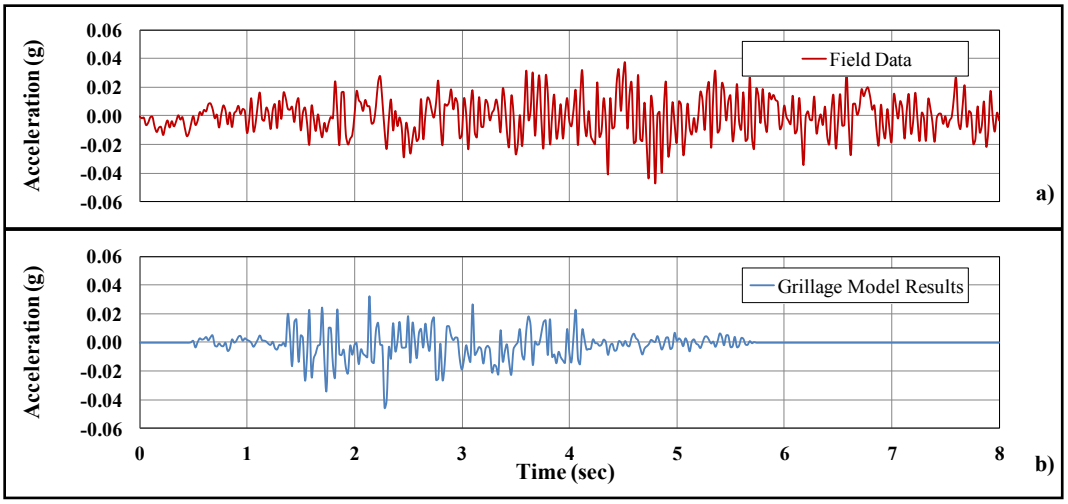

Figure 4-26: Comparison of Bridge E acceleration histories from a) random field data, and c) grillage model

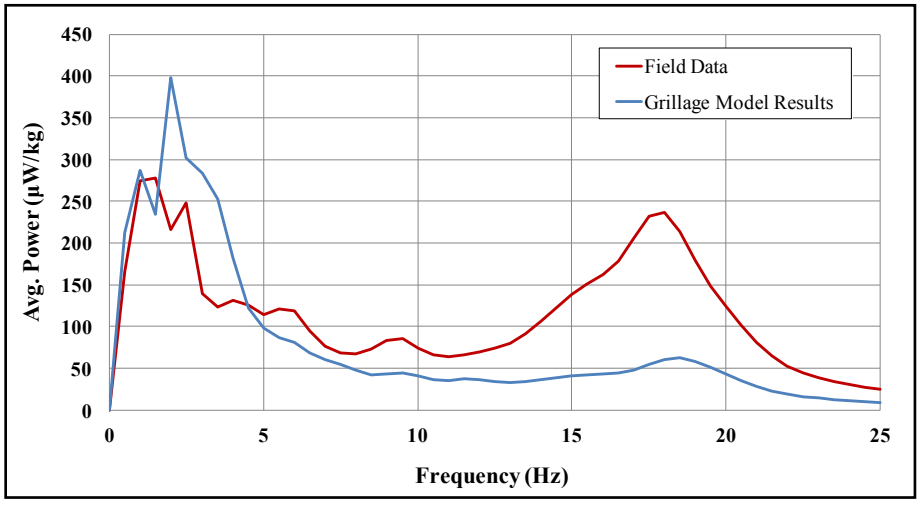

Figure 4-27: Response spectra of Bridge E from random field data, and grillage model analysis

4.5. COMPARISON OF THE TWO METHODS

Computer programs can easily estimate the dynamic behavior of a bridge. However, most bridges have a complex structural system and thus many assumptions must be made during the modeling process. Moreover, the engineer should determine the factors that may potentially affect the bridge response. Generally, there are two options for modeling the bridge: 1) developing a 3D finite element model, or 2) utilizing line elements to create a grillage model.

There are advantages and disadvantages to each method. The first method can potentially simulate more accurately the actual bridge behavior and produce more realistic results. 3D modeling should be employed when the level of bridge complexity plays a role in determining the harvesting power. In other words, if the bridge component, on which the engineer wants to install the harvester, has a complex geometry (i.e. hanger of Bridge A) and it cannot be simulated with line elements, then 3D modeling is the most preferable method. Nonetheless, this method requires significant amount of time to complete the bridge model, and computationally is more expensive than a grillage model.

Hence, the grillage method is highly desirable from modeling perspective, provided such a model produces acceptable results. Grillage modeling is proposed as the method to dynamically analyze bridges due to the simplicity and computational efficiency. The computational results indicated that the grillage modeling method produced very satisfactory results for typical highway bridges, and it was feasible to determine the energy harvesting potential for the bridge. This is because the properties of the line elements are determined in such a way that their structural characteristics closely match the properties of the actual structure. To validate the dynamic response of the bridges modeled with the grillage method against the dynamic response obtained from

the 3D FE models, a modal analysis was performed for each 3D and grillage model of the bridges under investigation. Table 4-5 provides a summary of the first five natural frequencies of the different bridge models. Most natural frequencies between the 3D and grillage models vary less than 10%, and consequently it is suggested both modeling methods can produce results with roughly similar frequency contents.

Table 4-5: Natural frequencies comparison of bridges under investigation

	Mode	Frequency (Hz)	
		3D Model	Grillage Model
BRIDGE A	1	2.41	2.27
	2	3.31	3.16
	3	4.00	4.30
	4	4.02	4.38
	5	5.19	5.35
BRIDGE B	1	0.80	0.82
	2	1.28	1.34
	3	1.77	1.84
	4	1.89	2.10
	5	2.14	2.23
BRIDGE C	1	6.03	6.15
	2	6.28	6.44
	3	7.53	7.61
	4	7.54	7.76
	5	12.21	12.41
BRIDGE E	1	1.85	1.66
	2	2.10	2.00
	3	2.92	2.67
	4	4.60	4.26
	5	5.32	5.08

Another major factor that can affect the dynamic results of both modeling methods is the truck load. It was previously mentioned that the 3D method distributes more accurately the truck loads among the girders due to the continuous deck, and

consequently the actual bridge is simulated in a better way. Different methods were presented in section 4.2.2 to estimate the load distribution in multi-girder bridges. It was found that both methods can produce results that closely resemble the load distribution computed from the 3D FE model. In addition, it was concluded that the lever rule distribution method is potentially the best way to quickly calculate the truck load distribution. Ultimately, the decision of the modeling method must be assessed on a case-by-case basis, and engineering judgment should be utilized to determine the most appropriate modeling method.

4.6. CHAPTER SUMMARY

This chapter focused on methods of modeling bridges, as well as presenting comparisons of results from measured data to predictions from computer analyses. Although the most accurate results for understanding the dynamic response of the bridges from the perspective of potential energy harvesting is through bridge instrumentation, a highly desirable technique is through a computer analysis due to the difference in financial costs and time savings. It was found that for typical highway bridges the grillage modeling method produced very satisfactory results and it is feasible to determine the energy harvesting potential for the bridge. Moreover, three different methods (i.e. 3D FE, lever rule, proposed method) were presented to estimate the load distribution in multi-girder bridges. Only the last two methods can be employed in grillage models. It was concluded that the lever rule distribution method is potentially the best way to hastily and accurately compute the distribution percentages of truck load. Finally, 3D modeling should be employed when the engineer wants to model every detail of the bridge or when the bridge component, on which the harvester would be mounted,

has a complex geometry (i.e. hanger of Bridge A) that cannot be represented with line elements.

The structural health monitoring (SHM) system, apart from being power independent, has to be reliable. A major component of the SHM system that can greatly affect its reliability is the sensor. Chapters 5 and 6 provide a summary of the reliability tests and the findings.

CHAPTER 5

Long-term Testing of Sensor Reliability

5.1. INTRODUCTION

The integrity of a bridge can undergo significant changes with time due to fatigue, corrosion, extreme loads, and several other factors. The periodic evaluation of the condition of the structure is therefore very important to ensure public safety as well as maximizing the life of the structure with the proper allocation of maintenance resources. The US highway system has numerous bridges that are required to be inspected at least every two years. However, even with established inspection practices, depending on the conditions of the structure, significant degradation can happen between inspections leading to a potential failure or complication. Therefore, an enhancement to the current periodic inspections is the potential incorporation of structural health monitoring systems to provide a steady stream of data that can provide a much better indication of the condition of critical bridge systems. Structural health monitoring is not a "cure-all" for the bridge infrastructure; however the incorporation of monitoring technology can provide an efficient means to compliment the current inspection practices and significantly improve the safety and long term viability of many bridges in the US inventory.

Structural health monitoring techniques have been in use for several years, however the topic has seen increased popularity in recent years due to technological advancements. The installation of monitoring systems on some bridge systems has the potential to enhance the safety and performance of the infrastructure system, particularly when used on vital links of the highway network that are subjected to significant traffic and therefore more likely to have significant truck traffic.

There are a number of possible advantages associated with the installation of monitoring systems of critical or unique bridges. One major advantage of the use of a monitoring system in aging structures is that the engineer can be quickly notified when problematic changes occur in the structure that may be a precursor to a potential failure or complication in the structure. In addition, depending on the structural system that is used, recorded data from a given bridge can provide valuable insight into the performance of a particular design or application of new materials used in the bridge. In some cases, structural health monitoring systems can be deployed during construction in unique bridge systems to control the construction process and validate that the stress levels do not exceed critical levels. Finally, long-term monitoring of bridges can help the engineer to understand potential changes in the loading magnitudes and patterns as well as traffic volume, which can be important when quantifying the structural deterioration or assessing the use of maintenance resources.

The goal of the overall investigation a part of which is outlined in this dissertation is to develop a monitoring system that can be installed on a bridge with a desired 10-year maintenance free life. While the power requirements and durability of the monitoring system is of obvious concern in meeting the desired life, similar concerns exist with regard to the durability and consistency of the sensors that the engineers depend on for reliable data. Typically, sensors are carefully installed at critical locations of the bridge where either damage already exists or is expected to occur. After monitoring the bridge for long-term and short-term periods of time, the engineer can assess how traffic and environmental effects influence its performance. However, the reliability of the sensor becomes very significant in long-term monitoring applications, because slight drifts in the sensor reading or increased electronic noise cause significant problems with regard to interpreting the data and will likely lead to erroneous conclusions regarding the condition

of the structure. One of the most common sensors that are used in field monitoring applications of bridges consists of strain gages that are used to track the strains in the structural elements. Crack propagation gages may also be used to track the growth of cracks in the primary structural elements of the system. Both of these gages are typically bonded to the base material of the structure using a variety of techniques. Partial or total debonding of the sensors or other degradation of the gages can lead to problematic readings; however the full impact on the problem is not clear.

To investigate the impact of excessive exposure on the reliability of strain gage readings, a series of tests were conducted on a variety of commercially available gages to consider the impact on the gage performance as well as identifying potential signs of gage degradation. A summary of the results from these tests are provided in Chapter 6. A series of different tests were conducted in multiple environments to evaluate the performance of the gages. Table 5-1 summarizes the sensor testing program and the main parameters of each sensor test.

The first testing phase consisted of a long-term environmental test series that was conducted to determine the durability of the sensors and their protective coatings (e.g. zinc-based spray, wax and silicon, etc.) against humidity, and other environmental effects that are expected in long-term bridge monitoring applications. The first testing phase included the long-term environmental tests of:

- Gages installed on test-boxes, and exposed to an outdoor environment (Section 5.3.1).
- Gages installed on steel bars, exposed to an outdoor environment, and periodically tested under axial loads (Section 5.3.2).
- Gages installed on test-boxes, and exposed to controlled conditions inside a humidity room (Section 5.3.6).

Another part of the first testing phase consisted of fatigue test series that were performed to determine if weldable gages have an influence on the fatigue performance of steel specimens and to reveal any debonding issues of the gages attached with adhesives.

Table 5-1: Summary of the sensor testing program

Test #	Test Goal	Test Phase	Temperature Range	Environmental Conditions	Loading Conditions
E1	Durability	1	20 °F - 145 °F	Variable outdoor environment	No load
E2	Durability	1	20 °F - 145 °F	Variable outdoor environment	Axial loads from 2 to 15 kips (monthly)
E3	Thermal effects	1	20 °F - 145 °F	Variable outdoor environment	Transverse loads of 35 & 70 lbs (weekly)
E4	Thermal effects	2	35 °F - 140 °F	Controlled environment (furnace, refrigerator, etc.)	No load
E5	Thermal effects	2	26 °F - 135 °F	Variable outdoor environment	No load & 35 lbs transverse load
E6	Durability	1	64 °F	Environ. chamber of constant temperature and 100% humidity	Unloaded
E7	Durability	1	64 °F	Environ. chamber of constant temperature and 100% humidity	Unloaded
E8	Fatigue	1	N/A	N/A	Cyclic load (35 ksi stress range)
E9	Fatigue & thermal effects	3	20 °F - 145 °F	Variable outdoor environment	Cyclic load (35 ksi stress range) & No load

A second phase of this testing program was developed based on the results of first testing phase. Foil and weldable gages protected with improved protection system recommended by WJE engineers. The main objective of the second testing phase was to better understand the relationship between temperature changes and thermally-induced strains recorded by the gages. In addition, the effect of size (e.g. mass) of the instrumented member and rate of heating on thermally-induced sensor readings was investigated. Last, the influence of loading conditions on thermally-induced strain was examined. The second testing phase included the following tests:

- Gages installed on steel bars, exposed to an outdoor environment, and periodically tested in bending (Section 5.3.3).
- Gages installed on unrestrained steel bars, and exposed to controlled temperature environment (Section 5.3.4).
- Gages installed on steel bars, exposed to an outdoor environment, and loaded in bending about the strong or weak axis of the bar (Section 5.3.5).
- Gages installed on steel bars and exposed to controlled conditions inside a humidity room (Section 5.3.7)

A third testing phase was created to evaluate the long-term performance of crack propagation gage and determine how temperature effects affect its behavior. For this testing phase a fatigue test was performed using a notched steel coupon that was instrumented with crack propagation (CP) gages. The two objectives of the fatigue tests were, first to better understand the behavior of the gages, and second to obtain data for comparing the fatigue test results with the environmental test results to determine if environmental effects can affect the reliability of the CP gage. All the results of the long-term testing of sensor reliability are discussed in Chapter 6.

5.2. SENSOR TESTING OBJECTIVES

Some of the primary factors that may affect the long-term performance of a bridge include steel corrosion, concrete degradation, and changes in the volume or distribution of traffic. Bridge performance can also be affected by events such extreme loading from oversized vehicles, seismic events, hurricanes, or bridge strikes from oversized vehicles. To monitor the external factors that affect the structural integrity of a bridge, sensors need to be installed at locations where are considered to be critical. These sensors provide important information for the long-term condition of the bridge, as well

as the condition after an extreme event. Thus, the reliability of the sensor output is very important to accurately evaluate the bridge behavior.

The quality of the sensor output is affected by several factors. The measured quantity (e.g. strain) can be reliable only if the sensor is accurately installed and properly monitored. Therefore, installation requires a good bond between the sensor and the surface of the instrumented structural component. In most applications, the bond is obtained with special adhesives or spot welds. Degradation in the quality of the installation such as debonding of the gages over time can greatly affect the accuracy of the measurements. In many situations, environmental contaminants can gradually degrade the performance of the sensors producing inaccurate results that can be misleading. In addition, sensors utilizing resistive sensing elements can be easily affected by changes in several external factors including temperature, humidity, and a number of other factors.

As previously described, three phases of sensor test series were developed and carried out in this study. The purpose of this testing program was to define the factors that influence the sensor performance. Thus, the following objectives were established for the testing program:

1. Evaluate the durability of several sensors against environmental effects that are expected during long-term monitoring of highway bridges (i.e. humidity, etc.)
2. Investigate the impact of the small spot welds of weldable gages on the fatigue life of the instrumented component.
3. Investigate the impact of cyclic loading on the adhesive performance of bondable gages.
4. Evaluate potential early indications of deteriorating/malfunctioning sensors

5. Improve the understanding of the relationship between temperature changes and thermally-induced strains recorded by the gages.
6. Investigate the effect of size (e.g. mass) of the instrumented member and rate of heating on thermally-induced sensor readings.
7. Define the influence of loading conditions on thermally-induced strain.
8. Evaluate the long-term performance of crack propagation gage.

5.3. LONG-TERM ENVIRONMENTAL TEST SERIES

Ideally, the goal from most instrumentation projects involving strain gages is to measure the stress-induced strain. However, changes in the ambient temperature as well as temperature gradients induced from uneven solar exposure results in thermally-induced strains that can be very difficult to properly account for. The thermally-induced strains occur due to the combination of two factors. First, the resistivity of the grid alloy changes with temperature, and second the differential deformation between the instrumented material and the strain gage due to different thermal expansion coefficients. The gages are manufactured utilizing different grid alloys to closely match the thermal expansion coefficient of the material to be instrumented. However, a slight difference between the thermal coefficients of the gage grid alloy and instrumented material always exists due to the variability of material chemical composition. Figure 5-1 illustrates the strain error due to different thermal expansion coefficients between the steel specimen (α_s) and the gage (α_g) – assuming that α_s is larger than α_g. The original position of a strain gage and a steel specimen is shown in Figure 5-1-(1). When the instrumented structural member and a gage are subjected to a uniform temperature change ΔT, the structural member and the gage expand or contract by an amount corresponding to their respective coefficients of thermal expansion. Figure 5-1-(2) shows the resulting thermal expansion

of the specimen and gage if both can freely expand. In this case, the gage expands by $\alpha_g \cdot \Delta T$, and the specimen by $\alpha_s \cdot \Delta T$. However, the gage is rigidly attached to the specimen and thus it is forced to deform the same amount as the specimen, which is significantly stiffer than the gage. As illustrated in Figure 5-1-(3), the gage must elongate by an additional strain of $(\alpha_s - \alpha_g) \cdot \Delta T$. This strain error is recorded by the gage.

Moreover, the gage readings can be affected by changes in the bond between the strain sensor and the base metal, or corrosion of the electrical connections. The most common reasons of strain gage deterioration are corrosion of the wire lead termination, and damage of protective coatings resulting in damage to the bond between the gage and the base metal. Several environmental tests were performed in this research investigation to evaluate the behavior of strain gages.

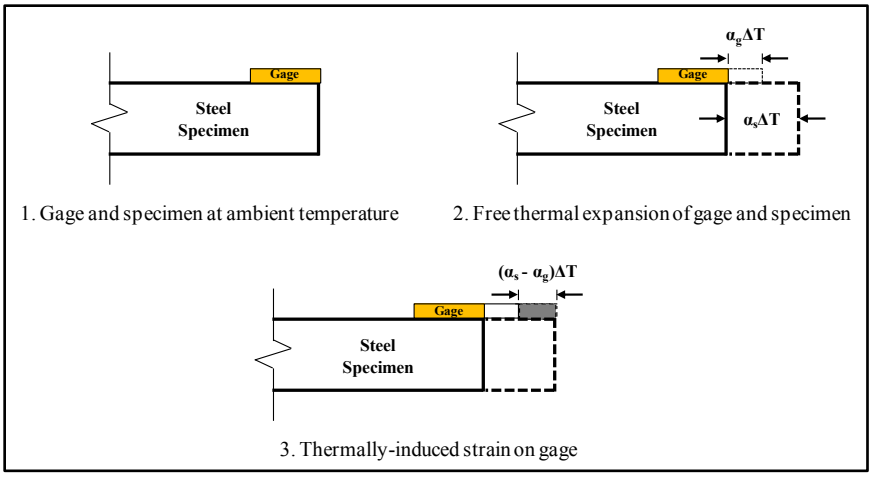

Figure 5-1: Thermally-induced strain between specimen and strain gage

5.3.1. Gages installed on test-boxes, and exposed to an outdoor environment

One of the initial goals of this research project was to evaluate the long-term response of different types of strain gages that are commonly used to monitor steel bridges. Several types of strain gages that are commercially available were reviewed. As

noted earlier, since the target maintenance-free life of the monitoring system is 10 years, consequently the target maintenance-free life of the sensors is also 10 years. However the long-term performance of the gages with respect to bond-life and stability of the electronic signal must be considered. All the strain gages that were investigated utilize similar technology. The main part of each gage is the active grid, which consists of a thin metallic foil grid. However, the grid is mounted on different backing materials for support, depending on the gage type. For example, the backing materials of a foil bondable gage and a weldable gage are flexible vinyl and stainless steel shims, respectively. To enhance their durability and resistance against environmental contaminants, the strain gages need to be protected with protective coatings (e.g. zinc-based spray, wax and silicon, etc.). All the protection systems and adhesive types employed for each gage in the first testing phase were recommended by the suppliers. Figure 5-2 illustrates the different types of strain gages and environmental protection coatings evaluated during the first testing phase.

As part of this testing phase, the strain gages shown on Figure 5-2 were installed on small scale test-boxes (Figure 5-3) to monitor their performance over time and obtain a measure of the durability against humidity, and other environmental effects that are expected in long-term bridge applications. The test boxes were 6 in. wide, 6 in. tall and 6 in. long. On the side of the test box, a 2-in. by 3-in. steel angle was welded. The test boxes were designed and fabricated to simulate exposure conditions that commonly exist in bridge instrumentation practices. Two gages were installed on the interior bottom and top face of the test-box (i.e. Inside Bottom and Inside Top on Figure 5-3). These locations simulate possible gage positions inside of box girder bridges. Two gages were installed on the outside top face and below the side angle (i.e. Outside Top and Angle on Figure 5-3) to simulate the conditions that are commonly found in the instrumentation of I-girder

bridges, where some of the gages are either totally or partially exposed to direct sunlight and rain. The gages were connected to a data acquisition system and were continuously monitored acquiring strain measurements from the unloaded specimens every 30 minutes.

	Code Name: HBW-W Type: Weldable Stainless Steel Shim Protection: Zinc-based Spray		Code Name: LEA-R Type: Weldable Stainless Steel Shim Protection: Zinc-based Spray
	Code Name: HBW-B Type: Bondable Stainless Steel Shim Protection: Zinc-based Spray		Code Name: LEA-L Type: Weldable Stainless Steel Shim Protection: Zinc-based Spray
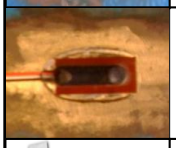	Code Name: HBP-B Type: Bondable Polyimide Shim Protection: Rubber Patch		Code Name: CEA-C Type: Foil Gage – Bondable Protection: Wax & Silicone Coating
	Code Name: HBWF-AMP Type: Weldable Stainless Steel Shim – Amplified Protection: Zinc-based Spray	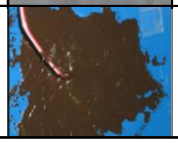	Code Name: CEA-J Type: Foil Gage – Bondable Protection: Wax & M-Coat J

Figure 5-2: Types of strain gages and protection coatings under evaluation

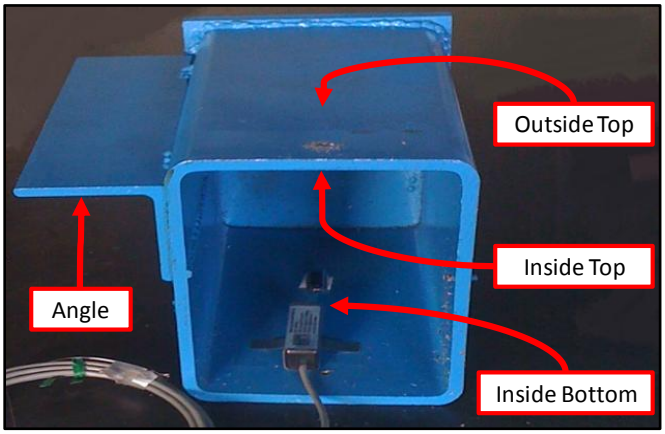

Figure 5-3: Typical steel test-box

Two sets of test-boxes were fabricated. One set of test boxes that are referred to as "outdoor conditions" were placed outside Ferguson Structural Engineering Laboratory (FSEL) and was exposed to variable weather conditions (Figure 5-4). The second set of

boxes that are referred to as “controlled climate” were placed inside a humidity room in Earnest Cockrell Jr. (ECJ) Hall on the main campus of the University of Texas. More details for this study are given in a later section. The goal of the first testing phase was to determine the advantages and disadvantages of each type of strain gage, with the general goal of narrowing down the types of gages that should be considered for long-term usage in bridge applications. Another goal of the tests included the evaluation of protection systems for the different gages.

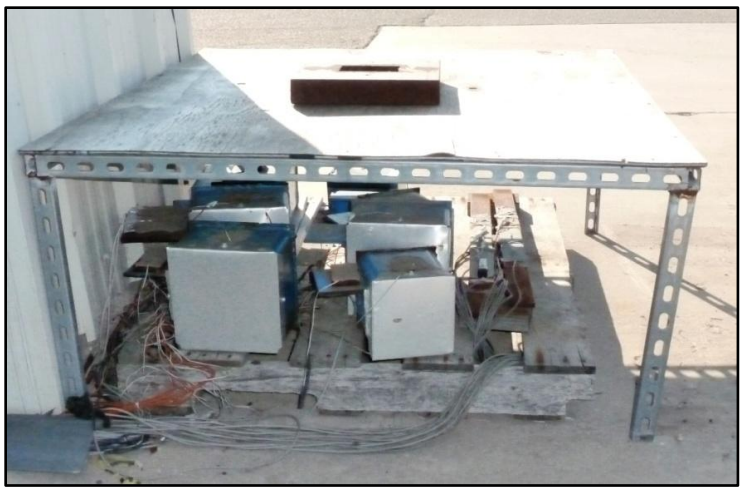

Figure 5-4: Steel test-boxes outside FSEL

Another important aspect of the environmental tests was to gain an indication of the performance of the sensors under variations in thermal conditions. Therefore, thermocouples were installed at six different locations to monitor fluctuations in the temperature conditions in the gages. The six thermocouple locations are:

1. Inside top face of the test-box.
2. Inside bottom face of the test-box.
3. Inside the test-box at the mid-height.
4. Below the side angle.

5. Outside top face of the test-box.
6. Open air (i.e. ambient) in the shade.

The combination of the strain and temperature readings provides an indication of how temperature fluctuations affect the stability of the gage readings.

5.3.2. Gages installed on steel bars, exposed to an outdoor environment, and periodically tested under axial loads

Concurrent with the steel test-boxes and as a second part of the first phase, two long rectangular steel bars (Figure 5-5) were instrumented with strain gages as shown on Figure 5-2. Each type of strain gage was installed in pairs on opposite faces of the steel bar. The steel specimens were 30 in. long, 3 in. wide and 3/8 in. thick. The steel bars were stored outside FSEL and monitored continuously recording strain measurements every 30 minutes. Once a month the steel bars were subjected to tensile loads using an uniaxial test frame (Figure 5-6) within the elastic region to ensure that the gages did not debond and to evaluate the repeatability of the strain readings.

Figure 5-5: Long steel bars instrumented with different types of gages

Figure 5-6: Testing of long steel bar

5.3.3. Gages installed on steel bars, exposed to an outdoor environment, and periodically tested in bending

As previously described a total of eight different combinations of strain gage types and protective coatings were evaluated as part of the first testing phase. Based upon durability tests on these gages, two strain gages were targeted for further investigation:

1. The bondable foil gage (CEA-J).
2. The weldable strain gage (HBW-W and LEA-R) with new protection systems.

A second phase of the testing program was developed to better understand the behavior of bondable and weldable strain gages, as well as the necessary environmental protection for the gages. The two major goals of this test series were to demonstrate the behavior of strain gages for different stages of deterioration (e.g. debonding, lead wire corrosion), and to determine the relationship between thermally-induced strain and temperature.

For this environmental test, fourteen steel bars 24 in. long, 3 in. wide and 3/8 in. thick were utilized. Twelve bars were exposed to the environment outside FSEL and were simply supported on two rails (Figure 5-7). The other two bars provided a baseline for this durability test and were stored indoors to be protected from environmental contaminants.

Figure 5-7: Twelve steel bars outside FSEL

Each steel bar was instrumented with two pairs of strain gages as shown in Figure 5-8 and Figure 5-9. Seven of the steel bars were instrumented with bondable foil gages and the other seven with weldable gages. Gages 1 and 2 on each steel bar were protected with microcrystalline wax and a heavy duty two-part polysulfide liquid polymer (PLP) compound (i.e. Protection Scheme 2). Gages 3 and 4 were protected with Protection Scheme 1 that included butyl rubber sealant, aluminum tape, and contact cement paint (Figure 5-10). Ten of the steel bars had intentional defects in the protective coatings. The defects in the protection consisted of paths for the environmental contaminants to reach the sensor, and thus the any potential deterioration of the strain gage would likely be

accelerated. The defects that were introduced were intended to represent a scenario of a poor strain gage installation. The defect was produced by introducing a wire that protruded into the gage area during the installation of the protective coatings (e.g. wax and heavy duty polymer compound) and pulling the wire out once the coating had set. The defects were located at different places of the strain gages as shown in Figure 5-11. The arrow shows the location of the temporary wire that was removed. Cases were considered with the defect on only one side of the gage (Types 1 and 2) and defects on two sides of the gage (Types 3 and 4). Table 5-2 summarizes all the combinations that were evaluated.

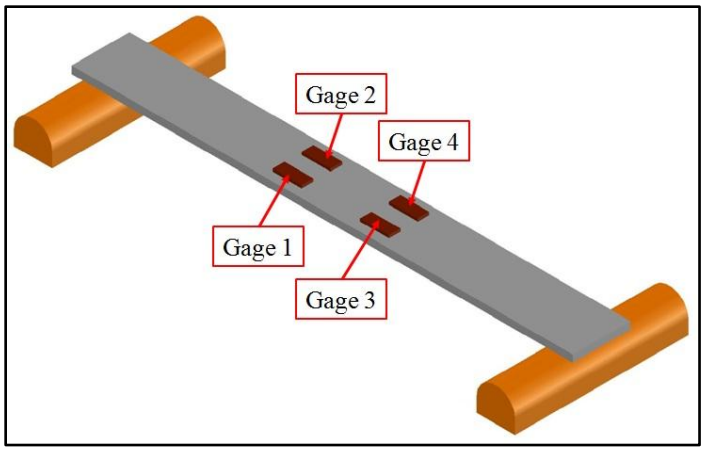

Figure 5-8: Steel bar specimen instrumented with strain gages

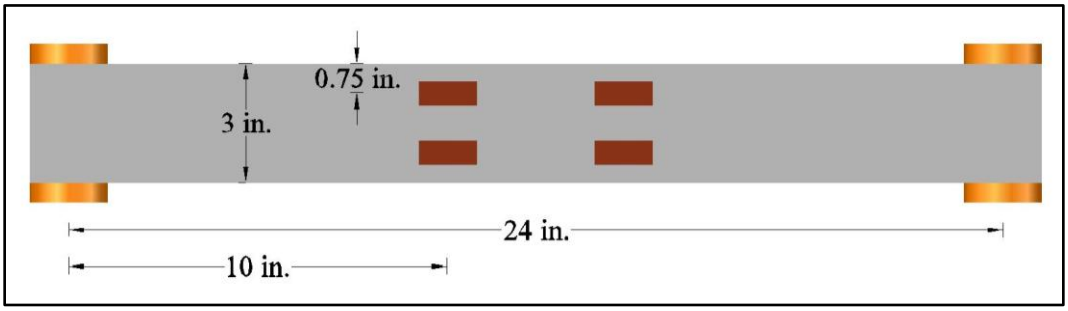

Figure 5-9: Geometry of the steel bar and location of the strain gages

Figure 5-10: Typical instrumentation of 14 steel bars

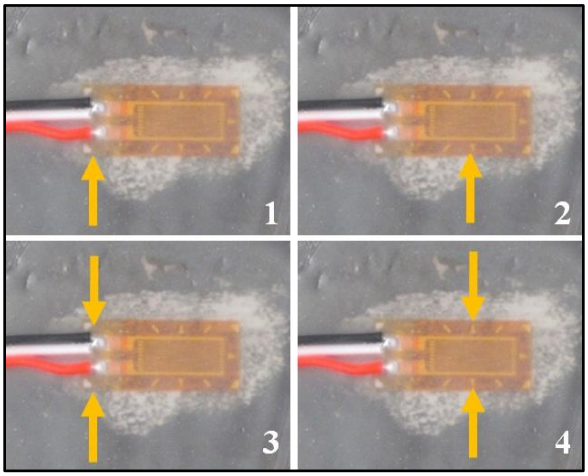

Figure 5-11: Location of the different defect types

The strain gages were continuously monitored strain measurements were recorded every 30 minutes. Once per week the simply supported steel bars were transversely loaded (weak axis bending) in place with two pieces of steel, which weighed 33 lbs. and 66 lbs, respectively. The weights were hung from the center of each bar, inducing 80 με and 160 με respectively at the location of the gages. The obtained strain readings were analyzed over time to determine if the gage performance changed.

Table 5-2: Combinations of strain gages and protection levels utilized in Tess E3

Type of Strain Gage	Steel Bar	Protection Level	
		Gage 1 & 2	Gage 3 & 4
Bondable Foil Gage	1 (Baseline)	Wax & PLP compound	Butyl Rubber Sealant, Aluminum Tape, and Contact Cement Paint
	2	Wax & PLP compound	Butyl Rubber Sealant, Aluminum Tape, and Contact Cement Paint
	3	Wax	Butyl Rubber Sealant
	4	Wax & PLP compound with defect type 1	Butyl Rubber Sealant, Aluminum Tape, and Contact Cement Paint with defect type 1
	5	Wax & PLP compound with defect type 2	Butyl Rubber Sealant, Aluminum Tape, and Contact Cement Paint with defect type 2
	6	Wax & PLP compound with defect type 3	Butyl Rubber Sealant, Aluminum Tape, and Contact Cement Paint with defect type 3
	7	Wax & PLP compound with defect type 4	Butyl Rubber Sealant, Aluminum Tape, and Contact Cement Paint with defect #4
Weldable Strain Gage	8 (Baseline)	Zinc Spray, Wax, and PLP compound	Butyl Rubber Sealant, Aluminum Tape, and Contact Cement Paint
	9	Zinc Spray, Wax, and PLP compound	Butyl Rubber Sealant, Aluminum Tape, and Contact Cement Paint
	10	Zinc Spray	Butyl Rubber Sealant
	11	Zinc Spray, Wax, and PLP compound with defect type 1	Butyl Rubber Sealant, Aluminum Tape, and Contact Cement Paint with defect type 1
	12	Zinc Spray, Wax, and PLP compound with defect type 2	Butyl Rubber Sealant, Aluminum Tape, and Contact Cement Paint with defect type 2
	13	Zinc Spray, Wax, and PLP compound with defect type 3	Butyl Rubber Sealant, Aluminum Tape, and Contact Cement Paint with defect type 3
	14	Zinc Spray, Wax, and PLP compound with defect type 4	Butyl Rubber Sealant, Aluminum Tape, and Contact Cement Paint with defect type 4

5.3.4. Gages installed on unrestrained steel bars, and exposed to controlled temperature environment

In addition to the second phase of environmental tests under actual conditions outside of Ferguson Structural Engineering Laboratory, another series of tests were conducted in a controlled temperature environment (e.g. furnace, refrigerator) to determine the behavior of weldable and bondable foil gages under different temperature levels. The objective of this investigation was to better understand the thermal effects on strain gage behavior and explain certain aspects of the gage response measured during the previous environmental tests (e.g. strain fluctuation at a given temperature).

For this test, four steel bars were utilized and each was instrumented with a foil gage, a weldable gage, and a thermocouple (Figure 5-12). The steel bars were 12 in. long and 1.5 in. wide. Two of the bars had a thickness of 1/8 in. whereas the other two had ½ in. thickness. The gages were protected from the environment with a rubber patch, aluminum foil tape, and contact cement. During this test series, the bars were free to expand or contract. Thus, all the recorded strain readings were equal to the thermally-induced strains of the gage due to the thermal effects.

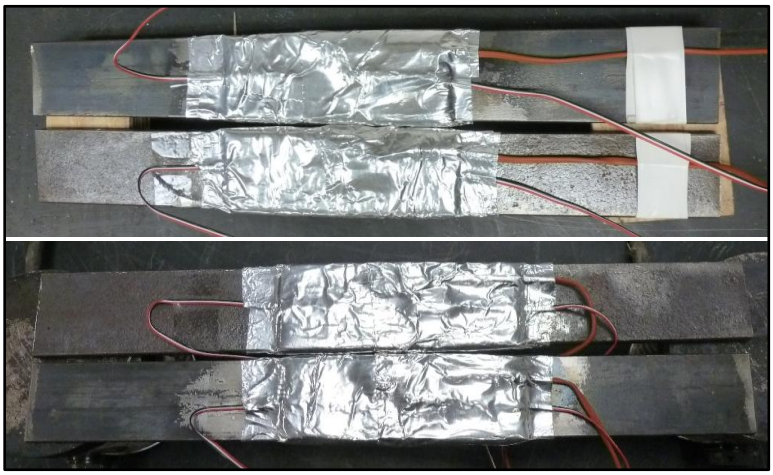

Figure 5-12: Small scale unrestrained steel bars

A refrigerator and a furnace were utilized to cool down or heat the bars to certain temperatures. The refrigerator could cool the bars down to 35 °F, and the furnace could heat the specimens to 140 °F. Parametric studies were performed to analyze the gage behavior. First, the effect of constant temperature at different levels (i.e. 40 °F, 60 °F, 80 °F, etc.) on the gage behavior was examined. Second, the influence of the rate of temperature change on the strain gage readings was studied. Methods for correcting the strain readings to account for the effect of the thermally-induced strain were evaluated using the empirical relationships that are provided by the strain gage manufacturers. These empirical equations can compute the thermally-induced strain as a function of the temperature, but do not include the effect of temperature change rate. This test series results were validated with the recorded data from the second phase environmental tests under an outdoor environment exposure, which is a real life scenario.

5.3.5. Gages installed on steel bars, exposed to an outdoor environment, and loaded in bending about the strong or weak axis of the bar

In addition, to ensure the applicability of the controlled temperature test results to any gage regardless of orientation (e.g. gage installed on the bottom flange or the web), and loading conditions, a test was conducted as part of the controlled environment test series. For this test, a 24 in. long, 3 in. wide, and 3/8 in. thick steel bar was instrumented with a foil gage, a weldable gage, and a thermocouple on each side. The gages were protected from the environment with a rubber patch, aluminum foil tape, and contact cement. WSN Strain and Thermocouple nodes were utilized to acquire data every 30 minutes.

This bar was first placed inside an air-conditioned room where the temperature fluctuated from 65 °F to 75 °F. The steel bar was then placed in a shaded room that did not have any climate control. The temperature recorded from thermocouples on the face

of the specimen ranged from 73 °F to 126 °F. Last, the bar was placed outside FSEL (Figure 5-13) in different orientations with respect to bending about the strong or weak axis of the bar (i.e. lying flat or vertical to the side). The bar was subjected to different loading conditions (i.e. unloaded or loaded with 35 lb), to determine how thermally-induced strain was affected by these parameters. The temperature of the steel when the bar was placed outside FSEL fluctuated from 26 °F to 125 °F.

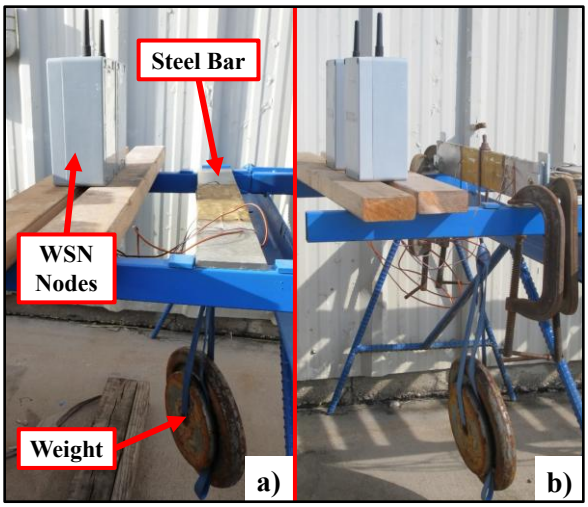

Figure 5-13: Loaded steel bar placed a) flat (weak axis bending), b) vertical (strong axis bending)

5.3.6. Gages installed on test-boxes and exposed to controlled conditions inside a humidity room

As it was previously mentioned, one set of steel test-boxes was placed inside a humidity chamber (Figure 5-14) at the basement of ECJ. Within the humidity room, the temperature and relative humidity were nearly constant to 64 °F and 100%, respectively. While the gages were not subjected to sunlight, which may contribute to degradation of the environmental protection, the environmental protection can be compromised by moisture penetration. Thus, the goal of this first phase environmental test was to determine the effect of moisture penetration on the strain gage performance.

Figure 5-14: Steel test-boxes inside humidity room

Initially, the steel test-boxes were constantly located inside the humidity chamber and serial port connectors (Figure 5-15) were used to connect the strain gages and data acquisition system. Similar to the other environmental tests, the gages in the humidity room were continuously monitored and strain measurements were acquired every 30 min.

After a few weeks, the gages exhibited significant drift in the strain readings and it was believed that was an indication of debonding of the gages from the surface of the steel. However, an autopsy of the gages did not reveal any serious debonding issues, and it was found that the drift of strain readings was due to corrosion of the serial port pins. The serial connectors were removed and replaced with a direct connection between the gages and the data logger through continuous cables. This change eliminated the problem of the large drift and the strain readings stabilized.

Figure 5-15: Serial port connectors

Few months after the initiation of this environmental test it was decided to alternate the steel test-boxes between the humidity chamber (64 °F, and 100% humidity) and a typical indoor room (Figure 5-16). The reason behind this change was to simulate a more realistic scenario of a bridge environment where humidity fluctuates and to examine how moisture fluctuation can affect the environmental protection.

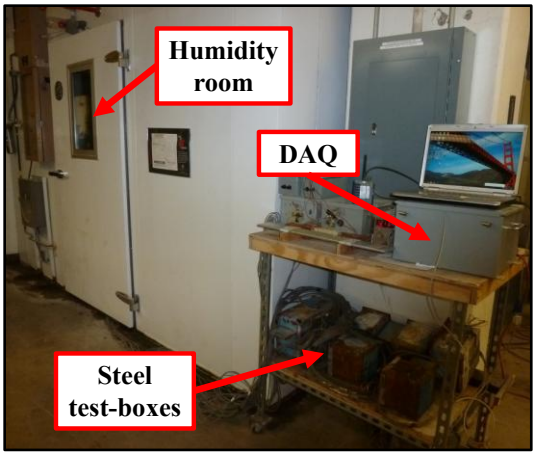

Figure 5-16: Steel test-boxes outside humidity room

5.3.7. Gages installed on steel bars and exposed to controlled conditions inside a humidity room

As previously mentioned, the bondable foil gage (CEA-J), and the weldable strain gage (HBW-W and LEA-R) were targeted for further investigation based on the initial durability tests of the steel test-boxes. To enhance the knowledge of the behavior of these types of gages for different stages of deterioration, as well as the durability of different types of environmental protection, two steel bars (Figure 5-17) were instrumented and cycled them between the humidity room and the typical indoor room. Each steel bar, which was 8 in. long, 3 in. wide and 3/8 in. thick, was instrumented with two foil and two weldable gages. The gages on one bar were protected with microcrystalline wax and two-part polysulfide liquid polymer (PLP) compound. For the gages on the other bar, a rubber

patch, aluminum tape, and contact cement paint were used as the protection scheme. On each of the two steel bars, two of the gages (i.e. one foil and one weldable gage) were protected without any defect, whereas the other two gages on the same bar were had a type 2 defect (Figure 5-11).

The NI wireless system was utilized to acquire strain measurements every 30 minutes. The use of a wireless data acquisition system had several advantages. First, the use of the wireless sensor network (WSN) strain node isolated the possibility of wire splice corrosion, and thus only the performance of the protective coatings and strain gages was evaluated. Second, the reliability of the WSN strain node and its ability to record strain values properly in a harsh environment was evaluated during this test. Finally, the durability of the environmental enclosure that protected the WSN strain node against humidity can be evaluated.

Figure 5-17: Steel bar inside humidity room

5.4. FATIGUE TESTS OF STRAIN GAGES

Fatigue damage is the process of crack growth in metal structures due to cyclic loads at sufficiently high amplitudes. The strain gages have metallic components and thus they can potentially be susceptible to fatigue. When fatigue damage starts to occur in a

strain gage, then the gage records a drift in the strain readings, which increases as the damage increases. This drift can build over time and produce misleading results. Several fatigue tests on strain gages have been reported in the literature (Vishay Micro-Measurements Group, Inc., 2007). For example, Figure 5-18 illustrates the fatigue test results of bondable strain gages. It can be easily seen that there is no fatigue damage in a strain gage for most structural applications where the strain level is below ±2050 με.

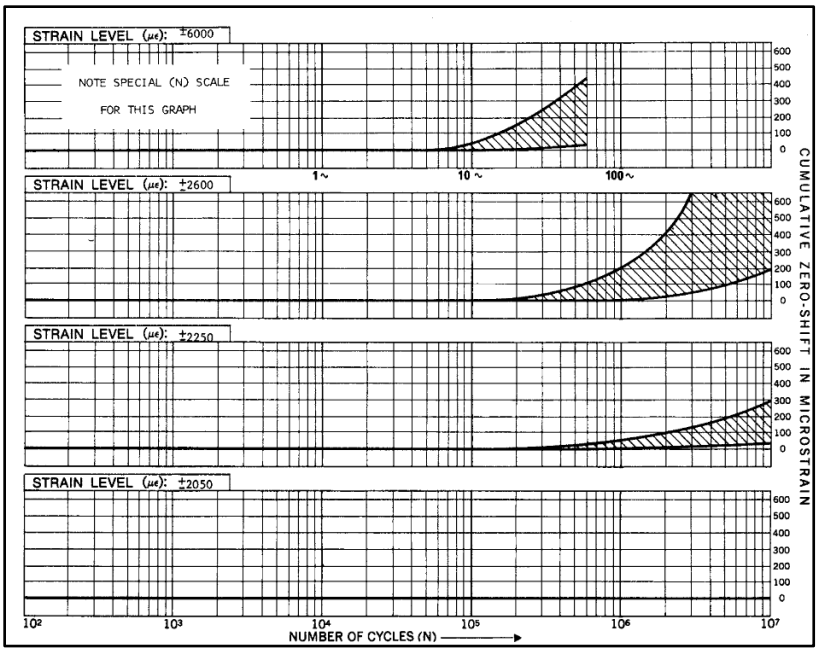

Figure 5-18: Strain gage fatigue test results (Vishay, 2007)

Any reference on the literature could be found related to fatigue damage on steel due to the small spot welds used to fasten weldable gages. Thus, a testing program, which was part of the first testing phase, was developed to determine if spot welds can initiate fatigue cracks in the steel, and to verify that bondable gages do not impact the fatigue life. As part of this testing program, three pairs of steel coupons were tested at a stress range of 35 ksi (Figure 5-19). The very large stress range was selected to identify

potential problems in an expedited manner. If fatigue failures were not observed at this stress range, they would not be expected when attaching strain gages to bridges where the likely stress ranges are typically substantially lower than 35 ksi. Two different types of gages were installed in pairs on opposite sides of each coupon. The first pair of coupons was instrumented using HBWF-AMP and HBW-W gages (Figure 5-2). The second pair of coupons was instrumented using LEA-L and LEA-R gages. The third pair of tensile coupons was instrumented using HBW-B and CEA-C gages.

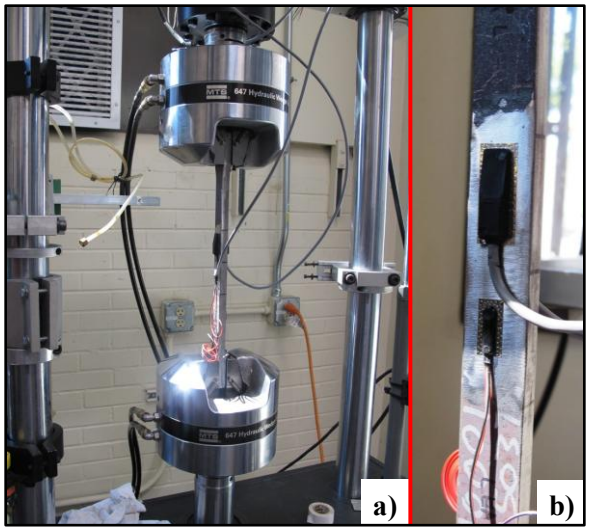

Figure 5-19: Fatigue test set up a) overall view, b) close up view of specimen

5.5. EVALUATION OF LONG-TERM PERFORMANCE OF CRACK PROPAGATION GAGES

In cases with existing cracks, a measure of crack growth is likely to be desired. For these applications crack propagation (CP) gages such as the one shown in Figure 5-20 are likely to be used. This type of sensor can provide significant information on the growth of a known crack. Moreover, it is commercially available and with the right environmental protection it can potentially last for 10 years. During this project, the type of crack propagation that was investigated was 2 in. long and 0.5 in. wide. The active grid

area of the gage contained 20 strands over a width of 0.4 in. As a crack propagates, it causes the strands to consecutively break and as a result the gage resistance increases. The crack growth can be determined by measuring the resistance at the end blocks of the gage

As in the case of the strain gages, the long-term response of crack propagation gages was evaluated to determine how the gage performance is affected by environment variables, like temperature and humidity. Thus, as part of this research project a third phase of this testing program was developed to better understand the behavior of this type of sensor. This evaluation test had three parts, which are summarized in Table 5-3.

The first part included a benchmark laboratory test of the crack propagation gage to verify its behavior in a controlled environment before installing them on the field. The benchmark test consisted of a fatigue test performed on a steel coupon with a notch (Figure 5-21). The steel coupon was 2 in. wide and 1/8 in. thick. The length of the notch was ¼ in. One crack propagation gage was placed on each side of the specimen just beyond the notch. The specimen was loaded cyclically between 5 ksi and 40 ksi. A crack would initiate at the notch location and as the crack propagated through the width of the CP gage the gage resistance changed. A data acquisition system was used to record the gage resistance every 2 sec. The results from this fatigue test were used to comprehend the gage readings on the field.

Table 5-3: Summary of the test series for the crack propagation gages

Test Series #	Description	Environmental Conditions	Loading Conditions
1	Benchmark laboratory fatigue test	N/A	Cyclic load (30 ksi stress range)
2	Outdoor exposure test to determine the thermal effects	Variable outdoor environment	No load
3	Monitoring of an active crack on Bridge A	Variable outdoor environment	Random traffic loading

The second part was an environmental test to identify the effects of environmental contaminants (e.g. humidity) on the gage behavior. This environmental test consisted of a steel bar instrumented with two CP gages and were placed outside FSEL. The gages were connected to data acquisition systems and were continuously monitored acquiring resistance measurements every 30 minutes. The test results indicated how the gage resistance was affected with ambient temperature fluctuation.

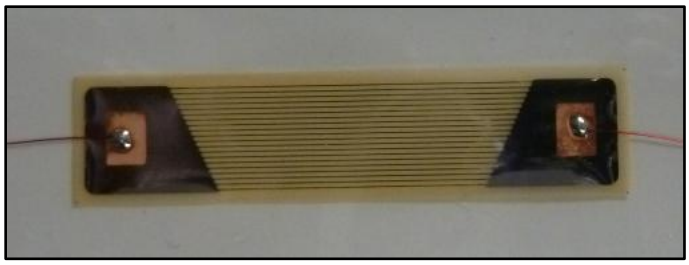

Figure 5-20: Crack propagation gage

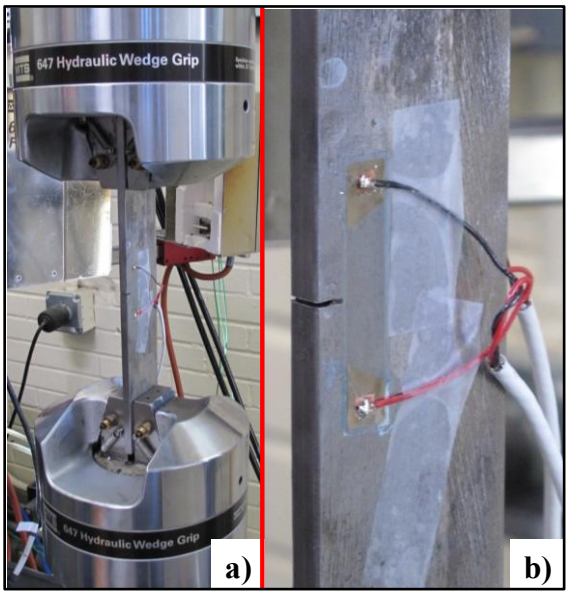

Figure 5-21: Laboratory fatigue test of the crack propagation gage a) overall view, b) close up view of specimen

The third part of this test series was the evaluation of CP gage performance on a real life monitoring scenario of a fracture critical bridge. Two crack propagation (CP) gages were bonded next to the tip of active cracks on Bridge A (Figure 5-22) to monitor their rate of growth. The crack propagation gages were installed utilizing a general-purpose cyanoacrylate bonding agent. To protect the bonding surface against environmental effects, two layers of environmental coatings were applied. A layer of microcrystalline wax and then RTV silicone were applied on top of the gage. The long-term response of the crack propagation gages at Bridge A provided the opportunity to further evaluate the behavior of the crack propagation gage. The recorded data were very important because they indicated, in a timely manner, the fast growth of a crack. More details of crack propagation data are given in the next chapter.

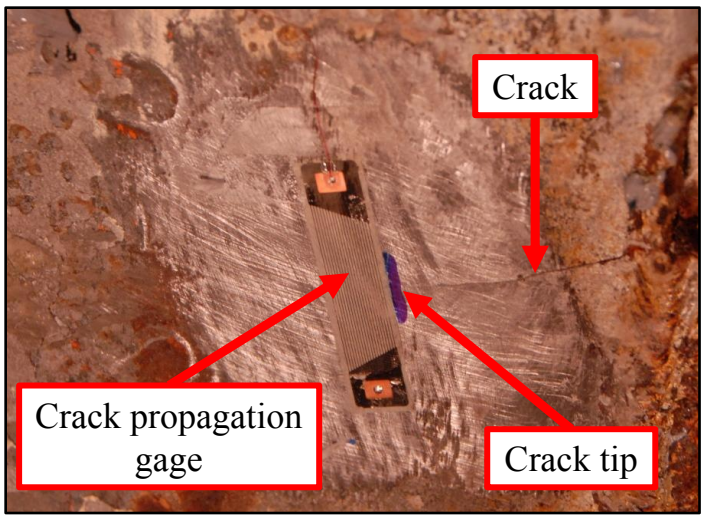

Figure 5-22: Crack propagation gage installed on Bridge A

CHAPTER 6

Results of Long-term Sensor Reliability

6.1. INTRODUCTION

Structural health monitoring (SHM) systems have been employed in the recent years to monitor the health and performance of structures. Many of these past applications have focused on problematic bridges or were used on specific applications to gather data for research studies. In cases that have been applied to deficient bridge systems, the primary goal of most of the SHM systems has typically been to track problems in the bridge. Many of the SHM systems that have been employed in the past typically consist of several measurement controllers and a variety of sensing technologies. The sensors are attached at critical locations of the structures to collect information to assist in the evaluation of the integrity of the structure. Thus, the reliability of the structural health monitoring systems highly depends on the long-term performance of sensors.

Bridges represent complex structures with highly variable support and loading conditions. In structural design, the engineer often focuses heavily on the impact of gravity and lateral loads on the structure; however there are a wide variety of other sources of stress in the structure from environmental factors. One of the difficult aspects in field monitoring projects is obtaining a measure of the data of interest in the highly complex structure, which therefore requires the evaluation of the impact of all of the sources of stress that affect the sensor readings. Ideally, the engineer desires to have the sensor provide a measure of the specific physical quantity (e.g. strain, crack growth etc.) that is the target of the instrumentation; however separating the effects of other sources of loading is a very challenging problem. Accounting for the effects of changes in the thermal environment of the bridge is a very common and difficult problem that must be

considered and accounted for. Sensor technology is based on the fundamentals of electronic circuits, and it has been well established that electronic circuits are affected by environmental variables (e.g. temperature). Yet, the environmentally-induced errors can be minimized by compensation or correction.

The focus of this chapter is results of the long-term reliability tests. Following this introductory section, the results of the long-term environmental tests of the gages and their protective coatings are summarized. These tests assisted in the identification of the most durable sensors against humidity, and other environmental effects expected in long-term bridge monitoring applications, as well as in determining the influence of thermal effects on gages. These environmental tests were divided into three testing phases. The first phase included:

- Environmental test results of gages installed on test-boxes, and exposed to an outdoor environment (Section 6.2.1).
- Environmental test results of gages installed on steel bars, exposed to an outdoor environment, and periodically tested under axial loads (Section 6.2.2).
- Environmental test results of gages installed on test-boxes, and exposed to controlled conditions inside a humidity room (Section 6.2.6)
- Fatigue tests results of strain gages (Section 6.3).

This chapter also highlights results from the second phase. The main objectives of the second testing phase were the investigation of potential methods to identify damaged or malfunctioned gages, the influence of thermal effects on the performance of the gages, and development of procedures to correct and minimize the thermally-induced strain on different types of gages. The second phase consisted of the following tests:

- Environmental test results of gages installed on steel bars, exposed to an outdoor environment, and periodically tested in bending (Section 6.2.3).

- Environmental test results of gages installed on unrestrained steel bars, and exposed to controlled temperature environment (Section 6.2.4).
- Gages installed on steel bars, exposed to an outdoor environment, and loaded in bending about the strong or weak axis of the bar (Section 6.2.5).
- Environmental test results of gages installed on steel bars and exposed to controlled conditions inside a humidity room (Section 6.2.7).

Finally, results from the investigation on the long-term performance results of crack propagation gages (third testing phase) are described. The testing phase on the crack propagation gages included both laboratory tests and the data from a field instrumentation.

6.2. LONG-TERM ENVIRONMENTAL TEST SERIES

The first objective of the long-term reliability of sensors was to indentify the most durable types of strain gages as well as the performance of various combinations of protective coatings. The methods of attaching the gages to the specimens as well as the corrosion protection were recommended by the suppliers of the gages. The suppliers provided guidance on the specific adhesives and protection systems. The durability of different types of strain gages was evaluated using series of tests that simulated environmental conditions that are expected to occur during long-term monitoring of highway bridges. The conditions included humidity, rain, and variations in the ambient temperature that the gages were subjected to. The results of these tests series are presented below.

6.2.1. Environmental test results of gages installed on test-boxes, and exposed to an outdoor environment

Monitoring of the gages attached to the steel test boxes located outside FSEL began in July 2010. After approximately 6 months (July 2010 - January 2011), it was observed that most strain gage readings fluctuated over a range of approximately 60 με for a temperature fluctuation of 60°F. The type of strain gage that exhibited the best performance was HBWF-AMP, which was a weldable sealed strain gage that utilizes an amplifier to amplify the signal before being sent to the data acquisition system. The amplification resulted in a reduction in the strain fluctuations to approximately 35 με (compared to 60 με as observed for many of the other gages) for the same temperature fluctuation. Figure 6-1 illustrates typical strain histories of amplified weldable gages installed at different locations of test-box.

After nearly 10 months (July 2010 - May 2011), the readings from four types of gages installed on the test-boxes outside FSEL experienced a significant drift in the readings (Figure 6-2). Because the test boxes were not subjected to external loads, the drift was an indication of gage deterioration or debonding. Autopsies of the gages that experienced significant drift were performed to reveal the cause of strain drift. Table 6-1 summarizes the types of damaged gages, the failure location, and the reason of failure. More details of the autopsy results are given below.

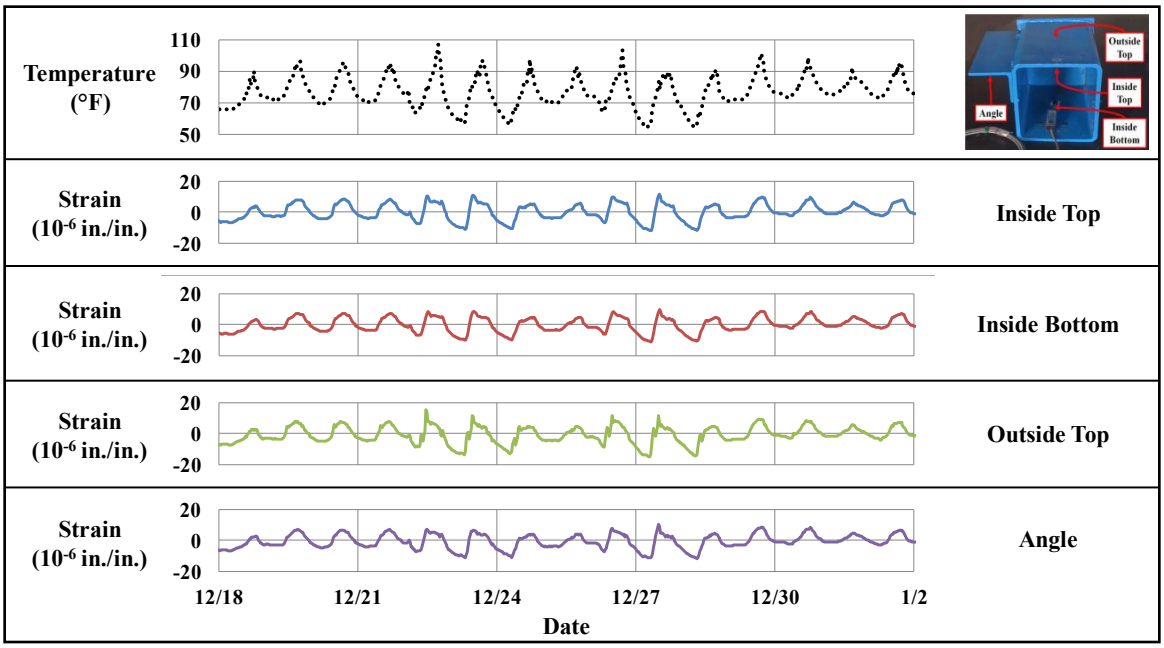

Figure 6-1: Typical strain history of amplified weldable gage (HBWF-AMP)

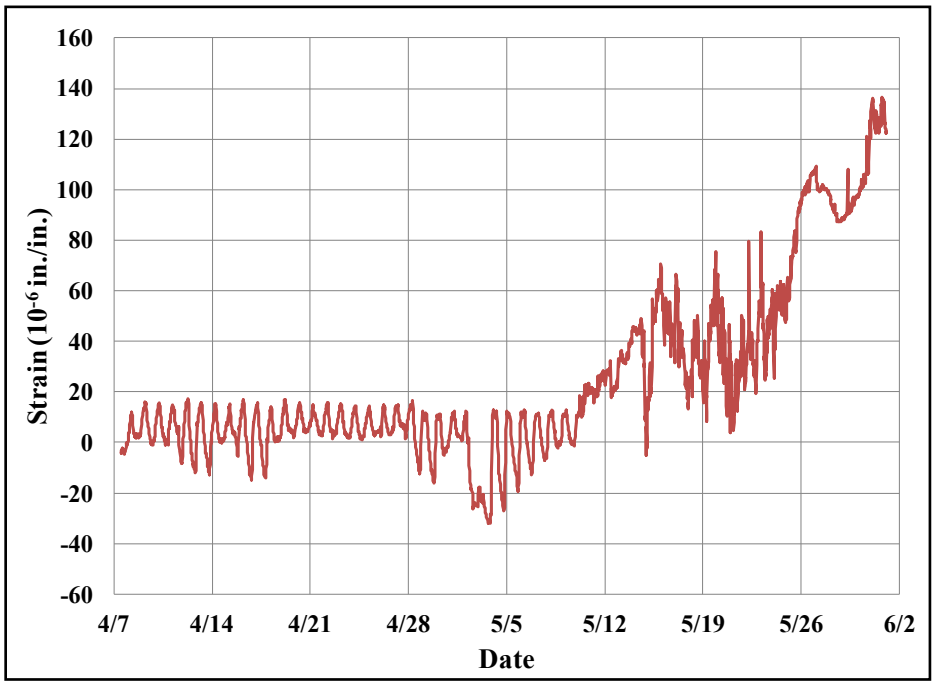

Figure 6-2: Typical drifting of strain readings

Table 6-1: Autopsy results of damaged gages (June 2011)

Damaged Gage		Failure location	Reason of failure
Weldable gage HBW-W		Inside Bottom	Debonding of the sealed gage from steel shim due to moisture penetration
Bondable sealed gage HBW-B		Inside Bottom Inside Top Outside Top	Debonding of the gage from specimen due to corrosion
Bondable sealed gage HBP-B		Angle	Debonding of the gage from specimen due to corrosion

The autopsy findings and the types of gages that were damaged are:

- **HBW-W gage** – These gages consist of a sealed gage attached on a stainless steel shim. The sensor was spot welded to the specimen and sprayed with zinc-based spray for protection from the environment. There were no signs of corrosion on the spot welds or between the stainless steel shim and the steel test specimen. However, the sealed gage debonded from the stainless steel shim (Figure 6-3) after approximately 11 months.
- **HBW-B gage** – This gage is composed of a sealed gage attached to a stainless steel shim. The gage is bonded to the surface of the specimen utilizing a special two-part adhesive – fast curing medium viscosity cyanoacrylate adhesive and cyanoacrylate activator (i.e. amine). For protection from corrosion and other contaminants, the gage was covered with zinc-based spray. These types of gages require the use of a viscous adhesive to be properly mounted on the steel. However, the viscous adhesive was not very resistant against moisture and the thick bonding layer that was produced between gage and steel likely played a role in the moisture penetration. As a result, corrosion and moisture penetration

(Figure 6-4) were found underneath the adhesive layer during the autopsy, causing the gage to debond.

- **HBP-B gage** – This gage is constructed by bonding a sealed strain gage onto a high-performance laminated polyimide film backing. The gage was attached to the steel specimen utilizing the same adhesive as in the case of HBW-B gage. The autopsy revealed that the presence of corrosion (Figure 6-5) between the gage and the specimen was the main reason of gage debonding after 11 months.

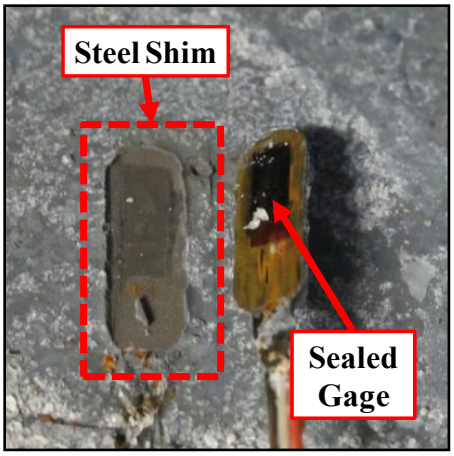

Figure 6-3: Debonding of HBW-W gage from the stainless steel shim

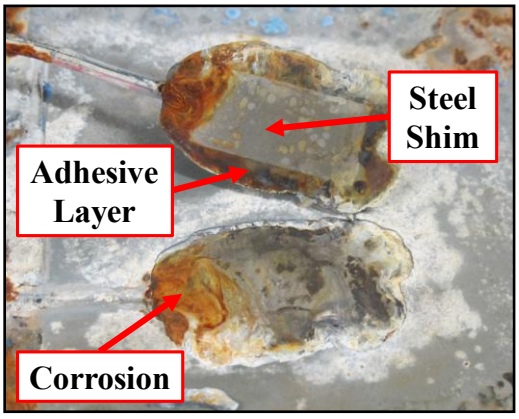

Figure 6-4: Failure mechanism of HBW-B gage

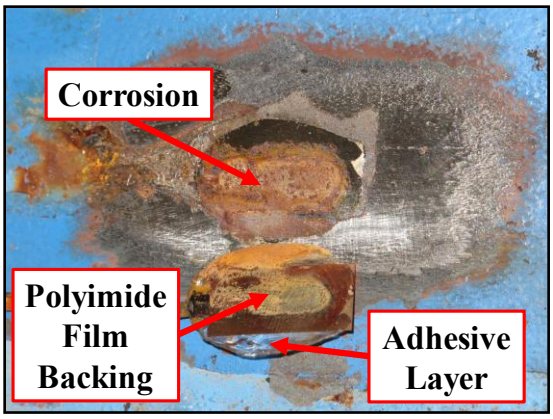

Figure 6-5: Debonding of HBP-B gage

On June 1, 2011 all the damaged gages were replaced with new gages. After replacing the damaged gages, the monitoring of the long-term response of the strain gages continued. No sign of deterioration was observed over the next few months. However, after almost 19 months (July 2010 – February 2012) from the beginning of the long-term durability evaluation, the amplified strain gages caused the data acquisition system to malfunction, and consequently the strain readings from the other gages were affected. Initially it was suspected that the data acquisition system was the main reason of this problem. Though, after replacing the data acquisition with a new one, the monitoring process did not improved. Then it was discovered that the Wheatstone bridge circuit inside the amplifier block of two gages (Figure 6-6) was damaged from moisture causing the shorting of the data acquisition circuits. Prior to these problems, the weldable strain gages with the amplifier (HBWF-AMP) recorded the lowest strain reading fluctuations. The strain range was lower because the signal was amplified before being sent to the data acquisition system. However, apart from causing problems to the data acquisition system, the amplifier required more power, which may limit the applicability of this type of gage for long-term applications. Moreover, the cost of purchasing the weldable amplified

gages (HBWF-AMP) was approximately five times greater than that of the bondable foil gages (CEA-J). The durability tests showed that the amplified weldable gage results were not sufficiently better than those of the bondable foil gage (CEA-J) to justify the higher initial costs. Thus, it was decided to stop investigating the long-term response of amplified strain gages and the gages were removed from the system.

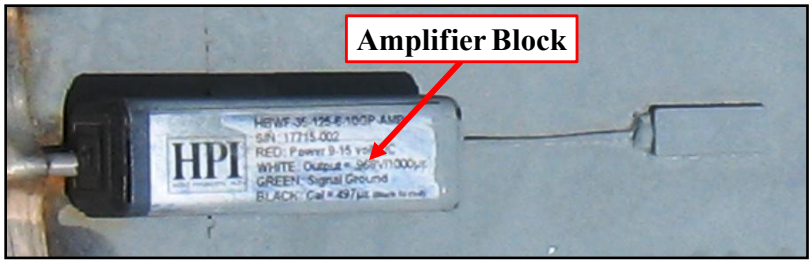

Figure 6-6: Amplifier block of amplified weldable gage

Based on the durability test results from the steel test-boxes outside FSEL, it was concluded that the bondable foil gage (CEA-J) exhibited the best overall performance. This type of gage had a similar performance to the amplified weldable gages (HBWF-AMP) without causing any problems to the monitoring procedure. Moreover, the bondable foil gage (CEA-J) – installed with a highly moisture resistant adhesive, and protected with wax and two-part polysulfide liquid polymer compound – did not experience any failure due to moisture, corrosion, or other environmental contaminants the last three years of the monitoring program. For the same period of time, there was not any observed failure due to debonding of the CEA-C bondable foil gage. However, in this sensing system the bondable foil gage was sealed against environmental contaminants with a layer of microcrystalline wax and a layer of silicone. Based on the supplier recommendations, this protective method was not considered to be as durable as the previous protective method that utilizes the two-part polysulfide liquid polymer

compound. The supplier's recommendation was verified by the humidity room test results, which are discussed in later sections.

The weldable sealed gages did not prove to be as durable as the bondable foil gages (CEA-C, CEA-J). Spraying the installation area with zinc-based spray, as recommended by the supplier, was not sufficient to prevent moisture from penetrating between the sealed gage and the shim. Yet, it was decided to improve the environmental protection and continue investigating these types of gages. WJE engineers were consulted about new methods for protecting weldable gages. WJE engineers frequently use weldable gages in the field since the gage welding procedures are not sensitive to the installation temperature as are adhesives.

The first step of the recommended protection method was to paint any soldered or open air connection with an air-drying solvent-thinned acrylic to insulate the exposed areas. Second, the lead wires need to be painted with an air-drying nitrile rubber coating, which acted as a primer and provides better bond between the wires and the butyl rubber sealant that was installed on top of the gage. The butyl rubber sealant was the main barrier to prevent moisture penetration. Last, to enhance the environmental protection, the entire area was covered with aluminum tape, and all the edges were painted with contact cement.

After replacing the zinc-based corrosion protection system with the new method for protecting weldable gages (February 2012), the durability of the weldable strain gages was greatly improved. Until July 2013, there has not been any observed damage to the weldable strain gage as a result of debonding from moisture penetration or other degradation.

6.2.2. Environmental test results of gages installed on steel bars, exposed to an outdoor environment, and periodically tested under axial loads

The different types of gages and protective coatings installed on steel bars were monitored for almost three years. The results of this test were used to evaluate the durability of the gages under investigation, and determine the relationship between temperature and thermally-induced strain in the gages.

The durability of the gages was assessed through continuously monitoring of the strain fluctuations, and periodically loading of the bars within the elastic region. The steel bars outside of FSEL, were exposed to surface temperatures ranging from 20°F to 145°F. For this temperature range, strain fluctuations that were larger than 100 με for the bondable foil gages, and 170 με for the weldable gages were used as an indication of a damaged gage. These thermally-induced strain fluctuation limits are based on the supplier specifications (Vishay Micro-Measurements Group, Inc., 2012). On the other hand, during the periodic uniaxial loading tests, the steel bars were consecutively subjected to tensile loads of 2, 4, 8, 10, and 15 kips, which were within the elastic range of the steel material. The loading tests were conducted to ensure that the gages were functioning properly and maintaining bond over time. If during loading a gage did not record the expected strain level, then the gage was malfunctioning and an autopsy was performed to identify any potential damage.

The first few months, all of the gages performed as expected and nothing unusual was observed. The repeatability in strain readings during the periodically uniaxial loading tests was another indication that the gages were functioning properly and reliably. Figure 6-7 illustrates the typical strain gage readings from three tensile tests performed on the steel bars. The red lines indicate the various loads that were applied to the bar. The gage

readings that are graphed demonstrated that the gages had good bond and provided repeatable results for the different load levels.

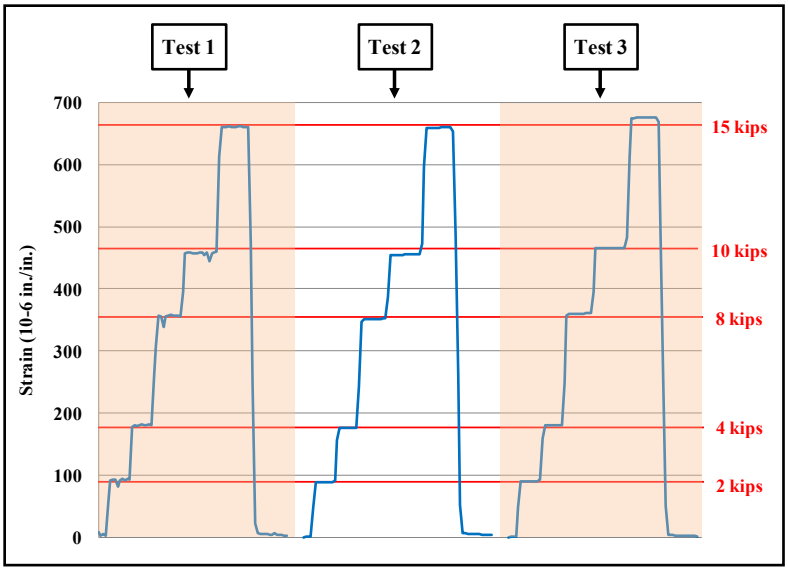

Figure 6-7: Typical strain gage readings of uniaxial loading tests of long steel bars

In mid-June 2011, the strain readings from all the gages were at the expected levels with the exception of the strain readings of the HBW-B gages. It was noticed that the HBW-B gages (bondable sealed gages with steel shim backing) recorded large strain fluctuations as shown in Figure 6-8 during the continuous strain monitoring while the gages were outside FSEL. To gain a further indication of the potential debonding problem, the steel bars were subjected to a uniaxial tension test. Figure 6-9 illustrates the measured response of strain gages during the uniaxial load test in June 2011. All the gages but the HBW-B reached the expected strain level. The strain level of HBW-B gage were very low (Figure 6-9). As indicated in Figure 6-10, the strain gage had debonded from the surface of the steel. The results of these tests were consistent with those from the steel test-boxes under an outdoor environment exposure, where the same gages were

the first to fail due to debonding. Two months later, the other bondable gage type (HBP-B) started to malfunction due to debonding. The rest of the gages did not show any sign of damage.

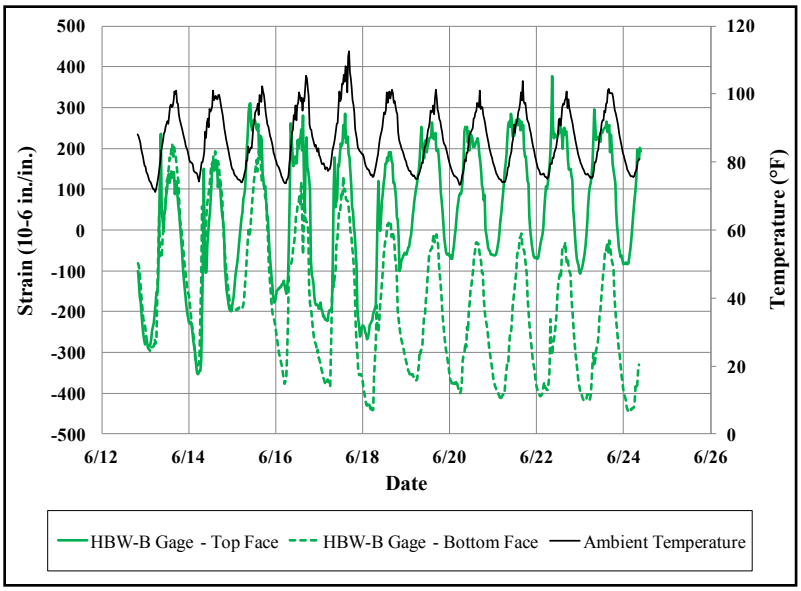

Figure 6-8: Large strain fluctuations of HBW-B gage due to debonding

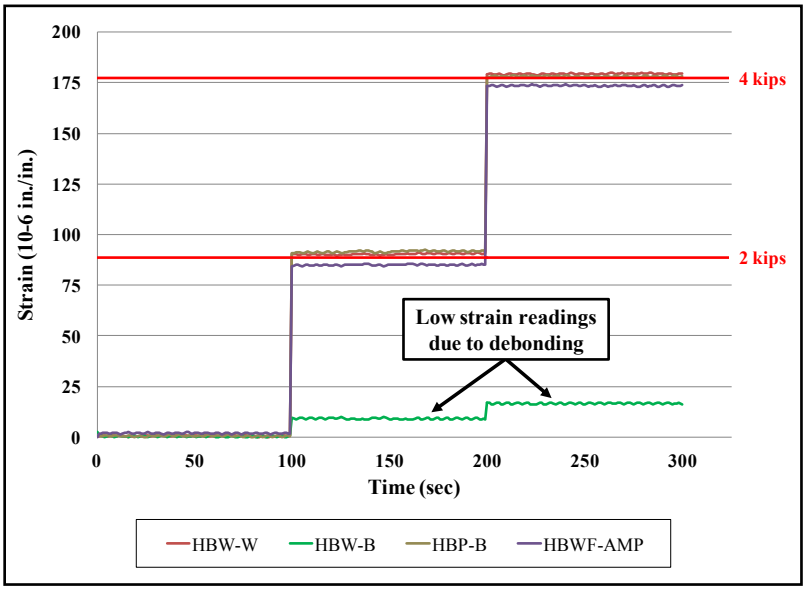

Figure 6-9: Measured response of strain gages during uniaxial load test (June 2011)

Figure 6-10: Debonding of HBW-B gage

The first data on thermally-induced strain was obtained from long steel bars exposed to an outdoor environment with variable temperatures. These steel bars were first placed inside an air-conditioned room where the temperature fluctuated from 65 °F to 75 °F. Inside that environment the foil and weldable gages recorded strain ranges of 10 με and 15 με, respectively. The long steel bars were then stored outside Ferguson Structural Engineering Laboratory (FSEL), where the temperature recorded from the thermocouple ranged from 20 °F to 145 °F. Representative thermally-induced strain histories from April 23 to May 7, 2011 are illustrated in Figure 6-11. It can be observed that temperature fluctuations have a significant effect on the strain data of the various sensors because the strain fluctuations follow the changes of temperature. The weldable strain gages (HBW-W, LEA-R, and LEA-L) fluctuated over a range of approximately 70 με due to thermal variations of approximately 60 °F. For the same temperature range, the bondable foil gages (CEA-C, and CEA-J) and the amplified weldable strain gage (HBWF-AMP) had a strain range of 40 and 48 με respectively. These two types of gages exhibited the best performance as indicated by the smaller strain range compared to the weldable gages with the same temperature fluctuation.

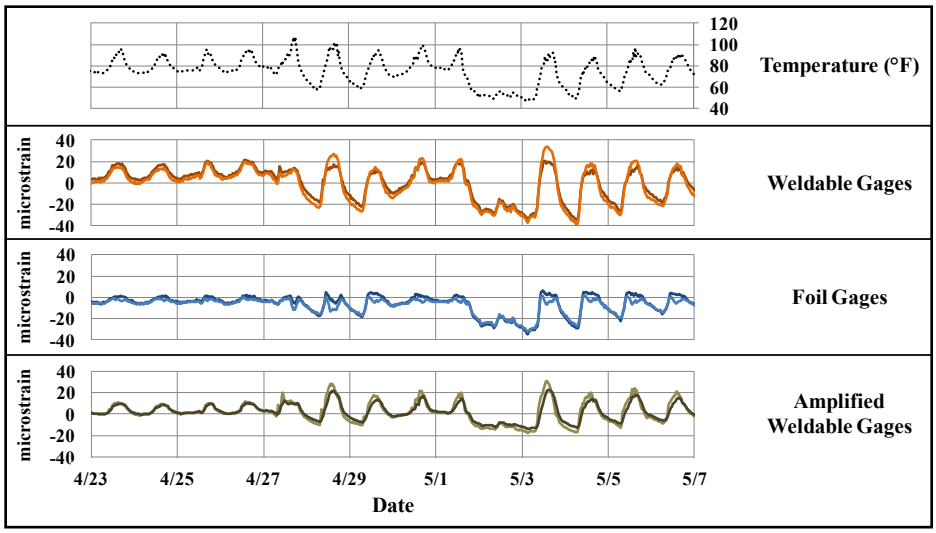

Figure 6-11: Typical thermally-induced strain histories of different gage types

6.2.3. Environmental test results of gages installed on steel bars, exposed to an outdoor environment, and periodically tested in bending

In cases where a gage may potentially be debonding from the structural elements, developing methods of recognizing potential problems with the sensors will provide an important trouble shooting method for engineers overseeing the bridge data. For this reason, a second phase of this testing program was developed and began in February 2012 to better understand how the gage response changes as the sensing system begins to deteriorate and potentially fails, as well as how the gage behavior is influenced by thermal effects. The recorded data of gages with insufficient protection were used to develop guidelines on how an engineer can detect malfunctioning gages.

In early March 2012, one of the bondable foil gages protected with only microcrystalline wax stopped working properly during a storm. As shown in Figure 6-12 the gage readings suddenly exhibited large strains. The reason behind the large strain fluctuations was the presence of moisture around the gage area. The moisture shorted the termination wire blocks of the gage causing the gage resistance to change. The change of

gage resistance was translated by the data acquisition system as a strain drift. A day later, when the gage area dried the strain readings tended to return to the normal levels. However, the presence of moisture below the environmental protection caused the gage to debond, and after that point the gage readings were out of range (Figure 6-12). In this case, the gage deterioration occurred very rapidly and there was not any opportunity to check the gage response during the periodical loading test.

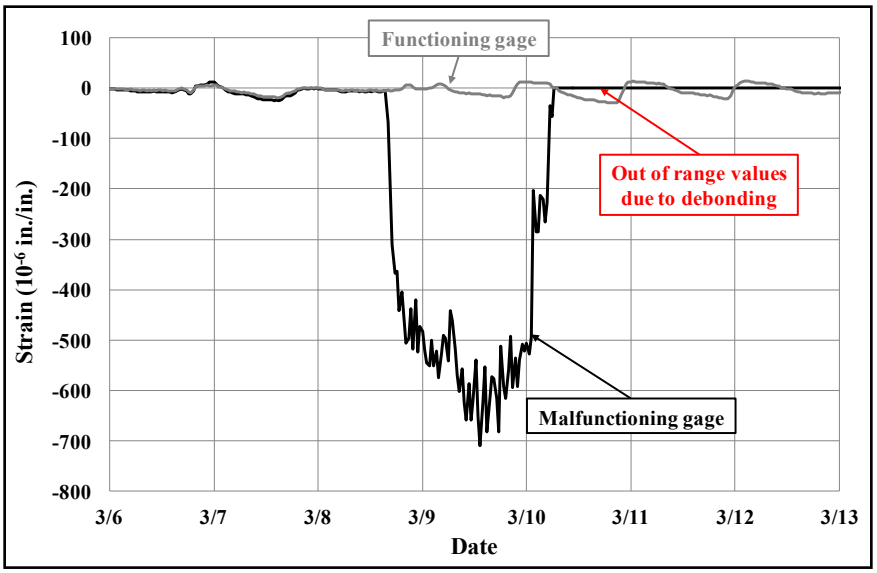

Figure 6-12: Typical gage response when moisture penetrates the protective coating

Over the next months, the performance of several different types of strain gages continued to be monitored. Some of the strain gages on the steel bars located outside Ferguson Structural Engineering Laboratory (FSEL) showed signs of deterioration and recorded large strain values (Figure 6-13). A closer investigation revealed that the large strain values occurred during rainy days when the moisture content was high. An interesting aspect of the performance of these gages was that their strain values returned to normal levels and recorded meaningful data once the gages areas dried sufficiently.

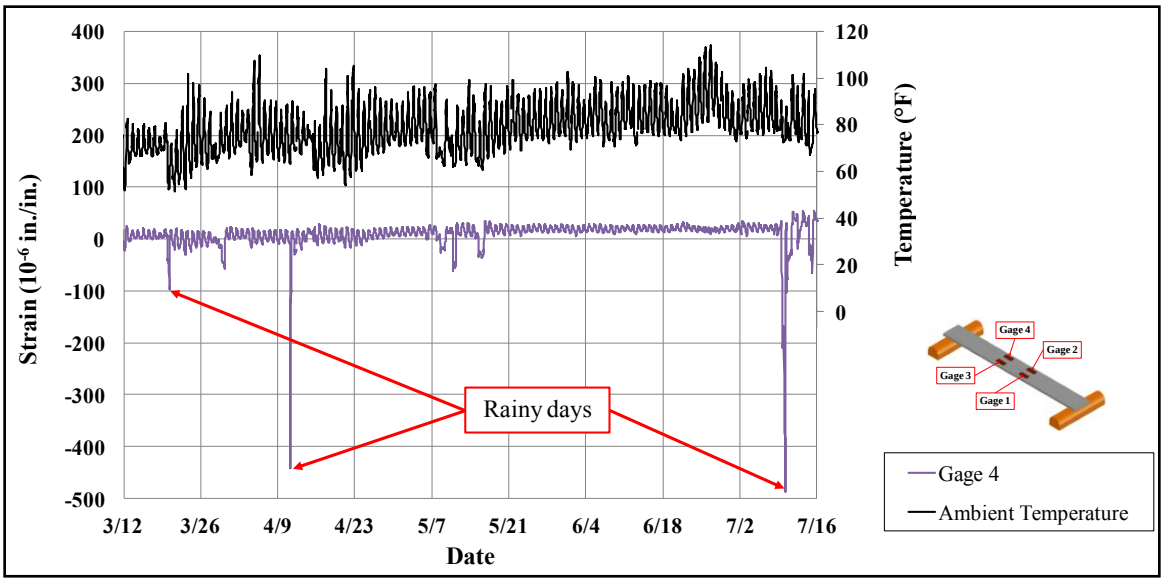

Figure 6-13: Strain history of strain gage on steel bar outside FSEL

In order to replicate this phenomenon, a moisture validation test was conducted. During this test the steel bars (Figure 6-14) were watered using a hose. In order to obtain a more detailed strain history, the gages were monitored at a scanning rate of 30 seconds. The most interesting results were recorded at the steel bar instrumented with bondable foil gages and protective coatings that had a defect at the mid-length of the gage from both sides (Figure 6-15). As previously described, two of the gages were protected with microcrystalline wax and the two-part polysulfide liquid polymer compound, and the other two with butyl rubber sealant, aluminum tape, and contact cement paint.

Figure 6-14: Watering steel bars located outside FSEL

Figure 6-15: Steel bar instrumented with bondable foil gages and defective protective coatings at the mid-length of the gage from both sides

Figure 6-16 shows the results of the steel bar that was affected by moisture. The Gage 4 strain value drifted immediately after direct moisture was applied to the steel bars. Upon completion of the wetting phase, the strain of Gage 4 started to change and generally within a couple hours, the gage area had sufficiently dried so that the readings returned to the same strain level as the other gages. After that point, it was decided to load that particular bar with 35 lb and keep it loaded for one day in order to determine if the four gages functioned properly. All the gages were working properly and were recording an approximately strain of -85 με (Figure 6-16), which was the expected strain

based on the loading. That same evening (7/9/2012) the bars were again subjected to moisture during a rain storm. During that storm the strain value of Gage 4 shifted again down to approximately -1000 με. Once again, when Gage 4 dried, the strain values returned to the same strain level as the other three gages. A day later, the steel bar was unloaded and all the four gages responded correctly to this loading change. Finally, Gage 4 shifted again from 7/10 to 7/11/2012 due to another storm but the readings returned to normal level when everything dried. Similar behavior was observed inside the humidity room from gages that their protective coatings had intentional defects.

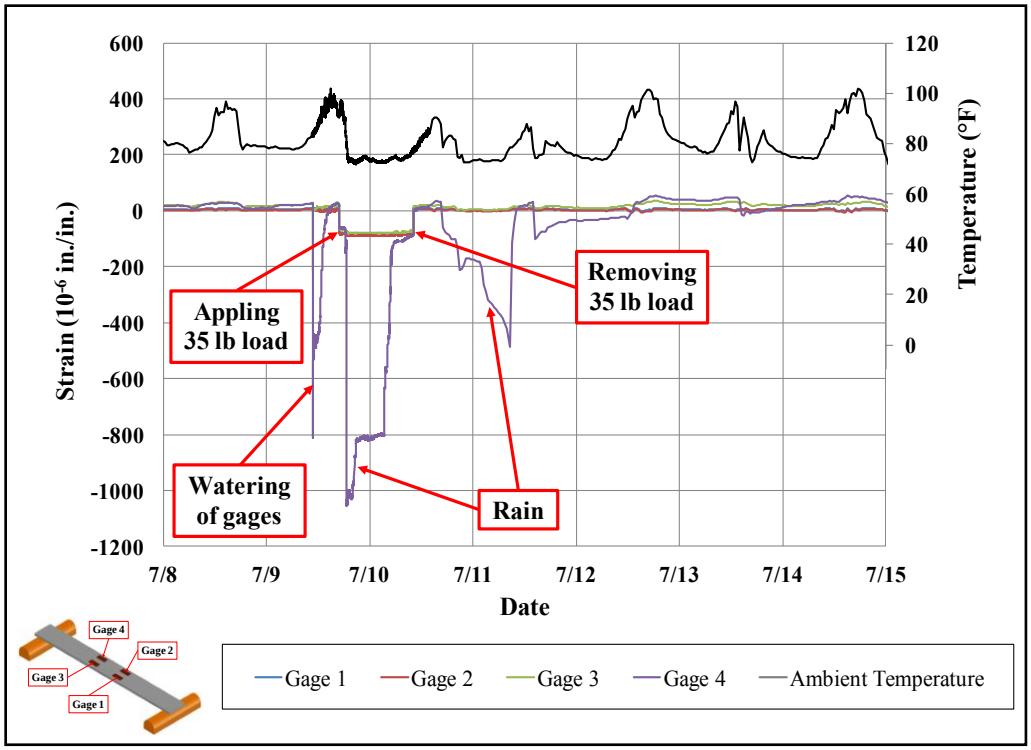

Figure 6-16: Strain history during moisture validation test

In addition, these steel bars were loaded to two different levels with weights of 35 lb and 70 lb, respectively. Figure 6-17 shows the typical loading results of a steel bar.

The data points, which correspond to each loading test, agree reasonably well with the calculated strain level based upon the geometry of the bars. The strain fluctuations of the loaded bars are due to the thermal effects of gages. Moreover, it was observed that the strain values recorded by weldable gages fluctuated more that the bondable foil gages. The thermally-induced strain on bondable foil gages and weldable gages is discussed in a subsequent section.

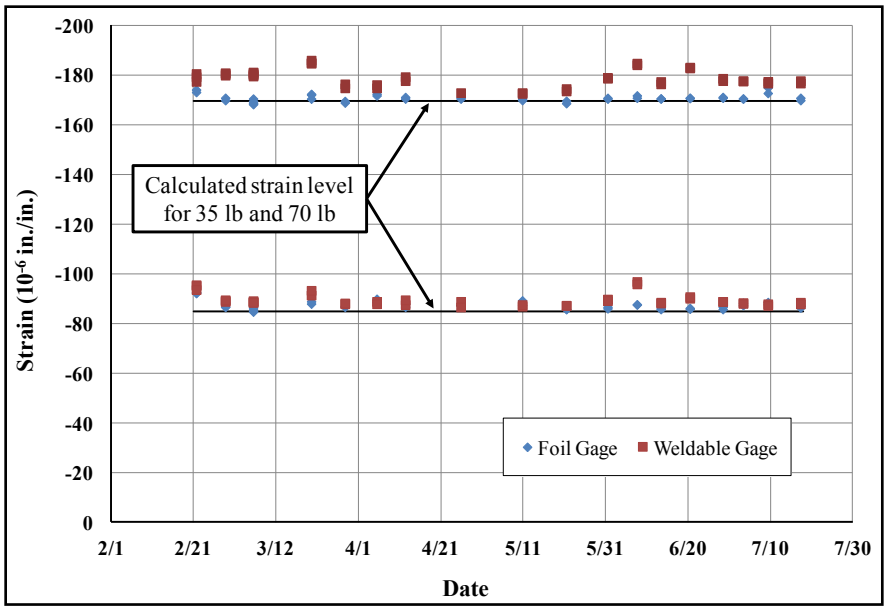

Figure 6-17: Typical loading results of steel bars outside FSEL

The results of these environmental tests support that the strain gage deteriorates very rapidly once the moisture penetrates below the protective coatings. There was no gradual drifting in the strain reading. The malfunctioning gages suddenly started to record large strain fluctuations. In many situations, such a sudden change in the gage readings may necessitate a visit to the bridge by a maintenance crew. In some cases, a decision may be made to simply allow the area to dry and to provide better environmental protection; however in most situations, the large cost will be associated with dispatching

a maintenance crew to the bridge and obtaining traffic control. In these cases, the engineer may decide to simply replace the gage so as to avoid another visit for a subsequent problem with the gages.

6.2.4. Environmental test results of gages installed on unrestrained steel bars, and exposed to controlled temperature environment

The main objective of this test series, which were part of the second testing phase, was the characterization of the thermally-induced strain ($\varepsilon_{err/\Delta T}$) of gages. Thus, steel bars, which could freely expand or contract, were instrumented with bondable foil and weldable gages, and were exposed to controlled environments (e.g. refrigerator and furnace) of temperatures ranging from 35 °F to 140 °F. A thermocouple was installed near the strain gage location to measure the temperature of both the specimen and the gage. There were four steel bars utilized in this test series. All the steel bars were 12 in. long, 2 in. wide, but two of the bars were 1/8 in. thick and the other two steel bars were ½ in. thick. Initially, the response of the gages was monitored at constant temperature levels (40 °F, 60 °F etc.) by placing the bars inside a refrigerator or a furnace as shown in Figure 6-18.

Figure 6-19 illustrates the recorded strain levels of the bondable foil gages and weldable gages at constant temperatures. Based on these data, it can be observed that the thermally-induced strain of bondable foil gages and weldable gage remains constant while the temperature remains constant. The strain fluctuation is 70 με for the foil gages and 100 με weldable gages when the temperature changes from 40 °F to 140 °F.

Figure 6-18: Steel bar placed inside a MTS furnace

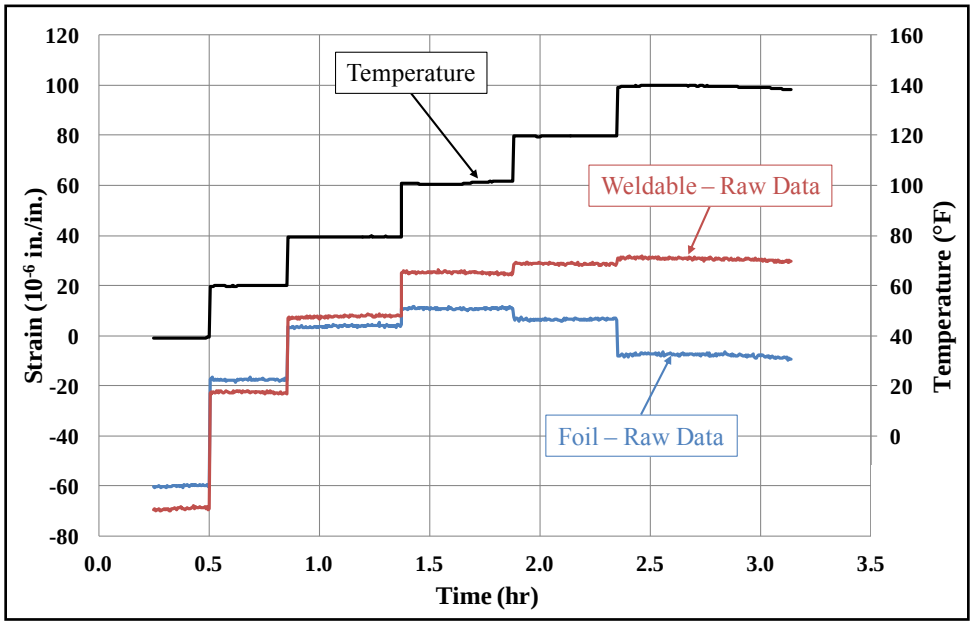

Figure 6-19: Response of foil and weldable at constant temperature levels

The second part of this test was to investigate the effect of that rate of heating on the gage response. For this reason, all the bars were first placed inside a refrigerator and

cooled to 35 °F. Once the desired temperature was reached, the steel bars were removed from the refrigerator and placed inside a cooler with ice. The cooler lid was left opened with different gaps to achieve the appropriate heating rate. Later, the bars were placed inside a MTS furnace (Figure 6-18) and heated to 140 °F with the same heating rates as the ones achieved before (i.e. refrigerator and cooler).

Figure 6-20 and Figure 6-21 illustrate the strain fluctuation of the bondable foil and weldable gages as the temperature changed. Theoretically, the recorded strain should have been zero for any temperature level since the bars could freely expand or contract. Yet, the gages recorded the thermally-induced strain. Based on Figure 6-20 and Figure 6-21, it can be observed that while there some relatively small differences in the recorded strains, the heating rate did not have a significant impact on the strains recorded for heating rates of 5 °F/hr, 20 °F/hr, and 60 °F/hr. The same basic behavior was observed for both foil and weldable gages. The data did show that there were larger strains recorded as a function temperature for the weldable gages compared to the foil bondable gages for the same temperature range. It should be noted going from 35 °F to 140 °F; the thermally-induced strain of bondable foil gages and weldable gage is 80 με and 110 με, respectively.

During this tests series, the size effect on the strain response was investigated. As it was mentioned above, the steel bars had different thicknesses (1/8 in. vs. ½ in.). Based on the data collected from this test, it was concluded that this difference in plate thickness did not exhibit a significant size effect with regard to the influence on the strain response. To enhance this finding, three steel plates with thickness of 1 in., 2 in., and 3 in. respectively were instrumented with bondable foil gages and weldable gages. These steel plate thicknesses are representative of the values of the flange thickness that are frequently used in bridge design. Figure 6-22 demonstrates the influence of steel plate

thickness on the surface temperature, as well on foil and weldable gage readings. As shown in Figure 6-22a, the temperature of the specimen surface remains almost constant regardless of the location (i.e. top vs. bottom surface) and it is independent of the plate thickness. The only deviation of temperature trends occurs when the steel specimen is cooling down. In this case, the temperature at the bottom surface of thicker plates (i.e. 3 in. and 2 in.) decreases at a lower rate compared to the top of the plate. On the other hand, the thickness of steel plates has a minor influence on the strain response as shown in Figure 6-22b and Figure 6-22c. The strain readings from both gage types are very similar for all the specimen locations and thicknesses. The strain recordings slightly fluctuated during the cooling phase of the specimen. During the cooling phase, the maximum strain range of the foil and weldable gages is 7 με and 11 με, respectively.

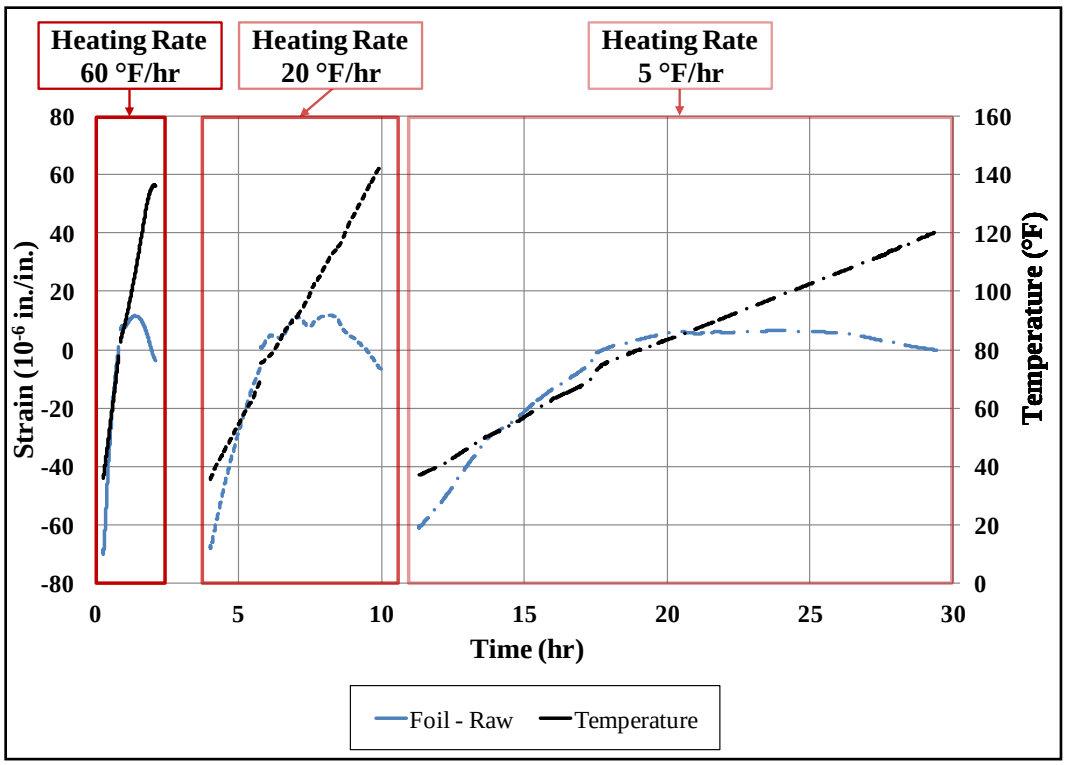

Figure 6-20: Bondable foil gage response at different heating rates

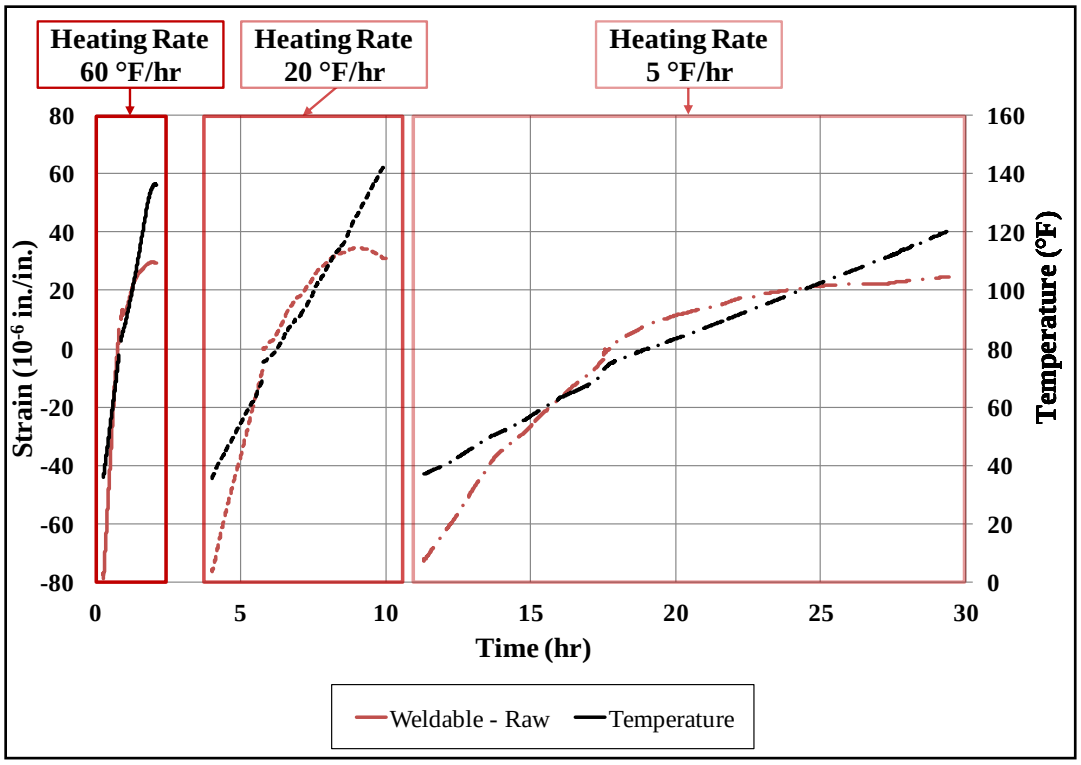

Figure 6-21: Weldable gage response at different heating rates

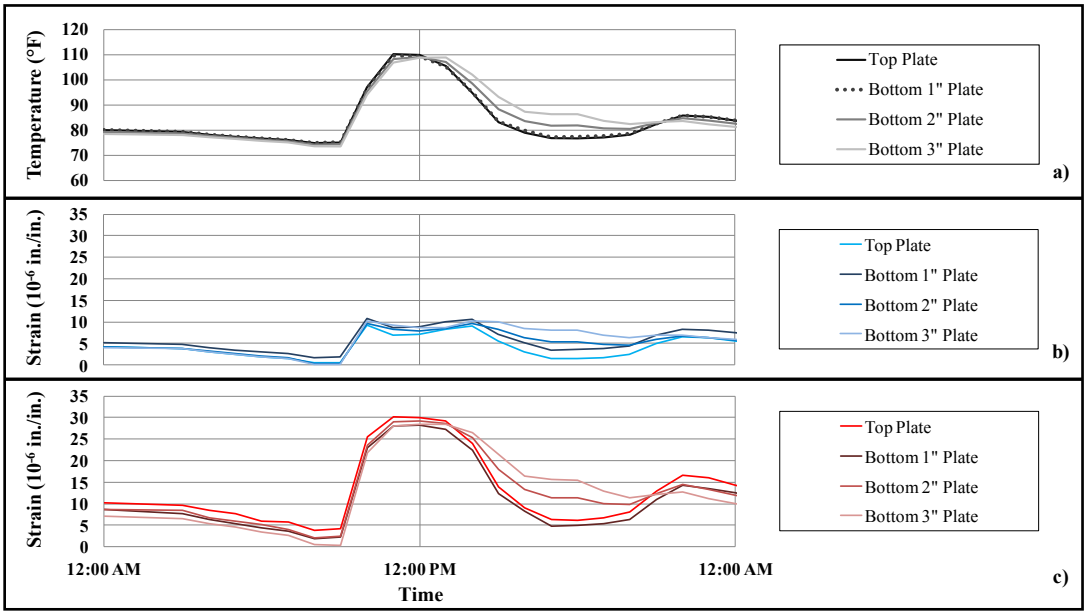

Figure 6-22: Influence of steel plate thickness on a) surface temperature, b) foil gage uncorrected data, and c) weldable gage uncorrected data

6.2.5. Environmental test results of gages installed on steel bars, exposed to an outdoor environment, and loaded in bending about the strong or weak axis of the bar

The main objective of this test series was to investigate the influence of member orientation (i.e. steel bar lying flat or placed vertical to the side), and loading conditions (i.e. unloaded or loaded with 35 lb) on thermally-induced strain was investigated. First, the steel bar was placed in two different configurations (i.e. flat and on its side). Figure 6-23 shows the trends of thermally-induced strains obtained from the unloaded steel bar for both orientations. For temperatures ranging from 25 °F to 130 °F, the thermally-induced strains recorded by the gages were approximately 80 με (foil gages) and 145 με (weldable gages). Thermally-induced strain in foil gages reduces for temperatures above 100 °F. This is due to the nature of the foil strain gage and the thermal properties of constantan, which is the alloy that the foil gage is made of. This strain gage alloy is processed in such a way to minimize the thermally-induced strain over a wide temperature range (50 °F - 100 °F) and as a result the foil gage is self-compensated for that temperature range. Figure 6-24 demonstrates the typical thermal output of constantan alloy foil gages. This graph is provided by the gage supplier (Vishay Micro-Measurements Group, Inc., 2012). For a temperature range from 50 °F to 100 °F, the thermally-induced strain curve of the self-compensated gage is almost flat and the slope of the curve starts to significantly decrease for temperatures below 50 °F and above 100 °F. In contrast, the thermally-induced strain of weldable gage increases very rapidly for temperatures between 20 °F and 80 °F. Above 80 °F, the increase rate is getting smaller and the thermally-induced strain remains almost constant for temperatures greater than 110 °F.

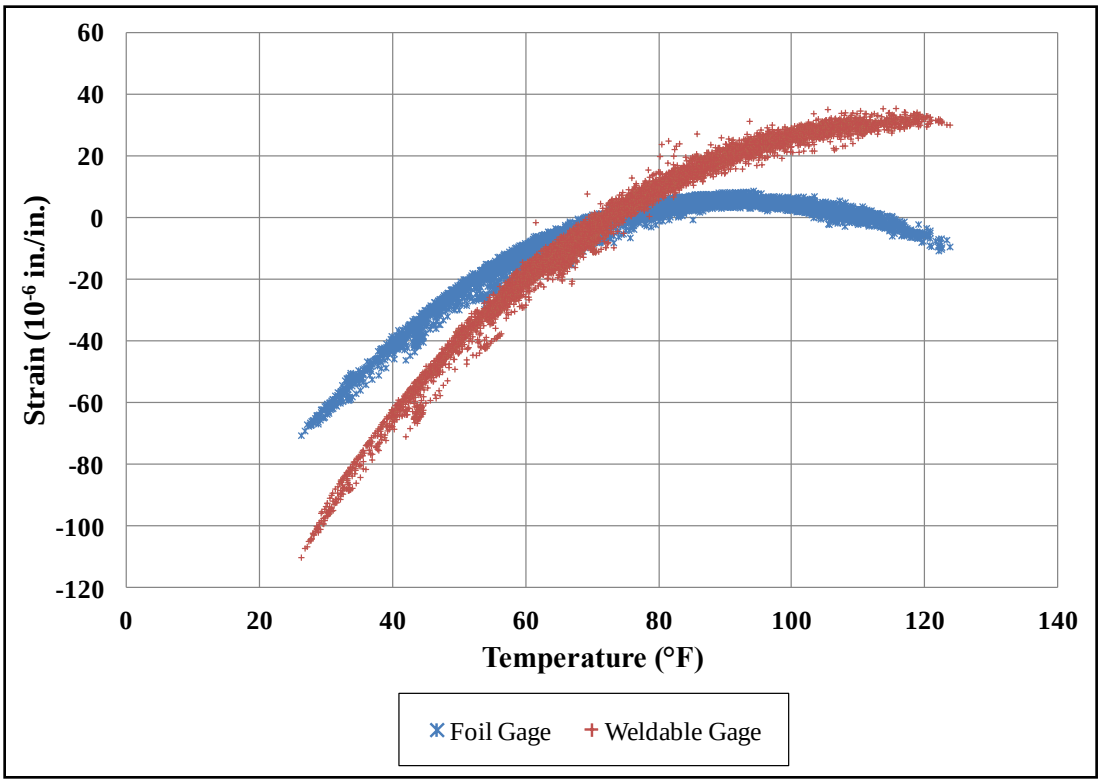

Figure 6-23: Accumulated strain history of gages from steel bar outside FSEL

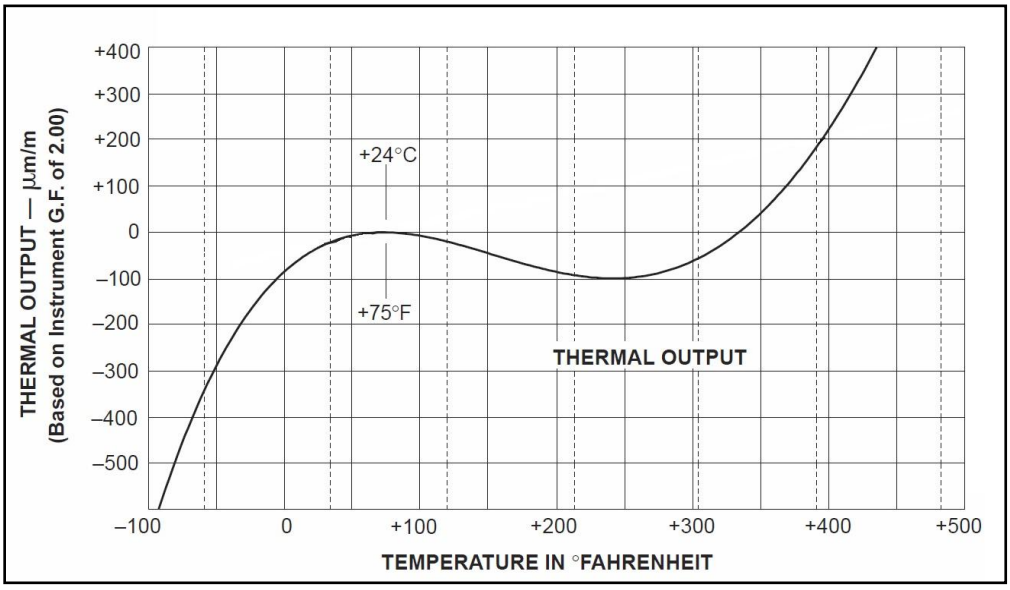

Figure 6-24: Typical thermal output of self-compensated constantan (A-alloy) foil strain gage with temperature (Vishay Micro-Measurements Group, Inc., 2012)

The next step was to continuously load the steel specimen in both configurations with 35 lb. It was found that the strain reading of the loaded steel bar for both orientations varied by almost 17 με (foil gages) and 50 με (weldable gages) for temperature varying from 68 °F to 130 °F. This case study demonstrated that the influence of temperature to thermally-induced strain is not affected by the orientation or the loading condition of the instrumented steel member.

6.2.6. Environmental test results of gages installed on test-boxes, and exposed to controlled conditions inside a humidity room

Similarly to the gages on the steel test-boxes located outside FSEL (Section 6.2.1), the gages in the humidity room were continuously monitored from the period July 2010 through June 2013. The first few weeks of this long-term environmental test, all the strain gages recorded very small strain fluctuations. This was an expected response since the gages were located inside an environment of a nearly constant temperature (64°F). However, the following weeks the strain readings from many gages started to drift significantly (Figure 6-25), and it was originally believed that the gages started to deteriorate. Despite the fact that the strain gages were exhibiting large drifts, their response continued to be monitored for the next two months (September - October 2010) to obtain significant information about the behavior of deteriorating gages. In October 2010, an autopsy was performed to determine the cause of drifting of the strain readings. Yet, there was no sign of deterioration or debonding at any gage. After a closer examination, it was discovered that the pins of the serial connectors, which were utilized to splice the cables connecting the strain gages to the data logger, had started to corrode. To protect the serial connectors from moisture and prevent corrosion of the pins, plastic shrink wrap was added around them. This solution did not improve the performance of the system because the next two months (November – December 2010) the strain

readings did not stabilize, and large strain drifts continued to occur in the data (Figure 6-25). Finally, the strain readings stabilized only when the serial connectors were removed and the gages were directly connected to the data acquisition system through continuous cables. This demonstrated that particular attention needs to also be paid to any of the sensor connections as well as the sensors themselves so as to obtain reliable data.

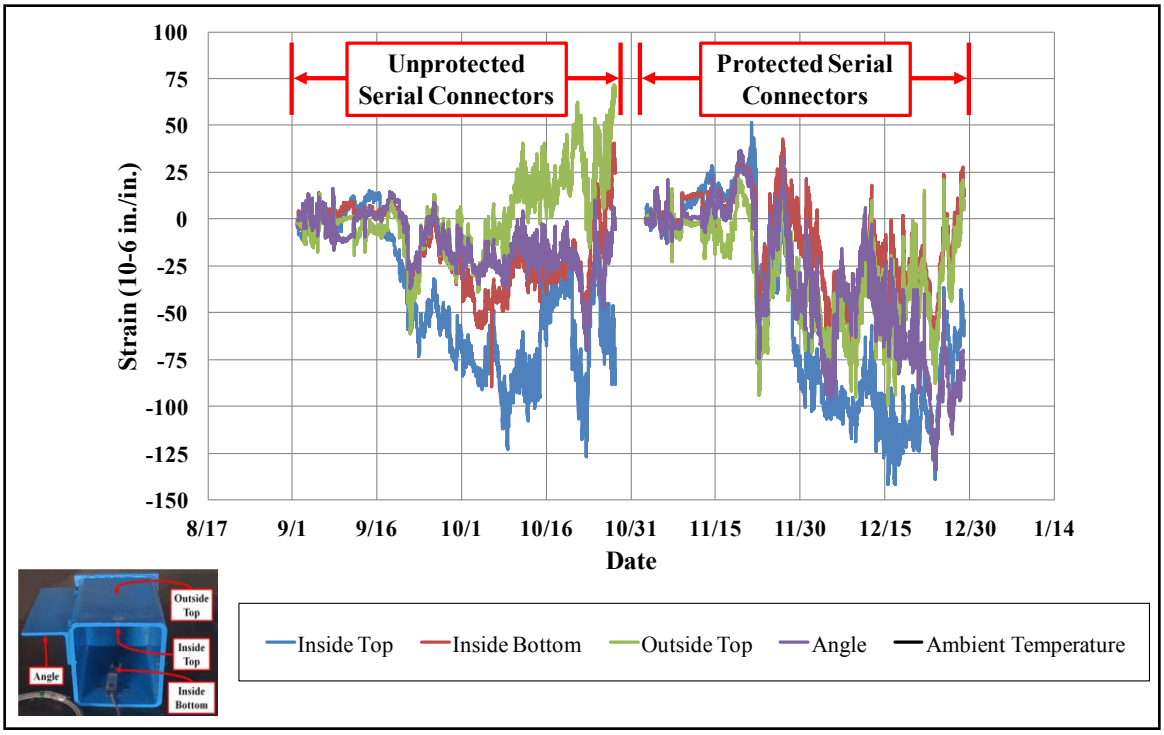

Figure 6-25: Typical strain drifting due to corroded serial connectors

After 8 months (July 2010 - March 2011) since the beginning of the humidity room test, the readings from the following types of gages showed signs of deterioration:

- HBW-W
- HBW-B
- HBP-B
- LEA-R
- LEA-L

As in the case of the test-boxes outside FSEL, the moisture that penetrated into the environmental protection was the main factor for the drifting in the strain readings. More specifically, the sealed weldable gages (HBW-W, LEA-R, and LEA-L) had the same failure mechanism, which was debonding of the sealed gage from the steel shim (Figure 6-3). The bondable sealed gages (HBW-B, HBP-B) failed due to corrosion development between the gage and the shim that lead to the debonding of the entire gage (Figure 6-4). As with the gages outside FSEL, the adhesive that was used to install the bondable sealed gages (HBW-B, HBP-B) was not durable against humidity. It was also concluded that the rubber patch alone was not a durable protective coating and it should be avoided to be used as a protective system in long-term monitoring applications. After the failure mechanisms of the gages were determined, the damaged gages were replaced.

In early June 2011 the bondable foil gage (CEA-C), which was installed on the inside bottom surface of the steel test-box, exhibited signs of deterioration. Once the protective coating of silicone was removed, it was possible to feel the moisture that had penetrated through the silicone and wax coatings. Moreover, the presence of moisture introduced corrosion between the steel surface and the gage (Figure 6-26). The existence of moisture and corrosion below the protective coating was the main reason of debonding.

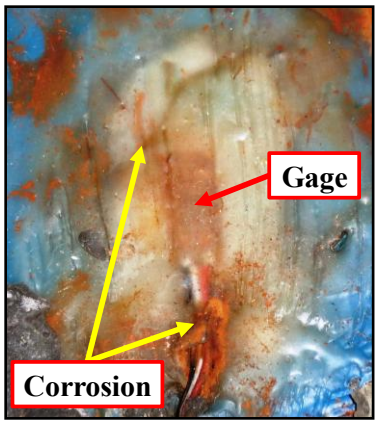

Figure 6-26: Corrosion below protective coatings of bondable foil gage (CEA-C)

After 13 months from the start of the humidity room test (July 2010 - August 2011), three amplified weldable strain gages (HBWF-AMP) exhibited a distorted response. The damaged gages were attached on the inside top and bottom surface, as well as the outside top face of the steel test-box. The examination of the damaged gages revealed that the amplified weldable gages failed in a similar fashion as the weldable sealed gages, which was the debonding of the sealed gage from the steel shim due to moisture penetration. Table 6-2 summarizes observations from the durability tests (i.e. types of damaged gages, location of failure, and failure mechanism) from March to August 2011.

Table 6-2: Summary of damaged gages inside humidity room

Damaged Gage		Failure location	Reason of failure
Weldable gage HBW-W		Inside Top	Debonding of the sealed gage from steel shim due to moisture penetration
Weldable gage LEA-R		Inside Top	Debonding of the sealed gage from steel shim due to moisture penetration
Weldable gage LEA-L		All locations	Debonding of the sealed gage from steel shim due to moisture penetration
Bondable sealed gage HBW-B		Inside Top Outside Top	Debonding of the gage from specimen due to corrosion
Bondable sealed gage HBP-B		Inside Bottom Angle	Debonding of the gage from specimen due to corrosion
Foil gage CEA-C	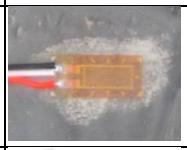	Outside Top	Debonding of the gage from specimen due to corrosion
Amplified weldable gage HBWF-AMP		Inside Top Inside Bottom Outside Top	Debonding of the sealed gage from steel shim due to moisture penetration

The results from this durability test support the findings of the long-term investigation of gages exposed to an outdoor environment. Once again, it was concluded that the bondable foil gage (CEA-J) exhibited the best overall performance. This type of gage did not experience any kind of deterioration in a humidity room, which is a relatively harsh environment compared to what the gages are likely to see in practice. Moreover, the weldable gages (HBW-W, LEA-R, and LEA-L) combined with the improved environmental protection showed very satisfactory results. Therefore, based

upon the results of this exposure test, it is recommended to employ the following two sensors for long-term applications:

1. Bondable foil gages (CEA-J) protected with microcrystalline wax and a heavy duty two-part polysulfide liquid polymer (PLP) compound (i.e. Protection Scheme 2).
2. Weldable gages (HBW-W, LEA-R, and LEA-L) protected with butyl rubber sealant, aluminum tape, and contact cement paint (i.e. Protection Scheme 1).

6.2.7. Environmental test results of gages installed on steel bars and exposed to controlled conditions inside a humidity room

The durability tests on the steel bars in the humidity room were initiated in April 2012. There were two main objectives:

1) Evaluate the behavior of the bondable foil gage (CEA-J) and the weldable strain gage (HBW-W and LEA-R), and

2) Determine the influence of defects on strain readings.

The durability tests also provided an opportunity to examine the durability of the prototypes of the IP enclosures that were manufactured for the WSN strain nodes in an aggressive environment from a moisture perspective.

This test series were developed as part of the second testing phase. In this series of tests, bondable and weldable gages were installed on bars with defects introduced into the protective coatings as outlined in Chapter 5. The gages quickly exhibited large strain fluctuations each time the steel specimens were inside the humidity room as shown in Figure 6-27. The cause of the unstable strain readings was the moisture that had reached the gage region through the defects. This argument was supported by the fact that all the strain readings stabilized (Figure 6-27) when the specimens were placed in the indoor room environment with low humidity. Similar behavior was observed during rainy days

by gages installed on steel bars located outside FSEL that had intentional defects on their protective coatings (Figure 6-13).

Finally, the reliability of the WSN strain node during this durability was excellent. The WSN strain node was able to record strain values properly under extreme conditions of the humidity room. In addition, the environmental enclosure sufficiently protected the WSN strain node against humidity, and there was no sign of moisture condensation inside the enclosure.

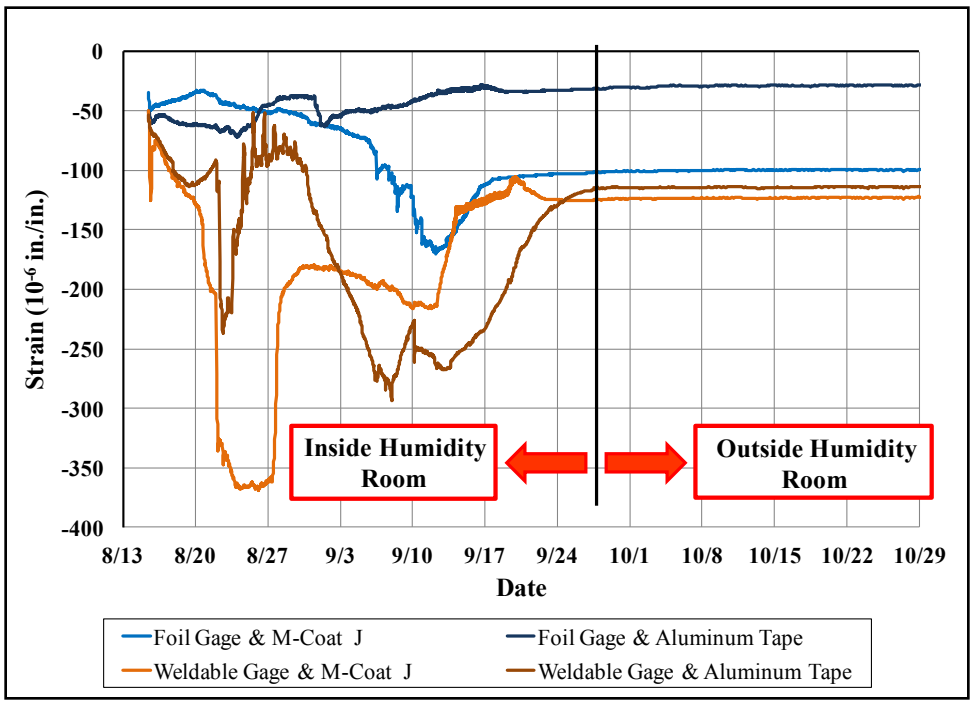

Figure 6-27: Response inside and outside the humidity room of gages with protective coatings that contained a defect

6.3. FATIGUE TEST RESULTS OF STRAIN GAGES

Due to the relatively large truck loads on bridges, fatigue is a major concern. The fatigue damage can accumulate in certain locations of a structure where a crack has initiated due to defects in the base metal or the welds. The impact of the cyclic loading on

the performance of strain gages that might be used in bridge instrumentation were of interest in the long-term performance of sensors used in structural health monitoring applications. There were generally two main concerns to be studied: 1) the impact of cyclic loading on the performance of bondable gages, and 2) the impact of cyclic loading on the performance of weldable gages. In the case of weldable gages, concerns exist about crack initiation as a result of the small spot welds as well as fatigue in the shim of the sensor itself.

Fatigue tests were performed to determine the impact of bondable and weldable gages on the fatigue life of the steel specimen. As part of this investigation, six steel coupons were tested under cyclic loads producing a stress range of 35 ksi. Each coupon had two pairs of gages installed on opposite sides of the specimen. The first two coupons were instrumented with pairs of amplified weldable gages (HBWF-AMP) and weldable gages (HBW-W). The second pair of coupons was instrumented using weldable gages (LEA-L and LEA-R) from a different supplier. The last pair of tensile coupons was instrumented with sealed bondable gages (HBW-B) and bondable foil gages (CEA-C).

The fatigue tests revealed that spot welds can initiate cracks in the steel specimen. The first pair of coupons failed after approximately 650,000 cycles. The failure occurred due to crack initiation at the spot welds (Figure 6-28). The second pair of coupons failed at approximately 750,000 cycles, and the failure mechanism was similar as above (Figure 6-29). Although fatigue cracks did develop in the spot welds, it should be noted that the stress range used in the tests were relatively high and the resulting fatigue category was a Category A fatigue detail, which is the same fatigue detail as if base metal piece did not have any weldable gages installed. Last, the third pair of specimens did not experience any sign of failure and the fatigue tests stopped after almost 6.5 million cycles. As expected, the bondable gages did not initiate any fatigue cracks in the base metal.

Nevertheless, it was found that the HBW-B gage did not function properly after 6.5 million cycles and during the uniaxial loading tests it recorded a lower strain level than the expected (Figure 6-30). The reason of this poor response was the debonding of the gage from the steel specimen. Table 6-3 tabularizes the results from the fatigue tests.

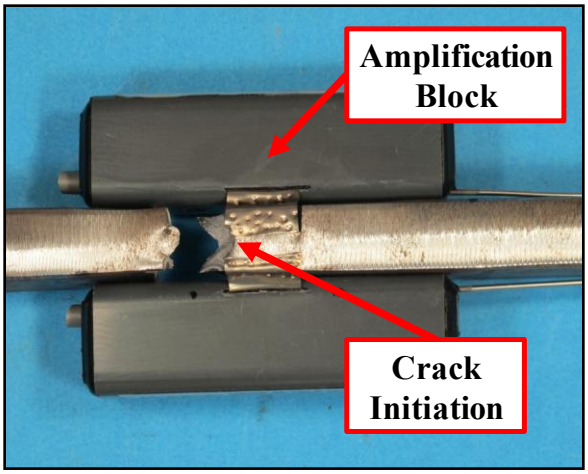

Figure 6-28: Typical fatigue failure of steel coupon with weldable gage (HBWF-AMP)

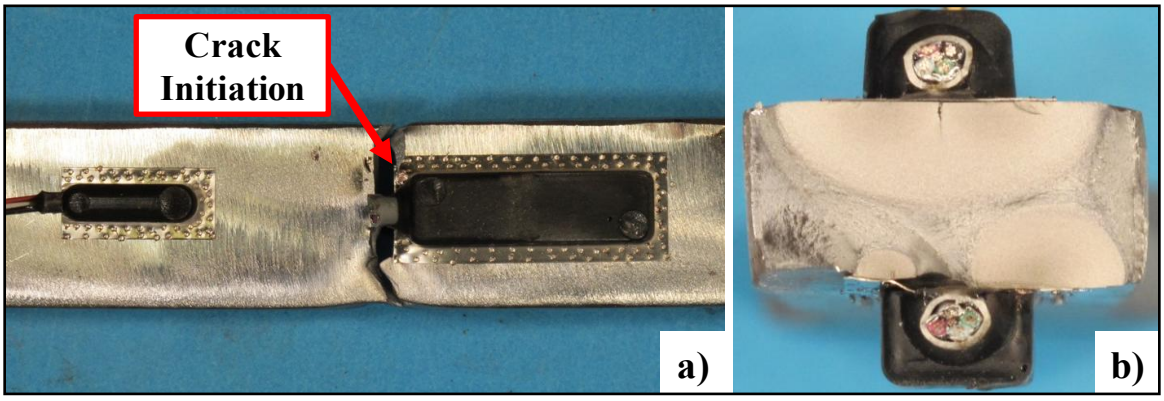

Figure 6-29: Typical fatigue failure for weldable gages (LEA-L, LEA-R), a) plan view, b) cross-section

Table 6-3: Summary of the fatigue tests

Coupon #	Gage	Number of cycles	Result
1, 2	Weldable gage (HBWF-AMP) 	653,138 (1) 651,093 (2)	Failed
	Weldable gage (HBW-W) 		
3, 4	Weldable gage (LEA-L) 	756,274 (3) 753,502 (4)	Failed
	Weldable gage (LEA-R) 		
5, 6	Bondable gage (HBW-B) 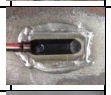	$6.5 \cdot 10^6$ (5, 6)	No failure
	Foil gage (CEA-C) 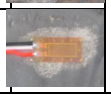		

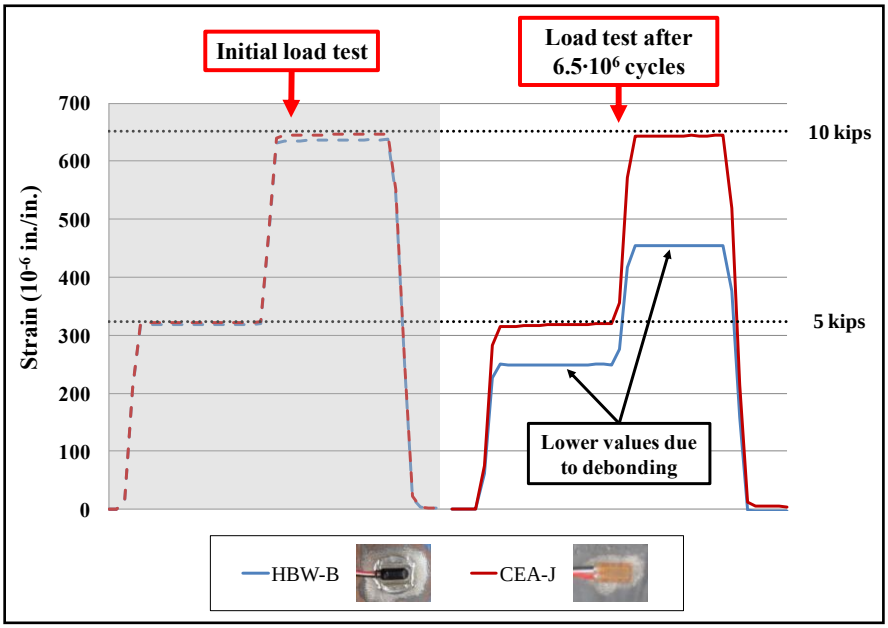

Figure 6-30: Loading results of bondable gages before and after the fatigue test

6.4. STRAIN CORRECTION PROCEDURE

In most field instrumentation applications, the desired data to be gathered are related to gravity or lateral load induced stresses. However, in addition to the direct force-

induced strains, additional strains will be induced due to changes in the thermal environment. Because the structural materials will expand and contract with the changes in the thermal conditions, strains will be induced into the structure and many cases these strains can introduce error into the field data. The accumulation of these errors over time can produce misleading results. The influence of temperature changes on strain gage measurements are often the most significant error associated with field instrumentation. Once an installed strain gage is connected to a data acquisition system, a subsequent change in the ambient temperature produces a thermally-induced strain. Depending on the boundary conditions of the structure, changes in the thermal environment can lead to real stress induced into the members as a result of potential constraints that restrict the thermal movements. In cases where the structure is free to expand or contract due to changes in the thermal characteristics, the strains do not correspond to induced stress in the members. Due to the complexities associated with thermally-induced strains, careful consideration is required to correct the gage measurements for potential errors that may develop, depending on the type of gage that is utilized.

Typically, the recorded strain in every environment consists of essentially two components as shown in Equation 4-1. The first component of the recorded strain (ε_{Total}) is the stress-induced strain (ε_{σ}) developed in the instrumented component due to external forces, thermal gradients, or a combination of both. The second component is the thermally-induced strain ($\varepsilon_{err/\Delta T}$), which is caused by temperature effects.

$$\varepsilon_{Total} = \varepsilon_{\sigma} + \varepsilon_{err/\Delta T} \qquad \textbf{Equation 6-1}$$

where:

ε_{Total} : total strain recorded by the gage.

ε_{σ} : stress-induced strain.

$\varepsilon_{err/\Delta T}$: thermally-induced strain.

Thermally-induced strain ($\varepsilon_{err/\Delta T}$) is caused by two concurrent factors (Equation 6-2). The first factor is a "virtual" strain, which is equal to $\left(\frac{\beta_G}{GF} \cdot \Delta T\right)$, caused by the resistivity change of the active grid alloy with temperature. β_G is the temperature coefficient of resistance of the grid conductor, and *GF* is the gage factor. The second effect causing the thermally-induced strain is the differential expansion between the specimen and the gage. This differential expansion happens due to differences in the thermal expansion coefficients of the sensor and the instrumented material as was demonstrated previously in Figure 5-1. When the ambient temperature of the structure change, the specimen and the gage expand or contract, but their relative deformations are not the same. Since the connection between the gage and the base material is relatively rigid, the gage is forced to undergo essentially the same deformation as the structural element. Thus, the differential deformation that the strain gage has to undergo to satisfy the compatibility requirements is recorded as a resistance change across the two wire terminal blocks of the gage. The differential strain is given in Equation 6-3.

Other less significant errors, namely gage-factor variation with temperature, Wheatstone-bridge nonlinearity, and transverse sensitivity, exist in the thermally-induced strain. However, these changes are relatively small and for the scope of this research, these errors were neglected. Information on how to correct these errors has been previously published in the literature (Vishay Micro-Measurements Group, Inc., 2010 & 2012).

$$\varepsilon_{err/\Delta T} = \left(\frac{\beta_G}{GF} \cdot \Delta T\right) + \varepsilon_{err/\alpha} \qquad \textbf{Equation 6-2}$$

where:

$\varepsilon_{err/\Delta T}$: thermally-induced strain.

β_G : temperature coefficient of resistance of the grid conductor.

GF : gage factor.

$\varepsilon_{err/\alpha}$: strain error due to different thermal expansion coefficients of specimen and gage.

$$\varepsilon_{err/\alpha} = (\alpha_s - \alpha_g) \cdot \Delta T \qquad \textbf{Equation 6-3}$$

where:

$\varepsilon_{err/\alpha}$: strain error due to different thermal expansion coefficients of specimen and gage.

α_s : thermal expansion coefficient of steel.

α_g : thermal expansion coefficient of gage.

ΔT : temperature difference.

An engineer needs the thermal expansion coefficients of steel (α_s) and gage (α_g) to compute the strain error $\varepsilon_{err/\alpha}$, and therefore to calculate the thermally-induced strain ($\varepsilon_{err/\Delta T}$). Based on Eurocode 3 (European Committee for Standardization (2005), Eq. 3.1a) the thermal elongation of steel ($\Delta l/l$) for temperature between 20 °C (68 °F) and 750 °C (1382 °F) is given in Equation 6-4:

$$\frac{\Delta l}{l} = 1.2 \cdot 10^{-5} \cdot T + 0.4 \cdot 10^{-8} \cdot T^2 - 2.416 \cdot 10^{-4} \qquad \textbf{Equation 6-4}$$

where:

l : length of steel member at 20 °C (68 °F).

Δl : temperature induced elongation.

T : temperature of steel member in °C.

The coefficient of thermal expansion of steel (α_s) as a function of temperature can be calculated by taking the first derivative of Equation 6-4 with respect to T. The relationship between thermal expansion coefficient (α_s) and temperature is shown in Equation 6-5:

$$\alpha_s = 1.2 \cdot 10^{-5} + 0.8 \cdot 10^{-8} \cdot T \qquad \textbf{Equation 6-5}$$

where:

α_s : coefficient of thermal expansion of steel 1/°C.

T : temperature of steel member in °C.

Equation 6-5 can be easily modified to obtain a relationship between the thermal expansion coefficient (α_s) and the temperature in °F. Equation 6-6 can be used to calculate α_s for temperature in °F:

$$\alpha_s = 6.59 \cdot 10^{-6} + 0.25 \cdot 10^{-8} \cdot \mathrm{T} \qquad \textbf{Equation 6-6}$$

where:

α_s : coefficient of thermal expansion of steel 1/°F.

T : temperature of steel member in °F.

The challenging aspect of the problem is obtaining an estimate of the gage coefficient of thermal expansion. Typically, vendors do not provide information about the expansion coefficient of gages. Gages are manufactured from special alloys that, theoretically, have the same coefficient of thermal expansion as steel. However, in reality the expansion coefficients of steel and the gage are slightly different.

All the results from the environmental tests described above verify that thermally-induced strain exists at any temperature level. Hence, all strain data must be corrected for

thermally-induced strain. There are several methods to compensate for thermally-induced strain. Thermally-induced strain can be corrected by utilizing a "dummy" gage, which is a gage installed to an unstrained/unrestrained specimen. The plate material that the dummy gage is installed on should be similar to the plate material that the active gage is installed on. Since the "dummy" and "active" gages are subjected to the same temperature fluctuations, then thermally-induced strain can be eliminated from the strain readings. That can be achieved by subtracting the strain values of the "dummy" gage from the "active" gage. Moreover, thermally-induced strain can be minimized by self-compensation of gages. The self-compensated strain gages are manufactured from special alloys (e.g. constantan) so that the thermal expansion coefficient of the gage matches that of the material under investigation.

The correction technique of the "dummy" gage cannot always eliminate the problem because it is very difficult to maintain an identical thermal environment between one "dummy" gage and several "active" gages distributed along the length and the width of the structure. Using several "dummy" gages increases the instrumentation cost, and defeats the purpose of having a simple and practical monitoring system. On the other hand, self-compensated gages can minimize the thermally-induced strain but only over a limited temperature range. Thus, for long-term monitoring applications it is always necessary to correct the gage output for thermally-induced strain.

One of the goals of this research program was to develop guidelines on how to correct the strain readings and account for the effect of the thermally-induced strain. The following two sections describe methods to correct thermally-induced strain in foil and weldable gages.

6.4.1. Correction method of thermally-induced strain in bondable foil gages

During the gage reliability testing program, it was realized that the most accurate technique to correct the thermally-induced strain in bondable foil gages is to utilize the correction formula provided by the strain gage suppliers. The correction formula (Equation 6-7) is an empirical fourth-order polynomial equation and it relates thermally-induced strain ($\varepsilon_{err/\Delta T}$) and temperature ($T$). The thermal coefficient factors (i.e. A_1, A_2...) are provided by the vendor on the gage package data label and are unique for each strain gage lot.

$$\varepsilon_{err/\Delta T} = A_1 + A_2 \cdot T + A_3 \cdot T^2 + A_4 \cdot T^3 + A_5 \cdot T^4 \qquad \textbf{Equation 6-7}$$

where:

$\varepsilon_{err/\Delta T}$: thermally-induced strain.

A_i : gage thermal coefficients factors.

T : temperature of steel member in °F.

This correction method is based on the thermal material behavior of the gage alloy. For long-term structural monitoring applications, the engineer should program the data acquisition system to subtract the thermally-induced strain computed by Equation 6-7 from the gage output strain. It should be noted that the correction formula produces the best results when the installed gages are balanced for zero strain at 75 °F. If the gages are zeroed at another temperature, then the output strain difference between the instrumented temperature and 75 °F must be subtracted from all the strain data.

This correction method was first used to eliminate the thermally-induced strain from the response of foil gages during the controlled temperature tests. Figure 6-31 demonstrates the response of foil gages at constant temperature levels. The corrected strain values are limited within a range of 8 με, proving that the empirical equation given

by the gage vendor produces very good results. Figure 6-32 shows the raw and corrected strain readings of foil gages exposed to different heating rates. In this case the correction technique does not produce as good result as in the previous case (i.e. foil gages exposed to constant temperatures), but it improves the output signal by 84%. For a temperature rise from 35 °F to 140 °F, the raw strain readings fluctuation is 80 με, while the corrected data fluctuate from -5 με to 7 με.

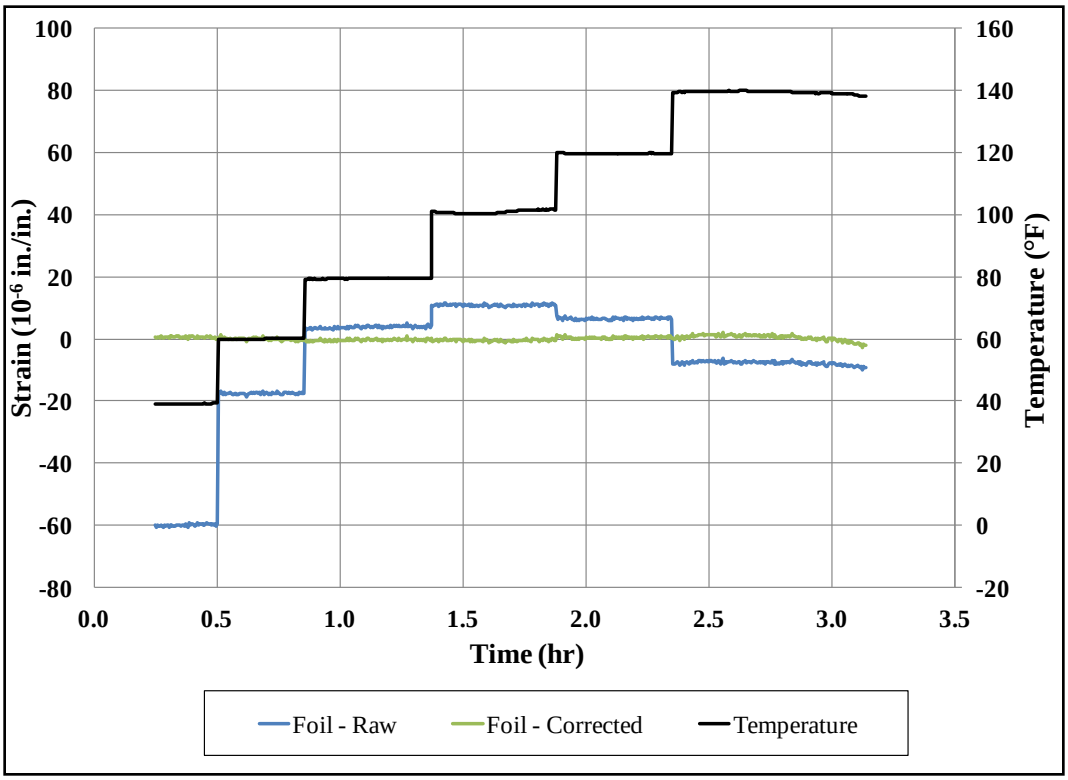

Figure 6-31: Corrected response of foil gage at constant temperature levels

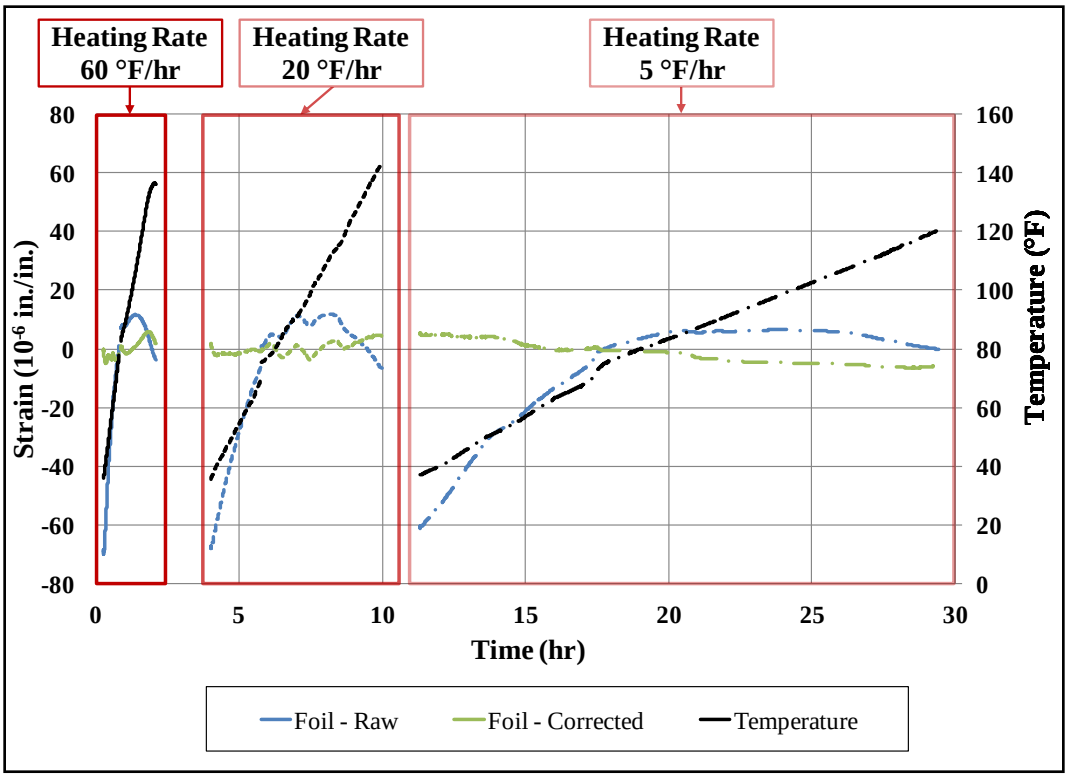

Figure 6-32: Correction of foil gage response at different heating rates

Besides the controlled tests, the recommended correction method was verified against data obtained from foil gages installed in steel bars outside FSEL. The thermally-induced strain (Equation 6-7) of the foil gages installed in steel bars outside FSEL was computed and then subtracted from the gage output strain. Figure 6-33 illustrates the strain histories (raw vs. corrected) of foil gages. Although there is some scatter in the data, the corrected strain values generally have good agreement with the expected strains of zero in this application. For temperatures ranging from 25 °F to 130 °F, the raw strain readings and the corrected strain values fluctuate 85 με and 12 με respectively. This is equivalent to an 86% decrease of the recorded strain. Thus, the output signal can be greatly improved by utilizing the thermal coefficients to remove the thermally-induced strain.

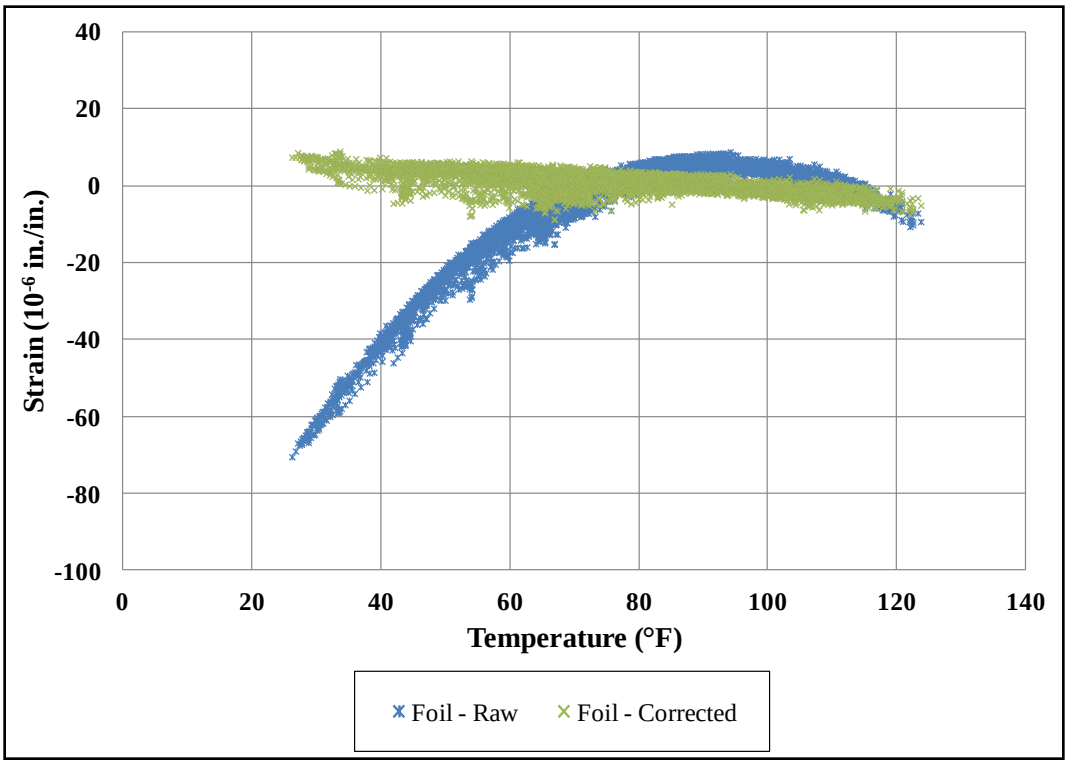

Figure 6-33 : Thermally-induced strain correction of foil gages located outside FSEL

It is worthwhile to mention that the recommended correction method has limitations. The gage thermal coefficients factors (i.e. A_1, A_2...) given by the vendor on the gage package information sheet label correspond to the average thermal properties of the gage alloy. Out of each strain gage lot, only a few samples of gages are tested to compute the thermal coefficient factors. Thus, some variations in the thermal properties of the gages are likely.

6.4.2. Correction method of thermally-induced strain in weldable gages

In most cases, the suppliers of weldable gages do not provide any information about the gage thermal properties and thus thermally-induced strains cannot be eliminated from the output data without calibration tests on the gages over the range of

temperatures to be expected. Such tests are not very practical in most situations. Moreover, there was no information in the literature on how to correct thermally-induced strain in weldable gages. For this reason, it was decided to develop correction methods through experiments. The data presented in the following discussion were collected from weldable gages installed on steel bars and exposed to different environments (i.e. outside FSEL, fridge, and MTS furnace). Finally, the weldable gage data were captured from two different types, namely HBW-W and LEA-R.

The accumulated strain data (Figure 6-34) correspond to the thermally-induced strain of weldable gages, because the strain readings were collected from steel bars that were unloaded and unrestrained. Based on these data, it was possible to determine the relationship between temperature and thermally-induced strain of weldable gages. Figure 6-34 demonstrates how the thermally-induced strain of weldable gages fluctuates for temperatures ranging from 25 °F to 140 °F. The next step was to analyze the data and develop an equation that relates thermally-induced strain and temperature. For this reason, a regression analysis was performed. A regression analysis is a statistical method to estimate the relationship among different variables. In this case there are two variables; the temperature (T) is the independent variable, and the thermally-induced strain ($\varepsilon_{err/\Delta T}$) is the dependent variable. A linear regression model was not used because it would not capture properly the non-linear relationship between temperature and thermally-induced strain. Thus, a polynomial regression model was utilized to develop the correction curve that best fit the accumulated test data based on the least squares approach.

The polynomial regression-fitted equation developed based on the test results of weldable gages is given in Equation 6-8:

For 20 °F ≤ T ≤ 112 °F

$$\varepsilon_{err/\Delta T} = -0.0173 \cdot T^2 + 3.95 \cdot T - 197.8$$ **Equation 6-8**

For 112 °F ≤ T ≤ 140 °F

$$\varepsilon_{err/\Delta T} = 0.13 \cdot T + 13$$

where:

$\varepsilon_{err/\Delta T}$: thermally-induced strain of weldable gages.

T : temperature of steel member in °F.

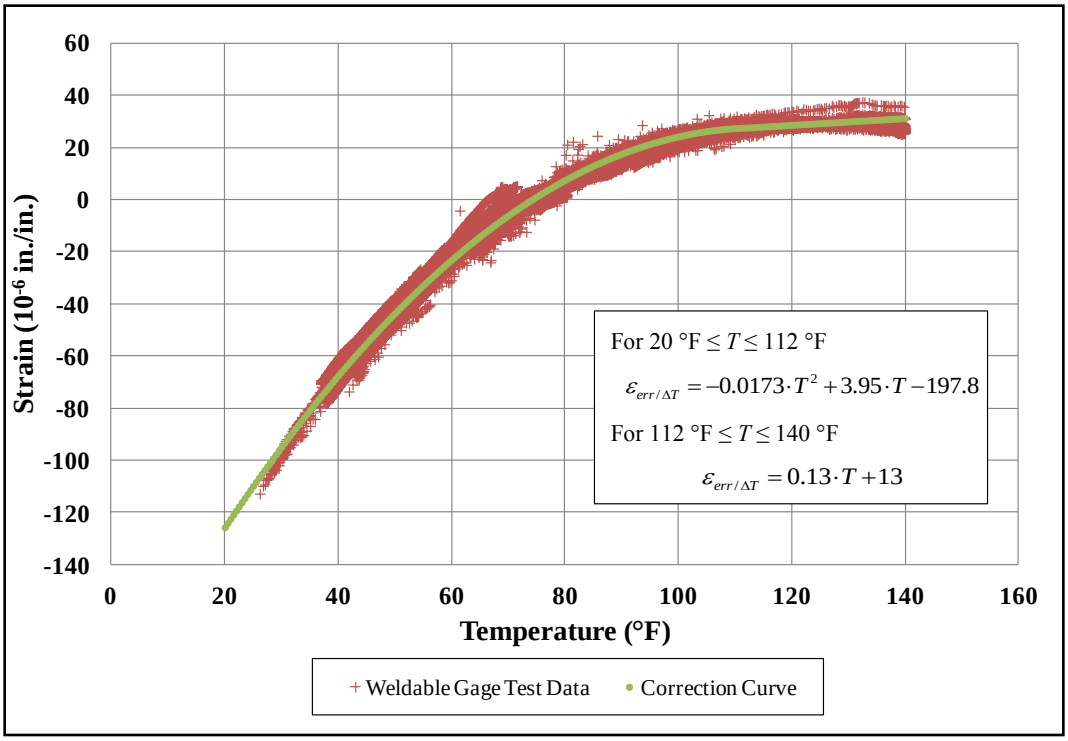

Figure 6-34: Weldable gage correction curve

The first step was to correct the thermally-induced strain of weldable gages exposed to constant temperature levels (Figure 6-35). During this test, the strain readings were very stable due to the nature of the test, and as a result the corrected output data fluctuated over a narrow range of strain. Figure 6-35 demonstrates that for temperatures

varying from 40 °F to 140 °F, the weldable gages record thermally-induced strains ranging from -70 με to 30 με. For the same temperature range, the corrected strain readings swing within a range of 8 με. Last, the strain readings recorded during the thermal tests with different heating rates were corrected to remove thermally-induced strain. Figure 6-36 shows that the recommended correction equation produces results that agree very well with the expected change of 0 με.

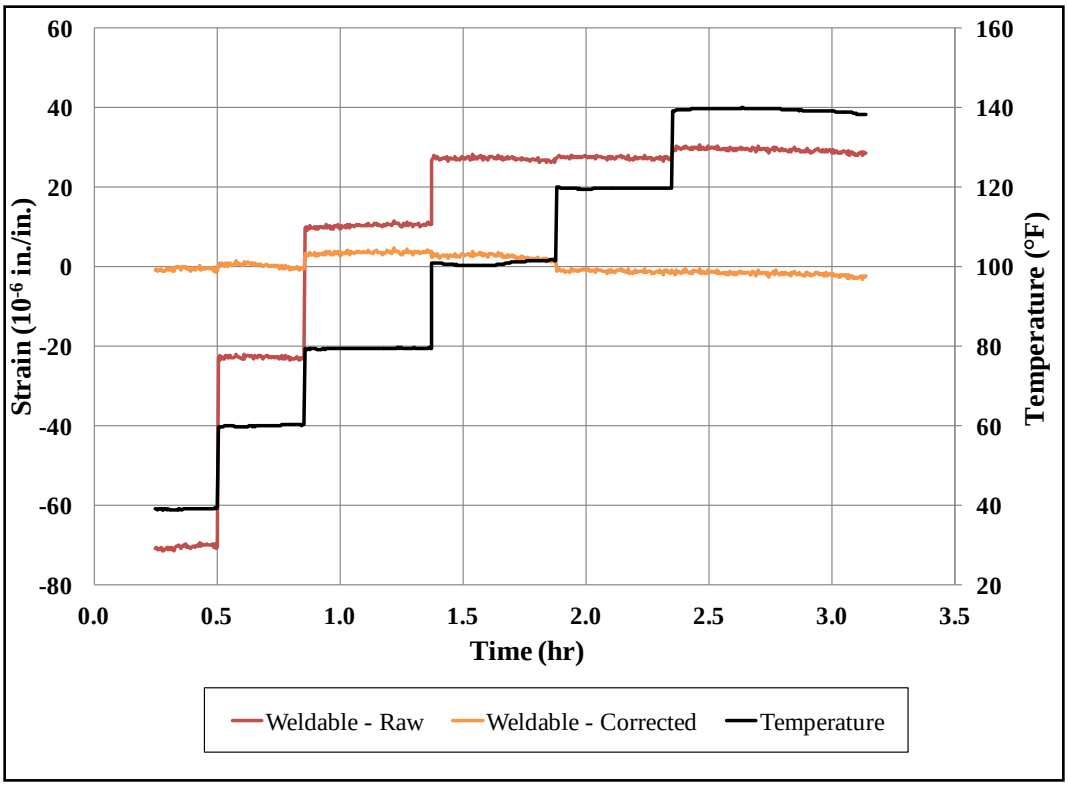

Figure 6-35: Corrected response of weldable gage at constant temperature levels

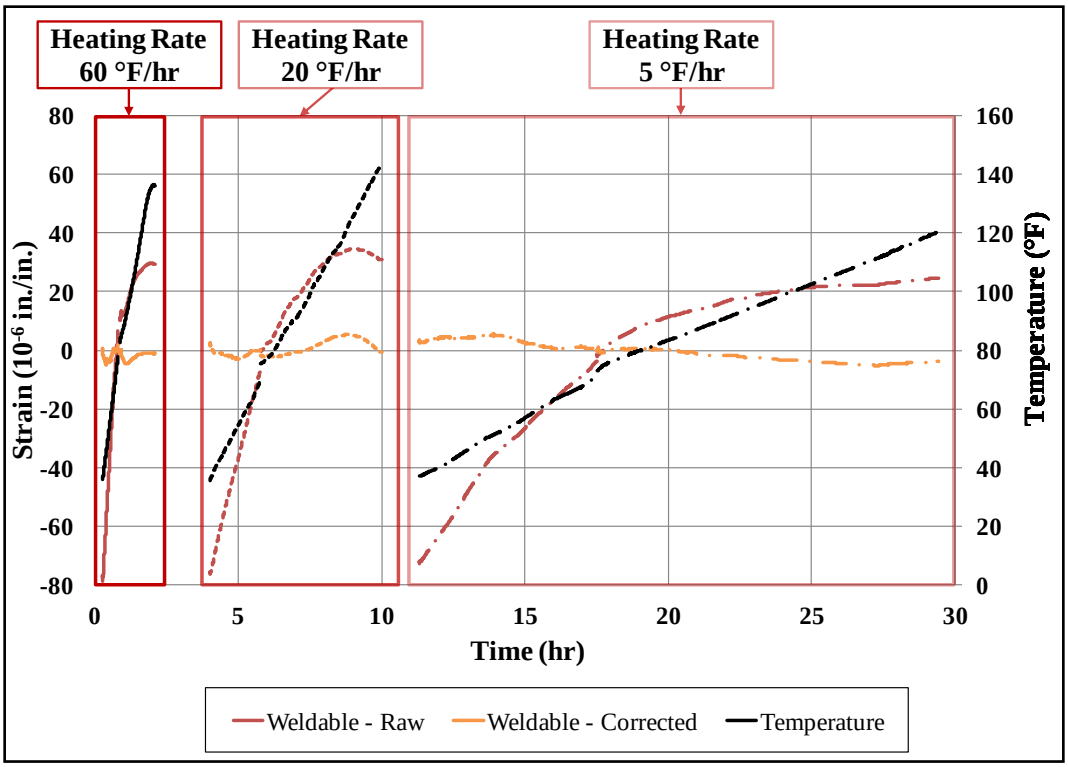

Figure 6-36: Correction of weldable gage response at different heating rates

The recommended correction equation was also validated against data of outdoor environment exposure test. Figure 6-37 shows the strain fluctuations of the raw and corrected data obtained from the gages outside FSEL. For temperatures varied from 25 °F to 130 °F, the uncorrected strain data ranged from -115 με to 35 με. In contrast, the corrected strain data are limited for the most cases within the range -7 με to 12 με. This is an indication that the developed correction equation significantly improves the raw data of the weldable gages.

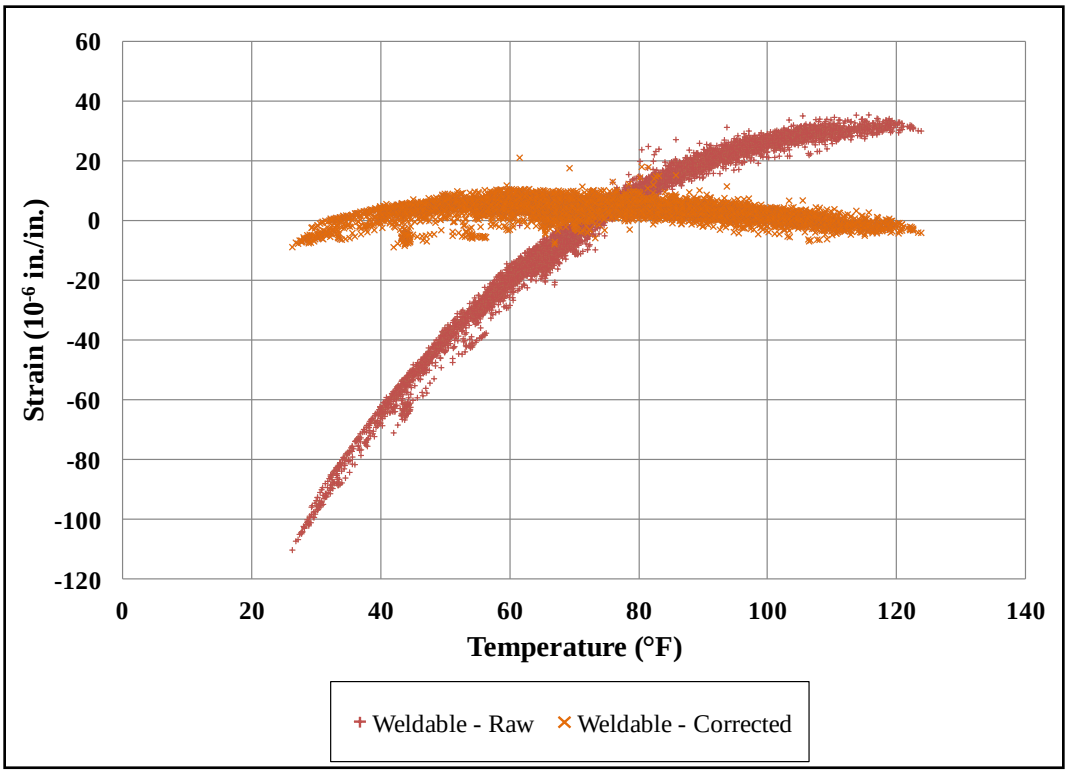

Figure 6-37: Thermally-induced strain correction of weldable gages outside FSEL

6.5. EVALUATION OF LONG-TERM PERFORMANCE OF CRACK PROPAGATION GAGES

As part of this research project, a third testing phase was developed to evaluate the long-term performance of commercial crack propagation (CP) gages. The crack propagation gages provide a convenient method for monitoring the rate of crack growth in a damaged structure. As outlined earlier, the sensor that was investigated consisted of 20 parallel wire strands. When a surface crack progresses through the width of the gage, then the strands successively break resulting each time in an increase of measured resistance.

A benchmark laboratory test of crack propagation gages was performed to validate the gage behavior in a controlled test before using this type of sensor in the field. During this test, a steel coupon with a ¼ –in. notch (Figure 5-21) was cyclically loaded at

to cause stresses to range from 5 - 35 ksi leading to fatigue damage to progress from a crack at the notch tip (Figure 6-38). To monitor the crack growth, one crack propagation gage was installed on each side of the specimen just next to the notch tip. As the crack propagated through the width of the CP gage, the wire strands of the gage broke resulting in a step-wise change of the gage resistance. The fatigue test was terminated when the fatigue crack had propagated through the entire width of the CP gage (Figure 6-39).

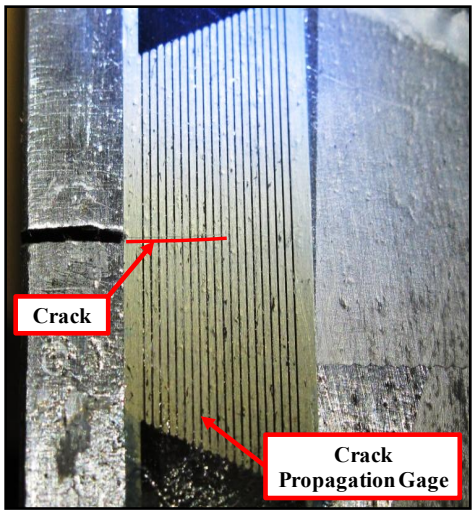

Figure 6-38: Crack propagating through the width of CP gage

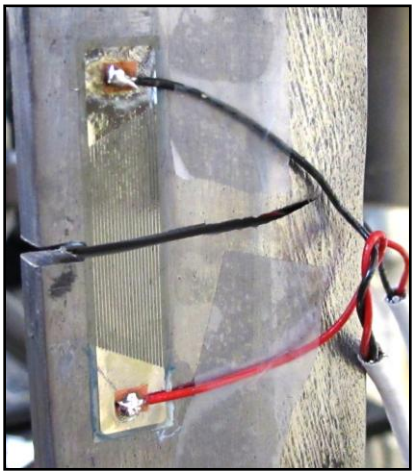

Figure 6-39: Fatigue crack propagated through the width of the CP gage

The results of the fatigue test are plotted in Figure 6-40. The CP gage on each side of the steel specimen tracked very closely the propagation of the crack. The strands of the gage have different lengths resulting in unequal resistance difference each time a strand breaks. It can be easily observed that the recorded resistance difference for the break of the first few strands is small (0.2-0.5 Ohm) but it exponentially increases as more strands break. The resistance difference corresponding to the last two strand breaks is 5 and 10 Ohms respectively.

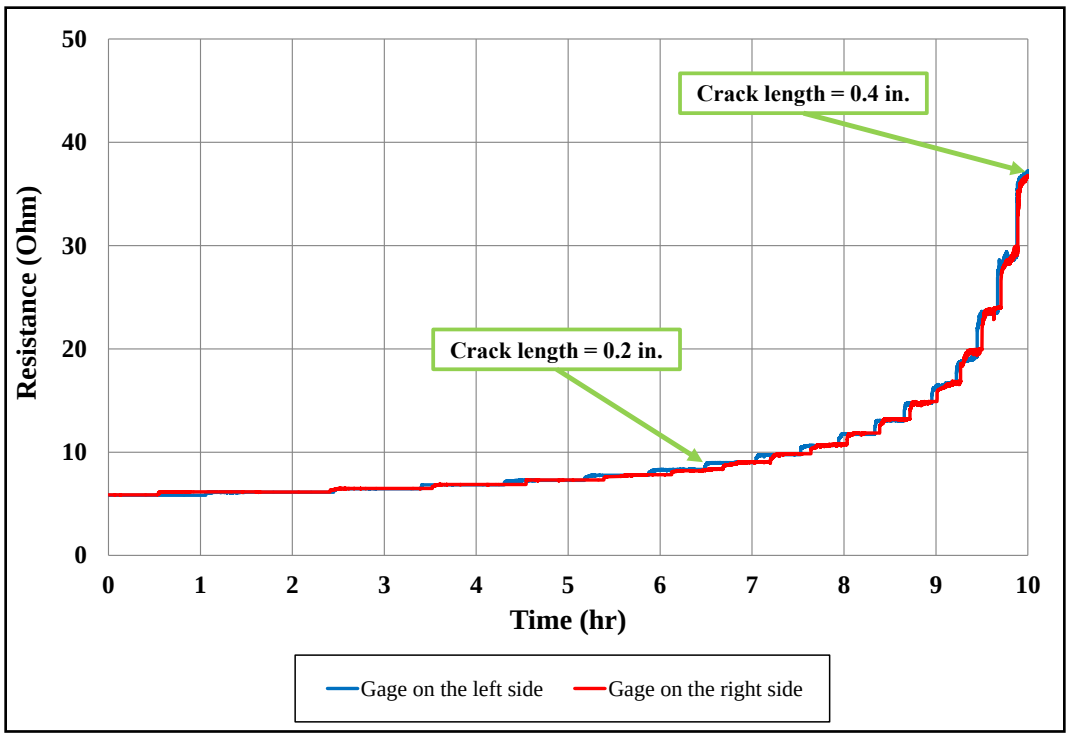

Figure 6-40: Crack propagation gage output during fatigue test

The benchmark laboratory test provided important information on the crack propagation gage behavior. However, concerns were raised about the magnitude of gage readings fluctuations due to thermal effects and if it is possible for an engineer to differentiate these effects from a slow crack growth. For this reason an investigation on

the impact of variations in the ambient temperature on the output of crack propagation gages was conducted. Two crack propagation gages were attached on an unstressed steel bar, which was then placed outside FSEL. The resistance of the two gages was monitored for several months to obtain a significant variation in the range of temperatures that were observed. Conducting the test with no wires broken is the most critical stage of the gage since the resistance changes become larger with each successive wire break. Therefore, temperature changes with no wire breaks are the most likely cases that might be misinterpreted as a potential wire break. The test results indicate that the resistance of the gages varies with the ambient temperature, but the reading fluctuations are relatively small (less than 0.1 Ohm). Figure 6-41 illustrates the recorded resistance and temperature of a typical month. The resistance values of Gage 1 and 2 are shown on the left vertical axis of the graph, and the temperature on the right vertical axis.

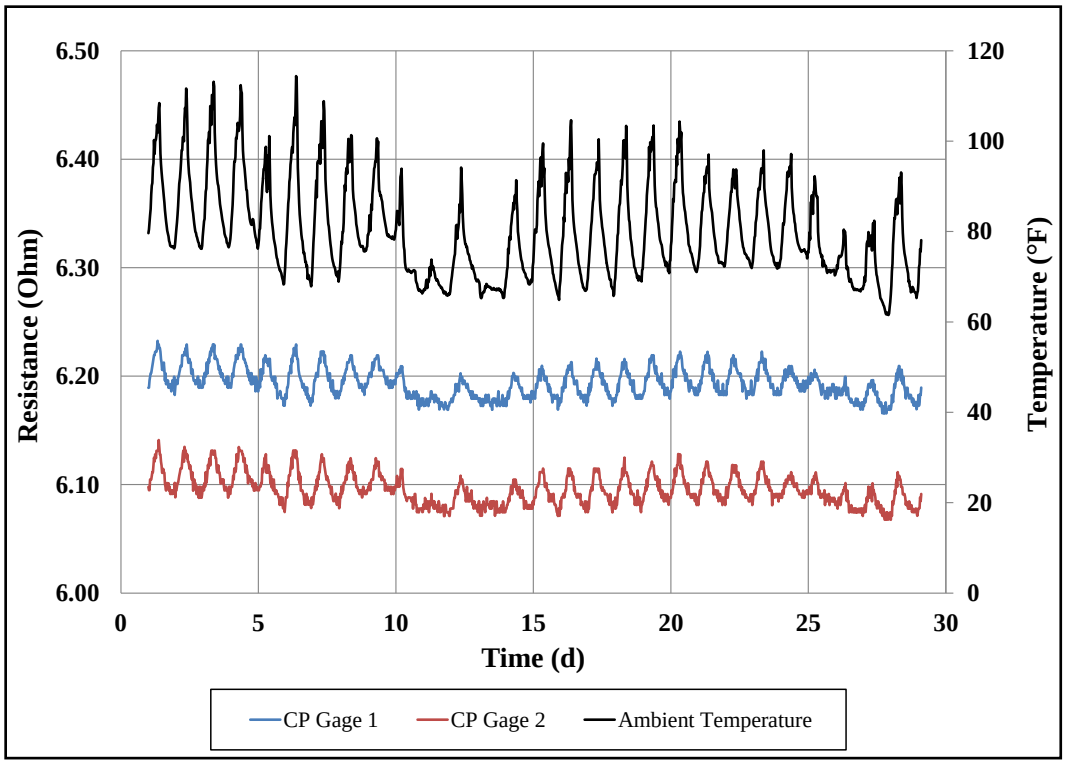

Figure 6-41: Long-term variation of crack propagation gages due to changes in ambient temperature

Even though the drift of the gage due to temperature was fairly small, it must be ensured that it is always less than the resistance change due to a wire break. Thus, the results of the fatigue test were compared with the results of the environmental test. Figure 6-42a illustrates that the range of fluctuating resistance due to thermal effects is approximately one-third of the observed resistance difference corresponding to the first wire break in the crack propagation gage (the initial step observed in Figure 6-40, which corresponds to a crack growth of 0.02 in.). In contrast, the variations due to thermal effects are extremely small compared with the observed resistance difference corresponding to the last wire break in the crack propagation gage (Figure 6-42b). Based

on these results, thermal effects are not expected to lead to misleading data from the crack propagation gages.

The reliability of the CP gages was also evaluated in the field on Bridge A. The crack propagation gages were utilized to monitor the crack growth of two active cracks on the bridge. The CP gages were installed just beyond the crack tip and they were recording data on a daily basis. By comparing the recorded data with the physical crack measurements during visual inspections, it was possible to gain an indication of the ability of the CP gage to reliably indicate crack growth over time.

In November 2010, crack propagation gages were installed at floor beams 34 and 38 of Bridge A (Gage 1 and 2 respectively). Due to power issues of the monitoring system, the resistance from the crack propagation gages was not continuously recorded from November 2010 to April 2011. However, it was possible to capture few data points during this period. The CP gage on floor beam 34 showed a considerable change in resistance, which was an indication of crack growth. The resistance of this gage was 8.7 Ω in November 2010, 12.3 Ω in January 2011, and out-of-range in April 2011. The change in resistance during that period suggested that the crack extended through the entire width of the gage. On the other hand, the crack propagation (CP) gage at floor beam 38 continued to show no crack growth.

To verify the validity of the CP gage results, a visual inspection was conducted. After removing the silicon and wax it was found that the crack propagated through the entire gage (Figure 6-43). The entire crack length was 2 in. in April 2011, with a growth of 0.75 in. since the visual inspection in September 2010. In contrast the crack on floor beam 38 did not propagate during that period, and thus it was accurate that the resistance of the CP gage at this location did not change.

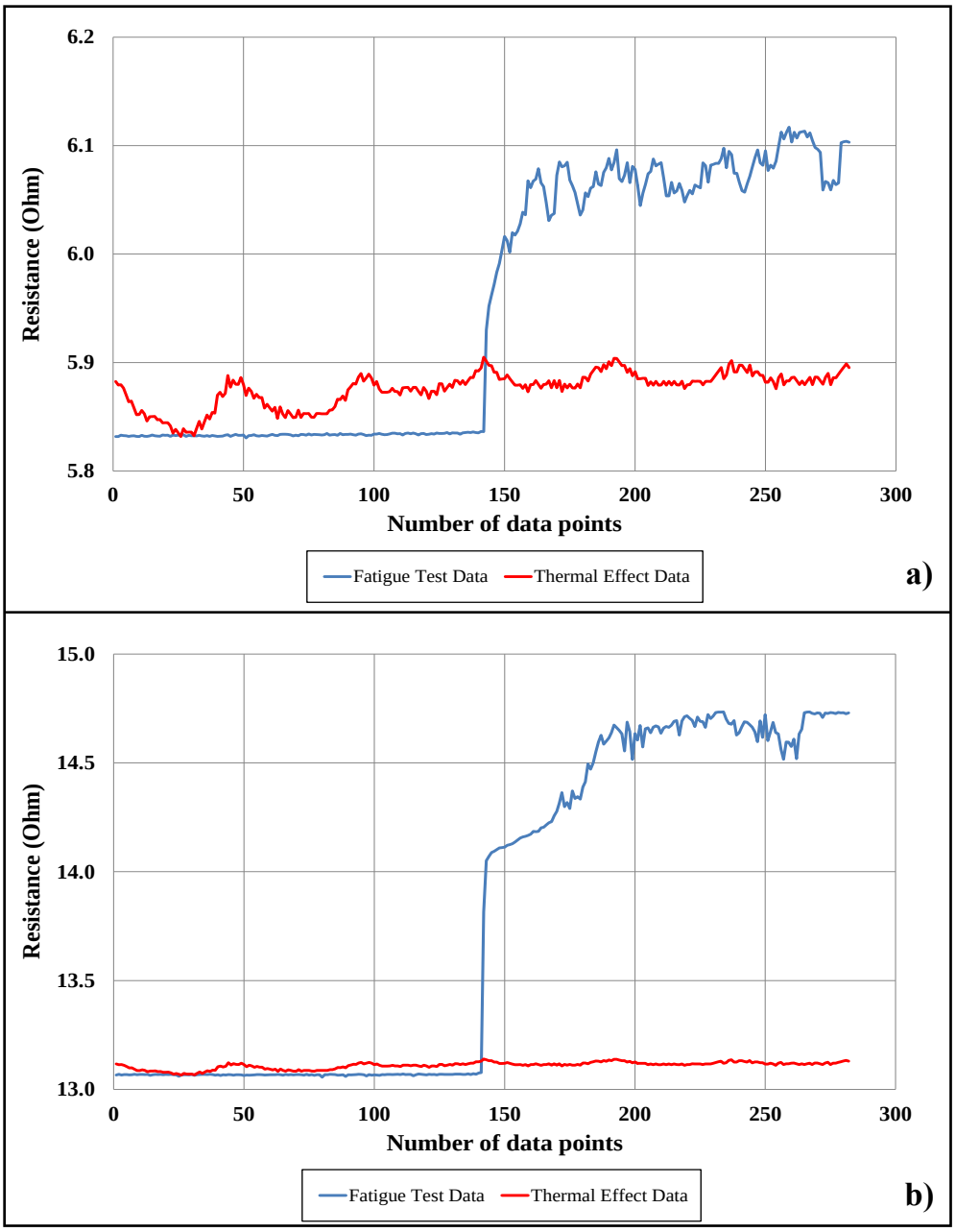

Figure 6-42: Comparison of resistance change in crack propagation gages and thermal fluctuations due to a) first wire break, b) last wire break

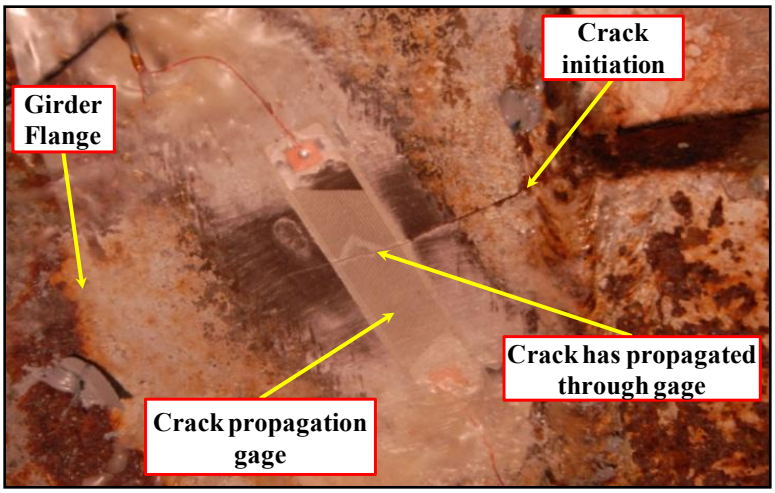

Figure 6-43: Crack on (FB 34) propagated through the Gage 1

Figure 6-44 presents the crack propagation gage resistance at floor beam 34 (Gage 1) and 38 (Gage 2) from April 25, 2011 to September 28, 2011. Due to the continued growth of the crack at floor beam 34, a new crack propagation gage was installed just beyond the crack tip on April 25, 2011. The first wire of the new crack propagation gage broke on 3 May 2011. The crack on floor beam 34 (FB 34) continued to propagate with an almost steady rate of 0.007 in. per day. By June 26, 2011, the crack propagated through the entire width of the second gage (20 strands). The crack at FB 34 grew an additional 0.5 in. in two months. During the same period, the crack on floor beam 38 did not propagate.

On July 22, 2011 the crack propagation gage on floor beam 34 was replaced. Shortly after and based on the results of the crack propagation gage on floor beam 34, the bridge owner decided to retrofit the cracked sections to reduce the rate of crack growth, and ensure the safety of the bridge until the replacement bridge is constructed. The retrofit started at the end of August 2011 and finished at the beginning of November 2011. During the retrofit period, the crack at FB 34 propagate 0.14 in. (7 broken strands),

and no crack growth was recorded for the crack at floor beam 38. At the end of the retrofit project, monitoring of both crack propagation gages stopped.

This field monitoring proved that crack propagation gages are reliable and effective at monitoring crack growth. In fact the recorded data were very important because in a timely manner the fast growth of a crack was indicated. Finally, the drift of CP gages due to temperature is minimal as compared with the change in resistance due to a wire break.

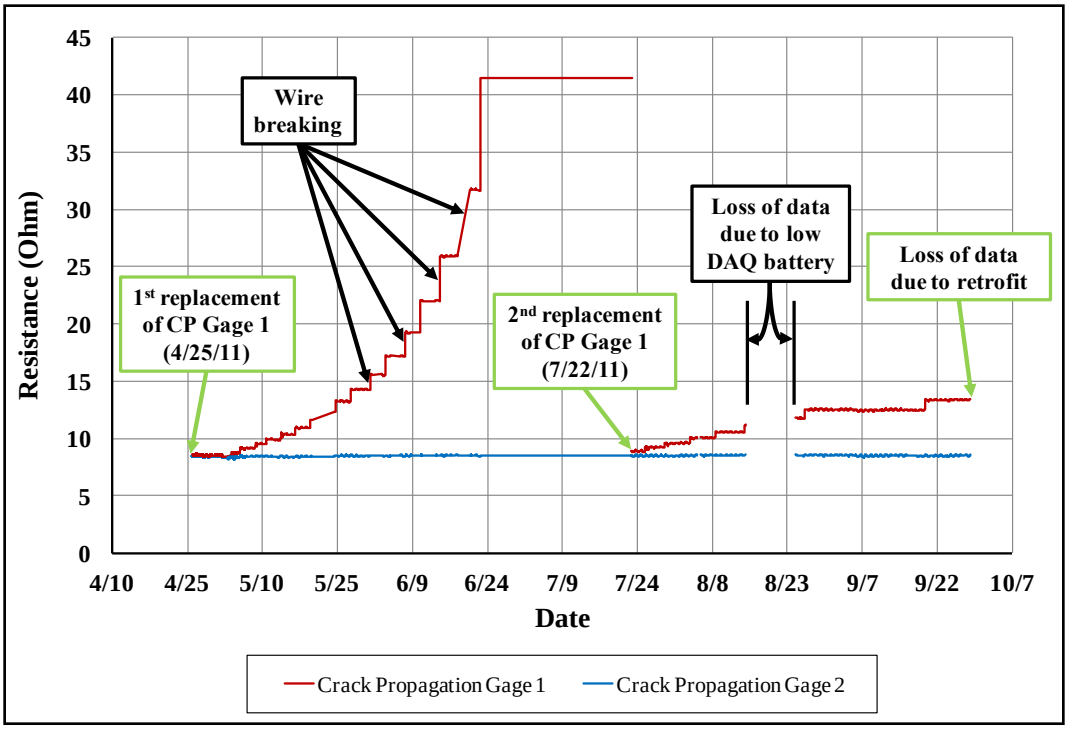

Figure 6-44: Crack growth at floor beam 34 (Gage 1) and floor beam 38 (Gage 2) during 4/25-9/28/2011

CHAPTER 7

Conclusions and Recommendations

7.1. INTRODUCTION

Highway bridges are a vital component of the US transportation network, providing the required infrastructure for traffic to pass over barriers, such as rivers or roadways. However, a significant portion of that US national bridge inventory has exceeded or is nearing the intended service life. Driven by this fact, the US Congress instructed more rigorous inspection standards of deficient bridges and new requirements that DOTs must follow when they report the bridge condition. Recently, the US Congress introduced the Strengthen And Fortify Existing (SAFE) Bridges Act (H.R. 2428). The main objective of the SAFE Bridges Act is to distribute funding to States in order to rehabilitate or replace their structurally deficient and functionally obsolete bridges.

To comply with the new federal requirements, many DOTs face problems acquiring the necessary resources to inspect, and rehabilitate their bridge inventory. With so many bridges nearing the end of their design lives, most DOTs do not have the adequate funds to replace these bridges and the operational lives of the existing inventory will likely have to be extended; however the importance of proper inspection of these older bridges will obviously be intensified. An efficient means of supplementing the inspection process is for DOTs to potentially employ monitoring systems to mitigate the cost associated with inspections, while also improving the safety of these bridges between inspection intervals. Monitoring systems can provide real-time continuous evaluation of deficient bridges and can assist DOTs to better allocate their resources and target their visual inspections. With regard to the type of monitoring system that is used, wired and wireless monitoring systems have advantages and disadvantages.

This dissertation is part of a research investigation focused on developing wireless monitoring systems. The research investigation was a part of a NIST-TIP research project entitled, "Development of Rapid, Reliable and Economic Methods for Inspection and Monitoring of Highway Bridges". Typically, wireless monitoring systems are less expensive than the wired systems because the substantial cost of purchasing cabling is minimized, and particularly with respect the cost of deployment. In addition, wireless monitoring systems are less susceptible to be affected by electromechanical noise that may exist at the bridge environment. On the other hand, the wireless systems usually require more power than a wired system due to the radio transmission requirements and wireless systems are prone to network interference and thus there is a possibility of data loss.

The research team envisioned a monitoring system independent of the power grid with a target maintenance-free life of ten years. Two main areas of concern with regards to the ten-year life are the ability to harvest energy to power the system as well as the necessary reliability of the sensors to withstand the potentially harsh field environment and not require periodic maintenance. From the perspective of power demand, the effectiveness of the wireless system depends on the feasibility to harvest energy. Due to the relatively large loads that result from moving trucks on the bridges, vibrations were targeted as a potential source of energy. However, the availability of energy to be harvested is highly variable within a given structure as well as at different locations of the structure. Therefore, one target focus area of this dissertation was on the possibility to estimate the vehicle-induced vibrations of a bridge based on computational analyses. The ability of the computer analysis to determine the feasibility to harvest adequate energy to power components of the wireless monitoring systems was also considered. The other major issue with the ten-year maintenance free life is the ability of sensors to withstand

the relatively harsh bridge environment. Therefore, another major focus of the dissertation is related to the durability of sensors and the environmental effects (e.g. temperature, humidity etc.) on the behavior of sensors in bridge environments. This chapter summarizes the conclusions and recommendations of the research that was discussed in the previous chapters.

7.2. RECOMMENDATIONS

All the information resulting from this research study was the basis to develop the recommendations, which are presented in this section.

7.2.1. Estimating vehicle-induced dynamic response of bridges

The bridges, which were analyzed during this research study, are typical bridge types that are widely used throughout the world. Apart from the structural system of the bridge, the traffic patterns can significantly impact the dynamic response of the bridge. Traffic patterns differ from bridge to bridge, and thus the engineer should determine the influence of truck load patterns on the bridge response. Regarding the truck loads, it is recommended to utilize typical truck loads from AASHTO (2012) or truck data from weigh in motion stations located near the bridges under investigation.

Two different modeling methods are suggested to dynamically analyze bridges. The two methods are 3D finite element and grillage modeling. The first method combines shell, beam, and truss elements to develop a 3D bridge model, whereas the second method employs simple line elements to represent the main bridge features (e.g. girders, cross-frames etc.). The 3D finite element modeling method must be utilized to analyze a bridge, when the structural system of the bridge is very unique and the component, on which the harvester would be mounted, has a complex geometry (i.e. hanger of suspended span) that cannot be represented with line elements. However, if such bridge

detail does not exist, the grillage method is highly desirable from a modeling perspective due to the simplicity and computational efficiency. The results presented in Chapter 4 support the adequacy of grillage modeling method to characterize the dynamic behavior of the bridge, and hence the engineer in practice is recommended to utilize this valuable tool to estimate the harvester power.

7.2.2. Reliability of sensors

The sensors that were examined during this study are commercially available. The durability of the sensors is greatly influenced by the type of protective system and adhesive agents. For exceptional long-term gage protection, it is recommended to employ the Protection Scheme 1 or 2 described in Chapter 2. Besides the protective coatings, the type of adhesive can greatly affect the gage performance. A rigid and durable bond between the sensor and the structural member surface is essential to obtain reliable data from the sensor. It is recommended to bond foil gages with epoxy resin and diethylaminopropylamine compound, because it creates a durable moisture-resistant bond. However, this adhesive type requires a substantial curing time and as the installation temperature decreases, the curing time is increasing. Hence, if the instrumentation has to take place in a cold environment (e.g. below 65 °F), then it is recommended to use weldable gages.

All strain gages are affected by thermal effects. To minimize the influence of temperature the engineer should use: a) scanning rates of 50-100 Hz), b) shunt calibration to calibrate the sensors, and c) high-precision completion resistors. Also, it is suggested to employ the correction methods outlined in Chapter 6 to eliminate thermally-induced strain. Finally, crack propagation (CP) gages should be used to track crack growth on bridges between bridge inspections.

7.3. CONCLUSIONS

The conclusions of this dissertation are divided into the two areas of focus, which were discussed in the previous chapters. The first major goal of this dissertation was to investigate the possibility of estimating the vehicle-induced vibrational response of the bridge with finite element programs. The second major objective was to identify durable sensors that can be employed to instrument structures, and determine their reliability. The conclusions of this study are summarized in the following sections.

7.3.1. Estimating vehicle-induced dynamic response of bridges

As mentioned in previous chapters, during this investigation two methods (i.e. 3D finite element modeling and grillage simple line modeling) were employed to analyze the instrumented bridges. It was concluded that both methods can be used to estimate vehicle-induced dynamic response of bridges.

1. The 3D finite element modeling method is the best representation of the girder system. In cases with irregular geometries or complex details, this modeling method is likely to best dynamically analyze a bridge. The engineer has the capability of modeling bridge details in greater detail with this method compared to line element solutions.

2. The grillage modeling method can accurately capture the most significant bridge modes of vibration and provide a reasonable accuracy with regards to computing the dynamic response of the bridge. This method greatly simplifies the structure and reduces the computational time.

3. In the bridges studied in this dissertation, most natural frequencies determined from 3D and grillage models vary less than 10%. This conclusion suggests that both modeling methods can produce results with roughly similar frequency content.

4. The use of the lever rule method provides a conservative numerical method to easily obtain reasonable approximate results of the truck load distribution. In this research study the results produced by the lever rule method were in a good agreement with the 3D model results.

5. The results of the truck load distribution computed with the proposed method were very comparable to the load distribution produced by the 3D model. The proposed method utilizes massless line elements that are positioned over the bridge girders as "deck joist" to transfer the applied truck point loads to them. The number of line elements and their relative distance is defined by the truck axles. The entire group of the loaded "deck joists" is positioned above the bridge girders and manually moved along the length of the bridge. Each time that the "deck joist" system is moved, a static analysis is performed to obtain the summation of reactions of each girder.

6. The potential vibrational energy is highly dependent on the truck traffic patterns. Therefore, the engineer should investigate the influence of traffic patterns on the dynamic response of the bridge under investigation.

7. If the weight of the harvester is comparable to the weight of the bridge member (e.g. slender brace) that is mounted, then the engineer should include the harvester weight in the analysis. Neglecting the harvester weight in the analysis can overestimate the power production.

7.3.2. Long-term sensor reliability

The reliability and durability of different sensors and their protection systems were the main focus of the second half of this dissertation. Even if the sensors were not evaluated for more than 10 years due to the limited project length (4-year project), the sensor studies revealed that foil bondable gages and weldable gage can potentially be

very reliable if they are protected sufficiently. Moreover, it was concluded that crack propagation gages can accurately monitor the crack growth of know cracks.

1. A layer of zinc-based spray is not adequate to protect weldable gages from environmental contaminants, such as moisture. Most of the weldable gages protected with this method failed due to debonding of the sealed gage from the stainless steel shim.

2. The butyl rubber patch alone is not a durable protective coating for long-term monitoring applications. The majority of bondable sealed gages that were protected with butyl rubber sealant debonded from the specimen surface.

3. Good long-term gage protection is achieved by utilizing the protection scheme 1, which consisted of the following: a) primer paint over gage lead wires to enhance the bond with the next protective layers, b) a solvent-thinned acrylic paint to insulate the open air connections and the metal shim of sealed gages from moisture, c) Teflon tape over foil bondable gages and solder connections, d) butyl rubber sealant on top of the gage, e) aluminum tape should cover the entire installation area, and f) contact cement paint to seal any imperfection of the aluminum tape.

4. An alternative durable protective system for long-term applications is protection scheme 2, which consisted of the same first three steps as protection scheme 1. The next step is to apply a layer of microcrystalline wax over the gage. Finally, a layer of a heavy duty two-part polysulfide liquid polymer (PLP) compound is applied on top of the wax to increase the protection against environmental contaminants.

5. The two-part (i.e. epoxy resin and diethylaminopropylamine compound) heavy duty epoxy should be used for superior and durable bonding performance. This bonding agent creates a tough, rigid, high strength bond that is resistant to moisture and most common solvents.

6. The general-purpose cyanoacrylate bonding agents are moisture-resistant but less durable than the two-part heavy duty epoxy, which was described above. This type of adhesive is easy to apply and it requires less curing time than the superior two-part heavy duty epoxy. Thus, for typical instrumentations where harsh environmental contaminants are not present, this adhesive is preferable.

7. The special two-part adhesive (i.e. cyanoacrylate adhesive and cyanoacrylate activator) is not durable against moisture. This adhesive is required to install bondable sealed gages, but its poor resistance to moisture caused the debonding of gages.

8. Bondable foil gages covered with protection scheme 1 or 2 have very durable performance. This type of gage did not experience any failure due to moisture, corrosion, or other environmental contaminants during the last three years.

9. Weldable gages sealed with the protection scheme 1 or 2 can provide an alternative robust sensing solution for long-term instrumentations. There were no problems with malfunctioning gages during the 16 months period that protection schemes 1 or 2 were utilized as the protective system of weldable gages.

10. The strain gage deteriorates very rapidly once the moisture penetrates below the protective coatings. There was no observation of any gradual strain reading drifting or fluctuation from the gages that debonded.

11. Weldable gages are affected by temperature fluctuations in greater degree than bondable foil gages. Depending on the temperature level, the thermally-induced strain recorded by weldable gages can be up to 40 με more than that of foil gages.

12. Loading conditions (i.e. unloaded or loaded), and size of the instrumented member (i.e. mass) have a negligible effect on thermally-induced strain. The strain

readings from foil and weldable gages are very similar regardless of the loading condition, specimen mass and location of gage.

13. The heating rate has no effect on the behavior of both foil and weldable gages, and the strain fluctuation depends solely on the temperature range.

14. The correction formula provided by the strain gage manufacturers is the most accurate technique to correct the thermally-induced strain in bondable foil gages. The correction formula is an empirical fourth-order polynomial equation that relates thermally-induced strain ($\varepsilon_{err/\Delta T}$) and temperature ($T$). Generally, the corrected strain values fluctuated within the range -5 με to 7 με.

15. The recommended correction equation to minimize the thermally-induced strain in weldable gages greatly improves the output signal. In most cases, the corrected output data fluctuate within the range -7 με to 12 με.

16. The fatigue tests revealed that spot welds can influence the fatigue life of the steel specimen, yet the fatigue life corresponds to a Category A fatigue detail. Spot welds can initiate cracks. Bondable gages do not initiate fatigue cracks, but the bondable sealed gage debonded after 6.5 million cycles.

17. Temperature fluctuation has a minor effect on the crack propagation gage readings. The environmental tests indicated that the drift of the gage due to temperature was less than the change in resistance due to a wire break.

7.4. FUTURE WORK

Considerable progress has been made during this research study towards modeling and dynamically analyzing bridges with grillage models, and understanding the environmental effects on gage behavior. However, much work is still needed in these two areas of research. Regarding the analysis procedures, the traffic patterns differ from

bridge to bridge and the dynamic analysis of multiple truck loads was limited in this investigation. Therefore, a further investigation of different types of bridges (e.g. cable-stayed, arch etc) and traffic patterns is recommended.

With regards to sensor reliability, the long-term reliability investigation of gages should be extended to cover more types of gages. This is due to the fact that the reliability test results cannot directly be extrapolated for all the types of sensors. Finally, it is worthwhile to investigate self-compensated weldable gages and determine the relationship between temperature and thermally-induced strain.

REFERENCES

Adams, P. H. (1983). *Transient Temperature Response of Strain Gages.* SAND-80-2689, Rev. 1, Sandia National Laboratory, Albuquerque, NM.

Al-Wazeer, A., Harris, B., & Dekelbab, W. (2008). *Applying "Fuzzy Concept" To Bridge Management*. FHWA Public Roads Magazine, vol. 72, No.1. Retrieved July 12, 2013, from Federal Highway Administration website: http://www.fhwa.dot.gov/publications/publicroads/08july/04.cfm

American Institute of Steel Construction (AISC), (2011). *Steel Construction Manual, 14th Edition.* Chicago, IL.

American Association of State Highway and Transportation Officials (AASHTO), (2012). *LRFD Bridge Design Specifications, Customary U.S. Units*, *6th Edition.* Washington, D.C.

ANSYS Inc., (2012) *ANSYS Structural Analysis Guide.* Canonsburg, PA

Billing, J. R. (1979). *Estimating the natural frequencies of continuous multi-span bridges.* Research Report 219, Ontario Ministry of Transportation and Communications, Research and Development Division, Ontario, Canada.

Blosser, M. L., Nowak, R. J., & Rothgeb, T. M. (1988). *Thermal-Structural Tests of a Water/Glycol Cooled Aluminum Panel*. Workshop on Correlation of Hot Structures Test Data with Analysis, NASA CP-3065, vol. I, pp. 158–178.

Computer & Structures Inc. (CSI), (2011). *CSI Analysis Reference Manual for SAP2000, ETABS, SAFE, and CSiBridge*. Berkeley, CA.

Crossbow Technology. (2012). *Accelerometer Product Catalog*. Retrieved October 12, 2012, from Crossbow Technology website: http://bullseye.xbow.com:81/Products/productdetails.aspx?sid=167

Dierks, E. C. (2011). *Design of an Electromagnetic Vibration Energy Harvester for Structural Health Monitoring of Bridges Employing Wireless Sensor Networks*. Master's Thesis, Mechanical Engineering Department, The University of Texas at Austin.

Ellis, B. L., & Smith, L. M. (2009). *Modeling and Experimental Testing of Strain Gauges in Operational and Failure Modes*. IEEE Transactions on Instrumentation and Measurement, vol. 58, No. 7, pp. 2222-2227.

European Committee for Standardization. (CEN), (2005). *Eurocode 3 - Design of steel structures - Part 1-2: General rules - Structural fire design, prEN 1993-1-2:2005 E.* Brussels, Belgium.

Fasl, J. D. (2013). *Estimating the Remaining Fatigue Life of Steel Bridges Using Field Measurements*. PhD Dissertation, Civil, Architectural, and Environmental Engineering Department, The University of Texas at Austin.

Fathali, M., & Sadegh, j. (2012). *Grillage analogy applications in analysis of bridge decks*. Australian Journal of Civil Engineering, vol. 10, No. 1, pp. 23-35.

Federal Highway Administration (FHWA), (2012). *Deficient Bridges by State and Highway System*. Retrieved September 4, 2012 from FHWA website: http://www.fhwa.dot.gov/bridge/nbi/defbr10.cfm

Geokon, Inc. (2012). *Geokon Products Catalog.* Retrieved October 12, 2012, from Geokon Inc. website: http://www.geokon.com/products/

Geokon, Inc. (2009). *Instraction Manual Model 4000 and 4050 – Vibrating Wire Strain Gage*. Lebanon, NH

Gomes, P. T. V., Maia, N. S., Mansur, T. R., & Palma, E. S. (2003). *Temperature Effect on Strain Measurement by Using Weldable Electrical Resistance Strain Gages*. Journal of Testing and Evaluation, vol. 31, No. 5.

Hitec Products, Inc. (2012). *Hitec Products Catalog.* Retrieved October 12, 2012, from Hitec Products, Inc. website: www.hitecprod.com/

Inamdar, S. A. (2012). *Design of a Solar Energy Harvesting System for Structural Health Monitoring Systems*. Master's Thesis, Mechanical Engineering Department, University of Texas at Austin.

Kowalik, A. R. (2009). *Fracture Critical Inspections of Twin Tub Girder Units - TxDOT's Perspective*. Retrieved September 4, 2012 from Ferguson Structural Engineering Laboratory website: http://fsel.engr.utexas.edu/research/5498_webinar/kowalik.pdf

Laman, J. A., Sellers, J. B., & Schulz, J. L. (2006). *Influence of Temperature on Highway Bridge Strain Measurements Using Vibrating Wire Gages.* Retrieved April 4, 2010 from Bridge Diagnostics, Inc. website: http://bridgetest.com/download/?id=1218

LePatner, B. B. (2012). *Save our bridges*. Retrieved January 12, 2013, from Save Our Bridges website: http://saveourbridges.com/basics.html

Mazurek, D. F., & DeWolf, J. T. (1990). *Experimental study of bridge monitoring technique.* Journal of Structural Engineering, vol. 116, No. 9, pp. 2532-2549.

McEvoy, T. K. (2011). *Wind Energy Harvesting for Bridge Health Monitoring*. Master's Thesis, Mechanical Engineering Department, University of Texas at Austin.

Memory, T. J., Thambiratnam, D. P., & Brameld, G. H. (1995). *Free vibration analysis of bridges*. Engineering Structures, vol. 17, No. 10, pp. 705-713.

Meng, J.-Y., & Lui, E. M. (2002). R*efined stick model for dynamic analysis of skew highway bridge*. Journal of Bridge Engineering, vol.7, No. 3, pp. 184–194.

New Jersey Department of Transportation (NJDOT), (2001). *Road user cost manual*. Retrieved September 4, 2012, from NJ DOT website: http://www.state.nj.us/transportation/eng/documents/RUCM/pdf/RUCManual.pdf

National Bridge Inventory (NBI). (2012). *Age distribution of highway bridges in the US*. Retrieved September 4, 2012, from NBI website: http://nationalbridges.com/

National Cooperative Highway Research Program (NCHRP) Report 133, (1972). *Procedures for Estimating Highway User Costs, Air Pollution, and Noise Effects*. NCHRP Report 133.

National Instruments Inc. (2012). *NI WSN-3214 (Programmable)*. Retrieved September 10, 2012, from National Instruments Inc. website: http://sine.ni.com/nips/cds/view/p/lang/en/nid/210012

National Instruments Inc. (2012). *NI WSN-3212 (Programmable)*. Retrieved September 10, 2012, from National Instruments Inc. website: http://sine.ni.com/nips/cds/view/p/lang/en/nid/207089

Olson, D. (2008). *I-35W engineer answers concerns about the new bridge*. Retrieved September 3, 2012, from MPR News website: http://minnesota.publicradio.org/display/web/2008/07/30/issues_2004/

Omega Engineering Inc. (2012). *Omega Thermocouple Wire*. Retrieved October 12, 2012, from Omega Engineering Inc. website: http://www.omega.com/

Patten, W. N., Sack, R. L., & He, Q. (1996). *Controlled semiactive hydraulic vibration absorber for bridges.* Journal of Structural Engineering, vol. 122, Issue 2, pp. 187-192.

Reichenbach, M. C. (2012). *Evaluating Vehicular-Induced Vibrations of Typical Highway Bridges for Energy Harvesting Applications*. Master's Thesis, Civil, Architectural, and Environmental Engineering Department, University of Texas at Austin.

Richards, W. L. (1996). *A New Correction Technique for Strain-Gage Measurements Acquired in Transient-Temperature Environments*. NASA Technical Paper 3593

Roundy, S., Wright, P. K., & Rabaey, J. (2003). *A study of low level vibrations as a power source for wireless sensor nodes*. Computer Communications, vol. 26, pp. 1131-1144.

Vishay Micro-Measurements Group, Inc. (2007). *Fatigue Characteristics of Vishay Micro-Measurements Strain Gage*. Micro-Measurements Group TN-508-1, pp. 83-90. Retrieved April 2, 2010, from Vishay Micro-Measurements Inc. website: http://www.vishaypg.com/docs/11058/tn5081.pdf

Vishay Micro-Measurements Group, Inc. (2010). *Errors Due to Wheatstone Bridge Nonlinearity*. Micro-Measurements Group TN-507-1, pp. 77-81. Retrieved April

2, 2011, from Vishay Micro-Measurements Inc. website: http://www.vishaypg.com/docs/11057/tn5071.pdf

Vishay Micro-Measurements Group, Inc. (2010) *Strain Gage Accessories*. Retrieved October 12, 2012, from Vishay Micro-Measurements Inc. website: http://www.vishaypg.com/docs/50001/sgaccess.pdf

Vishay Micro-Measurements Group, Inc. (2012) *Strain Gage Thermal Output and Gage Factor Variation with Temperature*. Micro-Measurements Group TN-504-1, pp. 1–14. Retrieved September 22, 2012, from Vishay Micro-Measurements Inc. website: http://www.vishaypg.com/doc?11054

Vishay Micro-Measurements Group, Inc. (2012). *Vishay Micro-Measurements Products Catalog*. Retrieved October 12, 2012, from Vishay Micro-Measurements Inc. website: http://www.vishaypg.com/micro-measurements/

Weaver, J. M., Wood, K. L., & Crawford, R. H. (2010). *Design of Energy Harvesting Technology: Feasibility for Low-Power Wireless Sensor Networks*. Proceedings of the ASME IDETC & CIEC Conference in Montreal, Canada. pp 1-11.

Weingroff, R. F. (1996). *Federal-Aid Highway Act of 1956: Creating the Interstate System*. FHWA Public Roads Magazine, vol. 60, No.1. Retrieved June 12, 2013, from Federal Highway Administration website: http://www.fhwa.dot.gov/publications/publicroads/96summer/p96su10.cfm

Wills, J. (1977). *Correlation of calculated and measured dynamic behavior of bridges*. TRRL Supplementary Report 275, Transportation Road Research Laboratory, Crowthome, UK.

Wilson, E. J. (1970). *Installation and Testing of Strain Gages for High-Temperature Aircraft Applications*. Society for Experimental Stress Analysis Fall Meeting, Boston, Massachusetts, pp. 136+.

Zimowski, K. A. (2012). *Next Generation Wind Energy Harvester to Power Bridge Health Monitoring Systems*. Master's Thesis, Mechanical Engineering Department, University of Texas at Austin.